University of Strathclyde Science

Relativistic electrons and radiation from intense laser-plasma sources

by Jordan G Gallacher B.Sc.

A thesis presented for the partial fulfilment of the requirements for the degree of Doctor of Philosophy

Department of Physics
University of Strathclyde
John Anderson Building
107 Rottenrow
G4 0NG

Supervisor: Prof. D. A. Jaroszynski

September 2010

‘This thesis is the result of the author’s original research. It has been composed by the author and has not been previously submitted for examination which has led to the award of a degree.’

Signed:
Date:

Abstract

Laser wakefield electron beams have excellent potential as drivers of ultrashort radiation pulses for applications across the medical and life sciences. This thesis presents measurements of electron beams and subsequent radiation arising from the interaction of intense lasers with underdense plasma. Electron beam production has been observed in experiments carried out at RAL, using the 40 fs, 20 TW Astra laser and at the university in Jena using the 80 fs, 20 TW JETI system. Quasi-monoenergetic electron multi MeV electron bunches with relative energy spreads of between 3-10% (FWHM) were generated by the interaction of tightly focussed laser pulses in a high pressure gas jet of helium. This thesis also presents measurements of the electron bunch duration by measuring the CTR generated when the bunch crosses the plasma-vacuum or metal vacuum boundary. This radiation is essentially a fingerprint of the temporal electric field profile of the electron bunch and is measured electrooptically using a ZnTe crystal. A novel cross-correlation measurement technique in BBO was employed to determine the upper limit of the bunch duration to be approximately 200 fs.The first demonstration of undulator radiation generated from laser wakefield accelerated electron beams was shown by coupling electron beams of 55-70 MeV to a 50 period undulator. This produced synchrotron light pulses in the 700 900 nm wavelength range. Simultaneous measurements of the electron energy with the optical undulator spectrum have confirmed a relative energy spread of 1% rms. This measurement marks an extremely important result in the development of laser driven FELs. A final proof of principle experiment to investigate the feasibility of generating ultrashort, tailored optical light pulses was carried out as a novel ultrashort tunable light source and has important implications in areas that require ultrahigh temporal resolution such as ultrafast chemical and biological processes.

Acknowledgements

The completion of this thesis marks the end of a chapter in my life, and would not have been possible without the encouragement and support of some key individuals. My deepest gratitude goes to my supervisor Prof. Dino Jaroszynski, who provided me with valuable guidance and direction in my endeavors. My sincerest thanks to you for your dedicated assistance and in bringing out the best in my research and development as a scientist. I would also like to say a big thank you to Riju, Albert, Mark, Bernhard, Enrico, and all of the TOPS group for their friendship and assistance over the years. I would also like to thank Andrey, whom I shared many good times with both, in, and out of the office. A large part of my research was conducted at the Rutherford Appleton Laboratory (RAL) using the Astra laser and I must express thanks to my colleagues whom I worked with there; particularly Chris Murphy, Alex Thomas, Christos Kamperidis, Anthony Gonsalves, Thomas Rowlands-Rees, Stefan Kneip and everyone else in the Imperial College group and the Astra team whom I have been acquainted with over the years. I would also like to express my gratitude to Alexander Debus, Fabian Budde, Hans-Peter Schlenvoigt and all of the Jena team who I have closely worked with over the last three years. Our dedication, teamwork and perseverance were central to the success of the undulator experiments. For the work carried out in the later stages of my PhD, I would like to say thank you to Jinhai Sun. His work ethic was inspirational during the year he spent at Strathclyde, and I will never forget the personal record we set together of thirty six consecutive hours in the laboratory, needless to say all the other 'all nighters' we pulled together thought our time as a team. My appreciation also goes to Nuno Lemos, Seth Brussaard and João Dias who I had the pleasure of working with on the ionisation front experiments. I will forever remember our heroic efforts in the lab and many interesting theoretical and experimental discussions during the 'wee' hours.

I would also like to thank Ken Carpy for his generosity and for the hours he dedicated in his spare time helping me with my mathematics during my late secondary school and 1*st* year university days. Thanks must also go to Ian Dunkin and Dave Sherrington, who provided me with invaluable advice, encouragement and a friendly ear when needed.

I would also like thank Claire for all her support and encouragement through my PhD studies and also for all the expert advice on Matlab scripts. Last, but certainly not least, I must thank my parents, Jennifer and Michael, thank you both for everything, especially all the inspiration, encouragement and support over the years.

The role of the author

The complex nature of experiments carried out using high power laser systems necessitates the involvement of a large team of people. This section outlines the role of the author in the work presented in this thesis.

The data presented in chapter 3 was the result of three experimental campaigns, two of which were carried out using the Astra 20 TW laser at RAL and one with the JETI 20 TW laser at Jena. During the first experiment (section 3.1) using the Astra laser in 2004 the author was responsible for alignment of the laser, data acquisition and the development of the electron spectra from the image plates using the Fuji image plate reader. This data was ultimately used in the 'dream beam' Nature publication in 2004. With regard to the second experiment (section 3.2) performed at Jena the author was responsible for setting up and aligning the electron spectrometer and the cross-correlator for the electro-optic detection of the electron bunch duration. The goal of this experiment was to electro-optically measure the duration of the electron bunches produced from the laser wakefield. Although this work was successfully completed, the results presented in chapter 5 rendered this work obsolete and are therefore not presented in this thesis, however, measurements of the generated electron beams are presented in section 3.2. In the third electron generation experiment (section 3.3) the author was involved in the alignment of the laser and the capillary, calibration of the energy meters, synchronisation of the discharge to the laser pulse, data acquisition, and post experiment analysis. Furthermore, for 3 days of the experimental run the author was assigned the role of laser operator, which involved being in charge of the experiment and laser operation.

The data presented in chapter 5 was carried out using the Astra laser in 2005. This was a follow-up campaign to the experiment described in section.3.2 which sought to measure the electron bunch duration from the laser wakefield. The author played an important role in the success of this experiment. Prior to the main experimental run, measurements had to be taken to characterise the electro-optic crystals using the THz test bed described in section 5.0.2 and shown in figure 5.2. Furthermore the author played a central role in the alignment, data acquisition and post experiment analysis which involved the characterisation of the spectral transmission of the THz filter used in the experiment.

The experiment presented in chapter 6 aimed to backscatter THz radiation off a relativistic ionisation front. The author was responsible for the planning, design and general running of the experiment and was actively involved in the analysis and interpretation of the data.

The final chapter presents the first ever demonstration of undulator radiation produced from laser wakefield accelerated electron bunches. The author was actively involved in all areas of the experimental tasks, including alignment of the laser beam, the electron beam, the undulator radiation detection system, the undulator, and the electron spectrometer. Furthermore, the author was involved in the post-experiment analysis and interpretation of the data, which included performing simulations and modeling the undulator radiation using Mathematica and Matlab scripts. These scripts were cross checked and verified using the SPECTRA code [5]. Moreover, the author also carried out calculations on the expected levels of transition radiation from the electron beam and plasma. These simulations were important to verify that the transition radiation would not impinge on desired measurements of the visible undulator radiation. Finally, the author was involved in the drafting of the Nature physics publication in 2008 [6] which resulted from this work. Following on from this, the author investigated the data in more detail and published a paper in Physics of Plasmas on the feasibility of using the undulator radiation as an electron beam diagnostic [7].

Contents

List of Figures

List of Tables

Chapter 1

Introduction

1.1 Relativistic laser-plasma interactions

Ultrahigh intensity lasers have become important tools in modern physics. The invention of chirped pulse amplification (CPA) [15, 16] resulted in a rapid evolution of high power laser science in recent years and has opened an exciting new window of investigation into novel light-matter interactions. The CPA technique, which involves amplification of a stretched laser pulse before re-compression, has made it possible to generate ultrashort laser pulses down to several femtoseconds with peak powers reaching 1 TW–1 PW levels. Laser pulses from advanced systems [17, 18] can be focused down to just a few micrometres using adaptive optics to create electromagnetic intensities up to 10^{21} Wcm^{-2}. At such intensities the electric fields exceed 10^{11} Vcm^{-1}, which is many times the binding energy of electrons in an atom. As a consequence gaseous or solid targets placed at focus will undergo rapid ionisation to form plasma.

A laser pulse can propagate in plasma if the electron density, n_e, is below the critical density, $n_{cr} = m\omega_0^2/4\pi e^2$, where m_e is the electron rest mass, e is the charge on an electron and ω_0 denotes the central (carrier) frequency of the laser pulse. Plasmas with $n_e > n_{cr}$ are known as overdense and plasmas with $n_e < n_{cr}$ are underdense. For a given laser wavelength $\lambda_0 = 2\pi c/\omega_0$, the critical density is found to be $\pi/r_e\lambda_0^2$, where $r_e = e^2/m_ec^2$ is the classical electron radius. For a typical solid-state laser with a wavelength of 800 nm, as is often used in laser wakefield acceleration, the critical density is 1.75×10^{21} cm^{-3}. This is 2 to 3 orders of magnitude higher than the plasma densities considered in this thesis (10^{18}–10^{19} cm^{-3}). Solid targets typically form overdense plasmas, meaning that the laser field cannot penetrate the plasma and is therefore reflected. On the other hand gas jet targets typically form underdense plasmas that allow the laser field to be transmitted through the plasma. The plasma formed in this manner will comprise the usual fluid-like mixture of electrons and ions, however in this case the motion of the plasma electrons is strongly dominated by the laser field. The propagation velocity of the laser pulse in plasma is the group velocity $v_g = c(1 - n_e/n_{cr})^{1/2}$, which is close to c, the speed of light in vacuum. The plasma refractive index is given by

$$\eta_p = ck_0/\omega_0 = \sqrt{1 - n_e/\gamma n_{cr}}. \tag{1.1}$$

Various physical regimes are encountered in laser-matter interactions depending on the intensity of the laser light. The electron quiver motion in the laser electric field provides a good differentiation between these different regimes. The quiver velocity is defined as $v_{os} = |eE_0/m_e\omega|$ where E_0 is the laser electric field strength. At modest light intensities up to 10^8 Wcm^{-2}, atomic electrons will oscillate at the frequency of the laser, $\omega = 2\pi c/\lambda = ck$, where ω, λ and k are the angular frequency, wavelength, and wavenumber, respectively. When the laser field is increased to $\sim 10^{15}$ Wcm^{-2} electrons are stripped from the atoms and oscillate at the laser frequency in a plane along the laser polarisation direction. At ultra-high light intensities of $\geq 10^{18}$ Wcm^{-2} plasma electrons are strongly driven by the laser field to form a 'relativistic plasma', where electrons oscillate at velocities approaching the speed of light, c. The resulting relativistic mass change of electrons causes the plasma frequency to vary as a function of the relativistic term, γ. A modified expression for the plasma frequency including relativistic effects is given by [8]

$$\omega_p = \left(\frac{n_e e^2}{\gamma m_e \varepsilon_0}\right)^{1/2}, \tag{1.2}$$

where $\gamma = \sqrt{1 + a_0^2/2}$ is the time averaged relativistic factor, ε_0 is the permittivity of free space and a_0 is the normalised vector potential, defined as $a_0 = eE_0/m_e\omega c$. In practical units, $a_0 = 0.85 \times 10^{-9}\sqrt{I}\lambda$, where I is the laser intensity in Wcm^{-2} and λ is the laser central wavelength in microns. When $a_0 \simeq 1$, the intensity of 1 μm laser light is $\sim 10^{18}$ Wcm^{-2}, and plasma electrons acquire relativistic velocities such that the electron mass, γm_e changes significantly. Furthermore, at relativistic intensities the magnetic component of the electromagnetic field becomes significant and influences the dynamics of the electron motion through the $v \times B$ term in the Lorentz force equation

$$F = e(E + v \times B), \tag{1.3}$$

where v is the velocity of the electron, and B is the magnetic field strength of the laser pulse. At high driving fields the motion of an electron is described by an average drift in the direction of the laser propagation, k, and in the frame that moves with the drift velocity - a figure of eight lying along the plane defined by the laser polarisation vector and k. The forward drift motion arises from $v \times B \propto E^2 k$. As the field strength increases ($a_0 > 1$), the longitudinal drift motion, which depends on a_0^2, dominates over the transverse motion. As will be discussed in the next section, the relativistic forward motion of the electrons is important for using plasma as an acceleration medium for the next generation of particle accelerators.

The quiver motion can be clearly separated from the much slower response of the plasma, which is driven by the ponderomotive force of the laser pulse. This is due to the finite amplitude of the quiver oscillation, which is proportional to the laser field amplitude, and the gradients of the laser pulse envelope. On a slow timescale these effects combine into a net force that expels the plasma electrons from the laser pulse region. The ponderomotive force is given by [19]

$$F_p = -m_e c^2 \Delta\gamma \approx -\nabla\sqrt{m_e^2 c^4 + e^2 \langle A^2 \rangle}, \tag{1.4}$$

where the Lorentz factor of the electron can also be expressed as $\gamma = (1 + p^2/m_e^2 c^2)^{1/2}$ and the brackets denote the average over the fast laser oscillation timescale. The ponderomotive force excites plasma waves by pushing plasma electrons aside from the path of the laser pulse, which results in charge separation. Due to this charge separation, strong Coulomb restoring forces are excited in the wake of the laser pulse producing the trailing density wake. The laser pulse and the induced wakefields are stationary in the co-moving frame that propagates with velocity v_g, as sketched in figure 1.3, where the pulse propagates in the z-direction. For effective wakefield excitation, the pulse must be short: the maximum amplitude of the accelerating wakefield is found when the pulse length is about half a plasma wavelength, depending on the particular shape of the laser pulse envelope. For this reason, wakefield acceleration using a ‘matched’ short laser pulse is also known as resonant laser wakefield acceleration.

1.2 Laser wakefield accelerators

There is currently a large body of work pushing forward the development of laser-plasma based electron accelerators [20]. This concept was originally suggested by Tajima and Dawson [21] in 1979, who realised that plasma could form the basis

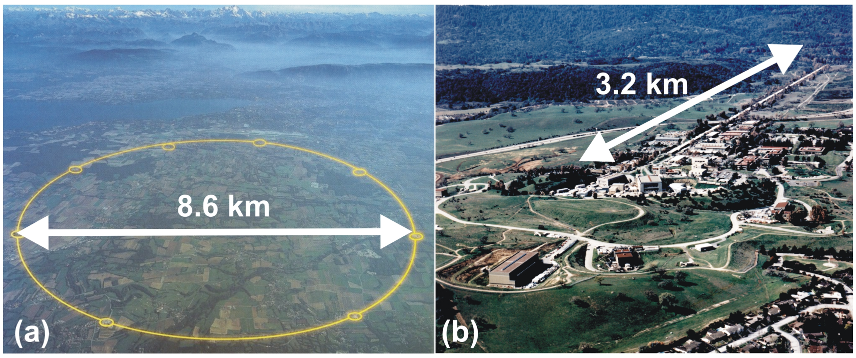

Figure 1.1: Accelerators: (a) Large Hadron Collider at CERN and (b) Stanford Linear Accelerator.

of a new generation of compact accelerators thanks to their ability to support much larger electric fields than conventional accelerators. They theoretically demonstrated that electrons can be trapped and accelerated in large amplitude relativistic plasma waves produced by a laser pulse traveling close to the speed of light in plasma. Conventional synchrotrons and linear accelerators are limited to operate with field gradients less than 100 $\mathrm{MVm^{-1}}$ due to electrical breakdown in the radio-frequency (rf) cavities. Plasma on the other hand has the advantage that it is already ionised, thus can theoretically sustain electric fields exceeding 100 $\mathrm{GVm^{-1}}$.

Progress in particle acceleration is driven by the quest for ever-greater collision energies of particles to probe the structure of matter. There are a number of large-scale facilities including the Stanford Linear Accelerator (SLAC) figure 1.1(b) which was instrumentally responsible for the discovery of the Tau Lepton in 1975 [22] and the Tevatron at Fermilab, which saw the discovery of the top quark in 1995 [23]. At the forefront of accelerator technology is the Large Hadron Collider [24] (LHC) at CERN, shown in figure 1.1(a), which was commissioned in September 2008. The collider is contained in a 27 km circumference tunnel 150 m underneath the ground and will ultimately achieve proton–proton centre of mass collision energies of 14 TeV. In March 2010 the accelerator set a world record becoming the worlds highest energy particle accelerator, having accelerated its twin beams of protons to an energy of 3.5 TeV. Currently, preparations are underway for the machine to run at maximum power which will achieve 7 TeV per proton beam.

The Large Hadron Collider marks the pinnacle of current conventional accelerator technology. However, like all conventional particle accelerators the acceleration gradient in the rf cavities is limited by material breakdown, the maximum field gradient of the LHC is 28 MV/m. If this limit is exceeded then plasma is produced by field emission from the cavity walls. Paradoxically, the laser-plasma accelerator uses plasma as an accelerating medium. By definition, plasma is already ionised and unaffected by material breakdown at high field strengths, as long as a fully ionised gas is used. Plasma can support fields 3–4 orders of magnitude higher than rf accelerators thus circumvent the need for kilometre long and large expensive facilities.

Early work on laser-plasma accelerators investigated the plasma beat-wave accelerator (PBWA) [21, 25]. The PBWA was a method of generating high-phase-velocity plasma waves in the absence of femtosecond laser technology. At the time of early investigations, laser pulse lengths were several hundred picoseconds long. Tajima and Dawson suggested using two laser pulses with slightly different wavelengths, such that their beat frequency, $\delta\omega = \omega_1 - \omega_2$, is matched to the plasma frequency, ω_p. This results in a train of shorter pulses which is able to drive up a plasma wave over many plasma periods and causes the plasma wave to resonantly grow. However, non-linear relativistic effects cause the wavelength of the plasma to increase and shift away from the resonance frequency, ultimately limiting the amplitude of the plasma beat wave. This is known as relativistic detuning.

Plasma waves can also be driven by the Coulomb field of a charged particle beam [26]. In this case it is the Coulomb force of the electron bunch instead of the ponderomotive force of the laser which drives plasma electrons aside and leads to charge separation. It has recently been demonstrated by a team at SLAC that the energy of the trailing section of an electron bunch can be doubled using an electron beam as a driver of relativistic plasma waves [27]. In this experiment a 42 GeV ultra-relativistic electron beam is focussed through an 85 cm column of lithium vapour. The strong radial Coulomb electric field of the propagating electron bunch ionises the region of gas at the front of the electron bunch and plasma electrons are 'blown out' from the path of the electron bunch, to produce a plasma density wake, leaving a column of positively charged ions. The ions attract the electrons, which results in a space charge oscillation in the wake of the electron beam. Most of the drive beam electrons lose energy to the plasma wave but a small fraction at the rear of the pulse is accelerated by the wake with a field gradient of 52 GV/m, effectively doubling their energy to 85 GeV. This shows great promise for the application of plasma accelerators by achieving, in one metre, energy gains equivalent to a 3 km section of SLAC. Clearly, this is an extremely attractive means to reduce the size and infrastructure of current large

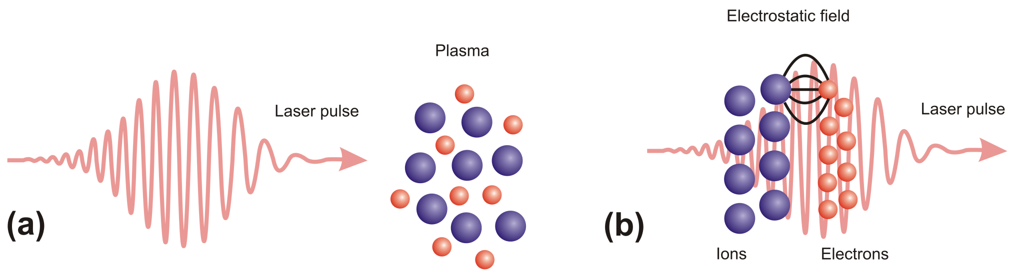

Figure 1.2: The laser wakefield mechanism.(a) A laser pulse interacts with a plasma, an ionised gas, composed of electrons and ions. (b) At relativistic light intensities, the electromagnetic force acting on the electrons pushes the electrons in the forward direction of the propagating laser pulse. The charge separation between the electrons and the ions in a plasma produces a large longitudinal static electric field which can reach 1 GV/cm (figure adapted from [8].)

scale accelerator facilities.

Laser wakefield acceleration (LWFA) is currently at the forefront of optical accelerator research. Underpinned by the recent advances in high intensity femtosecond laser technology, LWFA utilises the high phase-velocity plasma waves generated when a single pulse laser pulse interacts with plasma. When a ultrashort laser pulse with an intensity of $\geq 10^{18}$ Wcm^{-2}, wavelength of $\simeq$1 μm and a pulse duration of $\tau_L \simeq 2\pi/\omega_p$, propagates through underdense plasma the electrons are pushed away from other electrons by the ponderomotive force. This creates an electron density depression at regions of higher intensity, resulting in regions of charge separation with very strong accelerating and focusing forces. The concept of this acceleration structure is depicted in figure 1.3.

The ions in the plasma contribute to the charge separation (although non-neutral plasmas are possible) and have a much larger inertia than the electrons, thus remain relatively unperturbed by the laser field. This results in an electrostatic restoring force which causes the plasma electrons to oscillate back and forth from their equilibrium positions creating alternating regions of positive and negative charge. This produces an electrostatic longitudinal wave or 'wakefield' (figure 1.2) that propagates with a phase velocity nearly equal to the group velocity of the laser pulse, which is close to the speed of light for low density plasma. The phase and group velocities of electromagnetic radiation propagating in underdense plasma are given by, $v_\phi = c/\eta_p$ and $v_\phi v_g = c^2$, where $\eta_p = \sqrt{1-(\omega_p^2/\omega_0^2)}$ is the refractive index of the plasma and ω_0 is the frequency of the radiation field. The relativistic plasma wavelength or plasma period is defined as, $\lambda_p = 2\pi c/\omega_p$ and $\tau_p = 2\pi/\omega_p$, respectively. Plasma waves with relativistic phase velocities are capable of accelerating injected electrons, either from background electrons from the target plasma or electrons injected into the interaction region from an external electron source.

Optimum energy transfer between the laser pulse and plasma occurs when the laser pulse duration is matched to the plasma period, $\tau_p = 2\pi/\omega_p$ [28]. The matching of the laser pulse length or ponderomotive transit time to the plasma period induces a double ponderomotive kick to the plasma electrons which enhances the plasma wave amplitude. This acceleration regime is associated with short laser pulses, $\tau_p \leq 100$ fs and is known as the resonant laser wakefield accelerator.

Three ground breaking papers in 2004 saw the first ever observation of quasi-monoenegetic electron bunches produced from a LWFA [1, 2, 3]. Since then ongoing research in this field has been dedicated to increasing the energy [4, 29] and beam quality of the electron bunches from laser wakefield accelerators. In 2006 a group at LOA demonstrated a technique to improve the control of the injection of background plasma electrons into a wakefield [30]. Furthermore, Matlis *et al* has reported direct observations of wakefields using interferometric techniques [31]. This experiment involves capturing single-shot 'snapshots' of laser-wakefield accelerator structures for the first time, revealing detailed information about the evolution of multiple wake periods, and detecting structure variations such as wavefront curvature as laser-plasma parameters change.

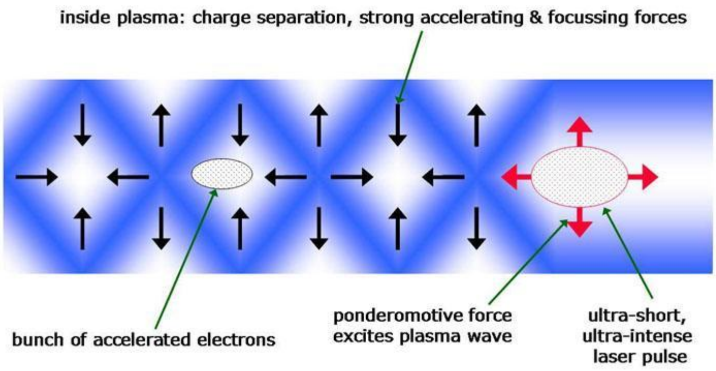

Figure 1.3: The ponderomotive force of an intense laser pulse propagating in plasma excites a plasma wave by pushing electrons from its path causing regions of space charge to form. These space charge 'structures' have strong accelerating and focussing forces.

The highest electron energy and best beam quality of LWFA electron bunches is currently limited by the highest intensity and shortest pulses available from advanced laser systems. Currently the highest achieved electron bunch energy is approximately 1 GeV with a 2.5 % r.m.s. energy spread [4]. It is expected that the advent of short pulse petawatt systems [18, 32] will increase the peak electron energy, reduce the energy spread and improve the emittance. Moreover, recently it has been demonstrated by a group at the Max-Planck-Institut für Quantenoptik at Garching that electron beams in the tens-of-MeV range can be produced with laser pulse energies of 40 mJ and pulse durations of $\sim$ 8 fs [33]. These pulses constitute a few optical cycles at 800 nm which is a previously unexplored parameter range in laser-driven electron acceleration. This experiment confirms previous theoretical models [34] by showing that these laser pulses can produce 'ultracold' electron beams i.e. with little or no low-energy electrons with a thermal spectrum. Furthermore they show excellent potential to scale up the laser pulse energy at such durations for future LWFA projects.

When short pulses are not available, an alternative regime known as the self modulated laser wakefield accelerator (SMLWA) may be employed [35, 36]. In this regime the laser pulse duration is long compared to the plasma period. For laser powers, P, approaching or exceeding the relativistic self-focusing threshold, $P_c \geq 17(\omega_0/\omega_p)^2$ GW, it is not necessary to match the pulse duration to the plasma period. At laser powers for which $P > P_c$ and $\tau_L > 2\pi/\omega_p$, the laser envelope can undergo an instability and become 'self-modulated' at the plasma frequency. The instability is promoted by a high plasma density and high a_0 [37, 38] and relies on the Raman scattering instability to break up a longer pulse into an intensity modulated pulse [39]. This pulse 'splitting' is due to the refractive index of the plasma dependence on the electron density, as given by equation 6.2. The laser pulse amplitude increases in regions with low electron density and decreases in regions with high electron density. In this way, the laser pulse can eventually break up into 'micropulses' of length $\simeq \lambda_p/2$.

These modulated pulses can drive up a plasma wave very efficiently, as they are resonant with the plasma wave. The stimulated forward Raman scattering (FRS) instability has been experimentally observed by many groups investigating the propagation of intense laser pulses through a gas jet [37, 38, 40, 41, 42]. The FRS instability occurs when a strong electromagnetic pump wave $(\omega_0, \mathbf{k}_0)$ interacts with an underdense plasma and drives longitudinal plasma waves, resulting in density perturbations. These small density fluctuations, δn_e, produce a transverse current, which generates a small scattered light wave. This scattered light wave in turn beats with the incident field to reinforce the density fluctuation via the ponderomotive force. Hence, the plasma wave and scattered light wave grow at the expense of the incident light giving rise to excitation of electromagnetic sidebands $(\omega_0 \pm \omega_p, \mathbf{k}_0 \pm \mathbf{k}_p)$ located at the sum and difference of the pump and plasma frequencies. These are termed as the stokes and anti-stokes shifts (Raman satellites). The frequency down-shifted wave is known as the Stokes wave, and the upshifted wave is called the anti-Stokes wave. When the interaction is such that these sidebands enhance or drive plasma waves, act back on and enhance the sideband growth the interaction becomes unstable. If strongly driven, these processes can lead to the generation of fast electrons by wave breaking and the self-modulation of the propagating laser pulse, which can drive the self modulated laser wakefield regime [43]. Such an instability is driven by the feedback loop sketched in figure 1.4.

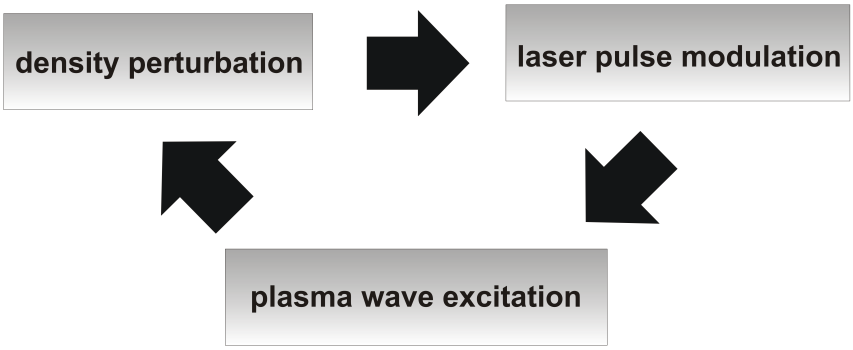

Figure 1.4: The feedback loop of a modulational instability such as Raman scattering.

SMLWA experiments have demonstrated potential as plasma-based accelerators [44, 45]. In 2006 an experiment demonstrated that SMLWA can be an efficient driver of quasi-monoenergetic electron bunches using 80 fs laser pulses to produce quasi-monoenergetic electron beams up to 80 MeV with a FWHM energy spread of 8.5 % [11]. This data is presented in chapter 3 and is an important result demonstrating that quasi-monoenergetic electron beams can be produced with strongly relaxed requirements on the laser pulse duration and plasma density. Furthermore, simulations have shown that the laser pulse is longitudinally modulated by the plasma wave, which causes the laser pulse to break up into smaller pulses that interact resonantly with the plasma wave [11]. These sub 10 fs laser high intensity pulse fragments contain about 5 % of the initial pulse energy and are sufficiently intense to generate quasi-monoenergetic electron bunches [11]. Although only a fraction of the initial energy is contained in the pulse fragment, the pulse is short and intense enough to form a bubble-like accelerating structure. The fragmentation of the laser pulse leads to the highly nonlinear broken wave regime [46]. The strong ponderomotive force of the laser creates a bubble-like electron void [47], which is capable of supporting a high longitudinal electric field. The laser pulse travels at the front of this structure and expels electrons, which stream around the arising cavity and can be trapped inside at a fixed phase of the longitudinal field, leading to the acceleration of electron bunches with a narrow energy spread [48]. This phenomenon has been explored theoretically [49, 50] and other experiments have been carried out where the ponderomotive expulsion force of the laser pulse is strong enough to completely expel background plasma electrons from its path [51]. This strongly driven LWFA mechanism is sometimes referred to as the 'bubble' regime due to the creation of free space acceleration bubbles devoid of electrons and can be accessed when the laser a_0 parameter is very high, (≥ 3). Furthermore, the acceleration cavity or 'bubble' has the advantage that it is enables guiding of the laser pulse over many Rayleigh lengths in homogeneous plasma without significant diffraction, thus no preformed plasma channel is needed.

The LWFA mechanism can also drive plasma waves with amplitudes large enough to modulate the laser pulse. The non-linear plasma density wave acts back on the laser pulse causing it to focus in space and time. The transverse radial focusing of the laser pulse or self-focusing of laser energy, occurs when a transverse variation in the refractive index of the underdense plasma exists. This variation in refractive index can be caused either by relativistic effects ($a_0 \geq 1$) due the radial laser intensity profile or by a transverse density depression, caused by a relativistic plasma wave or ponderomotive channeling by the laser pulse. The plasma can also compress the laser pulse longitudinally i.e. in time. Temporal laser pulse compression occurs when a refractive index gradient co-moves with the laser pulse, resulting in group velocity modulations across the laser pulse envelope. These refractive index gradients can be caused either by laser intensity gradients or by the presence of a relativistic plasma wave. Subsequently, frequency modulations of the laser envelope are associated with these longitudinal variations in refractive index as an account of corresponding phase velocity changes across the pulse. When a laser pulse envelope self modulates its spectral content in this way, this is known as photon acceleration, where the photons are frequency up-shifted or down-shifted depending on the sign or the refractive index gradient ($d\eta/dr$).

The pulse modulations and instabilities already discussed are important for the generation of electron beams. In particular the FRS instability can generate very high amplitude plasma waves with large field gradients. That said, although plasmas can support very large electrostatic field potentials, they do have a limit before they will 'break'. As will be seen in later sections the theoretical maximum limit of the plasma wave accelerating potential depends on the plasma temperature. If this limit is breached then the plasma wave will lose its coherence and break, much like the way a water wave breaks in the sea as it propagates towards the shore. In the l-D case the Langmuir wave break occurs when the quiver velocity of electrons, u, becomes equal to the phase velocity of the wave. For non-relativistic plasma wave phase velocities, the 'cold wave-breaking limit' was derived by Dawson and Oberman [52] using Gauss's law [53]

$$E = \frac{m_e c \omega_p}{e} \tag{1.5}$$

Wavebreaking occurs when the velocity of the plasma electrons exceeds the phase velocity of the plasma wave [54, 55, 56].

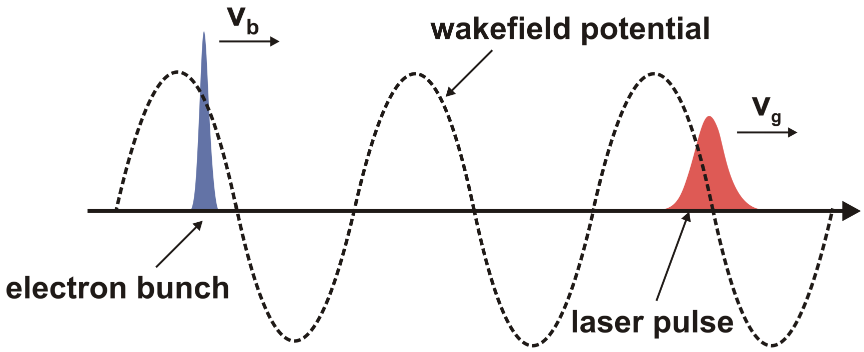

Figure 1.5: An illustration of phase slippage during laser wakefield acceleration: the laser pulse that propagates with velocity, v_g, excites a plasma wave on which an electron bunch with velocity, v_b, is accelerated. When v_b experiences a decelerating phase of the wakefield potential the electron bunch will lose energy.

After wavebreaking, energy is transfered from the plasma wave to background electrons in the plasma, causing them to be accelerated to relativistic energies. These electrons can then be 'caught' by the plasma wave and experience a further acceleration phase. This process is known as self-injection or self-trapping because the electrons originate from the background plasma.

In laser wakefield acceleration, the energy gain of the electrons is limited by phase slippage between the electrons and the plasma wave [57, 58], which results from the difference between v_g and the actual velocity v_z of an electron. Due to phase slippage, the electron eventually reaches a decelerating region in the wave. This process is called dephasing and it limits the acceleration distance for electron energy gain. The dephasing length is defined as the length over which the injected electron bunch experiences acceleration. In the 1D picture an analytical expression for the dephasing length can be calculated as $L_d \simeq \lambda_p \omega_0^2/\omega_p^2$, where λ_p is the plasma wavelength and ω_0 is the angular frequency of the laser field. During most of the acceleration the electron velocity v_z is larger than v_g and can be approximated by c. With this approximation, the dephasing length is estimated to be $L_d = (\lambda_p/2)/(c/v_g - 1)$. Therefore, the strongly underdense regime ($n_p \ll n_{cr}$) is preferred for laser wakefield acceleration, because a long dephasing length results from the group velocity $v_g = c(1-n_p/n_{cr})^{1/2}$ of the laser pulse being close to the speed of light.

The acceleration lengths of wakefield accelerators can be increased by choosing a particular laser focusing geometry [59]. It has been reported that short focal length geometries ($f \leq 300$ mm) can cause beam break-up and prevent stable propagation of the laser pulse [59], however it has also been shown that with the correct conditions (plasma density, spatial alignment) short focal length set-ups can also produce high quality electron beams [11]. The advantage of using a long focal length geometry ($f \geq 1000$ mm) for wakefield generation is that the laser can be self guided over a distance comparable with the dephasing length. The longer focal region in plasma increases the length over which the laser can remain intense enough to drive a wakefield i.e. the interaction length. This means that electrons can interact with the plasma wave for a longer time and hence gain more energy.

Another way to increase the interaction length is to use a pre-formed hydrogen plasma waveguide capillary. This method has been proposed [60, 61] and several experiments have been carried out using a discharge capillary filled with fully ionised hydrogen gas [62, 63, 64]. These capillaries are precision machined from alumina or sapphire using a high repetition rate laser with a Gaussian intensity profile [65, 66, 67]. They can be up to a few centimetres long and tens to hundreds of microns in diameter. In this configuration a preformed plasma channel is created in the capillary using either a high voltage (HV) discharge or an external heater laser beam [3, 68]. The resulting plasma has a characteristic parabolic radial density profile with a minimum on axis caused by cooling of electrons at the capillary walls. As the refractive index is inversely proportional to the electron density the parabolic density profile can counteract the natural diffraction of the laser beam thus creating a waveguide for the laser pulse capable of guiding it over many Rayleigh lengths up to cm scales with low loss [63, 64]. Recently GeV electrons have been produced in this manner with 5 % energy spread using similar capillary waveguides [4].

Having discussed the different regimes and mechanisms for laser accelerated electron beams it is appropriate to compare the current beam quality from wakefield accelerators with that of conventional accelerators. Electron beam quality can generally be defined by three parameters; high peak current, small energy spread and low emittance. These quality parameters are combined into a single figure-of-merit parameter known as the electron beam brightness. The transverse normalised brightness can be described as $B^N_{trans} \propto I/\varepsilon^N_x \varepsilon^N_y$ and longitudinal normalised brightness $B^N_{longit} \propto I/\sigma_\gamma$, where I and σ_γ are the electron beam current and electron energy spread respectively [69]. The electron beam emittance is roughly the product of the r.m.s. spot size and the r.m.s divergence of the electron beam. For a symmetric (and non-skewed), focused electron beam the emittance along the three cartesian spatial coordinates is given by $\varepsilon^N_{x,y,z} = \gamma\beta\sigma_{x,y,z}\sigma_{x',y',z'}$ where $\beta = v/c$, the normalised velocity of the particle, $\sigma_{x,y,z}$ is the root mean squared (r.m.s) source size, and $\sigma_{x',y',z'}$ is the r.m.s divergence of the particle beam [69]. A typical accelerator such as SLAC can produce an electron beam with energies of around 50 GeV, normalised emittances of 1 πmm mrad, and energy spreads of less than 0.1 % [70]. This compares to the best current measured laser-plasma electron beam parameters of: 1 GeV for the peak electron energy and , 1 πmm mrad, and energy spreads of ∼1 % respectively. Laser-wakefield accelerators are a fresh area of research and are fast approaching the same order of magnitude energy as conventional accelerators, which has the scope to potentially revolutionise the accelerator industry and the way science is done.

In order to make measurements of the quality of electron beams produced by laser wakefield accelerators, typical diagnostics include electron energy spectrometer to characterise the electron energy spectrum and bandwidth. This usually consists of a dipole magnetic field structure, which through the action of the Lorentz force disperses the electrons according to their energy. It is also important to measure the transverse electron beam profile to estimate the emittance, this typically involves inserting a scintillating screen into the path of the electron beam. Moreover, a more challenging measurement is to ascertain the electron bunch duration. This has recently been done by electro-optic detection using either the Coulomb electric field [71, 72] of the electrons or by the radiation fields associated with the electrons traversing a dielectric discontinuity i.e., the coherent transition radiation (CTR) [73, 74]. However, due to the frequency response (detection bandwidth) of the electro-optic crystals used in these experiments, the intrinsic temporal resolution is currently limited to ∼ 100 fs [73]. Comparing this with the predicted bunch length, which is estimated to be as short as ∼ 1–3 fs, defined by a plasma wavelength [75, 44], this detection method is some way off in resolution. This is the subject matter of Chapter 4 of this thesis, where it will be discussed more thoroughly.

1.3 Applications of short pulse laser-matter interactions

The interaction of ultra-high intensity laser pulses with plasma has a wide variety of applications, including particle acceleration [1, 76, 77], radiation production [6, 78, 79] and inertial confinement fusion [80, 81]. While it is true that a large proportion of current research is curiosity driven, an equally important motivating factor is that laser-plasmas have tremendous potential as primary sources of photons, electrons and ions for many other purposes. These sources are desirable not only for their relative compactness but also for their recent developments in beam quality.

Fast ion beams generated by high intensity laser irradiation of solid targets have recently demonstrated excellent beam qualities, including high brightness, high directionality and short burst duration. Although less developed than fast electron or x-ray sources these ion sources already exhibit exciting possibilities. For example, laser-accelerated protons in nuclear medicine are of particular interest to oncologists as low cost, compact sources for the production of radioactive isotopes [82, 83, 84] for positron emission tomography (PET), treating cancerous tumors [85, 86], hadron-therapy applications [87, 88, 89, 90, 91] and proton radiography [92]. Most ion sources involve the interaction of high intensity laser pulses with solid foil targets [76, 93, 94, 95], however Coulomb explosion interactions with gaseous cluster jet targets have also been employed [96].

Furthermore, short pulse laser systems have also been considered for the production of neutron beams [97, 98, 99], for fast neutron therapy, neutron radiography [100] and the transmutation of nuclear waste. Intense picosecond laser pulses can be focussed onto solid targets can produce fast protons and ions, which in turn drive neutron production [101, 102]. In addition, deuterated targets in solid form [103, 104] and also in a gaseous cluster phase [105] have been used for neutron production.

One of the most exciting developments in the field of inertial confinement fusion (ICF) to emerge as a result of short pulse laser technology is the fast ignition concept [106]. Standard ICF ignition is achieved by compressing a deuterium-tritium pellet to high density in such a way that a hot spot is generated in the centre of the target. This hot spot ignites and then propagates outwards burning the higher density fuel. However this technique holds stringent constraints on both the drive pulse and target. Over 1 MJ of laser energy is needed before significant gain is reached and the implosion symmetry has to be controlled to better than 1 % to prevent impurities mixing with the fuel. The fast ignition scheme theoretically offers a relaxation on the driver, compression, and uniformity requirements by up to an order of magnitude by using a high intensity, short laser pulse to deliver the energy to the compressed fuel via fast electrons [106]. Proof of principle experiments have already demonstrated fast electron heating of a compressed deuterium-tritium target using the cone-pellet arrangement [107], in this scheme the cone provides a clean path to channel a short 0.5 PW ignitor pulse to the centre of the fuel capsule [107]. However, these initial studies show that there remain many basic physics issues to be resolved before fast ignition becomes a viable option in inertial confinement fusion.

The advance in high intensity short pulse laser technology has heralded many new exciting ways to generate radiation pulses across the whole electromagnetic spectrum. These laser-plasma radiation sources include, the production of THz pulses [78, 108, 109, 110], extreme ultraviolet (EUV) [111], XUV [112] coherent X-rays [113, 114], and Gamma rays [115]. High harmonic generation (HHG) is currently an exciting area of research [116, 117, 118, 119] investigating the generation of extremely bright coherent X-ray pulses with femtosecond to attosecond durations (10^{-18} s) [120, 121].

This unprecedented temporal resolution allows mapping of electron motion on the atomic scale, making attosecond pulses extremely attractive to chemists wishing to access the ultrafast dynamics of electrons inside atoms and molecules, for example the making and breaking of chemical bonds. Furthermore attosecond pulses can act as an 'ultrafast-shutter camera' to produce images of the position of nuclei and electrons simultaneously in space and time with sub-atomic resolution. This will give scientists the opportunity to make 3D movies in real time which map electronic motion and molecular rotations.

Short pulse lasers have also dramatically increased the availability of radiation sources at THz frequencies, which up until recently was a relatively unexplored region of the electromagnetic spectrum. These sub-picosecond THz pulses have been produced using photoconductive antennas [122, 123] or through high intensity laser pulse interactions with gases [108].

The principal use of laser-plasma generated electrons is currently envisioned to entail the production of radiation. That is compact, laboratory scale sources of high brightness ultra-short pulse radiation suitable for, high resolution, time resolved experiments across the scientific community ranging from probing the dynamics of matter at short X-ray wavelengths [124] to applications spanning the health sciences [125]. This can be realised through the production of synchrotron radiation by passing the electron bunch through a periodic magnetic structure, called an undulator, or wiggler. Very recently this has been achieved for the first time using laser accelerated electrons [6]. The results of which will be presented in chapter 5 of this thesis in more detail. Although this is already a compact means of producing synchrotron light there exists scope to further compress these sources by using a plasma undulator [126]. The principle consists of the formation of an electrostatic ion channel, formed in a capillary/gas cell by the ponderomotive or space charge expulsion of electrons. This then forms a 'mini undulator' structure which serves to support betatron oscillations of electrons resulting in X-ray betatron radiation. In this regime everything happens on the scale of plasma wavelength i.e. the acceleration, electron undulation and radiation emission, which is of the order of micrometres in size, making this potentially an ultra compact radiation source.

Another way to generate tunable radiation is by controlled photon acceleration. Recent backscattering experiments have demonstrated that by colliding a 800 nm probe laser pulse in counter-propagation into a plasma wakefield can double Doppler frequency upshift the laser pulse to 7 nm [127]. Backscattering electromagnetic radiation from a relativistic ionisation front is an exciting proposition to create sub-cycle, attosecond pulses in the visible to x-ray region of the electromagnetic spectrum. In the past conventional experiments have involved using a gas filled microwave waveguide to frequency up-shift microwave radiation [128, 129, 130]. However with the availability of current high-density gas jet targets ($\sim 10^{19}\text{cm}^{-3}$) it is now possible to extend this phenomenon into the THz region of the EM spectrum. It is feasible that a 1 THz pulse produced by a semiconductor dipole antenna can be focused down and reflected off a relativistic mirror i.e., an ionisation front to be double Doppler up-shifted by a factor of $4\gamma^2$ to 500 THz (mid-visible). The subsequent Lorentzian frequency up-shift also accompanies a temporal compression of the same factor, transforming a 500 fs THz pulse into one of sub-femtosecond duration. An experiment to do this is presented in chapter 6 of this thesis. This technique is a very attractive way to realise a versatile tunable source of radiation as the pulses can be 'tailored' as required by controlling the input pulse parameters such as pulse energy, pulse shape, duration, bandwidth and frequency.

The use of a plasma wakefield as a relativistic mirror is a more preferential method to backscatter the radiation. This is because the wakefield has kinetic energy which can be directly transfered into the backscattered pulse. The photon number can thus be enhanced through the interaction of the probe pulse with the relativistic overdense front [131]. An ionisation front on the other hand, has no kinetic energy, thus cannot submit energy during the interaction. This results in a reduction in photon number and hence the energy of the backscattered radiation.

In summary, monoenergetic laser produced electrons [1, 2, 3] are excellent candidates to reduce the size and cost of conventional accelerator technology which is fast reaching a technological plateau. They could also serve as compact drivers of free-electron lasers to generate inherently, ultrashort, coherent light pulses suitable to serve the demand for high temporal and spatial resolution pump-probe experiments in physics, chemistry and biology. Current wakefield accelerator technology can produce electron beams with energies up to 1 GeV [4, 29] and energy spreads of 1 % [7]. It is therefore reasonable to assume that with the ultrahigh currents of these beams in conjunction with their small emittance and energy spread that in the coming years they will revolutionise the particle accelerator and free electron laser industry.

1.4 Future outlook

The construction of larger conventional accelerators is becoming prohibitively expensive. Even for applications requiring lower energy electrons the space and cost is a problem for example the Diamond Light Source, which uses undulators to generate X-rays from electrons accelerated to approximately 3 GeV in a synchrotron, occupies the space of approximately 5 football pitches and cost $\simeq$ 600 million to construct. Laser wakefield accelerators offer a compact and cheaper alternative. At a fundamental level, in order to continue with the development of laser wakefield accelerators it is necessary to continually advance high power laser technology. The performance of laser wakefield accelerators rely on the availability of the best possible laser pulse parameters, which includes, pulse energy, pulse duration, stability, focusability, and contrast ratio. Currently, advanced medium size laser systems [17, 132] have multi-terawatt peak power capabilities and can generate focused femtosecond pulses with intensities in excess of 10^{19} Wcm^{-2} with 10 Hz repetition rates. Larger scale systems such as the Petawatt Vulcan Laser at RAL [133] can achieve 10^{21} Wcm^{-2}. Petawatt systems with higher repetition rates and shorter pulse durations [18, 32, 134] are now becoming available to explore novel, nonlinear and relativistic physical processes previously uncharted. The Vulcan laser at RAL is currently being upgraded to a 10 PW system using optical parametric chirped pulse amplification (OPCPA) [135, 136]. This laser will deliver 300 J in 30 fs to provide focussed intensities of 10^{23} Wcm^{-2} to its user community [133]. The development of such laser systems, in the 10 PW range, will push laser wakefield accelerators to a new regime and already the applications of such laser powers has been considered theoretically [137]. The scalings predict the possibility to accelerate self-injected electron bunches to energies in excess of 10 GeV over a distance of 10 cm. Furthermore, staged acceleration is also under consideration as a possibility for future generations of LWFA accelerators. This technique would involve staging multiple 10 cm long capillaries waveguides in series for ultra-high energy gains. These ultrahigh energy electron beams could then be used as drivers of x-ray and gamma ray free-electron lasers for probing matter across all the life sciences.

In addition to utilising these cutting edge laser systems as drivers of LWFA's and radiation sources, these intense laser pulses could have a future role in our quest for clean energy production through the realisation of self-sustained and efficient nuclear fusion. The primary contenders in this field are the Laser Megajoule (LMJ) [138, 139] in France and the awaited National Ignition Facility [140, 141] (NIF) at Lawrence Livermore National Laboratories (LLNL). These are both military funded projects which will investigate indirect drive inertial confinement fusion. NIF will be the worlds largest laser consisting of 192 ultra-violet laser beams, which deliver 1.8 MJ of laser light energy in 10 ps onto a high Z hohlraum for conversion into x-rays. These x-rays will then superheat and compress a Deuterium-Tritium (D-T) target to achieve fusion and potentially produce a safe, virtually unlimited energy source powered by light. Furthermore there exist the HiPER project, which is a proposed European High Power laser Energy Research facility dedicated to demonstrating the feasibility of laser driven fusion as a future energy source. The facility will be a large scale laser system designed to demonstrate significant energy production from inertial fusion, whilst supporting a broad base of high power laser interaction science [142]. This is made feasible by the advent of a revolutionary approach to laser-driven fusion known as 'Fast Ignition' [106]. HiPER will use a unique laser configuration, currently estimated to employ 250 kJ in multiple, 3ω (wavelength $\lambda = 0.35\ \mu$m), nanosecond beams for compression and 70 kJ in 10–20 ps, 2ω beams for ignition. These are the estimated parameters of the system required to assemble the fusion fuel to an appropriate density and to ignite the fuel and induce a propagating burn wave to yield high gain [143, 144].

Although these large scale laser facilities (LMJ,NIF,HiPER) will deliver vast amounts of coherent laser power, they are very large and expensive infrastructures. The maximum damage threshold of the gain medium and the optics used to steer these beams necessitates that large expensive optics, gratings, and crystals are used in the laser chain. A technique to amplify short pulses in plasma is currently being investigated at Strathclyde [145, 146] and other institutions [147, 148, 149, 150]. In this scheme, a short seed pulse is amplified by a stretched and chirped pump pulse through Raman backscattering in a plasma channel. Unlike conventional CPA, each spectral component of the seed is amplified at different longitudinal positions determined by the resonance of the seed, pump and plasma wave, which excites a density echelon that acts as a 'chirped' mirror and simultaneously backscatters and compresses the pump. Experimental evidence [146] shows that Raman amplification has the potential to be used as an ultra-broad bandwidth linear amplifier. Many amplifiers with expensive and fragile metre-size gratings might then be replaced by a single amplifier composed of a 1 cm size plasma layer [151] to reduce the size and cost of future petawatt and exawatt laser systems [152].

Chapter 2

Laser-plasma Interactions

2.1 Electron motion in an electromagnetic field

The interaction of intense laser pulses with plasma at the most fundamental level is governed by the response of plasma electrons to the electric and magnetic fields of the laser. Although the presence of plasma leads to collective effects (e.g. plasma waves) as a starting point using the framework of Gibbon [153] we consider the motion of a single electron in the presence of electromagnetic fields $\mathbf{E}$ and $\mathbf{B}$ described by the Lorentz equation:

$$\frac{d\mathbf{p}}{dt} = -e(\mathbf{E} + \mathbf{v} \times \mathbf{B}), \tag{2.1}$$

from which follows the energy equation:

$$\frac{d}{dt}(\gamma mc^2) = -e(\mathbf{v}\cdot\mathbf{E}), \tag{2.2}$$

where $\mathbf{p} = \gamma m\mathbf{v}$, and $\gamma = \sqrt{1 + p^2/m^2c^2}$ is the relativistic factor. Considering an elliptically polarised plane wave travelling in the positive z-direction which can be represented by the vector potential

$$\mathbf{A}(\omega, \mathbf{k}) = \left(a_0\delta \cos\phi, a_0\sqrt{1-\delta^2}\sin\phi, 0\right), \tag{2.3}$$

where $\phi = \omega t - kz$ is the phase of the wave, a_0 is the normalised amplitude (v_{osc}/c), with $v_{osc} \equiv eE_0/m\omega$ and δ is the Jones polarisation parameter such that $\delta = \{\pm 1, 0\}$ for a linearly polarised wave and $\delta = \pm 1/\sqrt{2}$ for a circular wave. For simplicity it is now convenient to introduce the normalisations $t \to \omega t, z \to kz, \mathbf{v} \to \mathbf{v}/c, \mathbf{p} \to \mathbf{p}/mc$, and $\mathbf{A} = e\mathbf{A}/mc^2$. We can now proceed to use the well-known relations, $\mathbf{E} = -\partial\mathbf{A}/\partial t$, and $\mathbf{B} = \nabla \times \mathbf{A} = (-\partial A_y/\partial z, \partial A_x/\partial z, 0)$ to write the perpendicular component of equation 2.1

$$\frac{d\mathbf{p}_\perp}{dt} = \frac{\partial \mathbf{A}}{\partial t} + v_z \frac{\partial \mathbf{A}}{\partial z}, \tag{2.4}$$

which upon integration yields

$$\mathbf{p}_\perp - \mathbf{A} = \mathbf{p}_{\perp 0}, \tag{2.5}$$

where $\mathbf{p}_{\perp 0}$ is a constant of motion representing the initial perpendicular momentum of the electron. The longitudinal component of equation 2.1 and equation 2.2 gives

$$\frac{dp_z}{dt} - \frac{d\gamma}{dt} = -v_x \left(\frac{\partial A_x}{\partial t} + \frac{\partial A_x}{\partial z} \right) - v_y \left(\frac{\partial A_y}{\partial t} + \frac{\partial A_y}{\partial z} \right). \tag{2.6}$$

As the electromagnetic wave is a function of $t - z$ only (in vacuum or dilute plasma), the terms on the RHS vanish identically, so it is possible to integrate the RHS to get

$$\gamma - p_z = \alpha, \tag{2.7}$$

where α is a constant of motion yet to be determined. Using the identity $\gamma^2 - p_z^2 - p_\perp^2 = 1$ and choosing $\mathbf{p}_{\perp 0} = 0$, we can eliminate γ to get a relationship between the parallel and perpendicular momenta,

$$p_z = \frac{1 - \alpha^2 + p_\perp^2}{2\alpha}. \tag{2.8}$$

Since equation 2.5 shows that $p_\perp$ is equal to the laser vector potential, equation 2.8 represents the general solution for the motion of free electrons in an electromagnetic wave. To proceed we now specify α and integrate equation 2.5 and equation 2.8 by changing the variable:

$$\frac{d\phi}{dt} = \frac{\partial \phi}{\partial t} + \frac{p_z}{\gamma}\frac{\partial \phi}{\partial z} = \frac{\alpha}{\gamma}, \tag{2.9}$$

which gives

$$\mathbf{p} = \gamma \frac{d\mathbf{r}}{dt} = \gamma \frac{d\phi}{dt}\frac{d\mathbf{r}}{d\phi} = \alpha \frac{d\mathbf{r}}{d\phi}. \tag{2.10}$$

In the laboratory frame, the electron is initially at rest prior to the arrival of the electromagnetic waves, so that $t = 0$, $p_z = p_x = 0$, and $\gamma = 1$. From the conservation relation equation 2.8 it follows that $\alpha = 1$ in this case, leading to

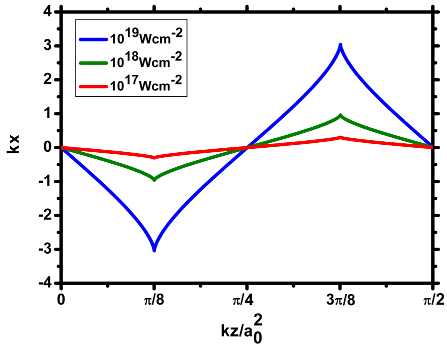

Figure 2.1: The electron orbits in the laboratory frame when immersed in a large amplitude, linearly polarised electromagnetic plane wave. The electric-field strengths corresponding to 800 nm laser wavelengths with intensities: $I = 1{\times}10^{17}$ Wcm^{-2} $\approx a_0 = 0.3$ (red line), $I = 1{\times}10^{18}$ Wcm^{-2} $\approx a_0 = 1.0$ (green line), $I = 1{\times}10^{19}$ Wcm^{-2} $\approx a_0 = 3.0$ (blue line).

the momentum components in the lab frame:

$$\begin{aligned}
p_x &= a_0 \delta \cos\phi, \\
p_y &= a_0 \sqrt{(1-\delta^2)} \sin\phi, \\
p_z &= \tfrac{1}{4} a_0^2 \left[1 + (2\delta^2 - 1)\cos 2\phi\right],
\end{aligned} \tag{2.11}$$

with the help of equation 2.10 we can integrate equations 2.11(a)-2.11(c) to obtain the laboratory frame orbits valid for an arbitrary polarisation δ:

$$\begin{aligned}
x &= a_0 \delta \sin\phi, \\
y &= -a_0 \sqrt{(1-\delta^2)} \cos\phi, \\
z &= \tfrac{1}{4} a_0^2 \left[\phi + \tfrac{2\delta^2 - 1}{2} \sin 2\phi\right].
\end{aligned} \tag{2.12}$$

This solution is shown graphically in figure 2.1. It is immediately apparent that regardless of polarisation the longitudinal motion has a secular component that will grow in time or with propagation distance. In the presence of the electromagnetic wave, the electron immediately starts to drift with an average momentum $p_D \equiv \overline{p_z} = a_0^2/4$, corresponding to a velocity

$$\frac{v_D}{c} = \overline{v_z} = \frac{\overline{p_z}}{\overline{\gamma}} = \frac{a_0^2}{4 + a_0^2}, \tag{2.13}$$

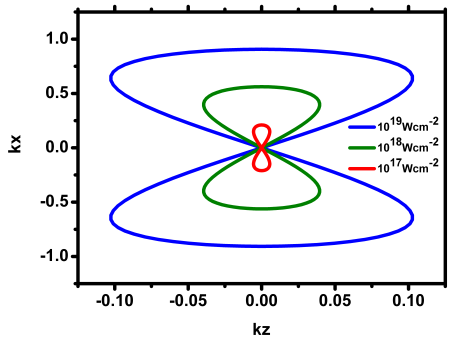

Figure 2.2: The electron orbits in the average rest frame when immersed in a large amplitude, linearly polarised electromagnetic plane wave. The electric-field strengths corresponding to 800 nm laser wavelengths with intensities: $I = 1\times10^{17}$ Wcm^{-2} $\approx$ $a_0 = 0.3$ (red line), $I = 1\times10^{18}$ Wcm^{-2} $\approx$ $a_0 = 1.0$ (green line), $I = 1\times10^{19}$ Wcm^{-2} $\approx$ $a_0 = 3.0$ (blue line).

where the overscore represents averaging over rapidly varying electromagnetic phase, ϕ (and $\overline{\gamma} = \alpha + \overline{p_z}$ has been used).

The fact that the electron drifts in the lab frame leads to another possible choice of constant α. Considering that the drift velocity vanishes for arbitrary pump strength, and setting $\bar{p_z} = 0$ in equation 2.8 yields

$$1 + \overline{A^2} - \alpha^2 = 0. \tag{2.14}$$

Averaging over a laser cycle to remove rapidly varying terms, and noting that $\overline{cos^2(\phi)} = 1/2$ gives

$$\alpha = \sqrt{\left(1 + \frac{a_0^2}{2}\right)} \equiv \gamma_0. \tag{2.15}$$

Plugging this back into equation 2.8 gives the momenta:

$$\begin{aligned} p_x &= a_0 \delta \cos\phi, \\ p_y &= a_0 \sin\phi \sqrt{(1-\delta^2)}, \\ p_z &= \tfrac{1}{4\gamma_0} a_0^2 \left(2\delta^2 - 1\right) \cos 2\phi. \end{aligned} \tag{2.16}$$

Noting that in this case, $\mathbf{p} = \gamma_0 \frac{d\mathbf{r}}{d\phi}$, we can integrate again to get the orbits;

$$\begin{aligned} x &= 2\delta q \sin\phi, \\ y &= -2q\sqrt{(1-\delta^2)}\cos\phi, \\ z &= \left(\delta^2 - \tfrac{1}{2}\right) q^2 \sin 2\phi. \end{aligned} \tag{2.17}$$

where $q = a_0/2\gamma_0$. Eliminating ϕ for linear polarisation $\delta = 1$ we obtain the well known figure-of-eight shown in figure 2.2.

2.2 The ponderomotive force

In the previous section the solutions derived are generally valid for plane waves. These analytical solutions, although useful, do not completely describe the details of electron motion caused by a real laser pulse. Tight focussing of an ultra-short laser pulse creates strong radial intensity gradients over a few wavelengths and few-cycle pulses are highly dispersive thus require a completely non-adiabatic approach. The ponderomotive force can be defined physically as the gradient of the time-averaged oscillation potential. Considering the non-relativistic case when a single electron oscillates near the centre of a focused laser beam in the limit $v/c << 1$ the equation of motion (equation 2.1) for the electron becomes [153]

$$\frac{\partial v_x}{\partial t} = -\frac{e}{m_e} E_x(\mathbf{r}). \tag{2.18}$$

Taylor expansion of the electric field then gives

$$E_x(\mathbf{r}) \cong E_0(x)\cos\phi + x\frac{\partial E_0(x)}{\partial x}\cos\phi + ..., \tag{2.19}$$

where $\phi = \omega t - kz$. To the lowest order we can say that:

$$v_x^{(1)} = -v_{osc}\sin\phi; \quad x^{(1)} = \frac{v_{osc}}{\omega}\cos\phi, \tag{2.20}$$

where $v_{osc} \equiv eE_0/m\omega$. Substituting back into equation 2.18 gives

$$\frac{\partial v_x^{(2)}}{\partial t} = -\frac{e^2}{m_e^2\omega^2} E_0 \frac{\partial E_0(x)}{\partial x}\cos^2\phi. \tag{2.21}$$

Multiplying by m_e and taking the cycle average yields the ponderomotive force on an electron [153],

$$F_p \equiv m_e \overline{\frac{\partial v_x^{(2)}}{\partial t}} = -\frac{e^2}{4m_e\omega^2}\frac{\partial E_0^2}{\partial x} = -\frac{e^2}{4m_e\omega^2}\nabla E^2. \tag{2.22}$$

Physically this implies a greater force for regions with larger E-field gradients as illustrated in figure 2.3(b). A single electron will thus drift away from the centre of a focused laser beam acquiring a velocity $v \sim v_{osc}$.

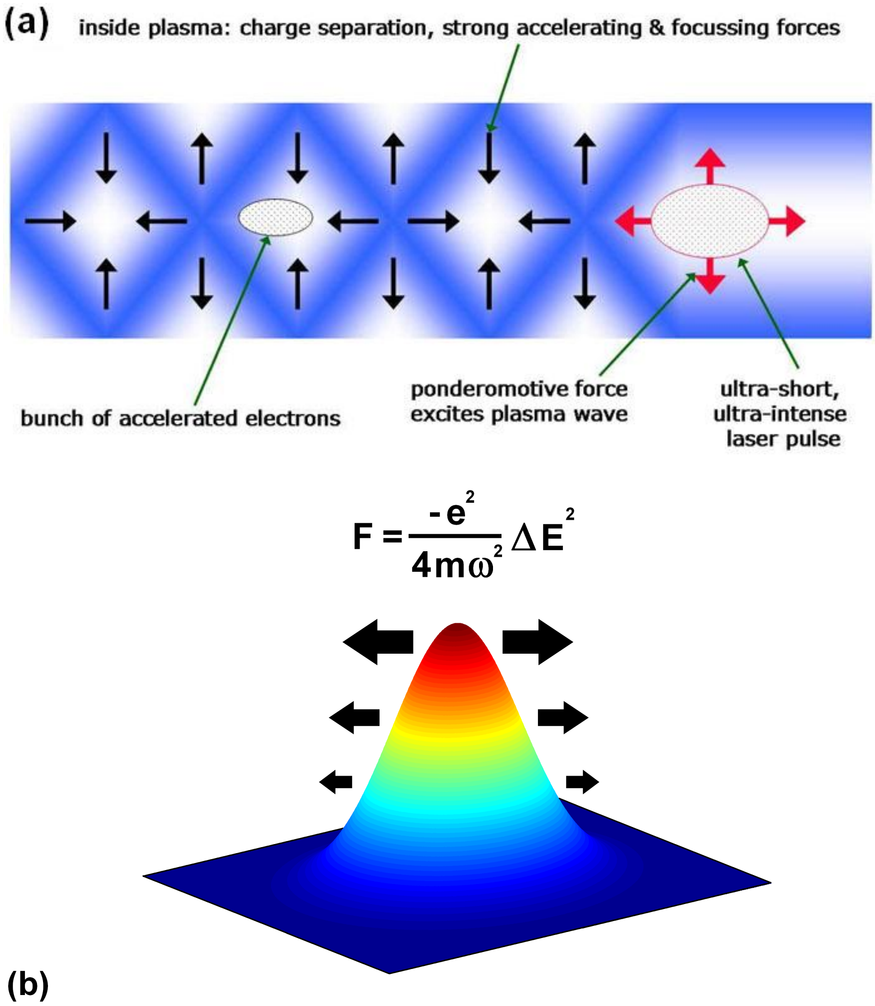

Figure 2.3: (a) The charge separation caused by the ponderomotive force of a high intensity laser pulse and subsequent accelerating forces. (b) The ponderomotive force is greatest at high electric field gradients and will drive charged particles to regions of lower field amplitude.

To consider a relativistic version of equation 2.22 we must rewrite the original Lorentz equation (2.1) in terms of the vector potential $\mathbf{A}$ to obtain

$$\frac{\partial \mathbf{p}}{\partial t} + (\mathbf{v}\cdot\nabla)\mathbf{p} = \frac{e}{c}\frac{\partial \mathbf{A}}{\partial t} - \frac{e}{c}\mathbf{v} \times (\nabla \times \mathbf{A}), \tag{2.23}$$

then separating the timescales of the electron motion into fast and slow components as,

$$\mathbf{p} = \mathbf{p}_s + \mathbf{p}_f \tag{2.24}$$

and using the following identity:

$$\mathbf{v} \times (\nabla \times \mathbf{p}) = \frac{1}{m\gamma}\mathbf{p} \times (\nabla \times \mathbf{p}) = \frac{1}{2m\gamma}\nabla\left|\mathbf{p}\right|^2 - \frac{1}{m\gamma}(\mathbf{p}\cdot\nabla)\mathbf{p}. \tag{2.25}$$

To lowest order, the fast (transverse) component of the electron momentum follows the vector potential: $\mathbf{p}_f = e\mathbf{A}/c$. Averaging over a laser cycle, we obtain the expression for the relativistic ponderomotive force

$$\mathbf{F}_p = \frac{dp_s}{dt} = -mc^2\nabla\overline{\gamma}, \tag{2.26}$$

where $\gamma = \sqrt{(1 + p_s^2/m^2c^2 + a_0^2/2)}$.

2.3 Relativistic plasma optics

As is well known in the field of non-linear optics, high intensity laser pulses can alter the dielectric properties (i.e. the refractive index) of the medium they traverse. The interaction of intense laser pulses in underdense plasma can be understood by similar concepts where the pulse dynamics are governed by the refractive index of the plasma expressed as [41]:

$$\eta_p(r) = \left(1 - \frac{\omega_p^2}{\gamma(r)\omega_0^2}\right)^{\frac{1}{2}}, \tag{2.27}$$

where $\gamma(r) = (1 + a_0^2(r)/2)^{1/2}$. This expression shows that the local plasma refractive index depends on the plasma electron density, laser intensity and laser frequency, through the appearance of ω_p, $\gamma(r)$, and ω_0 respectively. For a laser pulse with a Gaussian radial profile $a(r)$, the on-axis electrons experience higher relativistic driving fields than those at the wings by an amount that depends on the time averaged relativistic factor $\gamma(r)$. Consequently, electrons quivering in the center of the pulse will have more inertia than those oscillating in the

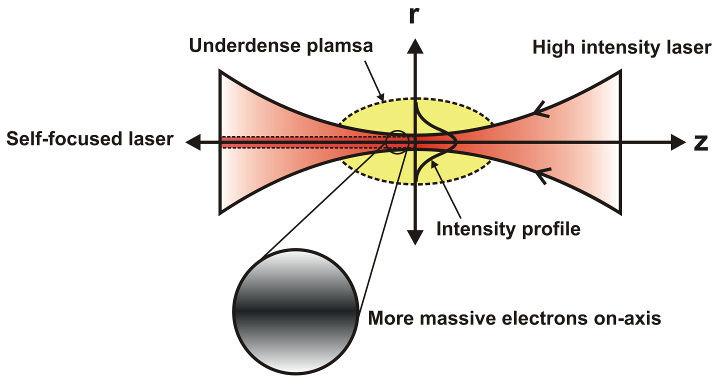

Figure 2.4: The relativistic self-focussing phenomenon in an underdense plasma is caused by the radial intensity dependence of the laser pulse. Relativistic effects cause a corresponding radial dependence of the electron inertia resulting in a radial refractive index gradient which focuses the laser pulse.

lower electric fields at the edge of the pulse. This radial variation of electron inertia across the intensity envelope translates to a corresponding modulation of the local plasma frequency, resulting in an on-axis maximum of the refractive index, $\eta_p(r)$. This condition $(d\eta_p/dr < 0)$, constitutes a 'positive' focussing effect which becomes stronger as the laser beam decreases in diameter and becomes more intense (figure 2.4).

Relativistic mass shifts are not the only effect responsible for refractive index modulations. The laser field can also produce plasma density perturbations through the action of the ponderomotive force. Furthermore, gradients in the refractive index can also cause local modulations of the laser frequency. These additional parameters can be accounted for by expansion of the refractive index as done by Mori [39]:

$$\eta(r) = 1 - \frac{1}{2}\frac{\omega_p^2}{\omega^2}\left(1 + \frac{\delta n}{n_0} - \frac{a(r)^2}{4} - \frac{2\delta\omega}{\omega_0}\right), \tag{2.28}$$

thus using the relation $v_\phi(r) = c/\eta(r)$ we can attain an expression for the phase velocity:

$$v_\phi(r) = c\left(1 + \frac{1}{2}\frac{\omega_p^2}{\omega_0^2}\left(1 + \frac{\delta n}{n_0} - \frac{a(r)^2}{4} - \frac{2\delta\omega}{\omega_0}\right)\right), \tag{2.29}$$

then using the relation $v_\phi v_g = c^2$, obtain a similar expression for the group velocity:

$$v_g(r) = c\left(1 - \frac{1}{2}\frac{\omega_p^2}{\omega_0^2}\left(1 + \frac{\delta n}{n_0} - \frac{a(r)^2}{4} - \frac{2\delta\omega}{\omega_0}\right)\right). \tag{2.30}$$

An estimate of the threshold power needed to make a laser beam self-focus due to relativistic effects can be obtained using geometrical arguments [153]. We consider

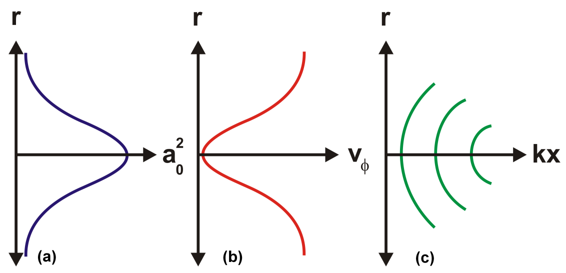

Figure 2.5: (a) The radial relativistic intensity a_0 dependence of a Gaussian laser pulse in an underdense plasma. (b) The greater on-axis electron inertia results in a corresponding on-axis phase velocity minimum with respect to the wings. (c) This results in a 'positive' focussing effect of the laser pulse.

a laser pulse with a radial profile $a(r) = a_0 \exp(-r^2/2\sigma_0^2)$, which has been focused to a spot size, σ_0, just inside a region of uniform, underdense plasma. Neglecting non-linear effects the beam will diffract with a divergence angle of [154]:

$$\theta_d = \frac{dr}{dz} = \frac{\sigma_0}{z_R} = \frac{1}{k\sigma_0}, \tag{2.31}$$

where $z_R = 2\pi\sigma_0^2/\lambda$ is the Rayleigh length. The phase velocity of the wavefronts passing through the relativistic plasma described by equation 2.28 can be approximated giving:

$$\frac{v_\phi(r)}{c} = \frac{1}{\eta_p} \approx 1 + \frac{\omega_p^2}{2\omega^2}\left(1 - \frac{a^2(r)}{4}\right). \tag{2.32}$$

Looking across the beam profile (figure 2.5) it is apparent that the phase fronts will travel more slowly at the centre (on-axis) than at the wings, given a velocity difference:

$$\frac{\Delta v_\phi(r)}{c} = \frac{\omega_p^2}{8\omega^2} a_0^2 e^{-r^2/\sigma_0^2}. \tag{2.33}$$

This phase front curvature causes the rays to bend by an amount determined by their relative path difference. The maximum path difference is:

$$\Delta L = |\Delta v_\phi|_{\max} t = \left|\frac{\Delta v_\phi}{c}\right|_{\max} z = \alpha r. \tag{2.34}$$

Thus the maximum focussing angle of the beam is:

$$\alpha^2 = \frac{\omega_p^2 a_0^2}{8\omega^2}. \tag{2.35}$$

Beam spreading due to diffraction will therefore be canceled by self-focussing effects if $\theta_d = \alpha$ yielding:

$$a_0^2 \left(\frac{\omega_p \sigma_0}{c}\right) \geq 8. \tag{2.36}$$

The result is a power threshold for relativistic self-focussing in a uniform underdense plasma given by the critical power:

$$P_c = 17.3 \left(\frac{\omega_0}{\omega_p}\right)^2 \text{GW}, \tag{2.37}$$

which can be reduced using higher electron densities, but this has the accompanying counteracting effect of increasing the refractive defocusing phenomenon.

2.4 Pulse compression

An electromagnetic light wave or laser pulse can undergo frequency shifts and pulse compression during propagation in underdense plasma due to co-moving longitudinal gradients in the refractive index. This can be a consequence of laser intensity gradients causing ponderomotive density fluctuations or due to the presence of a relativistic plasma wave. These spatial and temporal variations in refractive index $\eta(x, t)$ cause spectral changes as well as pulse compression to a light pulse propagating in plasma. Pulse compression occurs when a laser pulse co-moving with a relativistic density ramp or relativistic plasma wave induces longitudinal variations of the refractive index, causing different parts of the pulse to travel with different velocities. If the front of a laser pulse travels slower than the back then the pulse will be compressed. Considering two points, z_1 and z_2 inside the laser pulse initially separated by a distance L then the change in separation after some time, Δt is given by:

$$\Delta L = (v_{g2} - v_{g1})\, \Delta t. \tag{2.38}$$

We can write the change in group velocities in terms of the gradient of the group velocity and the initial separation L through $\Delta v_g \approx L(\partial v_g/\partial z)$. It is now also convenient to introduce a coordinate transform into a frame 'co-moving' with the group velocity of the laser pulse $v_g \simeq c$. Thus we choose variables (ξ, τ) such that $\xi = z - ct$ and $\tau = t$. We may now write the rate of compression as

$$\frac{1}{L}\frac{\partial L}{\partial t} = -c\frac{\partial \eta}{\partial \zeta}. \tag{2.39}$$

The longitudinal variations in the refractive index can be due to any of the three terms in the expansion (equation 2.28) of the refractive index (plasma density perturbations, laser intensity, or local frequency variations) and can lead to modulations of the laser pulse envelope - either through pulse stretching or pulse compression depending on the sign of the refractive index gradient.

2.5 Photon acceleration

As discussed previously, longitudinal variations in the refractive index result in pulse compression due to variations in the group velocity across the laser pulse. The longitudinal variation in the refractive index also modulates the phase velocity across the laser pulse, hence wavelength changes occur inside the laser pulse envelope as the wavefronts bunch together (photon acceleration) or spread away from each other (photon deceleration). The changes in frequency that result correspond to changes in photon energy as the laser pulse submits energy to drive the wakefield. This process is generally described as 'photon acceleration' for the case when photons gain energy and 'photon deceleration' when photons lose energy. This idea was first introduced by Wilks [155] and since then has been demonstrated experimentally among several groups worldwide using laser wakefields [156] and relativistic ionisation fronts [157]. To analyse this effect we consider two wavefronts separated by a phase difference of 2π, i.e. separated by one wavelength. If the phase velocity is different at two points, then in a time Δt these two wavefronts will have traveled different distances. Since we have defined these points to be wavefronts with a 2π phase difference, this corresponds to a change in the wavelength. If the change in the phase velocity is small over a wavelength then we can write the difference in the phase velocities as $\Delta v_\phi = \frac{\partial v_\phi}{\partial z}\lambda_0$ and the rate of change of wavelength is given by [9]

$$\frac{\partial \lambda}{\partial t} = \frac{\partial v_\phi}{\partial z}\lambda_0. \tag{2.40}$$

If we express this in terms of frequency rather than wavelength and the refractive index gradient rather than $\frac{\partial v_\phi}{\partial z}$ and change to the speed of light variables, we have an equation for the rate of photon acceleration:

$$\frac{1}{\omega}\frac{\partial \omega}{\partial \tau} = \frac{c}{\eta^2}\frac{\partial \eta}{\partial \xi}. \tag{2.41}$$

Equation 2.41 states that when there are refractive index gradients co-moving with the laser pulse then frequency shifts can occur. It should be noted that the pulse compression described in equation 2.39 and the photon acceleration described by equation 2.41 cannot occur on their own. Both are due to longitudinal gradients in the refractive index and so any refractive index gradient will result in the occurrence of both processes.

These spectral shifts of the driving laser pulse are a useful diagnostic [156]. If the driving laser pulse length is shorter than half a plasma wavelength then the laser radiation propagates entirely inside the initial red-shifting phase of the wakefield. This results in some of the pump laser spectrum being transferred to longer wavelengths. If there is no laser energy transferred to longer wavelengths in the measured spectrum, it is unlikely that a wakefield of significant amplitude was being driven by the laser pulse. When the pulse extends into the accelerating phase of the wakefield the back of the pulse is blueshifted. The energy gained at the back of the pulse originates from the front of the pulse, which drives the wakefield, and is red-shifted. As a result the laser spectrum broadens.

It is also possible for the pulse to be exclusively blue-shifted by photon acceleration if it is also ionising the plasma through which it propagates. The ionisation front, which co-propagates with the laser pulse, has an accelerating refractive index gradient. Despite the overall frequency increase of the light energy is conserved because some photons are absorbed in the ionisation process. An overall shift of the spectrum towards blue can be interpreted as evidence that the laser is creating electrons through ionisation as it propagates. This is often referred to as an ‘ionisation blueshift’.

2.6 Modulational instabilities

There are various types of ‘modulational instabilities’, classified according to the relation between the phase velocity, v_ϕ of the plasma wave and the electron and ion thermal velocities v_{th}^{e-}, v_{th}^{i+} respectively. When an incident pump scatters off a Langmuir wave the instability is known as Stimulated Raman Scattering (SRS). If the plasma wave satisfies $v_\phi \approx v_{th}^{e-}$ then the electrons experience strong Landau damping. In this case the plasma wave is no longer an eigenmode but a driven oscillation, of which any subsequent scattering is known as stimulated Compton scattering. Finally when, the pump scatters off an ion-acoustic wave ($v_{th}^{i+} \ll v_\phi \ll v_{th}^{e-}$), it is known as Brillouin scattering. In laser wakefield acceleration, the plasma is usually cold and the timescales involved are so short that ion motion can be neglected. Therefore, stimulated Raman Scattering is the most important parametric instability in laser wakefield research [43].

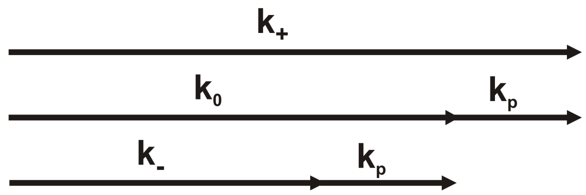

Figure 2.6: The phase matching conditions for forward Raman scattering, $\mathbf{k}_{\pm} = \mathbf{k}_0 \pm \mathbf{k}_p$.

2.7 Forward Raman Scattering (FRS)

As introduced in the previous section an important class of instability for laser wakefield excitation is Forward Raman scattering (FRS). When a strong electromagnetic pump wave $(\omega_0, \mathbf{k}_0)$ interacts with an underdense plasma it drives various longitudinal plasma waves, giving rise to density perturbations. Oscillating electrons in the presence of laser light with an electric field $E(r)$ leads to a small density fluctuation, δn, thus producing a transverse current, which generates a small scattered light wave. This scattered light wave in turn beats with the incident field to reinforce the density fluctuation via the ponderomotive force. Hence, the plasma wave and scattered light wave grow at the expense of the incident light giving rise to excitation of electromagnetic sidebands $(\omega_0 \pm \omega_p, \mathbf{k}_0 \pm \mathbf{k}_p)$ located at the sum and difference of the pump and plasma frequencies. We may write the frequency and wavenumber matching conditions such that the energy and momentum fields are conserved:

$$\begin{aligned} \omega_{\pm} &= \omega_0 \pm \omega_p, \\ \mathbf{k}_{\pm} &= \mathbf{k}_0 \pm \mathbf{k}_p. \end{aligned} \tag{2.42}$$

These are termed as the Stokes and anti-Stokes shift (Raman satellites). The frequency down-shifted wave is known as the Stokes wave, and the upshifted wave is called the anti-Stokes wave. When the interaction is such that these generated sidebands enhance or drive the plasma waves, which in turn acts back on and enhance the sideband growth the interaction becomes unstable.

The growth rate of the instability can be quantified by Γ_0 given by [153]

$$\Gamma_0 = \frac{\omega_p^2 a_0}{\sqrt{8}\omega_0 \left(1 + a_0^2/2\right)}. \tag{2.43}$$

In the non-relativistic limit, $a_0 \ll 1$, this reduces to the standard result [158, 159]:

$$\Gamma_0 = \frac{\omega_p^2 a_0}{\sqrt{8}\omega_0}, \tag{2.44}$$

and in the other extreme, where relativistic effects are considered $a_0 \gg 1$, the growth rate becomes [153]:

$$\Gamma_0 \simeq \frac{\omega_p^2}{\sqrt{2}\omega_0 a_0}, \tag{2.45}$$

and therefore falls off with increasing laser intensity. The maximum growth rate is found from equation 2.43 to be $\Gamma_{max} = \omega_p^2/4\omega_0$ at $a_0 = \sqrt{2}$.
There exist certain requirements in order to support the stimulated Raman instability the first of which being that all the EM waves must be able to propagate in the plasma thus $n_e \leq 1/4n_{cr}$. The driving laser pulse must also be longer than one plasma period, corresponding to the regime in which ponderomotive excitation of a laser wake by the laser pulse envelope ceases to play a role. Even though the laser pulse may still excite a wake in this regime its role is far overwhelmed by the Raman forward scattered Langmuir wave. If strongly driven, these processes can lead to the generation of fast electrons by wave breaking and the eventual self-modulation of the propagating laser pulse, which can in turn drive the self modulated laser wakefield regime [43].

2.8 Backward Raman Scattering (RBS)

For the Raman backward scattering (RBS), the instability has been shown by Gibbon [153] that the maximum growth for RBS occurs for

$$k = k_0 + \frac{\omega_0}{c}\left(1 - \frac{2\omega_p}{\omega_0}\right)^{1/2} \approx 2k_0, \tag{2.46}$$

for $\omega_p/\omega_0 \ll 1$. In this limit we have

$$\frac{\Gamma_{RBS}}{\omega_p} = \frac{\sqrt{3}}{2}\left(\frac{\omega_0}{2\omega_p}\right)^{1/3} \frac{a_0^{2/3}}{(1 + a_0^2/2)^{1/2}}, \tag{2.47}$$

which is maximum for $a_0 = 2$, after which it falls off as $a_0^{-1/3}$ for $a_0 \gg 1$. In the non-relativistic limit, we also recover the standard result for the strongly coupled regime [160].

2.9 3D self-modulation

Real laser-plasma acceleration experiments are not well described by 1D models since to reach the intensities necessary to drive plasma waves the laser must be focused to a spot whose size is of the order of the plasma wavelength. In section 2.3 transverse focusing occurs in a plasma density perturbation. The density profile of a 2D or 3D plasma wave means that some regions of the plasma wave actually focus the laser pulse due to the refractive index being greater on axis, whereas some regions enhance the diffraction of the laser pulse. These regions are half a plasma wave apart which leads to a modulation of the laser pulse envelope at the plasma frequency in a similar way to the 1D self-modulation instability.

2.10 Laser wakefield excitation

In 1979 Tajima and Dawson [21] proposed a method of coupling the transverse electromagnetic energy of a high power laser into longitudinal plasma waves with relativistic phase velocities. At a fundamental level the mechanism relies on the concept that when an ultrashort laser pulse propagates in underdense plasma, there is not enough time for the larger inertia ions to move significantly compared to electrons. At relativistic intensities the light pressure which is alternatively known as the ponderomotive force predominantly pushes the electrons forward in the same direction as the laser propagation, however there is also a radial push in the transverse direction to the pulse propagation, resulting in the electrons moving away from regions of high intensity. This sets up a space charge displacement causing the plasma ions to pull back the electrons to their original equilibrium position. However, the electrons overshoot their equilibrium position resulting in an electron plasma oscillation (Langmuir wave) at the characteristic plasma frequency, ω_p. This electrostatic plasma wave, driven by the ponderomotive force of the laser, adopts a relativistic phase velocity equal to the group velocity, $v_g \approx c(1 - \frac{\omega_p^2}{\omega_0^2})$ of the driving laser pulse in the plasma. The plasma wavelength $\lambda_p = 2\pi v_g/\omega_p$ also depends on the group velocity of the driving laser pulse, which can be very close to the speed of light for low density plasmas.

This makes relativistic plasma waves excellent candidates for the acceleration of charged particles, due to their relativistic phase velocities and ability to support very large longitudinal electric fields. Charged particles traveling close to the speed of light may interact with the plasma waves for a significant length of time leading to efficient energy coupling and acceleration.

In order to quantify the strength and effects of a laser induced wakefield we start

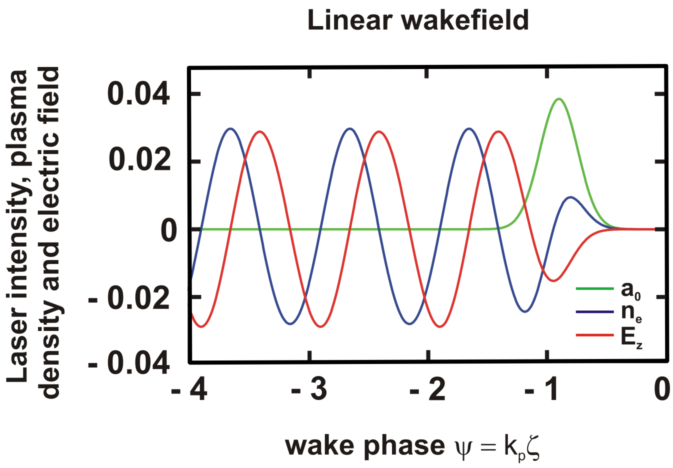

Figure 2.7: The solution of the small amplitude wakefield equation in the linear regime. The laser intensity envelope, a_0 (green line), the plasma density perturbation, n_e (blue line) and the longitudinal electric field profile of the wakefield, E_z (red line).

with an expression to describe plasma waves driven in the weak field limit [153]

$$\frac{\partial^2 n}{\partial t^2} + \omega_p^2 n = \frac{n_0}{2}\frac{\partial^2}{\partial z^2}\frac{v_x^2}{c^2}, \tag{2.48}$$

where n is the perturbed density and n_0 is the equilibrium density. It is now appropriate to assume the quasistatic approximation and to transform into a frame co-moving with the group velocity of the laser pulse $v_g \simeq c$. Thus we select (ξ, τ) as new variables, such that $\xi = z - ct$ and $\tau = t$. The partial derivatives in equation 2.48 thus become

$$\frac{\partial}{\partial x} = \frac{\partial}{\partial \xi}; \qquad \frac{\partial}{\partial t} = \frac{\partial}{\partial \tau} - c\frac{\partial}{\partial \xi} = -c\frac{\partial}{\partial \xi}, \tag{2.49}$$

following from this:

$$\frac{\partial^2}{\partial x^2} = \frac{\partial^2}{\partial \xi^2}; \qquad \frac{\partial^2}{\partial t^2} \simeq c^2\frac{\partial^2}{\partial \xi^2}. \tag{2.50}$$

In this approximation we may assume that the time τ is considered to be slowly varying during the transit time of the laser pulse, thus we can effectively set $\partial/\partial\tau = 0$ in the co-propagating frame of reference. In this new coordinate system, letting $a = v_x/c$ we attain the Eulerian transformation of equation 2.48:

$$\left(\frac{\partial^2}{\partial \xi^2} + k_p^2\right) n = \frac{n_0}{2}\frac{\partial^2}{\partial \xi^2} a^2, \tag{2.51}$$

and making use of Poisson's equation:

$$\frac{\partial^2 \phi}{\partial \xi^2} = -\frac{\partial E}{\partial \xi} = 4\pi en, \tag{2.52}$$

we can write down an equation for the wakefield potential (normalised to mc/e):

$$\left(\frac{\partial^2}{\partial \xi^2} + k_p^2\right)\phi = -k_p^2 \Phi_L, \tag{2.53}$$

where $\Phi_L = -\frac{1}{2}\langle a^2 \rangle$ is the normalised ponderomotive potential of the laser pulse, which we take to be averaged over the laser period $2\pi/\omega_0$, so that in terms of the slowly varying pulse envelope, $\Phi_L(\xi) = -\frac{1}{4}a(\xi)^2$.

Equation 2.53 is a driven Helmholtz equation which can be solved using Green's function [161] to attain a solution for $\phi(\xi)$:

$$\phi(\xi) = -\frac{k_p}{4}\int_{\xi}^{\infty} d\xi' \, |a(\xi)|^2 \sin\left[k_p\left(\xi - \xi'\right)\right]. \tag{2.54}$$

We can then retrieve the density, n, from equation 2.52 and using the relation:

$$E_z = -\frac{\partial \phi}{\partial \xi}, \tag{2.55}$$

retrieve the longitudinal wakefield left behind by the laser pulse. Numerical examples of these quantities are shown in figure 2.7.

In order to consider a relativistic treatment of laser wakefield generation we can again apply the quasistatic approximation in a Eulerian frame moving with the pulse. However, this time an arbitrary group velocity v_g, is chosen so that $\tau = t$ and $\xi = z - v_g t$. We may write down the momentum equation in this coordinate frame:

$$\frac{\partial}{\partial \xi}\left[\phi - \gamma\left(1 - \beta_g u\right)\right], \tag{2.56}$$

where $\beta_g = v_g/c$ and $u = v_z/c$ similarly we may write down the continuity equation for the charge density in this frame:

$$\frac{1}{c}\frac{\partial n}{\partial \tau} = \frac{\partial}{\partial \xi}\left[n\left(\beta_g - u\right)\right]. \tag{2.57}$$

Now by noting that the evolution timescale τ of the pulse envelope is typically the Rayleigh diffraction time, which is much longer than a laser period we may neglect $\partial/\partial\tau$ relative to $\partial/\partial\xi$. After some algebra and manipulation we can express the fluid quantities entirely in terms of the pump amplitude a and from

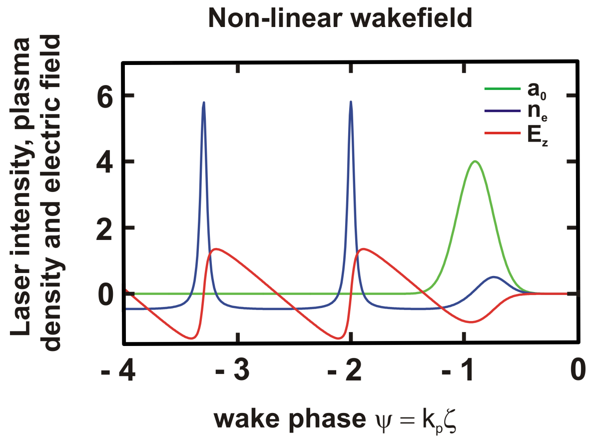

Figure 2.8: The solution of the non-linear wakefield equation. The laser intensity envelope, a_0 (green line), the plasma density perturbation, n_e (blue line) and the longitudinal electric field profile of the wakefield, E_z (red line).

Poisson's equation in the co-moving coordinates we attain:

$$\frac{\partial^2 \phi}{\partial \xi^2} = k_p^2 (n-1) = k_p^2 \gamma_g^2 \left(\frac{\beta_g}{\psi} - 1 \right)$$

$$= k_p^2 \gamma_g^2 \left\{ \frac{\beta_g (1+\phi)}{\left[(1+\phi)^2 - \gamma_g^{-2} (1+a^2) \right]^{1/2}} - 1 \right\}. \tag{2.58}$$

We may then integrate numerically equation 2.58 for a given pulse amplitude $a(\xi)$ at a given time τ. Again once we have the wakefield potential $\phi(\xi)$ we can attain the longitudinal electric field from equation 2.55 and the density from equation 2.52.

In the laser wakefield regime there exists an optimum pulse duration which can resonantly drive the most intense wake. The maximum plasma wave amplitude will occur when the pulse duration and/or plasma density are tuned to satisfy the condition, $\tau_p = 2\pi/\omega_p$. This resonant requirement can be understood by a relatively simplistic conception (figure 2.9). As the front end of the pulse enters a region of unperturbed plasma, the ponderomotive force pushes electrons in the forward direction and initiates plasma oscillations. Half way through, however the ponderomotive force reverses its sign, and the electrons receive another kick in the opposite direction.

The resonant condition is satisfied if the reversal of the ponderomotive force

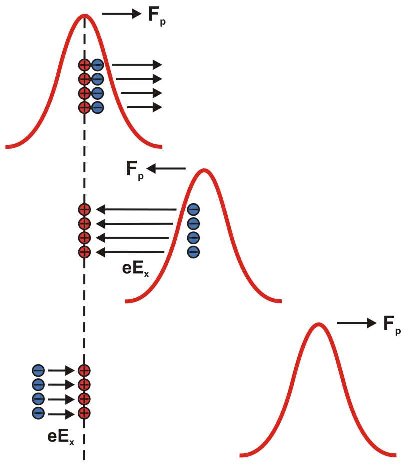

Figure 2.9: The optimum driving conditions for electron acceleration through laser wakefield excitation constitutes a double ponderomotive 'kick' on the electrons by the driving laser pulse.The ponderomotive force initially pushes the electrons in the forward direction away from their equilibrium position. The laser pulse then passes the electrons at their maximum extension distance from the ions, reverses its polarity and gives the electrons another 'kick' back towards the ions resulting in resonant wakefield growth.

polarity, at the back of the pulse takes place when the electrons at the point when they are starting their motion back towards their equilibrium position. This secondary 'kick' enhances the electron oscillation, setting up a larger wakefield and increased accelerating gradients. It is important to note that this consideration gives the optimum pulse duration for a given amplitude, however if the pulse energy is fixed, a shorter, thus more intense pulse will drive a stronger wakefield, meaning that the LWFA regime is currently limited by the maximum laser intensity and the minimum laser pulse length achievable by current laser technology. The pending availability of short pulse, petawatt systems will allow the LWFA mechanism to be driven to unprecedented amplitudes.

2.11 Plasma beat waves (PBWA)

In 1979 laser technology was insufficient to drive the LWFA mechanism due to pulse durations exceeding several hundred picoseconds. In the absence of femtosecond technology, as an alternative to access a regime where high phase velocity plasma waves could be generated, Tajima and Dawson proposed the beat wave wakefield accelerator (PBWA) [21]. In the beat wave scheme two laser pulses with different frequencies ω_0 and ω_1 are optically mixed in plasma to generate a beat-wave such that $\omega_0 - \omega_1 = \omega_p$ (figure 2.10). This beat-wave can be matched to the plasma frequency to resonantly drive a large amplitude plasma wave. This effectively results in a train of shorter pulses which are able to drive up a beat wave over several plasma periods. This is in contrast to the LWFA scheme, where a plasma wave is forcibly driven by a single laser pulse, the beatwave method relies on a more gentle build creating a plasma wave whose amplitude grows with time.

The beat-wave mechanism can evolve from a linear growth regime to drive non-linear plasma waves on the order of picoseconds, however there are a number of processes which not only limit the maximum plasma wave amplitude, but which act to destroy the coherence of the wake. The most important of these are linear detuning and relativistic detuning. Linear detuning is caused by a mismatch between the beat frequency $\Delta\omega = \omega_0 - \omega_1$ and plasma frequency, such that $\Delta\omega - \omega_p \neq 0$. Relativistic detuning occurs when the amplitude of the plasma wave becomes large enough to increase the effective mass of the electrons, resulting in a change of the local plasma frequency such that $\omega_0 - \omega_1 \neq \omega_p/\sqrt{\gamma}$ ($\gamma =$ Lorentz factor of oscillating electrons). This relativistic shift results in the plasma frequency drifting away from resonance, hence limiting the ultimate plasma wave amplitude. For perfect frequency matching, the maximum saturation amplitude of the plasma wave is given by

$$E_{\max} = \left(\frac{16a_1a_2}{3}\right)^{\frac{1}{3}} \tag{2.59}$$

where a_1 and a_2 are the vector potentials of the driving beams. This is the standard result, for plasma wave saturation by relativistic detuning, originally derived by Rosenbluth and Liu [162].

2.12 Self modulated laser wakefields (SML-WFA)

The SM-LWFA starts in a similar way to the LWFA. The front edge of the laser pulse provides the ponderomotive force required to excite a plasma wave. An initially long laser pulse $\omega_p\tau \gg \pi$ or $c\tau \gg \lambda_p$ encloses several plasma wavelengths. If the laser pulse is of high enough intensity, the forward Raman instability described in section 2.7 can modulate the laser pulse into a train of smaller pulses. This is due to areas of high and low density present in the form of a plasma wave causing longitudinal bunching of the photons within the laser pulse en-

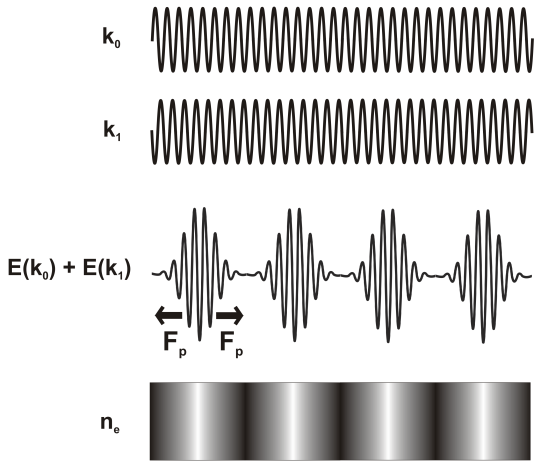

Figure 2.10: The beatwave mechanism is driven by the beating of two electromagnetic waves detuned by the plasma frequency ω_p, resulting in a train of shorter pulses which forms a density echalon in the plasma.

velope. Successive sections of the laser pulse are also transversely focused and diffracted respectively which results in the envelope of the pulse separating into pulses which automatically match the resonance condition for plasma wave generation ($\omega_p \tau = \pi$ or $c\tau = \frac{1}{2}\lambda_p$), thus effectively each pulse fragment interacts resonantly with the plasma wave in a similar way to the LWFA mechanism. This is a convenient effect for electron acceleration experiments where only long pulses are available. The laser pulse can self evolve due to the surrounding plasma conditions and enter into a more efficient resonant regime. The effect of the modulation instabilities on a 2D Gaussian pulse is shown schematically in figure 2.11.

2.13 Wavebreaking

Relativistic electrons can be generated through wavebreaking of large amplitude relativistic plasma waves which are created in the wake of the laser pulse as it propagates through an underdense plasma. There exists a physical limitation on how large an electric field a longitudinal plasma oscillation (wakefield) may support. This is obviously a crucial issue for particle acceleration as one requires that the electric field be as high as possible for optimum acceleration over a finite length of plasma. Physically, wavebreaking occurs when the velocity of particles in the wave approaches the phase velocity of the wave [54] in which they become trapped and accelerated. This process is extremely important to LWFA because it means that electrons from the background plasma can become trapped and accelerated, eliminating the need for an external source of electrons (there are a

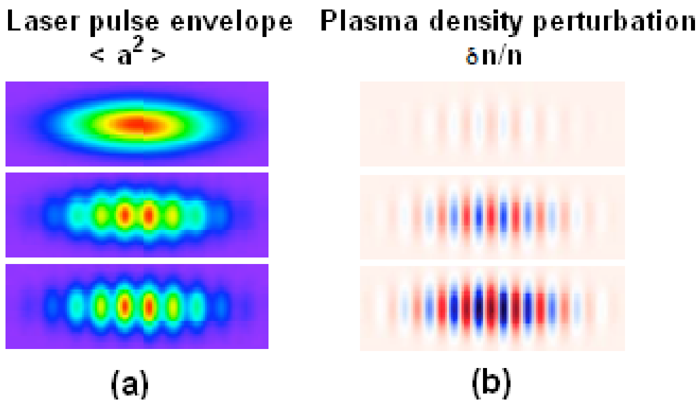

Figure 2.11: An illustration of the SMLWFA mechanism. (a) The laser pulse envelope splits into many small pulses due to longitudinal bunching of the photons and transverse focusing caused by the plasma conditions. (b) A subsequent density echelon is created which can further enhance the modulation. (figure adapted from [9].)

range of technical problems associated with external injection schemes). However this also limits the maximum achievable accelerating gradient within the plasma wave. That is because the electric field of the trapped electrons suppresses the electric field of the wakefield, which is known as 'beam-loading' [163].

In a 1D plasma wave it is possible to show that wavebreaking occurs when the amplitude of the displacement of electrons in the wave approaches the plasma wavelength - i.e. when the particle trajectories cross [164]. Wavebreaking in 3 dimensions also occurs when particle trajectories cross, however due to transverse effects can take place at lower amplitudes. Wavebreaking is an important process because it is a way in which electrons can be injected into plasma waves to be accelerated. Using the following expression:

$$\nabla \cdot E = -e\delta n/\varepsilon_0 \tag{2.60}$$

and

$$|ik_p E_0| = -en_0/\varepsilon_0 \tag{2.61}$$

and taking $v_p \approx c$ a plasma wave driven by a laser pulse of wavelength 800 nm in a plasma density of $n_e = 1.75 \times 10^{19}\text{cm}^{-3}$ can support electric fields of 400 GV/m.

If we assume the plasma is cold, and the quiver velocity of the electrons in the plasma wave equals the phase velocity of the plasma wave, $k_p = \omega_p/c$ then the maximum field which can be supported in the non-relativistic limit is

$$E_{\max} = \frac{m\omega_p v_p}{e}, \tag{2.62}$$

which is the ‘cold wave-breaking limit’ derived by Dawson and Oberman [52]. This picture treats wavebreaking as crossing of neighboring charge sheets, accompanied by nonlinear steepening of the plasma wave fronts until a density singularity is reached (figure 2.8).

The above wavebreaking expression needs modification when the phase velocity of the electrons are close to the phase velocity of a relativistic plasma wave. In this case the electrons must also be relativistic. When relativistic effects are taken in to account ($\gamma_p > 1$), the 1D cold relativistic wavebreaking limit increases to [153]

$$E_{\max} = \frac{mc\omega_p}{e}\sqrt{2}\,(\gamma_p - 1)^{1/2}\,. \tag{2.63}$$

In the case of a warm plasma thermal effects act to reduce the maximum attainable wave amplitude. There are two reasons for this: first, plasma pressure resists tendency for the density to explode; second, thermal electrons moving in the direction of the wave may be trapped at a lower wave amplitude than cold particles would be. These corrections were first introduced by Coffey [54] using the so called ‘waterbag’ model for the electron distribution function. It was demonstrated that the wavebreaking limit for a non-relativistic plasma wave in a warm plasma is

$$\frac{eE_{\max}}{m\omega_p v_p} = \left(1 - \frac{\mu}{3} - \frac{8}{3}\mu^{1/4} + 2\mu^{1/2}\right)^{1/2}, \tag{2.64}$$

where $\mu = 3kT_e/mv_p^2$, k is the Boltzmann constant, and T_e is the plasma electron temperature.

This was extended to a relativistic case by Katsouleas and Mori [55], who generalised Coffey’s waterbag model [54] to include relativistic fluid momenta. They found the relativistic wavebreaking amplitude in a warm plasma in the limit $\beta \simeq 1 \pm \sqrt{2}\omega_p\beta_p(\gamma_m - \gamma)^{1/2}$ (γ_m is the maximum oscillation Lorentz factor of the wave) to be:

$$\frac{eE_{\max}}{mc\omega_p} = \mu^{-1/4}\left(\ln 2\gamma_p^{1/2}\mu^{1/4}\right)^{1/2}. \tag{2.65}$$

This result, together with the non-relativistic limit, is illustrated in figure 2.12.

A plasma wave driven by a laser pulse of wavelength 800 nm in a plasma density of $n_e = 1.75 \times 10^{19}\text{cm}^{-3}$ can support electric fields of 1700 GV/m, more

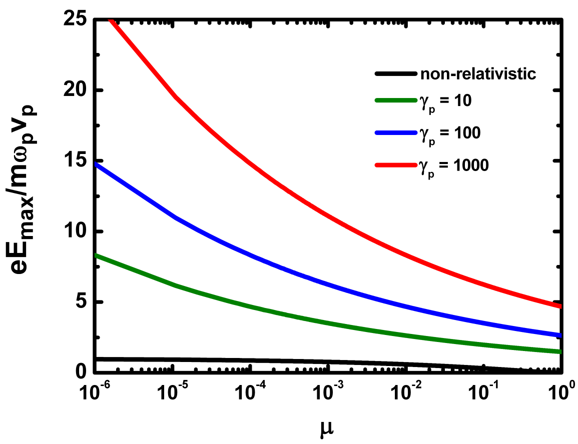

Figure 2.12: The wavebreaking amplitudes of longitudinal plasma oscillations for phase velocities corresponding to: non-relativistic plasma waves (black line), relativistic plasma waves with: γ_p = 10 (green line), γ_p = 100, (blue line) and γ_p = 1000 (red line).

than four times greater than the amplitude calculated with the non-relativistic expression of equation 2.62.

In a 2D or 3D situation transverse effects can lead to wave breaking for lower amplitude waves. This was shown by Bulanov [165] who considered a transverse variation in the plasma wavelength due to a transverse variation in the plasma density, such as would be found in plasma guiding channel. This effect is also evident for plasma waves driven by relativistic laser pulses ($a_0 > 1$). This transverse variation in the laser intensity leads to a variation in the plasma frequency because of the variation in the effective mass of the electrons. The effect of this is to produce plasma waves with curved wavefronts.

2.14 Electron self-trapping

It is possible that electrons may gain energy through external injection into an accelerating phase of a laser wake. This is conventionally done by using an RF electron source in conjunction with a laser wakefield. However the success of this method relies on overcoming challenging synchronisation criteria between the electron bunch and laser-wakefield. It is for this reason most LWFA experiments rely on the self-trapping mechanism whereby background plasma electrons can be trapped in the relativistic plasma waves. Although this method circumvents the need for synchronisation from an external source selection of the phase region in which electrons may be self injected also has challenging hurdles. There are several mechanisms which can be responsible for self injection, depending on the experimental conditions. Trapping can be achieved by temperature induced self injection [166], density gradients [167, 168], 2D wake curvature [165] and wavebreaking [54, 55, 164, 169].

2.15 Beam loading

In the previous section the concept of self injection was introduced. This section will describe how an ultrashort electron bunch is produced as more and more charge is injected into the wakefield. For the following explanation it is appropriate to mention that each phase region confined by one non-linear plasma period is termed a plasma bucket. As more and more electrons become trapped into the plasma buckets the electron bunch also drives its own wakefield.

The wakefields driven by these electron bunches can destructively interfere with the wakefield driven by the laser pulse, resulting in a damping of the wake strength. This phenomenon is known as beam loading [163]. While the total (laser and bunch driven) wake within the first bucket experiences little reduction in strength, the wake in the second bucket is affected by the bunch-driven wake of the electrons in the first bucket. The total wake in third bucket is reduced even more in strength, since it is affected by the bunch driven wakes of the electrons from the first and second bucket. The process continues and as a result the wakefield amplitude is only sufficient for self injection in the first few plasma buckets.

Beam loading can be responsible for the production of ultrashort electron bunches. The reason being that only the first few buckets are injected with the majority of electrons. Since typical plasma wavelengths are of the order of $\lambda_p \simeq 5$ - 10 μm ($\sim$ 15-30 fs), the total bunch duration can be estimated to be a fraction of this duration. Hence, in the ideal case that self injection takes place in the first bucket then electron bunches with durations of a few femtoseconds should be possible.

2.16 Dephasing

One of the main objectives of plasma wave generation via laser wakefields is, to achieve efficient acceleration of electrons over small distances. To accomplish electron acceleration it is usually necessary to inject electrons into a plasma wave with velocities close to the phase velocity of the wave. In this depiction the

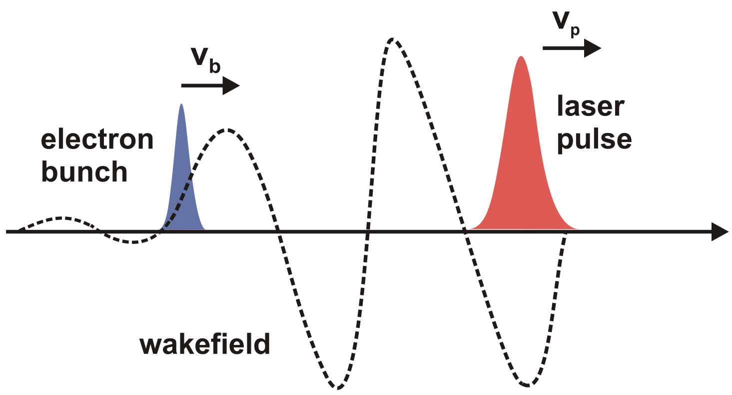

Figure 2.13: A schematic drawing of the beam loading effect, the electron bunch takes energy from the plasma wave.

electrons will be traveling slowly in the reference frame of the wave and will 'feel' an accelerating electric field for an increased time and propagation length. The electron therefore has to have enough energy to be trapped by the potential of the wave, analogous to a surfer catching a wave on the ocean. This means that the electron should possess a velocity close enough to the phase velocity of the wave in order that for the duration it remains in an accelerating phase of the wave it may acquire enough energy to catch up with the wave and be accelerated further. If the electron is not fast enough to be trapped then it will accelerate for a short time but then fall back with respect to the wave into the decelerating phase of the field and be decelerated. Conversely, if an electron being accelerated is traveling faster than the plasma wave, eventually it will outrun the wave and begin to be decelerated by the second half (decelerating phase) of the plasma wave. This is known as dephasing and happens after a length L_d, called the dephasing length.

Since relativistic plasma waves effectively travel at the group velocity of the laser pulse that generates them, there is a mismatch between the speed of the wave and the speed of the electrons.

To estimate the distance over which this occurs we first derive the group velocity of the laser pulse by differentiating the dispersion relation for electromagnetic waves in a plasma:

$$\omega^2 = c^2 k^2 + \omega_p^2. \tag{2.66}$$

The group velocity is thus:

$$v_g = \frac{\partial \omega}{\partial k} = c\sqrt{1 - \frac{\omega_p^2}{\omega^2}}. \tag{2.67}$$

It is convenient to express this velocity in terms of the relativistic factor $\gamma_g = (1 - (v_g/c)^2)^{-1/2} = (\omega/\omega_p)$. The dephasing length L_d is defined as the distance a particle travelling at c propagates in traversing the accelerating region of the wake, which has a length of $\lambda_p/2$. The slippage between the wave and the particle travelling at c is $z = (c - v_g)t_z$, where $t_z = L_z/c$ is the time taken and L_z is the distance over which the particle dephases in the wake by a distance z. Setting $z = \lambda_p/2$, yields an expression for the linear dephasing length

$$L_d = \frac{\lambda_p^3}{\lambda^2}. \tag{2.68}$$

It can be shown that in the high intensity ($a_0 \gg 1$) regime (bubble regime), the dephasing length becomes [170]:

$$L_d \approx a_0 \frac{\lambda_p^3}{\lambda^2}, \tag{2.69}$$

where a constant of order unity has been neglected [170]. The difference between this and the linear expression is due to a change in the effective plasma wavelength, and the fact that the phase velocity of the plasma wave is not equal to the group velocity of the laser pulse.

2.17 Pump depletion

As a plasma wave is excited, energy from the pulse is transferred to the wave, causing the wake amplitude and hence accelerating gradient to decrease with distance. In order to estimate the length over which this effect becomes important, we define the pump depletion length L_{pd} as the distance the pulse travels to lose one-half of its initial energy. This is calculated by equating the energy deposited into the wakefield to the laser pulse energy [171, 172].

The plasma wave generated by the laser pulse has an energy density associated with it. If the electric field of the plasma wave is E_z, then the energy density is $U_p = 1/2\varepsilon_0 E_z^2$. If we assume the volume of the plasma wave is simply the area of the laser focal spot multiplied by the length of the plasma column $V_p = \pi w_0^2 L$, then the total energy is $W_p = U_p V_p$. The energy density of the electromagnetic laser field is $U_L = \epsilon_0 E_L^2$. If we assume that the volume occupied by the laser is $V_L = \pi w_0^2 c\tau$ and that the total energy in the laser pulse is $W_L = U_L V_L$, then the length over which the laser loses energy can be estimated by equating the energy of the pulse to the energy of the plasma wave. Assuming the plasma wave electric field is given by equation [9] $E_z = a_0^2 m_e c\omega_p/e$. This occurs if the laser pulse length is such that $c\tau = \lambda_p/2$. The laser pulse electric field can be expressed in terms of the vector potential through $E_L = a_0 m_e c\omega_0/e$. Combining these equations provides us with the pump depletion length in the linear regime for $a_0 \ll 1$

$$L_{pd} = \frac{n_c}{n}\frac{\lambda_p}{a_0^2}. \tag{2.70}$$

Although at first glance it might appear benefcial that the pulse depletion length is longer than the dephasing length, it in fact shows that the laser energy is not being used effciently. It also means that the length of the plasma must be chosen carefully to terminate the interaction after a dephasing length so that electrons are not decelerated once they have reached their maximum energy.

We can see from the equation above the counter-intuitive relationship that increasing the laser energy for a given spot size and pulse duration decreases the depletion length and does not increase it as one may think. Moreover, equations 2.68, 2.69 and 2.70 illustrate that the dephasing and pump depletion lengths can be increased by operating at lower densities. Furthermore, it is clear that both the pump depletion length and the dephasing length increase for higher a_0 and that for $a_0 \geq 1$ the pump depletion and dephasing lengths are approximately the same, $L_d \approx L_{pd}$, implying efficient use of the pump laser energy. This means that the constraint that the length of plasma should be chosen to match L_d is relaxed.

2.18 Energy scaling

Having discussed the limitations to the energy gain of a wakefield accelerator, it is possible to predict the maximum energy gain (corresponding to one dephasing length) of a laser wakefield accelerator. This is given by

$$\Delta E = -e\int_0^{L_d} E_z(z)dz, \tag{2.71}$$

where E_z is the field experienced by the electrons after propagating a distance z from the point at which they were trapped or injected.

For $a_0^2 \gg 1$ the plasma wave is sinusoidal, so the value of $|E_z(z)|_{lin}$ averaged over one dephasing length is $2E_z/\pi$, where E_z is given by equation 2.55. The resulting expression for ΔE_{lin} is

$$\Delta E_{lin} = -e\,|E_z(z)|_{lin}\,L_d = m_e c^2\frac{n_c}{n_e}a_0^2. \tag{2.72}$$

2.19 Plasma Waveguides

A focused laser pulse will diffract such that its peak intensity decreases to half of its focal value over a length known as the Rayleigh range, $z_R = 2\pi\sigma_0^2/\lambda$. This means that a focused beam in plasma will naturally diverge and only remain intense to drive a wakefield over short distances, effectively limiting the distance that particles can be efficiently accelerated to at most a few Rayleigh ranges. However, it is possible to overcome this problem by using a plasma channel with a parabolic refractive index gradient to counteract the natural diffraction of the laser pulse. Using this method it is possible for a laser pulse to be guided through a capillary over several centimeters and remain intense enough to drive a wakefield over the same distance.

The basic mechanism for channel formation involves pre-forming a discharge plasma inside a hydrogen gas filled capillary. A temperature profile that is peaked on-axis is formed, and since the pressure gradients are equalised on a timescale much shorter than the period of the discharge, the plasma density increases with distance from the capillary axis. This results in a parabolic density profile with a minimum on the central axis hence the refractive index profile causes the wavefronts to bend inward due to the slower phase velocity on-axis. When this exactly counteracts the natural diffraction the pulse can be guided through the capillary with efficiencies of up to 85 % [173].

The propagation of ultra-short high intensity laser pulses through long-scale length underdense plasmas involves an intricate competition between three processes: relativistic self-focussing, diffraction, and ionisation induced refraction. The number of electrons that are produced via ionisation at a particular point of the beam path strongly depends on the prevailing local intensity. As a consequence, any intensity variation across the beam profile would give rise to a spatially varying index of refraction with an excess of electrons around the beam axis. This leads to defocusing because of the negative lensing effect associated with it. In addition the natural diffractional effects of the beam lead to a defocusing effect independent of density. A fine-tuning between focussing due to the waveguide and defocusing due to ionisation and diffraction can allow laser pulse guiding where the plasma channel effectively acts as a waveguide for the laser pulse. In a preformed plasma no ionisation occurs and the guiding is achieved by a balance between the natural diffraction of the laser and the 'tailored' lensing associated with tuning of the electron density profile.

This situation is illustrated in figure 2.14 as the dashed lines. As an example, for a laser pulse generated by a titanium:sapphire laser system, with a central

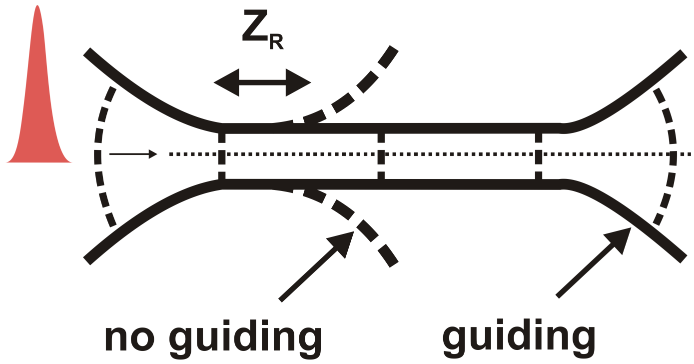

Figure 2.14: A schematic drawing showing the propagation of a laser pulse with (solid line) and without (dashed line) guiding. Pulse guiding allows the Rayleigh length to be significantly increased by counteracting diffraction creating ideal conditions for plasma accelerators.

wavelength of 800 nm, focused down to a spot size of 30 μm, the Rayleigh length is about 3.5 mm. It is obvious that for freely propagating drive laser beams, diffraction limits the acceleration length and thus the maximum energy of the electrons that can be obtained with laser wakefield acceleration. Therefore, it is essential that the laser pulse is optically guided as is shown in figure 2.14. There are several methods available to overcome the diffraction, for example: relativistic self-guiding [40, 174] and index guiding in a preformed plasma channel [63, 173]. When using the relativistic self-guiding method, the laser's phase velocity will decrease in regions of higher laser intensity (section 2.3). Therefore a laser pulse with a Gaussian spatial intensity profile, will lead to focussing of the pulse which counteracts the diffractive defocusing. The relativistic self-guiding can only be achieved when the laser power is sufficiently high; the power threshold is given by [153]

$$P_{crit}[\mathrm{GW}] \approx 17 \left(\frac{\omega_0}{\omega_p}\right)^2 . \tag{2.73}$$

A very attractive method to guide high intensity laser pulses is to propagate through a preformed plasma channel (guiding in empty waveguides is also possible and is described in reference [175]). Various techniques have been employed for example the igniter-heater technique [68] based on two laser pulses delivered consecutively. In this technique a short ($\leq$ 100 fs), intense ($> 5 \times 10^{14}$ Wcm^{-2}) 'ignitor' pulse produces initial ionisation to form plasma which is then heated and further ionised by a long ($\sim$ 100 ps) 'heater' pulse of relatively low intensity. Guiding of very intense laser pulses has been experimentally demonstrated using this technique [3].

In this type of guiding, the density of the plasma is tailored such that it yields a maximum refractive index on the axis, and a decreasing index with increasing distance from the axis. As a result, the laser phase velocity attains a minimum on the propagation axis and grows with the distance from the axis. This leads to a focussing of the laser pulse. When this focussing compensates for the diffraction, the laser pulse will be guided. A plasma channel preformed to the described shape can be produced by a number of techniques.

Here, a plasma channel is produced in a slow capillary discharge where, near thermodynamic equilibrium, heating by the discharge current and cooling of the plasma at the walls of the capillary generates the desired plasma density profile [19]. A channel created in this way has several advantages in comparison with the techniques previously described. First, as with all pre-formed channels, the guiding does not have a threshold intensity (as with relativistic self-guiding). This allows the generation of wakefields in the linear and weakly non-linear regime where the spatio-temporal structure of the wakefield is regular and ideal for a controlled accelerator. Furthermore, lower values of the plasma density can be used, in a range of 10^{17} to 10^{18} cm^{-3}. These lower densities imply a longer dephasing length, electrons can be accelerated over longer distances and, thus, gain more energies. Thirdly, gases with a low-Z number can be used, in particular hydrogen, which can be fully ionized. This significantly reduces absorption and defocusing losses compared to the use of high-Z gases. Finally, the relatively slow dynamics, due to operation near equilibrium, provides a relatively long temporal window of about 100 ns duration for low-loss waveguiding. This relaxes the timing constraints between the initiation of the discharge and the injection of the drive laser pulse and the electron bunch into the plasma channel. Which, in turn, allows for greater tolerance of jitter. Experimental details regarding this plasma channel will be presented in section 3.3. In a capillary discharge waveguide, it is possible to realise a plasma channel with an approximately parabolic increase of the electron density profile as described by [19]

$$n_e(r) = n_0 + \Delta \left(\frac{r}{r_c} \right)^2 , \tag{2.74}$$

where $n_e(r)$ is the plasma electron density, n_0 is the on-axis density, r is the distance to the axis, and r_c is the channel radius. For a laser beam with a Gaussian-shaped radial intensity profile, the best guiding (with the beam maintaining a constant cross section during propagation) occurs if the laser spot size, w_0, is matched to the channel radius, i.e., modematched when $\mathrm{w}_0 = r_c$. If the laser spot size does not match the channel radius, then the laser beam cross section will oscillate in size during the propagation with a characteristic wavelength of z_R (Rayleigh length) [19]. These undesired oscillations are due to the formation of beat-wave by different modes propagating in the channel. This is more commonly known as laser pulse 'scaloping' [19].

Considering the case of a lowest-order Gaussian beam propagating along the z-axis:

$$U(z,r,t) = \frac{iU_0}{z_R}\frac{w_0}{w(z)}e^{-[r/w(z)]^2}e^{i(kz-\omega t)}e^{ikr^2/2R(z)}e^{-i\psi(z)}, \tag{2.75}$$

where r is the radial distance from the z-axis, $R(z)$ is the radius of curvature of the wavefronts, and $\psi(z)$ is a propagation-dependent phase shift. The intensity of the beam is proportional to $|U|^2$, hence the intensity varies with distance from the propagation axis as $\exp\{-2[r/w(z)]^2\}$. The quantity $w(z)$ is known as the spot-size and is equal to the radius at which the intensity of the beam falls to $1/e^2$ of its value on axis. It may be shown that the spot size varies with propagation distance according to:

$$w(z) = w_0\sqrt{1+\left(\frac{z}{z_R}\right)^2}, \tag{2.76}$$

$$w_0 = \sqrt{\frac{\lambda z_R}{\pi}}. \tag{2.77}$$

In this case the focus of the beam - that is, where the spot size is smallest - occurs at $z = 0$. The focus refers to the beam waist, and the spot size at this point, w_0, is the waist size. As a beam propagates away from the waist its spot size increases, and consequently the intensity of the beam on axis decreases. A useful measure of this behaviour is defined by the Rayleigh range $z_R = \pi w_0^2/\lambda$, which corresponds to the distance from the beam waist at which the spot size increases by a factor of $\sqrt{2}$, hence the intensity is decreased by a factor of 2, compared to the value at focus. For LWFA intensities of $\sim 10^{18}$ Wcm^{-2} are required which typically requires focussing of the laser to a waist size of order $w_0 = 10\ \mu m$. In this case, radiation of wavelength, $\lambda = 1\ \mu$m has a Rayleigh range of only 0.3 mm, meaning that natural diffraction restricts the length of any interaction with the laser to a few millimetres at most.

In the discussion above we assumed that the refractive index of the medium through which the beam propagated was uniform. This is rarely the case in practice, in fact the refraction of the beam is frequently more important in determining the interaction length. Considering the propagation of an initially-plane wave through a medium for which the refractive index increases with r. In this case the phase velocity of the wavefronts will be slower at points away from the axis, consequently the wavefronts will develop a curvature which is concave with respect to the source, thus wave will diverge. The position R of a ray propagating through a medium of refractive index η is described by [176],

$$\frac{d}{ds}\left(\eta\frac{d\mathbf{R}}{\mathrm{ds}}\right) = \nabla\eta, \tag{2.78}$$

where s is the distance along the ray from some reference point.

Let us consider the idealised case of propagation through a region of cylindrical symmetry in which the refractive index increases linearly with distance from the propagation axis $\eta(r) = \eta_0 + \eta' r$ such that, $\nabla\eta = \eta'\hat{r}$. We may then write the position of the ray as $R = z\hat{k} + r\hat{r}$ and since the gradient of the refractive index has only one non-zero component the equation describing the position of the ray becomes

$$\eta_0\frac{d^2r}{dz^2} = \eta', \tag{2.79}$$

where we have used the fact that for a paraxial ray $s \approx z$ and $\eta \approx \eta_0$. The solution to this equation is simply $r(z) = r(0) + (\eta'/2\eta_0)z^2$, and hence if η' and η_0 are positive the ray will diverge - a process known as refractive defocusing. For example, a ray initially a distance r_0 from the axis will double its distance from the axis after propagating a distance $z_{ref} = \sqrt{2r_0\eta_0/\eta'}$. Hence we may estimate the distance over which the Gaussian beam will be defocused significantly by letting $r_0 = w_0$. Refractive defocusing frequently occurs when an intense laser pulse propagates through a gas or partially ionised plasma, and in such cases is referred to as ionisation induced defocusing. In order to estimate the strength of this defocusing we first note that in the non-relativistic regime the refractive index of the plasma may be written as

$$\eta = \sqrt{1 - \frac{n_e e^2}{m_e\varepsilon_0\omega^2}} \approx 1 - \frac{1}{2}\frac{n_e e^2}{m_e\varepsilon_0\omega^2}. \tag{2.80}$$

The approximation on the right-hand-side of equation 2.80 holds in a dilute plasma such that the plasma frequency ω_p is small compared to the radiation frequency ω. Hence for a dilute plasma the radial gradient in the refractive index depends on the radial electron density gradient as:

$$\frac{\partial\eta}{\partial r} \equiv \eta' \approx -\frac{1}{2}\frac{e^2}{m_e\varepsilon_0\omega^2}\frac{dn_e}{dr} = -r_e\frac{\lambda^2}{2\pi}\frac{dn_e}{dr}, \tag{2.81}$$

where $r_e = e^2/4\pi\epsilon_0 m_e c^2$ is the classical electron radius. Imagine an intense laser beam of spot size w_0 propagating through a partially ionised plasma, and let us suppose that the beam is sufficiently intense to double the electron density on axis (corresponding, for example, to ionisation of He^+ to He^{2+}). Since the intensity profile of the beam decreases rapidly with radius, the beam will be too weak to further ionise the plasma at a radii greater than of order w_0. Hence we may estimate $dn_e/dr \approx -n_e/w_0$. For a plasma with $n_e = 10^{19}$ cm^{-3} we find that for a beam with $w_0 = 10\ \mu m$ and $\lambda = 1\ \mu m$, $z_{ref} \approx 0.2$ mm, i.e. about equal to the Rayleigh range for diffraction.

We consider now in more detail the operation of gradient refractive index waveguides. In this approach a channel is formed in which the refractive index decreases with radial distance r from the axis. A refractive index profile of this form will cause the phase velocity to increase with r and hence the wavefronts of an initially-plane wave will become convex when viewed from the source. In this way the channel can counteract diffraction and refractive defocusing.

We may use the ray picture to investigate such a channel in a straightforward way. Let us suppose that the refractive index of the channel has the form

$$\eta(r) = \eta_0 - \frac{1}{2}\eta'' r^2. \tag{2.82}$$

In the paraxial approximation equation 2.78 becomes,

$$\frac{d^2 r}{dz^2} = -\frac{\eta''}{\eta_0} r, \tag{2.83}$$

which has solutions of the form $r(z) = r(0)\cos(2\pi z/L_{osc}^{ray})$ for rays which travel exactly parallel to the z-axis at $z = 0$, and where,

$$L_{osc}^{ray} = 2\pi\sqrt{\frac{\eta_0}{\eta''}}. \tag{2.84}$$

We see that the distance of the ray away from the axis oscillates as it propagates through the channel with a period, L_{osc}^{ray}. The period of this oscillation decreases as η'' increases. Conversely, if η'', the solutions to equation 2.83 yield rays which diverge away from the axis exponentially and the rays are refractively defocused.

2.19.1 Techniques for plasma waveguides

Until now we have considered the operation of gradient refractive index waveguides in a general way. Gradient refractive index guiding of high-intensity laser pulses must employ a core formed from plasma. In this technique the transverse gradient of the refractive index is achieved by a corresponding transverse gradient in the plasma density.

In an ideal parabolic plasma channel the electron density can be described by,

$$n_e(r) = n_e(0) + \Delta n_e \left(\frac{r}{r_{ch}}\right)^2, \tag{2.85}$$

where Δn_e is the increase in the electron density at $r = r_{ch}$.

From equation 2.80 the refractive index of the plasma channel may be written as

$$\eta(r) = 1 - \frac{1}{2}\frac{n_e(0)e^2}{m_e\varepsilon_0\omega^2} - \frac{1}{2}\frac{e^2}{m_e\varepsilon_0\omega^2}\Delta n_e \left(\frac{r}{r_{ch}}\right)^2, \tag{2.86}$$

from which we may identify the relations:

$$\begin{aligned} \eta_0 &= 1 - \tfrac{n_e(0)e^2}{2m_e\varepsilon_0\omega^2} \approx 1, \\ \eta'' &= \tfrac{e^2}{m_e\varepsilon_0\omega^2}\tfrac{\Delta n_e}{r_{ch}^2}. \end{aligned} \tag{2.87}$$

If such a beam is focused at the entrance of the channel. The matched spot size of a given channel is independent of the wavelength of the radiation as described by:

$$w_M = w = \left(\frac{2}{k}\right)^{1/2}\left(\frac{\eta_0}{\eta''}\right)^{1/4}, \tag{2.88}$$

$$w_M = \left(\frac{r_{ch}^2}{\pi r_e \nabla n_e}\right)^{1/4}. \tag{2.89}$$

2.20 Ponderomotive channeling

As we have already discussed the ponderomotive pressure from a laser pulse propagating in underdense plasma can expel electrons from regions of high intensity. Assuming that the laser pulse length is long compared to that of the plasma period $\omega_p\tau \gg 1$, we can consider the electron fluid response to be adiabatic. As a starting point to quantify ponderomotive expulsion of electrons we can write down a plasma fluid equation in vector form to include both longitudinal and transverse plasma velocity components [153]:

$$\frac{d}{dt}(\gamma\mathbf{v}) = c\nabla\phi - \frac{c}{2\gamma}\nabla a^2, \tag{2.90}$$

assuming that $\mathbf{v}$ varies much more slowly than the laser field. In the adiabatic limit, letting $\mathbf{v} \to \mathbf{0}$, and taking the divergence of equation 2.90 we retrieve:

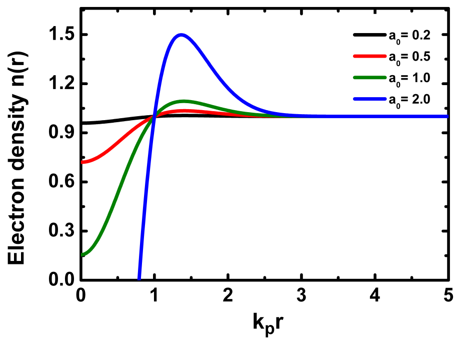

Figure 2.15: The radial ponderomotive expulsion of electrons at laser pump strengths corresponding to $a_0 = 0.2$ (black) $a_0 = 0.5$ (red) $a_0 = 1.0$ (green) $a_0 = 2.0$ (blue).

$$\nabla^2\phi = \frac{1}{2\gamma}\nabla^2 a^2 = \nabla^2\gamma, \tag{2.91}$$

where relativistic factor is a function of the pulse amplitude: $\gamma = (1+a^2)^{1/2}$. In this analysis we are concerned with the transverse response of the plasma. If the pulse is cigar shaped, we can take $\nabla = \nabla_\perp$ and apply Poisson's equation [153]:

$$\nabla_\perp^2\phi = k_p^2(n-1), \tag{2.92}$$

to obtain an expression for the density perturbation:

$$n = 1 + \frac{\nabla_\perp^2\gamma}{k_p^2}. \tag{2.93}$$

Equation 2.93 predicts that a tightly focused laser pulse with sufficient intensity can completely remove all electrons from the laser axis [153]. This effect is known as cavitation and is a very important mechanism for the development of plasma undulators through the production of bare ion channels. Considering a Gaussian pulse with a profile $a(r) = \exp(-r^2/2\sigma^2)$. After time averaging over the laser period, the density depression can be expressed as [153]:

$$\nabla_\perp^2\gamma = \frac{1}{4\gamma}\nabla_\perp^2 a^2 = \frac{1}{4\gamma}\frac{4a_0^2}{\sigma^2}\left(\frac{r^2}{\sigma^2}-1\right)\exp\left(-r^2/\sigma^2\right). \tag{2.94}$$

The deepest depression is on laser axis at $r = 0$, so we obtain a 'cavitation' condition, $n = 0$, for

$$\frac{a_0^2}{k_p^2\sigma_0^2} > 1, \tag{2.95}$$

or in more practical units:

$$I_{18}\lambda_\mu^2 > \frac{1}{20} n_{18}\sigma_\mu^2, \tag{2.96}$$

where σ_μ and λ_μ are the spot size and laser wavelength in μm, I_{18} and n_{18} are the laser intensity and plasma density in units of 10^{18} Wcm^{-2} and 10^{18} cm^{-3} respectively.

2.21 Wakefield guiding of short laser pulses

In section 2.3 we saw that relativistic effects can cause modifications in the plasma refractive index. When a plasma wakefield is created the refractive index can be modified not only by the relativistic electron quiver motion, but also by the longitudinal bunching of the plasma density caused by a wakefield. We can include this effect by recalling equation 2.28:

$$\eta(r) \simeq 1 - \frac{\omega_p^2}{2\omega^2}\left(1 - \frac{a_0^2}{4} + \frac{n}{n_0}\right), \tag{2.97}$$

where n is the perturbed plasma wakefield density,

$$\frac{n_e}{\gamma} = \frac{n_0}{1+\phi}, \tag{2.98}$$

where ϕ is the wake potential. Thus, the refractive index may be expressed:

$$\eta(r) = 1 - \frac{\omega_p^2}{2\omega^2}\frac{n_e}{\gamma n_0} = 1 - \frac{\omega_p^2}{2\omega^2}\frac{1}{1+\phi}. \tag{2.99}$$

The solution for ϕ can be found from equation 2.53 in both long and short pulse limits. For long pulses, we have $\phi \simeq a^2/2$ and recover equation 2.28. For short pulses we have $\phi \simeq k_p^2 a_0^2 \xi^2/8$, thus the refractive index is:

$$\eta(r) = 1 - \frac{\omega_p^2}{2\omega^2}\left(1 - \frac{k_p^2 a_0^2 \xi^2}{8}\right). \tag{2.100}$$

Physically this implies that the critical power requirement for self focussing depends on the position along the length of the pulse, thus pulses shorter than a plasma wavelength cannot be relativistically self guided. This important result was first pointed out by Sprangle *et al* [174].

2.22 Non-linear Thomson scattering - Wiggler radiation

Thomson scattering is scattering of light from free electrons. In the linear regime, electrons oscillate linearly via the Lorentz force at low light intensities i.e. when $a_0 \ll 1$. An electron that is initially at rest may acquire relativistic velocities in the fields of high intensity light and through this relativistic motion the electron may emit radiation at high harmonics of the light frequency [8]. If the electron acquires a relativistic energy before it encounters the high-intensity laser, there is an additional Doppler-shift of the scattered light. The electron oscillates with double excitation frequency and along laser propagation direction. Furthermore, the relativistic drift motion and a dependency on the initial phase [14] lead to spectral broadening of the scattered light. A certain harmonic number emits a wide frequency interval which overlaps with other harmonics. Thomson-scattered light is emitted from the plasma at regions of relativistic intensity [177]. This is predominantly the region of self-focussing where the laser pulse intensity is very high, e.g. in a plasma channel (or relativistic channel). Thomson-scattering occurs at discrete harmonics of the laser frequency, thus imaging the second harmonic laser light emitted from a plasma channel is a very useful diagnostic to optimise wakefield acceleration [11]. Non-linear Thomson scattering is generated by exactly the same mechanism as wiggler radiation. However, Thomson scattered light is generally associated with plasma interactions and wiggler radiation is usually generated by electrons traversing a magnetic insertion device (chapter 7). Currently the 'mini' undulator or 'plasma' undulator is being investigated where the plasma is used to generate the betatron oscillations [126, 178].

Chapter 3

Laser wakefield acceleration: Experimental results

3.1 Experiment 1: Monoenergetic electrons from LWFA

The main purpose of this experiment was to observe monoenegetic electron beams produced from laser wakefield acceleration. The experiment aim was to focus an intense short laser pulse onto a helium gas jet and produce a plasma channel or wake as a medium for background plasma electrons to be trapped into the wakefield and accelerated to tens of MeV. Ultimately, it was to observe and characterise electron beams which exhibit monoenergetic features i.e. controlled acceleration.

The experiment described in this section used the Astra laser at the Rutherford Appleton Laboratory. A layout of the laser system is illustrated in figure 3.1 showing the laser pulse parameters from the oscillator through to the target chamber. The laser system is based on chirped pulse amplification in titanium sapphire to produces laser pulses with a bandwidth of 20 nm (intensity FWHM), which have a central wavelength of 800 nm. The vacuum compressor gratings are typically tuned for optimum pulse compression to produce Fourier-limited pulses with a FWHM pulse length of τ = 40 fs (cτ = 12 μm). These pulses were then directed into the main target chamber where they are focussed and interact with a helium gas jet. The plasma density was a linear function of the gas backing pressure.

Figure 3.2 illustrates the experimental set-up. Inside the target chamber the 600 mJ laser pulses were focused by an f/16.7, 90° off-axis parabola. The focused

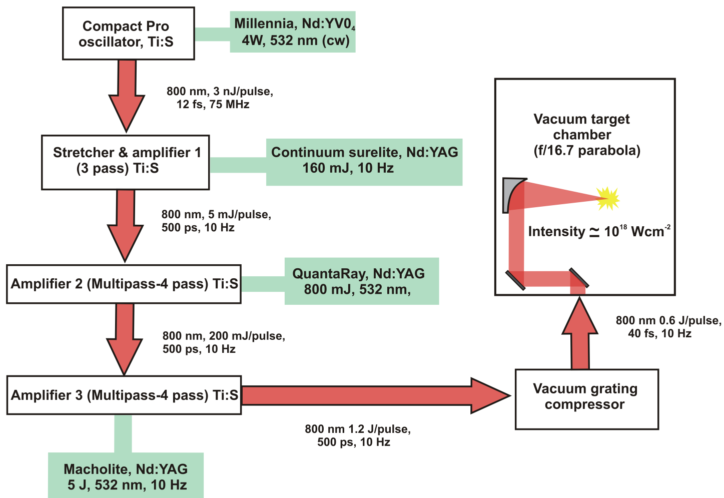

Figure 3.1: The laser chain of the 12 TW Astra laser system at the Rutherford Appleton Laboratory (RAL) showing the laser parameters at each stage of the CPA amplification process.

spot size was 25 μm (intensity FWHM), resulting in a peak intensity of 2.5×10^{18} Wcm^{-2} corresponding to a laser strength of $a_0 = 1.1$. The Rayleigh length was approximately 600 μm. The ultrashort (40 fs) driver pulses were focused onto the edge of 2 mm supersonic helium gas-jet. The plasma density was varied from $n_e = 3 \times 10^{18}$ cm^{-3} to $n_e = 5 \times 10^{19}$ cm^{-3} by varying the gas-jet backing pressure from 40–80 bar. In this density range, the wavelength of relativistic plasma waves produced is between 0.33 and 2 times the laser pulse length ($c\tau$ = 12 μm). The plasma electron density, n_e, which scales as a function of gas jet backing pressure was determined by collecting and analysing a portion of the laser light transmitted after interaction with plasma. The transmitted spectrum was observed over the spectral range from 400 to 1000 nm and by observation of the Raman forward scattered Stokes and anti-Stokes shift or 'Raman satellites' of the laser pulse, $\Delta\omega = \omega_p$, it was possible to retrieve the plasma density dependence on gas backing pressure. The electron energy spectrum was measured using an electromagnetic spectrometer which deflected the electrons onto photosensitive imageplates (Fuji BASMS2325) which were read using an imageplate reader (Fuji BAS1800II). Other important diagnostic systems consisted of a transverse imaging system to measure the spatial dimensions of the plasma channel, which was typically around 200 μm long. Radiochromic film was inserted into the electron beam as a means to observe the transverse electron beam profile, which was measured to be less than 10 mrad.

The onset of electron acceleration was observed at densities above $n_e = 7 \times 10^{18}$ cm^{-3}. Below this value, corresponding to $\lambda_p = c\tau$, no electrons were

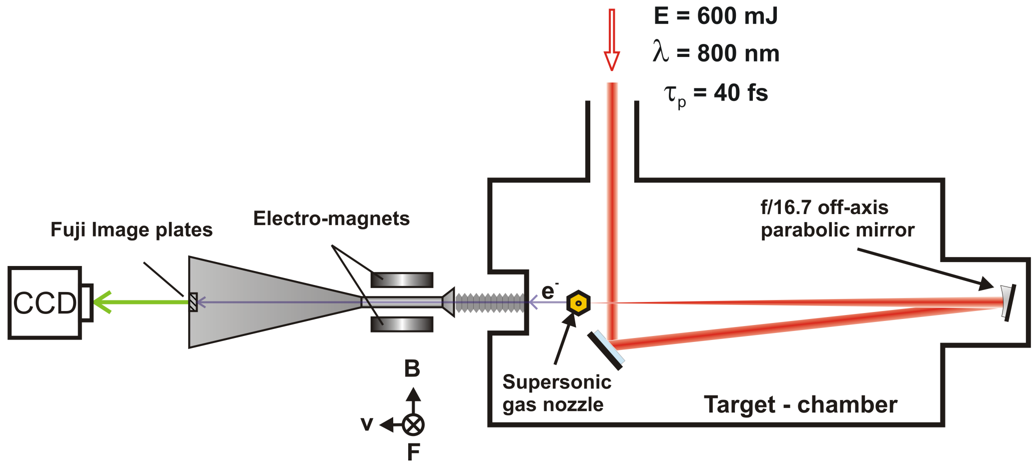

Figure 3.2: The experimental set-up for the electron acceleration experiment using the Astra laser at the Rutherford Appleton laboratory.

observed. The density was steadily varied between $n_e = 1.6 \times 10^{19}$ cm^{-3} and $n_e = 3 \times 10^{19}$ cm^{-3} and electrons up to 100 MeV were observed in the lower density range. Approximately 10 % of the electron energy spectra had several 'spikey' components, each with an energy bandwidth of less than 20 %. As the density was increased further from $n_e = 3 \times 10^{19}$ cm^{-3} to $n_e = 5 \times 10^{19}$ cm^{-3} the maximum energy of the electrons shifted to lower energies and the energy spectra adopted a broad Maxwellian shape. It was found that monoenergetic features were optimum in the density range, $n_e = 1.5 \times 10^{19}$ cm^{-3} to $n_e = 2 \times 10^{19}$ cm^{-3}. In particular, at a density of $n_e = 2.0 \times 10^{19}$ cm^{-3} a single narrow peak with a FWHM energy spread of less than 3 % was observed (figure 3.3). For this particular laser shot around 1.4×10^8 electrons ($\sim$ 10 pC of charge) were accelerated to 72 MeV with an energy bandwidth of 3 % . Under the same experimental conditions the electron spectra consistently showed a narrow energy spread. For quasi-monoenergetic electron spectra with the lowest energy spread (<10 %) the electron beam energy varied between 50–80 MeV.

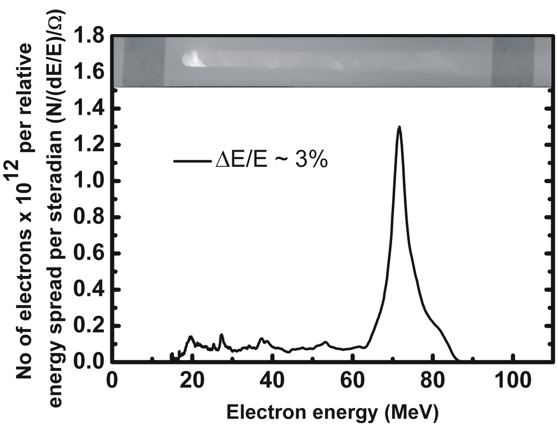

Figure 3.3: The monoenergetic relativistic electron spectrum obtained using the Astra laser focused onto a helium gas plume with an electron density, $n_e = 2{\times}10^{19}$ cm^{-3}. The laser parameters were E_L = 500 mJ, τ_L = 40 fs, $I_L = 2 \times 10^{18}$ Wcm^{-2}. The electron spectrum was peaked on 72 MeV and had an energy spread, $\Delta E/E$ = 3% FWHM [1].

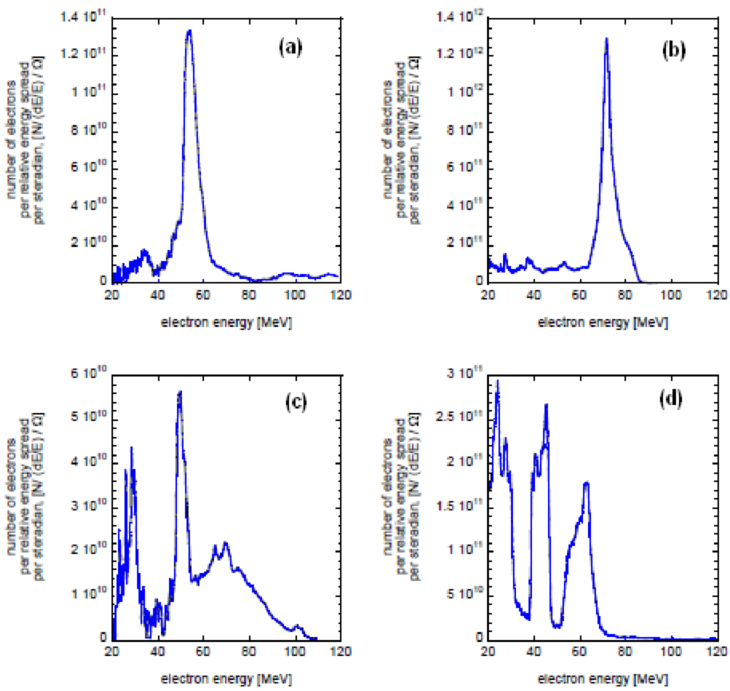

Figure 3.4: Electron energy spectrum at various plasma densities. (a) n_e = 1.5 $\times$ 10^{19} cm^{-3}, laser energy $\simeq$ 470 mJ. (b) n_e = 1.7 $\times$ 10^{19} cm^{-3}, laser energy $\simeq$ 480 mJ. (c) n_e = 1.8 $\times$ 10^{19} cm^{-3}, laser energy $\simeq$ 495 mJ. (d) n_e = 1.8 $\times$ 10^{19} cm^{-3}, laser energy $\simeq$ 430 mJ.

3.1.1 Experiment 1: Discussion

As there are no externally injected electrons in this experiment the only possible source for the energetic electrons observed is from within the plasma itself. Evidently there is a process which leads to the injection of electrons into a particular phase of the plasma wave, leading to very similar accelerating fields and hence yields a narrow energy spread bunch. It is very likely that the source of this injection is wavebreaking. If the wave breaks in only a small localised region then the remaining plasma wave can retain a coherent structure. The electrons which break from the wave are effectively injected into the remaining plasma wave and can be accelerated. If wavebreaking can inject electrons into a particular phase of the wave then there must be an effect that prevents this from happening continually - that is the wave must break for a short period of time only, or else there will be a continual stream of electrons, resulting in a longer electron bunch that will acquire a larger energy spread as it is accelerated in the plasma wave. There must also be a process occurring which, at higher density, results in the energy spread of the electron beam becoming random i.e. leading to the maxwellian type spectra observed. This randomisation is likely due to the trapped electrons becoming dephased in the plasma wave. At higher density the plasma wavelength has a slower phase velocity and a shorter wavelength - this means relativistic electrons outrun the wave much faster than they do at lower density.

The presence of ‘spikey’ spectra were readily observed in this experiment as seen in figure 3.4. The spikes of quasimonoenegetic electrons sometimes appeared in one, two or even three energy space intervals. In the case where two or three were observed the number of electrons and the energy was reduced in each consecutive spike. It is possible that electrons were trapped by successive plasma wave buckets and accelerated to consecutively lower energies. In the instance of the spectrum shown in figure 3.3 it is probable that only the first plasma wave-bucket was driven to wavebreaking resulting in a single quasimonoenergetic electron spectrum. It is also a possibility that injection occurred into the same wavebucket but at different times, which would also result in this multi-peaked spectra. The reproducibility of the peak electron bunch energy in this experiment was around 40 %. This relatively large variation in electron energy could be attributed to, shot to shot variations in laser pulse energy, pulse duration and focal spot size which were ± 5 %, ± 12 % and ± 11 % respectively.

The plasma wavelength for the electron shot shown in figure 3.3 is calculated to be 8.4 μm. Using equation 2.69 the dephasing length can be calculated to be $L_d \approx$ 1 mm. We can now take this acceleration distance and calculate the maximum energy achieved at dephasing using equation 1.5. The maximum acceleration field at a plasma density of 2×10^{19} cm^{-3} can be calculated to be $E_{max} = 380$ GeV/m, yielding an energy of 380 MeV at dephasing. This is a factor of 5.5 larger than was observed experimentally. Taking this acceleration field at this plasma density an acceleration distance of 190 μm is necessary to achieve a 72 MeV electron beam. Furthermore, comparing the laser pulse length of 40 fs to the plasma oscillation period of 28 fs for the optimised plasma density of 2×10^{19} cm^{-3} (density which yielded the best monoenergetic features), this confirmed that the experiment was performed in the LWFA regime and not the SMLWFA. The electron density at which the plasma oscillation period and the laser pulse length were equal (40 fs) was calculated to be 1×10^{19} cm^{-3}. Furthermore, experimentally, this was the threshold density which below this value no monoenergetic electrons were observed. Narrow energy spread electron beams were observed inside the density window between 1×10^{19} cm^{-3} and 2×10^{19} cm^{-3}. The peak energy varied between 40 and 70 MeV, the relative width varied between 3 and 60 % and the number of electrons varied by more than an order of magnitude. For cases when the experimentally controlled variables were nominally the same, some shots showed narrow energy spread features while other shots showed no relativistic electrons at all. The shot to shot variations in electron signal is one of the main drawbacks to the practical use of LWFA electron beams, however recently progress has been made in stabilising electron beam production [30]. The main cause for these fluctuations can be attributed to shot to shot variations in plasma density possibly due to the Parker series 9 solenoid pulsed valve. The laser pulse duration of Astra is known to have typical shot to shot variations of the order of 12 % which could also cause significant fluctuations in the repeatability of monoenergetic electron production. Furthermore, the contrast ratio of the laser pulse to the ASE pre-pulse could also have been varying on a shot to shot basis, affecting the electron beam stability.

It is also possible that some laser shots were producing electron beams but they did not enter into the electron spectrometer and were ‘dumped’ into the aluminium side walls. Possible explanations for this electron beam pointing variability could be due to the hosing instability being stronger for some laser shots over others. Moreover, the laser beam pointing stability could have been affected by the presence of vibrations transmitted into the opto-mechanics from the large vacuum pumps used for both the compressor gratings and the main interaction chamber.

3.2 Experiment 2: Monoenergetic electrons from SMLWFA

The main purpose of this experiment was to observe monoenegetic electron beams produced from laser wakefield acceleration in the self modulated regime. The experimental objective was to focus an intense short laser pulse onto a helium gas jet and accelerate electrons. Ultimately, it was to observe and characterise electron beams which exhibit monoenergetic features.

The experiment presented in this section was carried out using the 10 TW, Jena Ti:sapphire laser (JETI) [10]. A layout of the laser system is depicted in figure 3.5 showing the laser pulse parameters at each stage of the chirped pulse amplification process.

The JETI laser delivered laser pulses with a central wavelength of 800 nm, a pulse duration of 80 fs and an energy of 600 mJ, on target. The experimental set-up is shown in reference [179]. The pulses were focused by an f/2.2 off-axis parabolic mirror, down to a FWHM spot diameter of 4.5 μm producing an intensity of 5×10^{19} Wcm^{-2}, corresponding to $a_0 = 0.85 \times 10^{-9}\sqrt{I}\lambda = 5$. The focal spot was positioned on the rising edge of a subsonic He gas jet with a Gaussian electron density profile with a peak value of 4×10^{19}cm^{-3} corresponding to a plasma wavelength equal to $\lambda_p = 2\pi c/\omega_p = 5$ μm. This was around 5 times shorter than the laser pulse length of $c\tau = 24$ μm. When the laser pulse encounters the gas plume it fully ionises the gas and relativistically self-focuses, resulting in a 200 - 300 μm long plasma channel corresponding to approximately 10 Rayleigh lengths. The relativistic channel shown in figure 3.8 is illuminated from the self-emission of non-linear Thomson scattered laser light perpendicular to the laser polarisation. This radiation is emitted near to the second harmonic of the laser light and was used as a transverse diagnostic to measure the spatial characteristics of the relativistic channel. A 5–10 % fraction of the laser light transmitted through the gas jet plasma was coupled outside the vacuum chamber using a glass pick-off optic, and attenuated before being focused onto the input of an optical spectrometer with a detection range of 400-1050 nm. The collected optical spectra gave a good indication of the plasma density through the detection of Raman ‘satellites’ and also gave an insight into other mechanisms occurring during the laser wakefield interaction.

The electron spectra were measured using an electron spectrometer equipped with two permanent magnets with a peak on-axis magnetic field, $B_{max} = 0.45$ T. The entrance aperture of the spectrometer was placed on the laser axis and 21

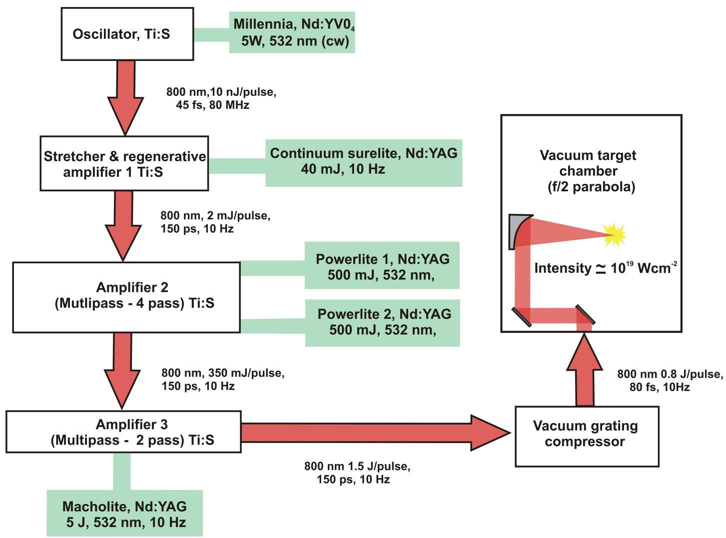

Figure 3.5: A schematic layout of the 10 TW JETI laser system at the institute for optics and quantum electronics, Friedrich-Schiller-Universität, Jena [10]. The diagram shows the laser parameters at each stage of amplification throughout the CPA laser system.

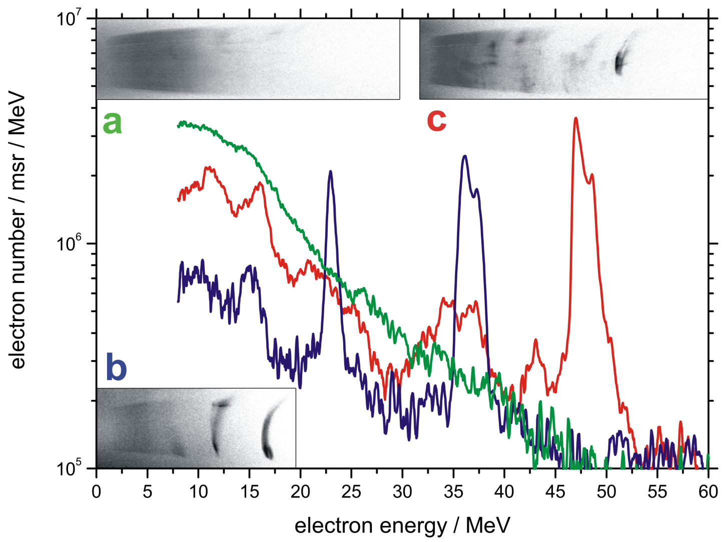

Figure 3.6: The electron spectra produced from the electron acceleration experiments in the SMLWA regime at Jena [11]. A laser shot producing: (a) A broad Maxwellian electron energy distribution (green line, raw image – top left inset). (b) A double peaked quasi-monoenergetic electron distribution with peaks at 23 MeV and 36 MeV (blue line, raw image – bottom left inset). (c) A single peaked quasi-monoenergetic electron distribution peaked on 47 MeV with a FWHM energy spread of 4 MeV, $\Delta E/E = 8.5$ %, (red line, raw image – top right inset).

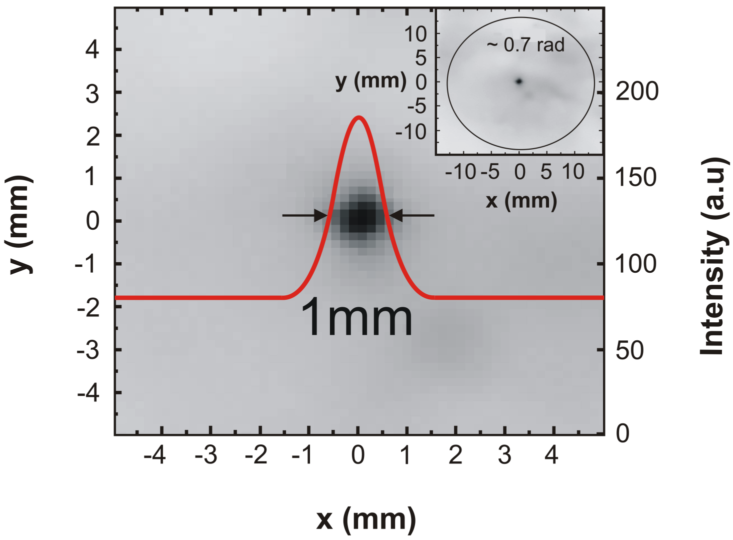

Figure 3.7: The transverse electron beam profile after optimisation. The width of 1 mm at 120 mm distance between focus and screen corresponds to an opening angle of < 10 mrad. The well collimated beam sits on top of a pedestal of electrons with a broad divergence of approximately 0.7 rad (inset) [11].

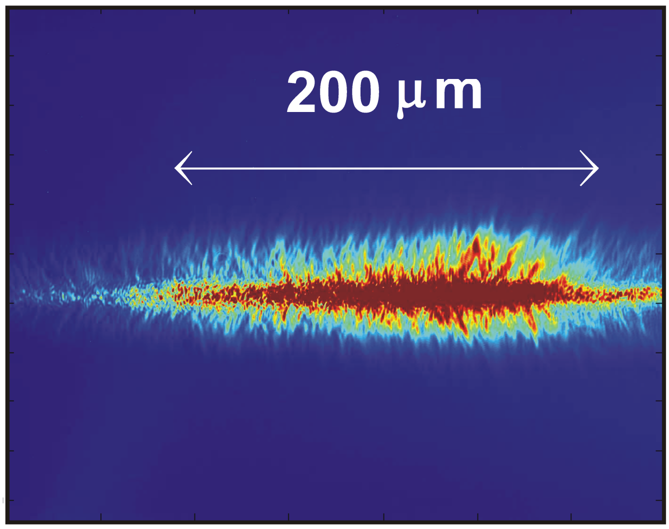

Figure 3.8: An image of the 200 μm relativistic plasma channel observed on the electron acceleration experiment using the JETI laser. The image was taken with a blue filter to capture the self emission of the 2ω Thomson scattered light.

cm upstream from the laser focus. The electrons were detected using the same image-plate technique, as described in section 3.1.

The mono-energetic electron output of the wakefield accelerator was found to strongly depend on the spatial position of the laser focus relative to the peak of the gas jet density profile. Without optimisation of this overlap the electron spectra exhibited a broad exponential profile (figure 3.6(a)). Mono-energetic electron generation was optimised by using the transverse Thomson scattering diagnostic, to achieve the brightest and longest plasma channel, and also by maximising the γ dose signal on an radiation detector (Ram-ion ionisation chamber), positioned downstream of the central laser axis and just outside the vacuum chamber. The detector was placed around 5–10° to the electron beam axis. This angle was small enough to the axis that a substantial dose of radiation could be detected for optimisation of the plasma channel. The translation of the gas-jet relative to the laser focus was optimised on each axis whilst looking at the reading on the radiation monitor. In order to keep a safe distance from the radiation a CCD camera was directed at the LCD display of the radiation detector and the output was relayed to the experimental control room behind sufficient lead shielding. Once this 'sweet-spot' had been found, electron spectra with one or two quasi-monoenergetic peaks were observed, as shown in figure 3.6(b)–(c). Under the same experimental conditions the peak of the electron energy spectra shifted strongly from shot to shot. In figure 3.6(b) two distinct peaks at 23 MeV and 36 MeV are clearly shown and in figure 3.6(c) just one single peak at 47 MeV is shown with a FWHM energy spread of 4 MeV ($\Delta E/E = 8.5$ %).

After data had been collected on electron spectra the electron spectrometer was removed and measurements of the transverse electron beam profile were taken using Konica KR scintillating screen positioned 12 cm after the gas jet and imaged with a CCD camera. In cases where the position of the laser focus was not optimised onto the gas jet it was found that the transverse profile of the electron bunch had a very broad angular distribution. The optimum laser focal spot positions over the gas plume was again found by obtaining the maximum γ dose, at this point, the electron beam profile changed to a very narrow spot figure 3.7 with a divergence angle of < 10 mrad. Assuming the source size of the electron emission region to be around 1 μm this translates to a normalised transverse emittance of approximately 1 πmm mrad.

3.2.1 Experiment 2: Discussion

It is important to highlight two main differences between this experiment and the experiment discussed in the previous section, which are the laser pulse length and the laser focusing geometry. In this experiment, the pulse length is twice as long (80 fs) as that described in the previous section (40 fs). The focusing conditions also differed considerably. This experiment used an f/2.2 parabola to focus the laser beam onto the gas jet, whereas in the previously described experiment an f/16.7 was implemented for this purpose.

The results of this experiment show that quasi-monoenergetic electrons can be produced with strongly relaxed requirements on the laser pulse duration. For optimal electron acceleration it is usually necessary for the longitudinal and transverse dimensions of the laser pulse at focus to roughly match one half of the plasma wavelength in order to drive the strongest wakefields ($\tau_p \approx \lambda_p$). In this experiment selection of a dense gas jet (high plasma density n_e) and strong focusing (high a_0) promoted the Raman forward scattering instability. This results in the laser pulse experiencing self-modulation and longitudinal compression during propagation through the gas jet. In this regime the laser pulse fragments into small micro-pulses each containing $\sim$ 5 % of the total pulse energy, each with a duration of 5–10 fs. This process allows access to a regime where the laser ponderomotive force is strong enough to create a region void of any electrons just behind the laser pulse. As the laser pulse traverses further it expels electrons which stream round into the cavity and can be injected into a fixed phase of the longitudinal field, leading to the acceleration of electron bunches with a narrow energy spread.

This is a very encouraging result as it suggests that ultrashort laser pulses such as those used in section 3.1 (<50 fs) are not necessary for efficient driving of laser wakefields. The plasma tailors the laser pulse shape through driven instabilities such as forward Raman scattering to reach the required parameters for monoenergetic electron acceleration.

What is also interesting to observe is again the presence of two defined energy ‘spikes’ of electrons. Figure 3.6(b) shows clearly two distinct peaks, one at 23 MeV and the next at 36 MeV. A speculative explaination for this is that two consecutive wavebuckets were driven to non-linear wavebreaking. The electron spectrum in figure 3.6(c) shows only a single quasimonoenergetic peak at 47 MeV with a FWHM of 4 MeV and it is possible in this case that only the first wavebucket was driven to wavebreaking.

In particular, at a density of 4×10^{19} cm^{-3} a single narrow peak with a FWHM

Experimental Parameter	**Expt. 1 (Astra)**	**Expt. 2 (JETI)**
Laser pulse energy, E_L	600 mJ	600 mJ
Laser pulse duration, τ_p	40 fs	80 fs
Laser spot size (FWHM), w_0	25 μm	4.5 μm
Laser Intensity, I_L	2.5×10^{18} Wcm^{-2}	5×10^{19} Wcm^{-2}
Rayleigh length, z_R	600 μm	20 μm
Plasma channel length L_p	200 μm	200 μm
a_0 parameter	1.1	5
Focussing optic f-number	f/16.7	f/2.2
Electron bunch peak energy	72 MeV	47 MeV
Electron beam energy spread, $\Delta\gamma/\gamma$	~ 3 %	~ 8 %
Electron beam divergence, σ_γ	$<$ 10 mrad	$<$ 10 mrad
Plasma density, n_e	2.0 $\times 10^{19}$ cm^{-3}	4×10^{19}cm^{-3}
Plasma wavelength, λ_p	8.4 μm	10 μm
Dephasing length, L_d	1 mm	8 mm
Accelerating field, E_{Max}	382 GeV/m	317 GeV/m
Critical power, P_{cr}	1.9 TW	2.7 TW

Table 3.1: A comparison of the experimental parameters between the electron acceleration experiments carried out using the Astra and JETI laser systems.

energy spread of less than 3 % was observed (figure 3.3). For this particular laser shot around 1.4×10^8 electrons ($\sim$ 10 pC of charge) were accelerated to 47 MeV with an energy bandwidth of 3 %

Table 3.1 highlights the differences in the experimental parameters between experiment 1 (ASTRA) and experiment 2 (JETI). Although the laser pulse energy is comparable in both experiments, the laser vector potential (a_0) is a factor of five greater for the JETI experiments than in the Astra experiment. The plasma density was also a factor of two larger in the JETI experiment than on the Astra experiment, which resulted in a dephasing length of 8 mm for the JETI experiment and 1 mm for the Astra experiment. The higher a_0 in the JETI experiment also serves to increase the effect of relativistic self focussing, which allows a plasma channel approximately 20 times the Rayleigh length to be created for efficient energy gain.

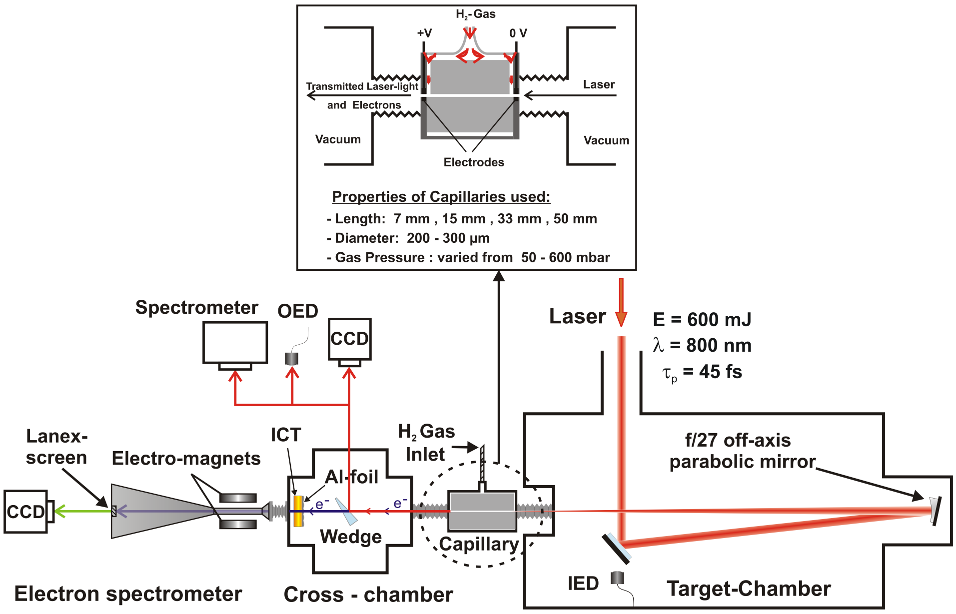

Figure 3.9: The laser pulse guiding experimental set-up using the ASTRA laser at the Rutherford Appleton Laboratory (RAL). The laser pulse was focussed onto the entrance of the capillary and synchronised with a high voltage discharge. The preformed plasma allowed the laser pulse to drive a wakefield over many Rayleigh lengths.

3.3 Experiment 3: Monoenergetic electrons from capillary guided LWFA

In terms of energy gain, the laser wakefield accelerator performance depends on the length over which the laser pulse is sufficiently intense to drive a wake. The effective acceleration length of the SMLWA discussed in section 3.2, is limited to at most a few Rayleigh lengths, z_R = 100 - 300 μm due to diffraction and defocussing of the laser. In cases where more laser energy is available the spot size can be enlarged to increase the Rayleigh length hence the corresponding acceleration length. However, an alternative means of increasing the acceleration length is by using a preformed plasma discharge channel in a capillary waveguide (figure 3.11). The technique and physics of optically guiding a laser pulse using a preformed plasma channel has been discussed in section 2.19. This section presents experimental results on wakefields driven in waveguides using the Astra laser.

This experiment used the Astra laser system at the Rutherford Appleton Laboratory (RAL) (figure 3.1). The Astra laser delivered laser pulses centered on 800 nm with pulse durations of 45 fs and an energy of 600 mJ on target. The laser pulses were focused by an f/27 off-axis parabolic mirror to a spot size of 34

μm (FWHM intensity) at the capillary entrance.

Figure 3.9 shows the experimental layout. The experiments employed 15 mm long sapphire capillaries of inner diameter D = 200 μm or 300 μm. Hydrogen gas was flowed into the capillaries via channels of diameter 650 μm and length 10 mm located 4 mm from each end. A discharge was driven through the capillary (figure 3.11) by connecting across the capillary a 1.7 nF capacitor charged to a voltage between 15 and 30 kV. The discharge current was measured by a Rogowski coil.

The delay t between the onset of the discharge current and the arrival of the laser pulse at the entrance of the waveguide was controlled by a digital delay generator (Stanford Research Systems). The timing jitter in t was measured to be less than 1 ns. A portion of the laser radiation transmitted by the capillary was reflected by an optically flat wedge placed 0.6 m behind the capillary exit. After a second reflection from the surface of a wedge (not shown), the beam was collimated and refocused by two f-15 achromatic lenses to the entrance slit of a grating spectrometer with a 12-bit CCD, and a microscope objective. The spectral response of the imaging system and spectrometer was measured using a calibrated broadband source. The energies of the pulses entering and leaving the waveguide were measured by spectrally flat photodiodes behind a dielectric mirror prior to the paraboloid (IED) and after the interaction in the capillary (OED) respectively. Electrons accelerated within the waveguide pass through a 4 mm diameter hole in the first wedge, where they are dispersed by a magnetic spectrometer, and recorded by imaging a phosphor (Lanex) screen with a 12-bit CCD camera. Calibrated image plates were used to measure the charge of the electron bunch [180, 181, 179] and aluminium foils inserted in the optical path prevented laser radiation from entering the spectrometer.

The laser was operated in two distinct modes: a short pulse mode in which the laser was fully compressed to a bandwidth limited pulse duration of 45 fs (FWHM), corresponding to a peak intensity, $I_{sp} = 8\times10^{17}$ Wcm^{-2} and normalised vector potential, $a_{0sp} = 0.6$; a long pulse mode in which a glass block prior to the compressor was removed, yielded pulses of 150 fs (FWHM) and a peak intensity, $I_{sp} = 2.4 \times 10^{17}$ Wcm^{-2}, corresponding to $a_{0sp} = 0.33$. Experiments were performed using the short pulse for initial hydrogen pressures in the range 80 to 600 mbar. Quasi-monoenergetic electron beams were observed with energies up to approximately 200 MeV and bunch charge of order 100 pC measured with an ICT for capillaries with D = 200 μm, but no electron beams were observed for D = 300 μm. It is important to note that although the ICT was implemented in the experiment the charge values cannot be attributed to single energy components

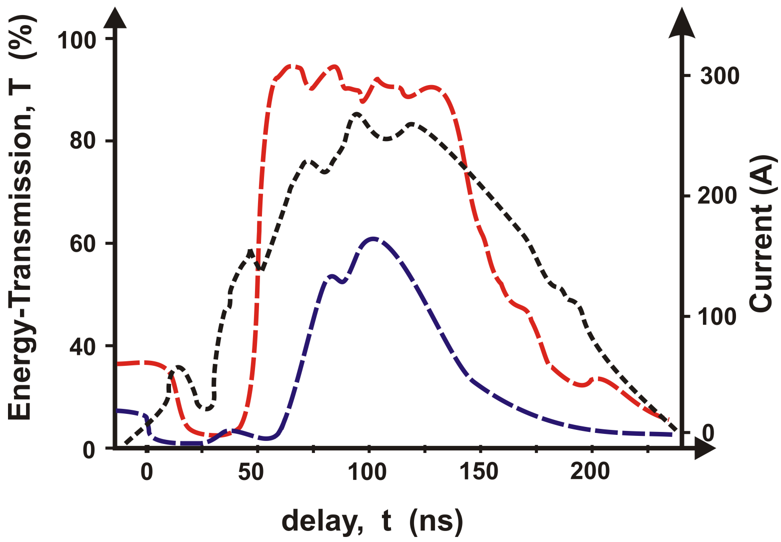

Figure 3.10: The laser pulse energy transmission through the capillary as a function of the delay between the discharge pulse and the laser pulse in short pulse mode (blue curve) and long pulse mode (red curve). The dashed black line shows the time profile of the discharge current.

in the spectrum.

Figure 3.10 shows the averaged fractional laser energy transmission for long (red curve) and short laser pulses (blue curve) as a function of delay, t. It is seen that for the long pulses the transmission was approximately 0.95 for 70 ns to 140 ns.

The behavior of the short pulses was distinctly different. As shown by the blue curve in figure 3.10 the peak energy transmission was only 0.6, consistent with deposition of energy into a plasma wave, and the range of delays for which the transmission was high was shorter. This behavior suggests that at the higher intensity of the short pulse, guiding was more sensitive to the state of the plasma channel, consistent with a stronger laser-plasma interaction. A stronger interaction may also explain the distortion of the short pulse fluence profile shown in figure 3.13, although at these larger bandwidths, chromatic aberration effects may contribute.

Some examples of electron spectra produced from the capillary interaction are shown in figure 3.15(a) to 3.15(d). Figure 3.14 shows the raw electron spectrum as seen on the Lanex screen with the energy axis superimposed. The electron bunch energy was centred at 130 MeV and had an FWHM energy spread of 19 %. A line-out of this spectrum is shown graphically as the red curve in figure 3.15(a). The energy spreads of the electron beams varied from 20–75 %. The onset of electron beam generation was observed to be critically dependent on the

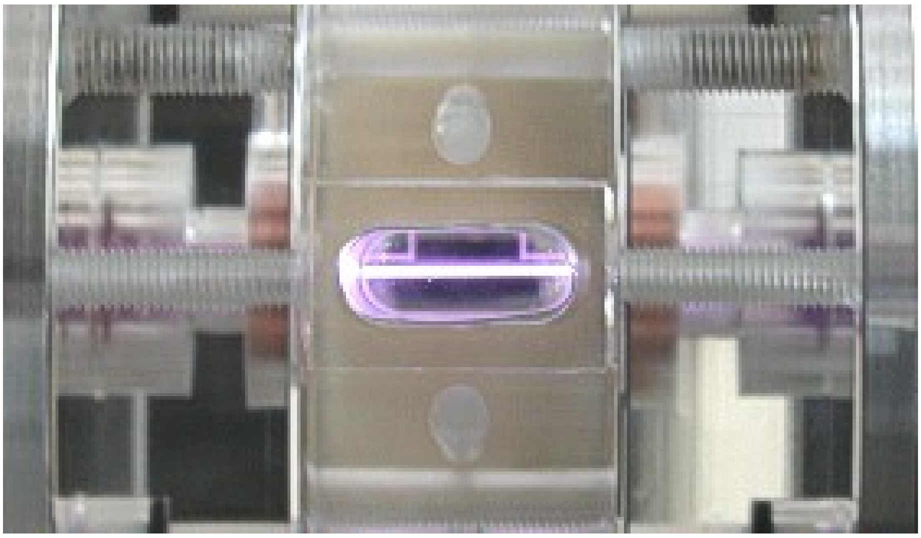

Figure 3.11: The discharge across the capillary.

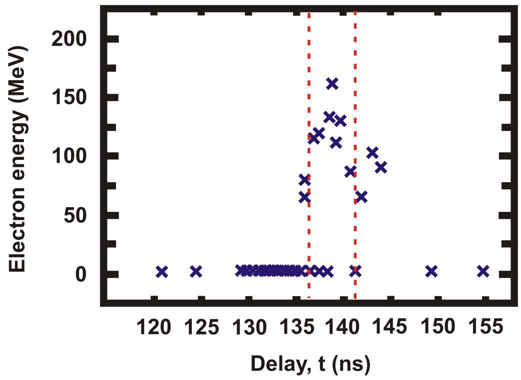

Figure 3.12: The electron bunch energy, E, plotted as a function of the delay, t, between the discharge across the capillary and the arrival time of the driving laser pulse.

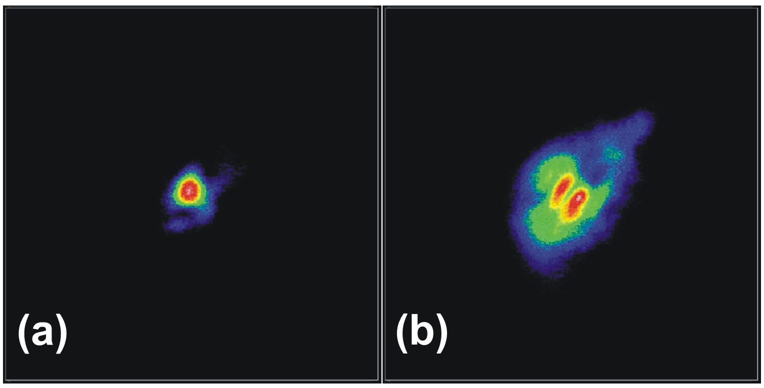

Figure 3.13: The transmitted beam profiles of the capillary guided laser spots in (a) long pulse mode and (b) short pulse mode.

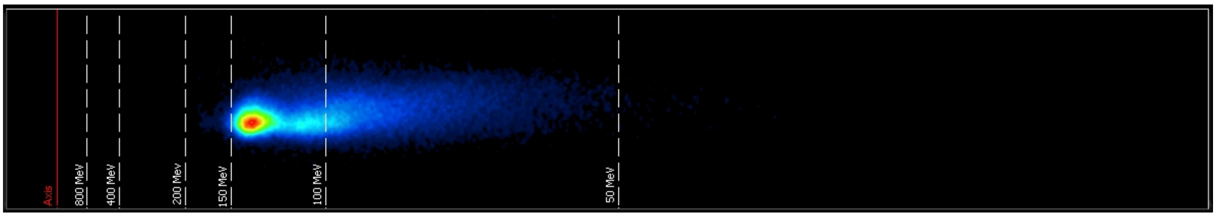

Figure 3.14: A false colour image of the raw electron energy spectrum on the Lanex screen. The energy axis scale is marked on the picture

delay, t, between the discharge current across the hydrogen discharge plasma and the arrival of the driving laser pulse. This is clearly shown in figure 3.12 which demonstrates that in the delay range 130 ns $< t <$ 135 ns no electron beams were observed. Conversely, in the delay range 137 ns $< t <$ 141 ns 7 out of 9 shots produced quasi-monoenergetic electron beams.

Data collected on the long pulse guiding through the capillary signified that the plasma channel was formed for a duration of at least 70 ns; the broadening of the spectra of the transmitted short pulse after interaction with the plasma indicated that there was strong wakefield formation over a 50 ns delay window; however electron beams were only observed for a range of delays corresponding to a 5 ns window. This is illustrated by the dashed red lines in figure 3.10. It was also important to note that electron beams were not observed for negative delays i.e. when the laser pulse interacts with a neutral gas.

3.3.1 Experiment 3: Discussion

Electrons were only generated in D = 200 μm capillaries, which indicates that in these experiments the properties of the plasma channel were critical to the LWFA process. Comparing the dependence on delay of guiding and electron acceleration allows further insight as to how the presence of a plasma channel affected the LWFA process. The short pulse transmission was relatively low ($\sim$ 0.3). This can possibly be attributed to pulse depletion, furthermore the short pulse exit modes were distorted, relative to the long pulse exit mode (figure 3.13).

The high peak transmission and compact exit modes for t = 50 − 80 ns show that beams of intensity $\sim 10^{18}$ Wcm^{-2} can be guided over at least 14 z_R using the hydrogen-filled discharge capillary waveguide. Furthermore, the fact that the laser energy transmission, $T = 0.3$ for negative delays but $T = 1$ after the onset of the current demonstrates that the laser spot was guided by the plasma channel (formed by the current) and not by the walls of the capillary (present for all delays). Moreover, it was observed that the transmission increased sharply between

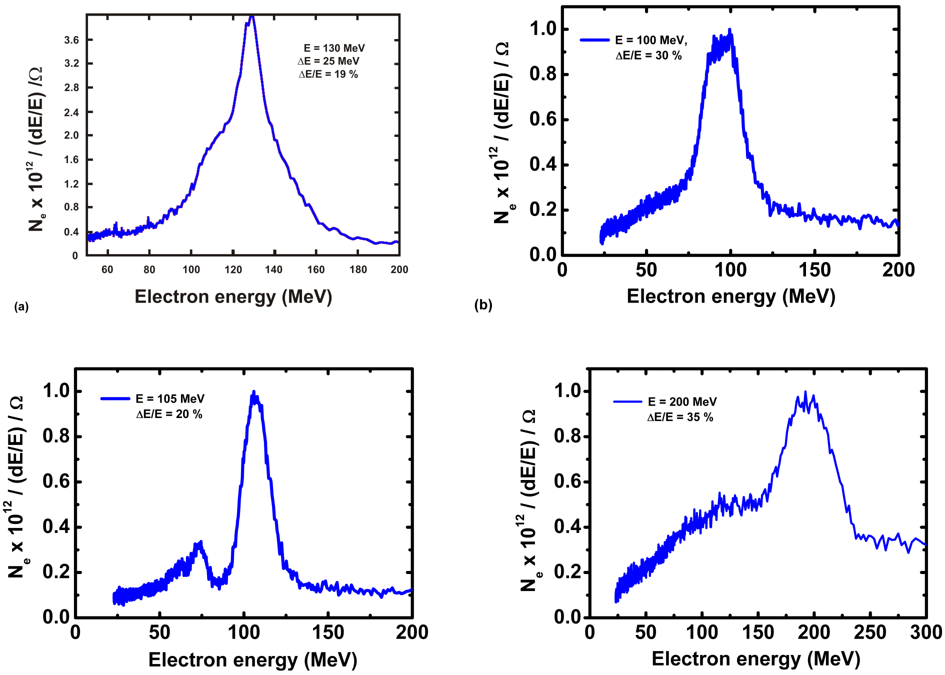

Figure 3.15: The electron spectrum ejected from the capillary (a) centred at 130 MeV with a FWHM energy spread of 19 %. (b) centred at 100 MeV with a FWHM energy spread of 30 %. (c) centred at 105 MeV with a FWHM energy spread of 20 %. (d) centred at 200 MeV with a FWHM energy spread of 35 %.

t = 40 ns and t = 50 ns (when p = 160mbar) corresponding, presumably, to the formation of a plasma channel suitable for guiding. For higher pressures that rise occurred at later delays, which is most likely due to the fact that more hydrogen atoms required ionisation during the channel formation process, requiring more energy from the discharge current.

At negative t, for which no plasma channel was present, the maximum energy that could be achieved was $\sim$ 110 MeV at an electron density of 2×10^{19} cm^{-3}. In work by another group, the maximum energy of electrons accelerated in a gas jet (of length 2mm) using the same laser was $\sim$ 80 MeV at an electron density of 2×10^{19} cm^{-3} [1], suggesting that despite several technical differences in setup the shots recorded at negative delays are equivalent to those incident on a gas jet.

The highest energy of electrons accelerated in the plasma channel was approximately double the energy of electrons accelerated at negative delays or in gas jets. For L = 15 mm the maximum energy of 200 MeV is reached for p = 400 mbar ($n_e = 8.7 \times 10^{18}$ cm^{-3}). The energy drops away either side of that pressure.

There were considerable shot-to-shot fluctuations in the measured electron energy. The likely source of that instability was the non-linear evolution of the laser pulse as it became sufficiently intense to induce electron trapping. The length over which that evolution occurs would have varied from shot-to-shot, so that the subsequent length over which electrons were accelerated (before either depletion of the laser pulse or the end of the capillary) also varied. The highest energy electron beams within the scatter would be those that were accelerated for exactly one dephasing length.

Chapter 4

Electro-optic detection of relativistic electron bunches

4.1 Introduction

Since the first demonstration of monoenergetic electron beams from laser wakefields in 2004 [1, 2, 3], many groups have reported their progress on laser wakefield acceleration [4, 30, 9]. In order to probe the underlying physics and applicability of laser wakefields a wide variety of diagnostics have been implemented. It has been imperative to characterise the properties of the plasma density profile [60, 182], the plasma wake profile [31], the electron bunch properties (energy spread [183, 184], charge distribution [185], emittance [186, 187], pointing stability [188] and the laser pulse properties before and after the plasma interaction [156, 189]). To date, it has been shown by the community that electron bunches can be generated with several pC of charge [185], energies up to 1 GeV [4, 29, 190], and as will be demonstrated in chapter 5 of this thesis energy spreads of 1 % [7, 184].

However, experimentally, little has been done to characterise the temporal characteristics of the electron bunch which in theory should be typically of the order (or a fraction) of a plasma wavelength (5–30 μm, [density range of 1.2×10^{18} cm^{-3} – 4.5×10^{19} cm^{-3}]) [44, 75] hence the production of 2 fs electron pulses from a LWFA should be feasible [191]. Confirmation of the 'true' electron bunch length remains a crucial challenge in the laser wakefield research field to demonstrate the production of high quality electron beams for drivers of free electron lasers and various high resolution pump-probe experiments. This thesis presents experimental measurements of the temporal profile of laser wakefield accelerated electron bunches using electrooptic techniques.

Methods employed at conventional accelerator facilities to measure electron bunch lengths involve probing either the self-fields of the electron bunch i.e. the Coulomb field, or alternatively the radiative field which is usually based on the emission of coherent radiation by the electron beam.

Traditionally, measuring the Coulomb field has been done using scanning delay techniques, which involve placing a non-linear crystal such as ZnTe in close proximity to the electron beam. The electric field of the passing electron bunch induces birefringence in the electro-optic sampling crystal (EOS) which is then probed by a synchronised laser pulse considerably shorter than the electron bunch. The delay between the laser pulse and the electron bunch is varied, to build up a map of the Coulomb electric field of the bunches averaged over many laser shots as a function of position. More recently a single shot version of this technique has been developed [71, 192, 193] which makes use of chirped laser pulses that are longer than the electron bunch [193]. In this technique each wavelength component of the chirped pulse corresponds to a unique position in space, hence the electric field of a passing electron pulse can be encoded onto the chirped pulse as the Coulomb field and laser pulse co-propagate in the non-linear crystal. By measuring the ellipticity or polarisation rotation of as a function of wavelength in a spectrometer the transverse electric field of the electron bunch can be measured/resolved in a single-shot.

Another method widely used by conventional accelerator laboratories relies on coherent transition radiation produced when an electron bunch passes an interface between two dielectrics (dielectric discontinuity). Usually a thin aluminium foil is placed in the electron beam path at an angle of 45° with respect to the electron beam axis. The CTR (OTR) leaves the foil perpendicular to the beam direction and can be coupled out from a vacuum chamber for direct measurement with a broadband spectrometer [194, 195, 196]. The coherent transition radiation emitted by a particle bunch carries information about the bunch length. For example, for bunches with a Gaussian longitudinal distribution and a fixed number of particles, the total energy emitted as CTR is inversely proportional to the r.m.s. bunch length. Additionally, the CTR can be sent to an interferometer to obtain the autocorrelation trace of the particle bunch electric field, and therefore yield a measurement of the bunch length and shape through Fourier anaylsis using the bunch form factor [197, 198, 199, 200]. Direct spectral measurements of coherent synchrotron radiation have also been performed [201]. Furthermore, electron-beam microbunching at the exit of a self-amplified spontaneous-emission free-electron laser (SASE FEL), has also been measured by observation of coherent transition radiation (CTR) [202, 203].

It is possible to extend these methods for LWFA experiments. It was experimentally demonstrated by Leemans *et al* [108, 109] and van Tilborg *et al* [73, 74], that the plasma-vacuum boundary acts as a sufficient dielectric discontinuity provided the transition radiation emission region is smaller than the formation length, L_{form} [204]:

$$L_{form} = \frac{\lambda}{2 - 2\beta\cos\theta}, \tag{4.1}$$

where λ is the radiation wavelength, $\beta = v/c$ and θ is the peak emission angle. The formation length is defined as the length it takes for an electron at velocity β to 'slip' back by half a wavelength ($\lambda/2$) with respect to the radiation wavelength. Physically, it is the distance over which the Coulomb field and the radiation field become disentangled. Although the expression for L_{form} is derived for a vacuum environment, it also holds for an underdense region of plasma. The dielectric function in a plasma can be approximated by [204]

$$\varepsilon(\omega) = 1 - \frac{\omega_p^2}{\omega^2}, \tag{4.2}$$

where ω is the angular frequency of the radiation. From equation 4.2 it can be seen that for frequencies $\omega \leq \omega_p$, the plasma-vacuum interface acts as a strong dielectric discontinuity resulting in LWFA generated CTR. The mechanism and driving force behind the production of transition radiation relies on the Coulomb electric fields of relativistic charged particles. LWFA electron bunches are excellent candidates to drive this process [108]. The next section describes the characteristics of the Coulomb electric fields of electron bunches.

4.2 The Coulomb fields of relativistic electron bunches

In order to understand the physical mechanisms responsible for the generation of transition radiation, it is necessary to first understand the Coulomb fields associated with an electron bunch. A useful starting point is to consider the electric fields of a single electron which can be derived from the Liénard-Wiechert potentials. The potentials at observation point x, at a distance R, from a moving point charge are given by [205]

$$\phi(x,t) = Q\left[\frac{1}{(1-\beta\cdot \mathrm{n})\,R}\right]_{ret}, \tag{4.3}$$

$$\mathrm{A}(x,t) = Q\left[\frac{\beta}{(1-\beta\cdot \mathrm{n})\,R}\right]_{ret}, \tag{4.4}$$

where $Q = q/4\pi\varepsilon_0$ (q is the charge of the particle) and the subscript ret denotes the condition that the expression inside the square brackets has to be evaluated at a retarded time, $t' = t - R(t')/c$. With respect to figure 4.1(b) it can be shown that the retarded time is defined as the latest time at which a light signal emitted from position z_{ret} would be received at position z_{pres} before time t. This is a direct consequence of the finite value of the speed of light, c, being the maximum speed at which information may travel. The unit vector **n** points from the retarded position towards the point of observation, $P(x,z)$.

Using equation 4.3 and 4.4 along with the relation $\mathrm{E} = -\nabla\phi - \partial\mathrm{A}/\partial t$ the electric field due to a relativistic point charge can be expressed as [69]

$$E(x,t) = Q\left[\frac{\mathrm{n}-\beta}{\gamma^2(1-\beta\cdot\mathrm{n})^3R^2}\right]_{ret} + Q\left[\frac{\mathrm{n}\times\left((\mathrm{n}-\beta)\times\dot{\beta}\right)}{(1-\beta\cdot\mathrm{n})^3R}\right]_{ret}. \tag{4.5}$$

In this equation the electric field is split into a velocity field which is independent of acceleration, and an acceleration field, which depends linearly on $\dot{\beta}$ ($\dot{\beta} = d\beta/dt$). The electro-optic sampling method can be utilised to measure both fields and is commonly used as a temporal diagnostic of electron beams. By placing a non-linear crystal such as ZnTe very near to the electron beam axis the velocity field i.e. the Coulomb field can be probed. The potentials at the observation point P follow from equation 4.3 and equation 4.4 and are given by [69]:

$$\phi(x,y,z,t) = Q\frac{\gamma}{\sqrt{\left(\gamma(z-\beta ct)\right)^2 + x^2 + y^2}}, \tag{4.6}$$

$$A_z(x,y,z,t) = \beta c\phi(x,y,z,t), \tag{4.7}$$

The electric fields at position P can be calculated either from equations 4.3 and 4.4 or from equation 4.5 yielding

$$E_x(x,y,z,t) = \gamma Q\frac{x}{\left(\gamma^2(z^2-\beta ct)^2 + x^2 + y^2\right)^{3/2}}, \tag{4.8}$$

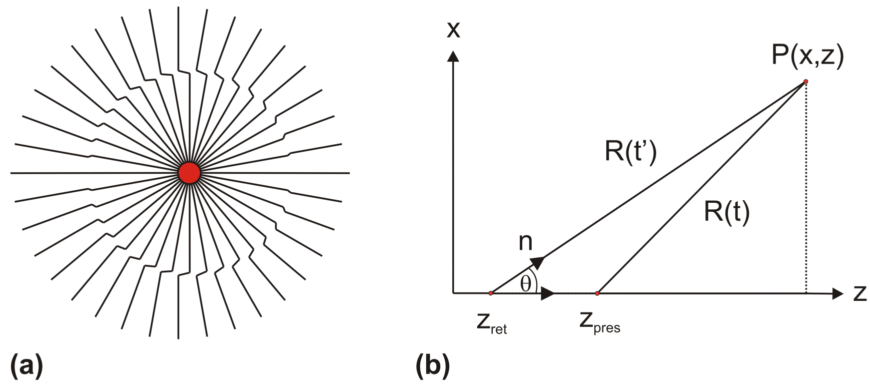

Figure 4.1: (a) The 'kink' in the electric field lines produced when a point charge undergoes an acceleration. The fastest that this information can propagate outwards is the speed of light. (b) The geometry used to calculate the potentials of a relativistic point charge moving at a constant velocity in the z direction.

$$E_y(x, y, z, t) = \gamma Q \frac{y}{(\gamma^2(z^2 - \beta ct)^2 + x^2 + y^2)^{3/2}}, \tag{4.9}$$

$$E_z(x, y, z, t) = \gamma Q \frac{z - \beta ct}{(\gamma^2(z^2 - \beta ct)^2 + x^2 + y^2)^{3/2}}, \tag{4.10}$$

For $\gamma = 1$ the observer sees the static Coulomb field as seen in figure 4.2(a). As γ increases the electric field lines are compressed perpendicular to the direction of propagation (z-direction) as depicted in figure 4.2(b-c). This is a result of Lorentz contraction in the z-direction and can be derived using a Lorentz transformation of the static Coulomb field in the rest frame of the particle, to the observer frame of reference. The maximum electric field along the x-axis, E_x, increases

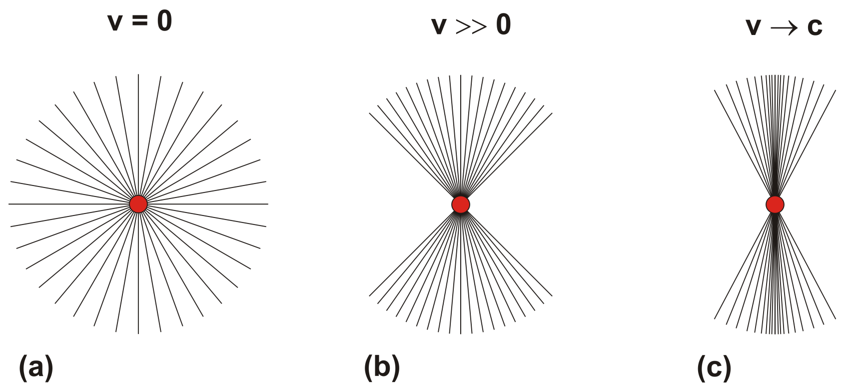

Figure 4.2: (a) The electric field lines for a stationary point charge. (b) The electric field lines for a point charge traveling at relativistic velocity. (c) The electric field lines for a point charge moving at a highly relativistic velocity are compressed perpendicular to the direction of propagation.

proportionally to γ while the FWHM time duration of the transverse field is

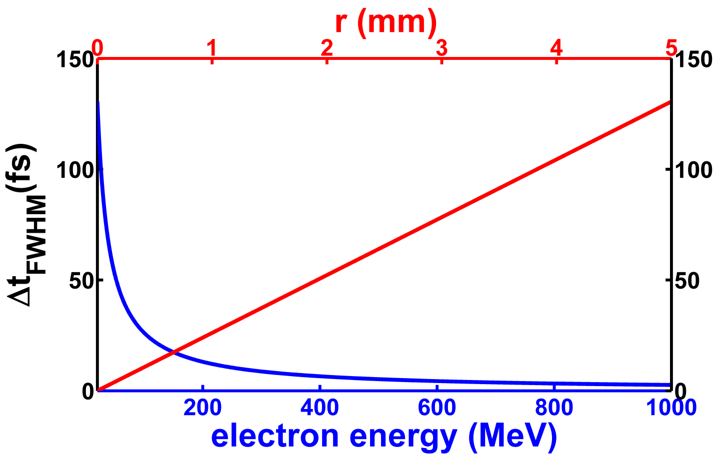

Figure 4.3: The relationship between the duration of the Coulomb electric field and electron energy for a radius of 1 mm (blue curve). The variation of the duration of the Coulomb field with radius for a 100 MeV electron bunch (red curve).

inversely proportional to γ [69],

$$E_x = \frac{Q\gamma x}{r^3}, \tag{4.11}$$

$$\Delta t_{FWHM} = \frac{2r\sqrt{2^{2/3}-1}}{\gamma\beta c}, \tag{4.12}$$

with $r = \sqrt{x^2+y^2}$. Hence, the maximum E_x field, due to a moving charge, is γ times the static Coulomb field. Electro-optic measurements of the relativistic Coulomb fields of electron bunches utilise the E_x field because it is unipolar and scales linearly with γ. Conversely the E_z field is independent on γ and has bipolar properties (E_z changes sign when the charge passes the observer). Inspection of equation 4.12 reveals that the time resolution is linearly dependent on r and inversely proportional to γ, thus for the optimum temporal resolution the electron beam energy should be very large and the crystal should be positioned as close to the beam axis as experimentally practical i.e. without inducing damage to the crystal. In practice both these parameters cannot be infinitely large or small respectively, thus ultimately, the maximum resolution is defined by the opening angle of the electric field lines.

An alternative technique is to measure the CTR emitted when an electron bunch traverses a dielectric discontinuity. The longitudinal distribution of this radiation field is a 'signature' or 'blueprint' of the electron bunch length. Furthermore, probing the CTR does not have the γ dependence temporal resolution issues associated with probing the Coulomb field. However, other temporal resolution

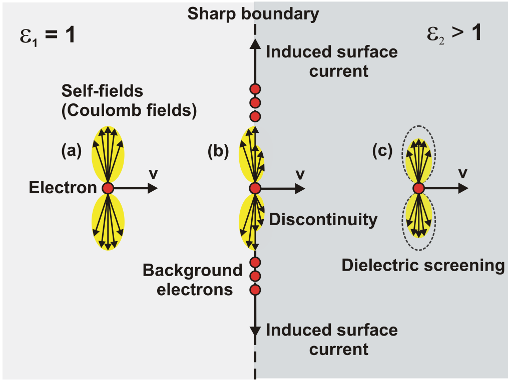

Figure 4.4: (a) The electron propagates in vacuum, where $\varepsilon_1 = 1$. (b) At the interface between two media a discontinuity is formed. (c) While propagating in the second medium, where $\varepsilon_2 > 1$. The discontinuity of the (Coulomb) self-fields at the sharp boundary leads to the generation of a surface current of background electrons, which in turn emits transition radiation.

limits associated with detection exist which will be described in the forthcoming section 5.

4.3 Transition Radiation

Transition radiation is produced by relativistic charged particles when they cross the interface of two media of different dielectric constants i.e. a dielectric discontinuity. Mathematically, the emitted radiation is the homogeneous difference between the two inhomogeneous solutions of Maxwell's equations of the electric and magnetic fields of the moving particle in each medium separately. Physically speaking, the electric field of the particle is different in each medium due to dielectric screening, thus the particle will 'shake off' the difference in electric field as energy in the form of a propagating wave when it crosses the discontinuity boundary. A simplistic schematic of the mechanism of transition radiation is shown in figure 4.4. We consider a single electron moving (a) through a medium with a dielectric constant of $\varepsilon_1 = 1$, then (b) passing a sharp boundary, and (c) into a second medium with a different dielectric constant $\varepsilon_2 > 1$. As discussed in section 4.2 the Coulomb field of electrons with relativistic velocities exhibit a more transverse nature due to Lorentz contraction in the direction of motion. As the electron propagates into the second medium ($\varepsilon_2 > 1$), the self-fields of the bunch experience partial screening by the background electrons. The effectiveness of this screening is proportional to the dielectric constant, whereby complete field cancellation occurs when $\varepsilon_2 = \infty$. As the electron passes through the sharp boundary as seen in figure 4.4(b), an apparent discontinuity in the electric field arises. However, this would be a violation of Maxwell's equations but in reality, electrons at the surface are moved transversely in order to cancel out the discontinuity. It is this bunch driven surface current (dJ/dt) at the boundary between two differing dielectric interfaces that is the driving force behind the emission of electromagnetic radiation.

The spectral characteristics of transition radiation generally exhibit a very broad bandwidth due to the inherently short duration of the electron drive pulse. Collective effects have strong implications on the radiated spectral intensity. For example, considering a bunch of electrons with a longitudinal length, σ_z. The total electro-magnetic field depends on the contribution from each individual electron. Hence, radiation at relatively short wavelengths $\lambda \leq \sigma_z$ will sum up incoherently and the radiation intensity scales as $I_{TR} \propto N$. Conversely, radiation at longer wavelengths $\lambda > \sigma_z$ will experience coherent build up as the summation of the radiation fields interfere constructively with each other. This leads to a quadratic relation between the radiated intensity and the number of electrons $I \propto N^2$. Since typical electron bunches have between $N \cong 10^7$ - 10^9 electrons, the spectral intensity at wavelengths $\lambda > \sigma_z$ can be very large. Analysis of the radiation spectrum is therefore a way to retrieve information about the bunch profile. Identifying the spectral region that defines the onset of coherence is a good indication that the bunch length is near to that wavelength. i.e. if coherent radiation is observed at 3.3 μm then this suggests the bunch length is around 10 fs in duration.

Transition radiation was treated analytically by Ginzburg and Frank [206] for a planar boundary of infinite extent. However, in some cases the Ginzburg-Frank equation is not applicable because it assumes that the radiation screens are of infinite size and that the radiation is observed in the far-field. Casalbuoni [207] introduced a generalised version of the Ginzburg-Frank formula that allowed computation of the transition radiation emitted from a screen of arbitrary shape and size at any distance from the source. The only condition being that the dimensions of the screen and the distance to the observation point must be large compared to the wavelength of the radiation. As this is often the case, this is a powerful method, capable of treating realistic experimental set-ups.

4.4 Transition radiation by a single electron

When an electron propagates past the boundary from vacuum to an infinite metal plane, only backward radiation is emitted as no radiation can propagate inside the metal. This is however not the case for a metallic screen with a finite thickness which will be dealt with in the next section. The angular and spectral energy density of backward transition radiation in the far-field from a single electron is given by the Ginzburg-Frank formula [206]:

$$\frac{d^2U}{d\omega d\Omega} = \frac{e^2}{4\pi^3\varepsilon_0 c}\frac{\beta^2\sin^2\theta}{\left(1-\beta^2\cos^2\theta\right)^2}, \tag{4.13}$$

where $\beta = v/c$. The angular distribution of the radiation emitted from a 40 MeV electron is shown in figure 4.5. Clearly, the radiation is emitted in two lobes each peaked at an angle of $1/\gamma$. Also important to note is the characteristic zero intensity on-axis which gives transition radiation radial polarisation characteristics. This 'doughnut' shaped radiation pattern arises from the radial nature of the Coulomb field that drives the process. Figure 4.5 shows the spatial radiation pattern for a single electron according to equation 4.13.

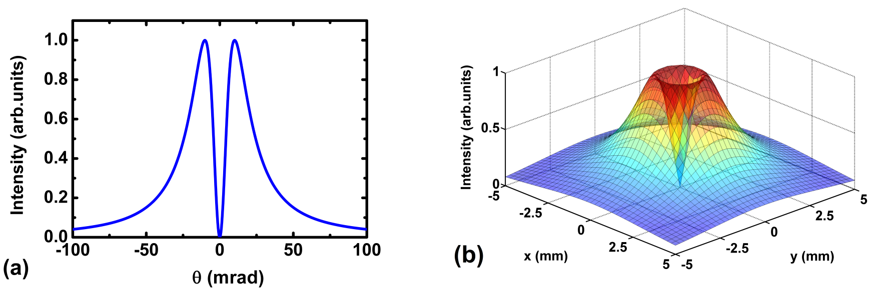

Figure 4.5: (a) The angular distribution of the radiation emitted from a 40 MeV electron according to the Ginzburg-Frank formula. (b) A simulation (3D radial map) of the transition radiation intensity distribution at an observation plane 1 m from the radiative source according to the Ginzburg-Frank formula.

The angular distribution has a maximum intensity at an angle given by [207]:

$$\theta_{\max} = \arcsin\left(\frac{\sqrt{1-\beta^2}}{\beta}\right) = \arcsin\left(\frac{1}{\beta\gamma}\right) \simeq \frac{1}{\gamma}. \tag{4.14}$$

So far we have discussed only the case where an electron traverses a boundary into an infinite plane. In this case the transition radiation spectral energy density is independent of frequency, provided one stays below the plasma frequency of the metal. The next section introduces the effect of transition radiation generated from finite boundaries and the radiation propagation therein.

4.4.1 Transition Radiation from finite planes

Most practical situations involving transition radiation involve the use of finite size radiators. e.g. metallic foil disks, finite plasma vacuum interfaces, etc. It is therefore appropriate to investigate this framework. Following the framework of Casalbuoni [207] We consider a finite metallic disk of radius, a as our transition radiation (TR) source and use a cylindrical coordinate system $(\rho, \phi, z = 0)$ on the disk. The observation screen is at a distance $D >> a$ from the TR source. Designating E_r as the Fourier component of the radial electric field of the incident electron. Taking the Fourier transform of the radial electric field of the electron is thus

$$E_r(\rho, \omega) = \frac{-e\omega}{(2\pi)^{3/2}\varepsilon_0\beta^2\gamma c^2} K_1\left(\frac{\omega\rho}{\beta\gamma c}\right), \tag{4.15}$$

where K_1 is a modified Bessel function. Because of the cylindrical symmetry, the field on the observation screen will be radial as well. Without loss of generality we can therefore choose our target point to be located on the x-axis of the observation screen, $P = (x, y = 0, z = 0)$.

The electric field at $\mathbf{P}$ will then have only an x component. A small area element at an arbitrary point $Q = (\rho, \phi, 0)$ of the TR source screen at $z = 0$ yields the following contribution to the horizontal field component at $\mathbf{P}$:

$$dE_x(P, \omega) = \frac{-ik}{2\pi} E_r(\rho, \omega)\text{cos}\phi \frac{\exp(ikR')}{R'} \rho d\rho d\phi, \tag{4.16}$$

where $k = \omega/c$ and $R' = \sqrt{D^2 + (x - \rho\text{cos}\phi)^2 + (\rho\text{sin}\phi)^2}$ is the distance between Q and P. The $1/\rho$ divergence of $E_r(\rho, \omega)$ for $\rho \longrightarrow 0$ is canceled by multiplication with the area element $\rho d\rho d\phi$. The electric field , E_x, at P is given by integratiing the radial electric field over the area of the TR source:

$$E_x(P, \omega) = \frac{-ik}{2\pi} \int_0^a \int_0^{2\pi} E_r(\rho, \omega)\text{cos}\phi \frac{\exp(ikR')}{R'} \rho d\rho d\phi. \tag{4.17}$$

Since we restrict ourselves here to the far-field case, the square root is only expanded up to first order in ρ,

$$R' = \sqrt{D^2 + (x - \rho\text{cos}\phi)^2 + (\rho\text{sin}\phi)^2} \approx R = \frac{x\rho\text{cos}\phi}{R}, \tag{4.18}$$

with $R = \sqrt{D^2 + x^2}$. The distance $R' = QP$ in the denominator of the integrand of equation 4.17 can be replaced by the distance R between the centre of the TR screen and the observation point P:

$$\frac{\exp(ikR')}{R'} \approx \frac{\exp(ikR)}{R}\exp(-ik\rho\sin\theta\cos\phi), \tag{4.19}$$

we can define the angle θ by $\sin\theta = x/R$ and rewrite equation 4.17 as:

$$E_x(P,\omega) = \frac{-ik}{2\pi}\frac{\exp(ikR)}{R}\int_0^a\int_0^{2\pi} E_r(\rho,\omega)\cos\phi\exp(-ik\rho\sin\theta\cos\phi)\rho d\rho d\phi. \tag{4.20}$$

Inserting E_r from equation 4.15 the field at point $P = (x, 0, D)$ yields:

$$E_x(P,\omega) = \frac{iek^2}{(2\pi)^{5/2}\varepsilon_0\gamma c\beta^2}\frac{\exp(ikR)}{R}\int_0^a\left[\int_0^{2\pi} K_1\left(\frac{k\rho}{\beta\gamma}\right)\cos\phi\exp(-ik\rho\sin\theta\cos\phi)d\phi\right]\rho d\rho \tag{4.21}$$

Integration over the azimuthal angle yields the Bessel function J_1 :

$$\int_0^{2\pi}\exp(-ik\rho\sin\theta\cos\phi)\cos\phi d\phi = -i2\pi J_1(k\rho\sin\theta). \tag{4.22}$$

Integration over the radius gives:

$$\begin{aligned}\int_0^a J_1(k\rho\sin\theta)K_1\left(\frac{k\rho}{\beta\gamma}\right)\rho d\rho &= \frac{\beta^3\gamma^3\sin\theta}{k^2(1+\beta^2\gamma^2\sin^2\theta)}\left[1-T(\theta,k)\right]\\ &= \frac{\beta^3\gamma^3\sin\theta}{k^2(1-\beta^2\cos^2\theta)}\left[1-T(\theta,k)\right].\end{aligned} \tag{4.23}$$

Thus the Fourier transformed electric field on the observation screen becomes:

$$E_x(\theta,\omega) = \frac{e}{(2\pi)^{3/2}\varepsilon_0 c}\frac{\exp(ikR)}{R}\frac{\beta\sin\theta}{1-\beta^2\cos^2\theta}\left[1-T(\theta,k)\right], \tag{4.24}$$

with

$$T(\theta,k) = \frac{ka}{\beta\gamma}J_0(ka\sin\theta)K_1\left(\frac{ka}{\beta\gamma}\right) + \frac{ka}{\beta^2\gamma^2\sin\theta}J_1(ka\sin\theta)K_0\left(\frac{ka}{\beta\gamma}\right). \tag{4.25}$$

4.4.2 Radiated energy of transition radiation

So far we have dealt with the TR electric fields for single electrons for a single frequency component on the source and image planes. We now turn our attention to computation of the spectral density distribution of the transition radiation. Our starting point considers the simple case of an electromagnetic wave traveling in z direction, without a dependence on x and y. This pulse can be expressed as a superposition of plane waves:

$$E_x(z,t) = \frac{1}{\sqrt{2\pi}} \int_{-\infty}^{\infty} E(\omega) \exp\left[i\omega\phi\right] d\omega = \frac{2}{\sqrt{2\pi}} \int_{0}^{\infty} E(\omega) \exp\left[i\omega\phi\right] d\omega, \tag{4.26}$$

where $\phi = z/c - t$. The Fourier components of the magnetic field are given by:

$$B(\omega) = \frac{E(\omega)}{c}. \tag{4.27}$$

The Poynting vector gives the energy flow:

$$\mathbf{S} = \frac{1}{2\mu_0} \mathbf{E} \times \mathbf{B}^* \qquad , S_z = \frac{1}{2\mu_0} E_x \times B_y^* \tag{4.28}$$

and the total energy per unit area, flowing through the detector plane at $z = 0$, is

$$U = \int_{-\infty}^{\infty} S_z(0,t) dt = \frac{1}{2\mu_0} \int_{-\infty}^{\infty} \left[E_x(0,t) B_y^*(0,t)\right] dt. \tag{4.29}$$

In terms of the Fourier components the energy flow can be expressed as:

$$U = \frac{1}{\pi\mu_0} \int_0^{\infty} d\omega \int_0^{\infty} d\omega' E(\omega) B^*(\omega') \int_{-\infty}^{\infty} dt [\exp(-i(\omega - \omega')t)]. \tag{4.30}$$

The time integration yields $2\pi\delta(\omega - \omega^{'})$, hence

$$U = \frac{2}{\mu_0 c} \int_0^{\infty} |E(\omega)|^2 \, d\omega \qquad \text{and writing} \qquad U = \int_0^{\infty} \frac{dU}{d\omega} d\omega, \tag{4.31}$$

we get for the spectral energy density:

$$\frac{dU}{d\omega} = \frac{2}{\mu_0 c} |E(\omega)|^2 . \tag{4.32}$$

Transition radiation not only depends on frequency but also exhibits an angular dependence. Thus putting equation 4.24 into equation 4.32 and remembering that the area element dS at the point P on the observation screen is $dS = R^2 d\Omega$, we obtain for the spectral energy as a function of the angle, θ [207]:

$$\frac{d^2U}{d\omega d\Omega} = \frac{e^2}{4\pi^3 \varepsilon_0 c} \frac{\beta^2 \sin^2\theta}{(1 - \beta^2 \cos^2\theta)^2} \left[1 - T(\theta, \omega)\right]^2 , \tag{4.33}$$

with

$$T(\theta, \omega) = \Omega J_0 \left(\frac{\omega a \sin\theta}{c}\right) K_1\left(\Omega\right) + \frac{\omega a}{c\beta^2\gamma^2 \sin\theta} J_1 \left(\frac{\omega a \sin\theta}{c}\right) K_0\left(\Omega\right), \tag{4.34}$$

where $\Omega = \omega a/c\beta\gamma$. Equation 4.33 is the generalised Ginzburg-Frank formula for a transition radiation source of finite radius a. The correction term $T(\theta, k)$ (equation 4.25) has been written here as a function of θ and $\omega = kc$. Inspection of equation 4.33 reveals the frequency dependence of the radiated energy. The term $T(\theta, \omega)$ depends on the product $\omega a \propto a/\lambda$. This means that the angular distribution remains invariant if the disk radius a and the wavelength λ of the TR are scaled by the same factor. Note however, that the generalized Ginzburg-Frank formula is only valid in the far-field regime because in the derivation of R$'$ we have only expanded to first order.

So far the derived expressions only consider transition radiation characteristics in the far-field limit, i.e. when radiation propagates to an observation plane at a distance D which is large compared to the wavelength of the radiation and also large compared to the radius a of the disk. The Ginzburg-Frank formula is valid only when the TR screen is large enough and at a sufficiently large distance from the source. The next section will consider transition radiation characteristics in the near field limit.

4.4.3 Transition radiation in the near-field limit

To consider the near-field case we now expand the distance R' between an arbitrary source point Q and the observation point P to second order in the small quantity $\rho/R \ll 1$ where $R = \sqrt{D^2 + x^2}$ is the distance between the center of the TR source and the observation point P. (Note that $x/R = \sin\theta$ is usually also much smaller than 1)

$$\begin{aligned} R' &= \sqrt{D^2 + (x - \rho\cos\phi)^2 + (\rho\sin\phi)^2} \\ &\approx R - \frac{x\rho\cos\phi}{R} + \frac{\rho^2}{2R}. \end{aligned} \tag{4.35}$$

The second term is responsible for far-field diffraction. If, in addition, the third term is taken into account, one can also describe the near-field diffraction pattern. The electric field at P is in second order in ρ:

$$E_x(P, \omega) \propto \int_0^a \left[\int_0^{2\pi} K_1\left(\frac{k\rho}{\beta\gamma}\right) \cos\phi \exp(-ik\rho\sin\theta\cos\phi) \exp\left(\frac{ik\rho^2}{2R}\right) d\phi \right] \rho d\rho. \tag{4.36}$$

The integration over the azimuthal angle can be carried out yielding $J_1(k\rho\sin\theta)$.

Thus the angular dependence of the intensity to second order is [207]

$$\frac{dU^{(2)}}{d\omega d\Omega} \propto \left| \int_0^a J_1(k\rho \sin\theta) K_1\left(\frac{k\rho}{\beta\gamma}\right) \exp\left(\frac{ik\rho^2}{2R}\right) \rho d\rho \right|^2. \quad (4.37)$$

The integral in equation 4.37 can only be solved numerically [207].

4.4.4 Transition radiation far-field condition

It has already been established that the Ginzburg-Frank formula is applicable when the disk radius a is very large and the observation screen is sufficiently far away, i.e in the far-field. Casalbuoni *et al* demonstrate that the effective source screen radius can be defined as [207]:

$$r_{eff} = \gamma\lambda. \quad (4.38)$$

The first condition for obtaining the Ginzburg-Frank angular distribution is that the TR source screen radius has to exceed the effective source radius:

$$r_{screen} \equiv a \geq r_{eff} = \gamma\lambda. \quad (4.39)$$

When this condition is fulfilled the term $T(\theta,\omega)$ in the generalised Ginzburg-Frank formula is much smaller than unity. If however, the screen radius, a is well below the effective source radius the correction term, $T(\theta,\omega)$ becomes significant. The condition for far-field diffraction can be written as:

$$D > \gamma r_{eff} = \gamma^2\lambda. \quad (4.40)$$

This condition can be understood by considering the Frensnel zone construction in light optics. The radius of the n^{th} Fresnel zone is given by $r_n = \sqrt{n\gamma D}$. The far-field is safely reached when only the first Fresnel zone contibutes, i.e. when

$$r_1^2 > r_{eff}^2 \Rightarrow D > \gamma^2\lambda. \quad (4.41)$$

4.4.5 Total radiated energy of transition radiation

The total spectral density radiated by an electron crossing a boundary from vacuum to an infinite metallic plane is obtained by integrating equation 4.13 over

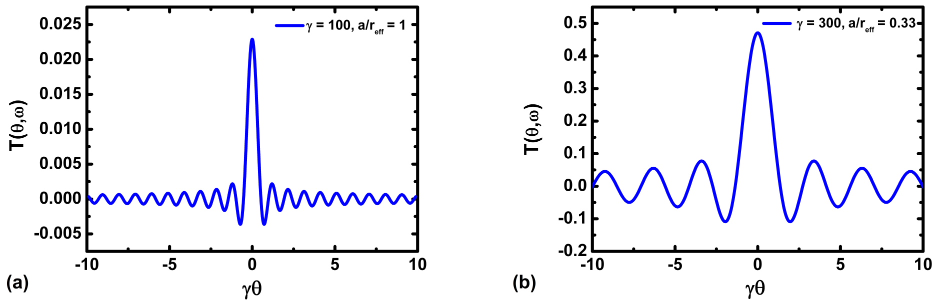

Figure 4.6: (a) The correction term $T(\theta,\omega)$ plotted for $\gamma = 100$ and $a/r_{eff} = 1$ and (b) $\gamma = 300$ and $a/r_{eff} = 1/3$.

the backwards hemisphere [207]

$$\frac{dU}{d\omega} = 2\pi \int_0^{\pi/2} \frac{d^2U}{d\omega d\Omega} \sin\theta d\theta = \frac{e^2\beta^2}{2\pi^2\varepsilon_0 c} \int_0^1 \frac{1-u^2}{(1-\beta^2u^2)^2} du, \tag{4.42}$$

with $u = \cos\theta$. The integration can be done analytically and yields for the energy per ω interval, radiated by one electron:

$$\frac{dU}{d\omega} = \frac{e^2}{8\pi^2\varepsilon_0 c}\left(\frac{1+\beta^2}{\beta}\ln\left(\frac{1+\beta}{1-\beta}\right) - 2\right) \approx \frac{e^2}{2\pi^2\varepsilon_0 c}\left(\ln\gamma + \ln 2 - 0.5\right). \tag{4.43}$$

4.5 Coherent transition radiation from electron bunches

In the previous sections we have dealt with the radiation emitted by single electrons. When the radiation wavelength is much shorter than the electron bunch dimensions all electrons radiate incoherently and the TR intensity scales linearly with the number of electrons per bunch:

$$I_{TR} = NI_1. \tag{4.44}$$

This is usually the case in the optical regime, so optical transition radiation (OTR) is predominantly incoherent. In the terahertz regime, however, the radiation wavelength becomes comparable to the transverse and longitudinal bunch size. In this situation the particles radiate coherently via constructive interference (figure 4.7(a)). Hence the coherent transition radiation (CTR) intensity grows quadratically with the number N of electrons in the bunch:

$$I_{CTR} = N^2 I_1, \tag{4.45}$$

therefore we can write

$$\frac{d^2U_{bunch}}{d\omega d\Omega} = \frac{d^2U_{GF}}{d\omega d\Omega} N^2 \left|F(\omega)\right|^2 \left[\frac{2c}{\omega r_b \sin\theta} J_1\left(\frac{\omega r_b \sin\theta}{c}\right) - \frac{2c\beta\gamma}{\omega r_b} I_1\left(\frac{\omega r_b}{c\beta\gamma}\right) T(\theta,\omega)\right]^2 . \tag{4.46}$$

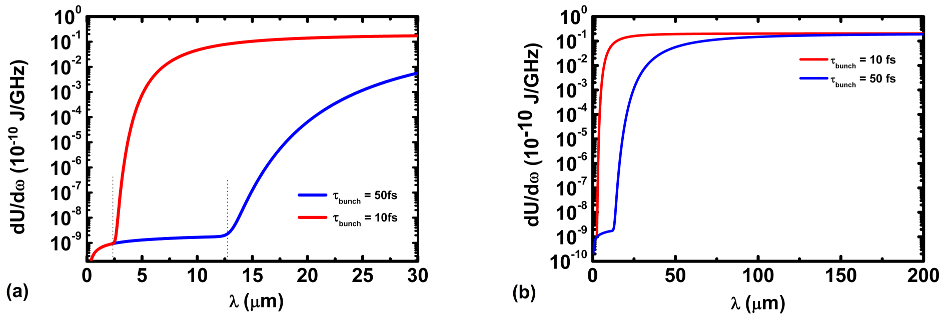

Figure 4.7: (a) The integrated spectral radiation distribution for a 10 fs electron bunch (red line) and a 50 fs electron bunch (blue line). The dashed lines show the onset of coherent radiation emission ($I \propto Q^2$) when the bunch length is equal to the radiation wavelength.(b) The integrated spectral radiation distribution for a 10 fs electron bunch (red line) and a 50 fs electron bunch (blue line) plotted out to longer wavelengths to show when the signals meet.

4.5.1 Propagation of CTR by Fourier transform

A powerful method to compute the diffraction profiles of radiation propagating through an optical system involves the use of Fourier transforms. The analytical and semi-analytical expressions derived in the previous sections are based on cylindrical symmetry which may not be appropriate in many practical cases. The Fourier method is capable of dealing with geometrically asymmetric situations and has the additional advantage that radiation can be modelled when propagating through a whole optical system consisting of apertures, drift spaces and focusing elements (parabolic mirrors).

To explain the basic principle of electromagnetic wave propagation by Fourier transformation we generalise equation 4.17 for a transition radiation source using Cartesian coordinates and choose general points $Q = (\xi, \eta, 0)$ on the source screen and $P = (x, y, D)$ on the observation screen. The two field components at P are

[207]:

$$E_x(P,\omega) = -\frac{ik}{2\pi} \underbrace{\iint}_{\text{TR source}} E_x(Q,\omega)\frac{\exp(ikR')}{R'}d\xi d\eta, \tag{4.47}$$

$$E_y(P,\omega) = -\frac{ik}{2\pi} \underbrace{\iint}_{\text{TR source}} E_y(Q,\omega)\frac{\exp(ikR')}{R'}d\xi d\eta. \tag{4.48}$$

The distance $R' = \bar{QP}$ is expanded up to the second order:

$$\begin{aligned} R' &= \sqrt{D^2 + (x-\xi)^2 + (y-\eta)^2} \\ &\approx D + \frac{x^2+y^2}{2D} - \frac{x\xi + y\eta}{D} + \frac{\xi^2+\eta^2}{2D}. \end{aligned} \tag{4.49}$$

We assume that $(\xi^2 + \eta^2) \ll D^2$ and $(x^2 + y^2) \ll D^2$. The horizontal component of the Fourier-transformed electric field at an arbitrary point $P = (x, y, D)$ on the observation screen is then given in terms of the horizontal field component on the source screen by the integral [207]:

$$\begin{aligned} E_x(P,\omega) = &\frac{-ik}{2\pi}\frac{\exp(ikD)}{D}\exp\left(\frac{ik(x^2+y^2)}{2D}\right) \\ &\underbrace{\iint}_{\text{TR source}} \cdot E_x(Q,\omega)\exp\left(\frac{ik(\xi^2+\eta^2)}{2D}\right)\exp[-i(k_x\xi + k_y\eta)]d\xi d\eta. \end{aligned} \tag{4.50}$$

A corresponding expression holds for the vertical component.
Introducing the 'transverse' wavenumbers

$$k_x = k\frac{x}{D}, \qquad k_y = k\frac{y}{D}, \tag{4.51}$$

with $k = 2\pi/\lambda = \omega/c$. The integral in equation 4.50 can be written as a two dimensional Fourier transform [207]

$$F_x(k_x,k_y) = \frac{1}{2\pi} \underbrace{\iint}_{\text{TR source}} G_x(\xi,\eta)\exp[-i(k_x\xi + k_y\eta)]d\xi d\eta, \tag{4.52}$$

with the integrand:

$$G_x(\xi,\eta) = E_x(\xi,\eta,\omega)\exp\left(\frac{ik(\xi^2+\eta^2)}{2D}\right). \tag{4.53}$$

For the y-component we get correspondingly:

$$F_y(k_x,k_y) = \frac{1}{2\pi} \underbrace{\int\int}_{\text{TR source}} G_y(\xi,\eta)\exp[-i(k_x\xi + k_y\eta)]d\xi d\eta, \tag{4.54}$$

$$G_y(\xi,\eta) = E_y(\xi,\eta,\omega)\exp\left(\frac{ik(\xi^2+\eta^2)}{2D}\right). \tag{4.55}$$

The coordinates of point P are related to the transverse wave numbers by:

$$x = D\frac{k_x}{k}, \qquad y = D\frac{k_y}{k}, \tag{4.56}$$

$$\varphi_{parabolic} = -\frac{k\xi^2}{2f}. \tag{4.57}$$

4.6 Electromagnetic wave propagation in crystals

Having discussed the theoretical framework of transition radiation we now turn our attention to describing the electrooptic effect, which is how the transition radiation is detected and the corresponding electron bunch lengths are resolved. A useful starting point is to describe the propagation of electromagnetic waves in both isotropic and non-isotropic media.

The propagation of a light wave in vacuum is a perfect example of wave propagation in an isotropic medium, so that μ_0 and ϵ_0 remain scalar constants. The phase velocity of a light wave in vacuum is given by

$$c = \frac{1}{\sqrt{\mu_0\varepsilon_0}}, \tag{4.58}$$

where μ_0 and ϵ_0 are the permeability and permittivity of free space respectively. However in a dielectric material the phase velocity is given by. $v_\phi = c/n$, where $n = \sqrt{\epsilon/\epsilon_0}$ is the index of refraction of the medium.

In an isotropic medium the induced polarisation is parallel to the electric field and related to it by a scalar factor independent of the direction along which the field is applied. The relationship between the dielectric polarisation density, $\mathbf{P}$, and the electric field of a propagating wave $\mathbf{E}$ in an isotropic homogeneous medium can be expressed as [12]

$$\mathbf{P} = \epsilon_0\chi_e\mathbf{E}. \tag{4.59}$$

This situation changes when light propagates in anisotropic dielectric crystals. Since the crystal is made up of periodic arrays of ions atoms (or ions) with differing binding forces the induced polarisation becomes dependent on the magnitude and direction of the applied field.

Therefore the polarisation density component vectors in an anisotropic crystal are given by [12]

$$\begin{aligned} P_x &= \epsilon_0 \left(\chi_{11} E_x + \chi_{12} E_y + \chi_{13} E_z \right), \\ P_y &= \epsilon_0 \left(\chi_{21} E_x + \chi_{22} E_y + \chi_{23} E_z \right), \\ P_z &= \epsilon_0 \left(\chi_{31} E_x + \chi_{32} E_y + \chi_{33} E_z \right), \end{aligned} \tag{4.60}$$

where the χ_{ij} coefficients are the electric susceptibility tensors which characterise how easily the dielectric polarises in response to the applied electric field along a given direction. Clearly, this depends on the choice of the x, y and z crystal axes relative to the crystal structure. It is therefore mathematically convenient to define x, y and z in such a way that the off diagonal elements vanish to leave:

$$\begin{aligned} P_x &= \epsilon_0 \chi_{11} E_x, \\ P_y &= \epsilon_0 \chi_{22} E_y, \\ P_z &= \epsilon_0 \chi_{33} E_z, \end{aligned} \tag{4.61}$$

These directions are commonly known as the crystal's principal dielectric axes.

4.7 Birefringence

The phenomenon of birefringence is a direct consequence of the dielectric anisotropy of a crystal. To address the physics of birefringence in depth it is useful to consider the binding forces present in crystal lattices as springs with varying stiffness or spring constants. If the atoms in the crystal are not arranged in a completely symmetric fashion then the binding forces on the electrons will be anisotropic i.e. different along certain directions. It is the interplay between the binding forces between electrons and the electric field of the light wave that govern the propagation dynamics of a light wave in the crystal. Light propagates in a medium by exciting the electrons, which are driven by the E-field. These electron excitations then re-radiate secondary wavelets, which recombine and produce a refracted wave, which continues through the medium. The phase velocity of an optical light wave and therefore the index of refraction are determined by the variation between the frequency of the light wave and the resonance frequency of the atoms. Physically this means that if the lattice forces present in a material are identical in two directions for example, x and y, then the optical properties along these axes are identical also. The unique axis, in this case, the z direction, is known as the optic axis.

Light propagating along the optic axis will have no component of electric field parallel to the optic axis regardless of polarisation and so will act as one would expect, obeying Snells Law. However, if the light propagates in any other direction, it will be split into two rays namely the ordinary (o-wave) and the extraordinary (e-wave). This is due to the fact that the e-wave propagates with a different phase velocity as it has a component of electric field parallel to the optic axis.

While birefringent crystals all exhibit this phenomenon, the degree to which the effect is observed varies somewhat. Birefringence is therefore quantified by the difference between the refractive index of the e-wave and that of the o-wave, $\Delta n = n_e - n_o$, where n_e and n_o are the refractive indices of the e-wave and the o-wave respectively.

One use of birefringent materials is as retardation plates or waveplates. If a linearly polarised beam propagates through a birefringent crystal that is suitably orientated, the e-wave and o-wave will be retarded by differing amounts. As a result, when the beams recombine on exiting the crystal, they will have experienced a phase retardation [12]

$$\Delta\Gamma = (n_s - n_f)\,\frac{\omega l}{c}, \tag{4.62}$$

where n_s and n_f are the refractive indices of the slow and fast eigenwaves (which are orthogonally polarised), respectively, ω is the angular frequency of the light beam and l, the thickness of the crystal. From this equation it is clear that by varying its thickness, a birefringent crystal or waveplate can rotate the polarisation of light as required.

Furthermore another use of birefringent crystals only applies to a particular class of birefringent crystals whose birefringent properties are dependent on the electric field that the crystal is immersed in. Such crystals exhibit a linear electro-optic effect, the strength of which is denoted by the Pockels coefficient, K_p. This is related to the induced birefringence by

$$\Delta n = n_0^3 K_p E, \tag{4.63}$$

where Δn is the induced birefringence, n_0 is the refractive indice with no applied external electric field and $\mathbf{E}$ is the applied electric field strength. As a consequence of this relationship the refractive indice changes linearly with the applied electric field. This relationship is the basis for a Pockels cell, which is simply an appropriate birefringent electroooptic crystal immersed in a controllable electric field. Thus a Pockels cell in conjunction with a polariser can be applied to produce a form of high-speed optical shutter suitable for switching out ultrashort laser pulses in modern laser systems [10, 12].

4.8 Electro-optic effect in anisotropic crystals

In a homogeneous medium the electric displacement vector is given by [12]

$$D = \varepsilon\varepsilon_0 E, \tag{4.64}$$

where the relative dielectric permittivity is a scalar quantity. In an electrooptic crystal the direction of the electric field with respect to the crystallographic axes can influence the polarisation state. In this case the permittivity is a symmetric tensor given by [12]

$$\varepsilon = \begin{bmatrix} \varepsilon_{11} & 0 & 0 \\ 0 & \varepsilon_{22} & 0 \\ 0 & 0 & \varepsilon_{33} \end{bmatrix} = \begin{bmatrix} \varepsilon_x & 0 & 0 \\ 0 & \varepsilon_y & 0 \\ 0 & 0 & \varepsilon_z \end{bmatrix} \tag{4.65}$$

It is always possible to carry out a principal axis transformation to an orthogonal coordinate system in which $\mathbf{E}$ and $\mathbf{D}$ are related by a diagonal matrix

$$D = \varepsilon_0 \begin{bmatrix} \varepsilon_x & 0 & 0 \\ 0 & \varepsilon_y & 0 \\ 0 & 0 & \varepsilon_z \end{bmatrix} \begin{bmatrix} E_1 \\ E_2 \\ E_3 \end{bmatrix}. \tag{4.66}$$

The components of ε are then the principal axis and the principal refractive indices are given by:

$$n_x = \sqrt{\frac{\varepsilon_x}{\varepsilon_0}}, n_y = \sqrt{\frac{\varepsilon_y}{\varepsilon_0}}, n_z = \sqrt{\frac{\varepsilon_z}{\varepsilon_0}}. \tag{4.67}$$

In general for a given direction in a crystal there exist two possible linearly polarised modes, these are commonly known as the rays of propagation. Each mode has a unique direction of polarisation and a corresponding index of refraction. By using the index ellipsoid, the mutually orthogonal polarisation directions and the indices of the two rays can be deduced

$$\frac{x^2}{n_x^2} + \frac{y^2}{n_y^2} + \frac{z^2}{n_z^2} = 1. \tag{4.68}$$

The refractive indices n_x, n_y and n_z are the refractive indices along each of the principal axes. For any other direction in the crystal the refractive index can be determined from the ellipsoid surface distance from the origin. Usually $\mathbf{D} = \varepsilon\mathbf{E}$ and we can define an impermeability tensor given by

$$\eta = \frac{\varepsilon_0}{\varepsilon} = \begin{bmatrix} 1/n_1^2 & 0 & 0 \\ 0 & 1/n_2^2 & 0 \\ 0 & 0 & 1/n_3^2, \end{bmatrix} \tag{4.69}$$

where the directions x, y, and z correspond to the principal dielectric axes defined as the directions in the crystal along which the electric displacement vector, $\mathbf{D}$ and electric field vector, $\mathbf{E}$ are parallel. It is the existence of these two unique rays known as the ordinary and extraordinary with different indices of refraction, which causes birefringence.

Since the propagation characteristics in crystals are fully described by means of the index ellipsoid, the effect of an electric field on the propagation is expressed most conveniently by giving the changes in the constants of the index ellipsoid.

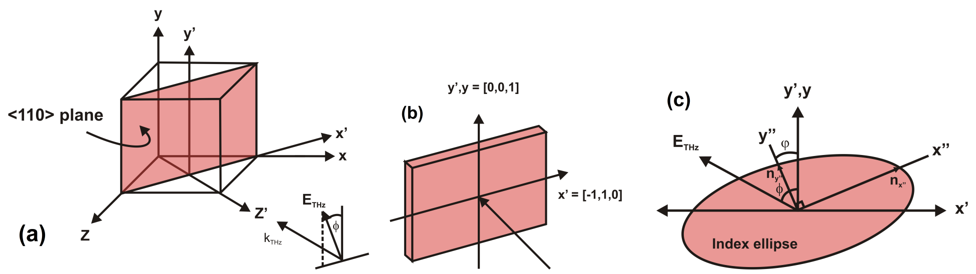

Figure 4.8: (a) The coordinate system of a ZnTe crystal cut in the $\langle 110 \rangle$ plane. (b) A 'slice' of ZnTe cut in the $\langle 110 \rangle$ plane. (c) The index ellipsoid projected onto the $\langle 110 \rangle$ plane of a ZnTe crystal.

4.9 Electro-optic properties of ZnTe

For the electrooptic experiments presented in this thesis ZnTe was used. It is therefore appropriate to describe the electrooptic properties of this crystal. A good starting point is to express the index ellipsoid, used for calculating the optical properties of an anisotropic medium. The crystal coordinate system is defined as (x, y, z). The index ellipsoid is expressed as [204]

$$\sum_{ij} \eta_{ij} x_i x_j = 1 \qquad i, j, k = 1, 2, 3 \tag{4.70}$$

with $(x_1, x_2, x_3) = (x, y, z)$ and $\eta_{ij} = \epsilon_0 \epsilon_{ij}^{-1}$. Equation 4.70 can also be interpreted as

$$\eta_{xx}x^2 + \eta_{xy}xy + \eta_{xz}xz + \eta_{yx}yx + \eta_{yy}y^2 + \eta_{yz}yz + \eta_{zx}zx + \eta_{zy}zy + \eta_{zz}z^2 = 1. \tag{4.71}$$

Equations 4.70 and 4.71 describe a 3D index ellipsoid, characterised by three principal orthogonal axes, each oriented at a specific orientation in the crystal system (x, y, z). The refractive indices along the principal axes of the ellipsoid are defined as n_1, n_2, and n_3. Due to the Pockels effect, also referred to as electro-optic (EO) effect, each element η_{ij} will be a function of the bias electric field $\mathbf{E} = (E_x, E_y, E_z)$, or

$$\eta_{ij} = \eta_{ij,0} + \sum_k r_{ijk} E_k, \qquad i, j, k = 1, 2, 3 \tag{4.72}$$

with r_{ijk} the linear electro-optic or Pockels coefficient. Note that r_{ijk} has 27 elements. However, since η is symmetric ($\eta_{ij} = \eta_{ji}$, the 9 element combinations (i, j) can be combined to 6, each labeled by a single index I, with $I = 1$ for $(i, j) = (1, 1), I = 2$ for $(i, j) = (2, 2), I = 3$ for $(i, j) = (3, 3), I = 4$ for $(i, j) = (3, 2)$ and $(i, j) = (2, 3), I = 5$ for $(i, j) = (3, 1)$ and $(i, j) = (1, 3)$, and $I = 6$ for $(i, j) = (2, 1)$ and $(i, j) = (1, 2)$. This allows for replacement of η_{ij} byη_I, and r_{ijk} by r_{Ik}, which now has 18 elements. In crystals with cubic 43m crystal configuration, such as zinc telluride (ZnTe) and gallium phosphide (GaP), the number of non-zero elements in r_{Ik} can be further reduced and equation 4.72 can be written as [204]

$$\begin{bmatrix} \eta_1 \\ \eta_2 \\ \eta_3 \\ \eta_4 \\ \eta_5 \\ \eta_6 \end{bmatrix} + \begin{bmatrix} \eta_{1,0} \\ \eta_{2,0} \\ \eta_{3,0} \\ \eta_{4,0} \\ \eta_{5,0} \\ \eta_{6,0} \end{bmatrix} + \begin{bmatrix} 0 & 0 & 0 \\ 0 & 0 & 0 \\ 0 & 0 & 0 \\ r_{41} & 0 & 0 \\ 0 & r_{41} & 0 \\ 0 & 0 & r_{41} \end{bmatrix} \begin{bmatrix} E_x \\ E_y \\ E_z \end{bmatrix}. \tag{4.73}$$

The cubic 43m crystals are isotropic, and with no THz field applied $n_1 = n_2 =$

$n_3 = n$. In this case, $\eta_{1,0} = \eta_{2,0} = \eta_{3,0} = 1/n^2$ and $\eta_{4,0} = \eta_{5,0} = \eta_{6,0} = 0$, such that equation 4.71 reads $(x^2+y^2+z^2)/n^2 = 1$. The situation changes if a bias electric field is applied. Since the crystals used for the experiments in this thesis were cut along the $\langle 110 \rangle$ plane, that same geometry will be considered here. The axes of the $\langle 110 \rangle$-cut crystal are labeled (x', y', z'). The two coordinate systems (x, y, z) and (x', y', z') are depicted in figure 4.8(a). It is assumed that the THz pulse is normally incident on the $\langle 110 \rangle$ crystal plane. The electric field E_{THz} is linearly polarized, at angle ϕ with respect to the z' axis, as shown in figure 4.8(a) and figure 4.8(c). The THz electric field vector can be expressed in the crystal system (x, y, z) as $E = E_{THz} = E_{THz}(\sin\phi/\sqrt{2}, -\sin\phi/\sqrt{2}, \cos\phi)$. The index ellipsoid in the (x, y, z) system, defined by equation 4.70 with each element given by 4.73, can then be expressed as [204]

$$\frac{x^2+y^2+z^2}{n^2} + \frac{2r_{41}E_{THz}\sin\phi}{\sqrt{2}}yz - \frac{2r_{41}E_{THz}\sin\phi}{\sqrt{2}}zx + 2r_{41}E_{THz}xy\cos\phi = 1. \tag{4.74}$$

For the EOS experiments presented in this thesis, the laser beam used for probing of the index ellipsoid is collinear with the THz pulse. For this reason, the index ellipse at the $x' - y'$ plane needs to be characterised. Equation 4.74 can be rewritten for the (x', y', z') system, and by setting $x' = 0$ the ellipsoid projection on the $y' - z'$ plane is found. The two principal axes of the ellipse set up a third coordinate system $y'' - z''$, and one can calculate the angle φ between z'' and z' to be

$$\tan 2\varphi = -2\tan\phi. \tag{4.75}$$

The geometry of the system is depicted in figure 4.8(c), with the index ellipse rotated by φ with respect to the z' axis. The difference in index of refraction between the two principal axes $\Delta n = (n_{z''} - n_{y''})$ (figure 4.8(c)), can be found to be [204]

$$\Delta n = (n_{z''} - n_{y''}) = \frac{n^3 r_{41} E_{THz}\sqrt{1+3\sin^2\phi}}{2}, \tag{4.76}$$

with n the index of refraction at probe laser wavelength λ_0 (800 nm for experiments in this thesis). As equation 4.76 demonstrates, Δn scales linearly with the THz field and is maximum for $\phi = 90°$, in which case $\varphi = \pm\, 45°$.

The index of refraction for visible and infrared light can be approximated using the useful parameterisation [208]

$$n(\lambda) = \sqrt{4.27 + \frac{3.01\lambda^2}{\lambda^2 - 0.142}}, \tag{4.77}$$

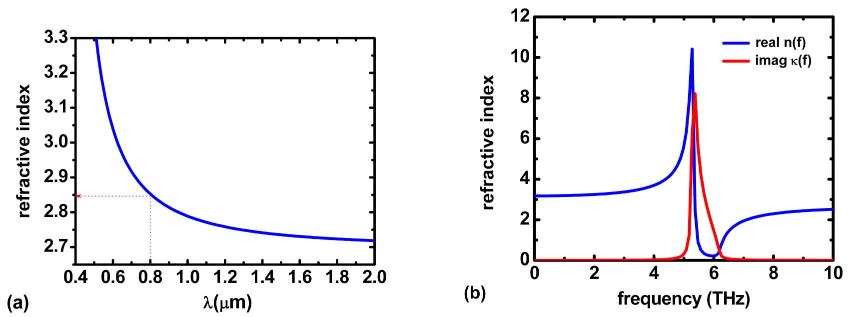

Figure 4.9: (a) The refractive index for light from wavelengths 400 nm–2 μm propagating in ZnTe. The dashed line represents the probe wavelength used for the experiments in this thesis $n_{800nm}^{ZnTe} = 2.85$.(b) The real and imaginary parts of the refractive index of ZnTe for light in the 0.1–10 THz frequency range.

where λ is the photon wavelength in μm. The index of refraction for frequencies far below the optical range the complex dielectric function $\epsilon(f)$ of a non-conducting crystal can be written in the form [208]

$$\varepsilon(f) = \varepsilon_{el} + \sum_i \frac{s_i f_i^2}{f_i^2 - f^2 - i\Gamma_i f}, \tag{4.78}$$

where the first term is the contribution from the bound electrons and the second term the contribution from lattice oscillations which are treated as damped harmonic oscillators. The coefficient ϵ_{el} is constant in the THz frequency range. The sum extends over all lattice oscillations which couple to the electromagnetic field. The quantities f_i, Γ_i and s_i are the eigenfrequency, damping constant and oscillator strength of the lattice oscillation i respectively. For the electro-optic crystals such as ZnTe and GaP, a good description of $\epsilon(f)$ in the THz regime is obtained by restricting the sum to the lowest transverse-optical (TO) lattice oscillation [208]

$$\varepsilon(f) = \varepsilon_{el} + \frac{s_0 f_0^2}{f_0^2 - f^2 - i\Gamma_0 f}. \tag{4.79}$$

The complex index of refraction is given by taking the square root

$$n(f) + i\kappa(f) = \sqrt{\varepsilon(f)}. \tag{4.80}$$

4.10 Phase-matching and propagation of THz and laser pulses

The refractive index of ZnTe decreases with increasing wavelength in the optical regime. In the THz region below the TO resonance n increases with the frequency. The short THz and Ti:Sa laser pulses propagate with the group velocity [208]

$$v_g = \frac{c}{n}\left(1 + \frac{\lambda}{n}\frac{dn}{d\lambda}\right) = \frac{c}{\left(n + f\frac{dn}{df}\right)}, \tag{4.81}$$

which is in both cases lower than the phase velocity of the contributing harmonic waves. The phase and group velocities of THz frequencies (0.1-5.3 THz) propagating in ZnTe are shown in figure 4.10(a). For comparison also the optical group velocity at $\lambda = 0.8\ \mu$m is plotted. While at low frequency the THz pulse propagates with a somewhat higher speed than the laser pulse, there is a growing mismatch in the velocities when one approaches the TO resonance of 5.3 THz in ZnTe and 11 THz in GaP.

For ideal electro-optic sampling conditions the THz pulse and the laser pulse should propagate at the same speed. The difference in speed leads to a reduced time resolution. The electro-optic efficiency is characterised by a response function which depends on the THz frequency, f and the crystal thickness, d [208]

$$G(f,d) = \frac{2}{1 + n(f) + i\kappa(f)}\frac{1}{d}\int\limits_0^d \exp\left[2\pi i f z\left(\frac{1}{v_\phi(f)} - \frac{1}{v_g(f)}\right)\right]dz, \tag{4.82}$$

where $v_\phi(f)$ is the phase velocity at the THz frequency, f and v_g is the optical group velocity at the laser wavelength. The factor

$$A_{trans}\left(f\right) = \frac{2}{1 + n\left(f\right) + i\kappa\left(f\right)}, \tag{4.83}$$

is the frequency dependent transmission coefficient for the transition of the THz electric field from vacuum into the electrooptic crystal [208]. The electrooptic response function of ZnTe is shown in figure 4.10(b) for crystals of thickness 100 μm, 300 μm, and 1 mm. It is obvious that high THz frequencies can only be reached in sufficiently thin crystals. The TO resonance sets an upper limit of about 4.5 THz to the accessible frequency range.

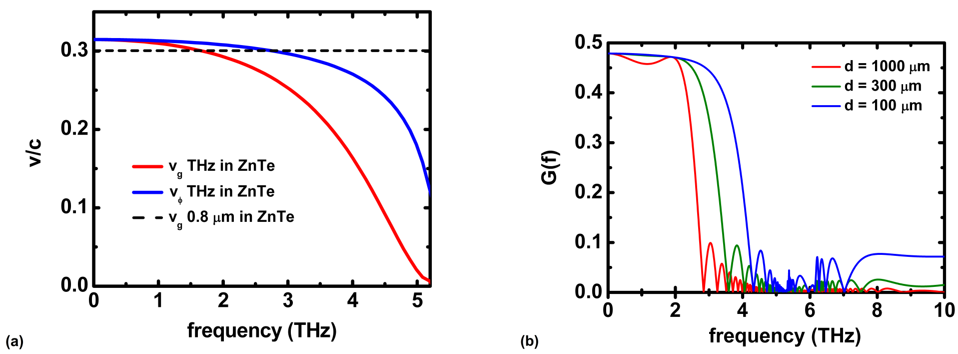

Figure 4.10: (a) The phase velocity, v_ϕ (blue curve) and group velocity, v_ϕ (red curve), of THz radiation in ZnTe. The black dashed line indicates the group velocity of 800 nm light in ZnTe. (b) The response functions for ZnTe crystals of varying thickness. The blue, green and red curves represent a 100 μm, 300 μm, and 1 mm thick crystal respectively.

4.11 Simulations of propagation of THz and optical light pulses in ZnTe

A more physical approach based on the framework of Casalbuoni *et al* [208] in which both the THz pulse and the optical laser pulses are propagated as wave packets through the EO crystal is now presented. The electric field at the position of the crystal has the time dependence we call $F_E(f)$ the Fourier transform of the electric field pulse, which in this special case can be computed analytically or, for more complicated distributions, by an FFT (Fast Fourier Transform) algorithm. At the interface between the vacuum and the EO crystal, some fraction of the incident THz wave is reflected, the remaining part is transmitted into the dielectric crystal. The amplitude transmission coefficient depends on frequency and is given by the expression

$$A_{trans}(f) = \frac{2}{n(f) + i\kappa(f) + 1}. \tag{4.84}$$

The Fourier component of the transmitted electric field pulse is

$$F_{trans}(f) = F_E(f)\frac{2}{n(f) + i\kappa(f) + 1}. \tag{4.85}$$

To propagate the THz pulse inside the EO material we subdivide the crystal into ten thin slices of thickness $\delta = d/10$. The Fourier component at slice j is given by [208]

$$F_{slice\_j}(f) = F_{trans}(f)\exp\left(i\frac{2\pi f}{c}n(f)d_j - \frac{2\pi f}{c}\kappa(f)d_j\right), \tag{4.86}$$

where $d_j = (j+0.5)\delta$ is the depth of slice j. The phase propagation is determined by the refractive index $n(f)$, the attenuation by the extinction coefficient $\kappa(f)$. The time profile of the pulse at slice j is then simply obtained by applying the inverse FFT to equation 4.86

$$E_j^{THz}(t) = IFFT\left[F_{trans}(f)\exp\left(i\frac{2\pi f}{c}n(f)d_j - \frac{2\pi f}{c}\kappa(f)d_j\right)\right]. \tag{4.87}$$

This framework is used in section 5.3 to model the time profile of the THz pulse as it evolves through a 300 μm thick ZnTe crystal. One can easily see that the pulse width increases with increasing depth in the crystal, and that oscillations gradually develop. These high frequency oscillations lag behind the main pulse since the THz refractive index grows approaching the TO resonance at 5.3 THz (see figure 4.9(b)). It must also be mentioned that the Ti:Sa probe laser pulse will change its shape as it traverses the EO crystal due to the non-linear optical refractive index variation across the pulse bandwidth (figure 4.9(a)) i.e. dispersion or chirp.

The detrimental effects of group velocity mismatch and pulse distortion are of course reduced by choosing a thinner crystal, but at the price of a lower detector signal. A quantitative analysis will be presented in the next section.

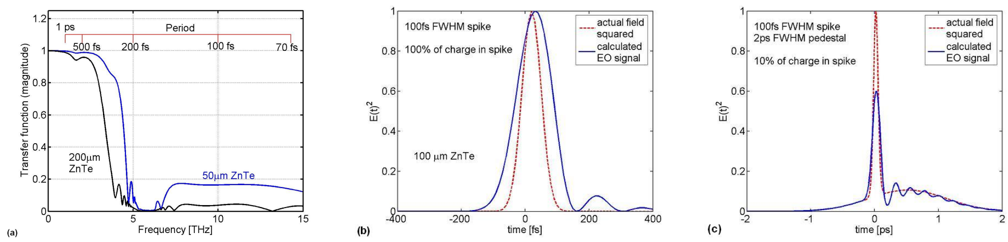

Figure 4.11: (a) The transfer function for a 200 μm and a 50 μm ZnTe crystal. (b) The calculated EO signal with no pedestal for a 50 μm thick crystal. (c) The calculated EO signal on top of a 5 ps pedestal.

4.12 Multiple reflections in ZnTe crystal

The THz pulse can undergo a reflection at the exit surface of the crystal, move back, and after a second reflection at the front surface, move again through the crystal in forward direction. This is sometimes referred to as the Fabry-Perot effect. The double-reflected pulse will be scanned by the laser if the laser pulse is delayed by the travel time $2d/v_{THz}$. The Fourier transform of the double-reflected THz pulse, just behind the front surface of the EO crystal, is given by

$$F_{double}(f) = F_{trans}(f) A_{ref}^2 \exp\left(i\frac{2\pi f}{c} n(f)(2d) - \frac{2\pi f}{c}\kappa(f)(2d)\right), \tag{4.88}$$

where $A_{ref} = [1 - n(f) - i\kappa(f)]/[1 + n(f) + i\kappa(f)]$ is the amplitude reflection coefficient. This second signal is much weaker, about 20% of the first peak, mainly due to the reflection coefficient which enters quadratically. The next reflection will produce a pulse at twice the delay but with a signal amplitude of only a few per cent of the main peak. This and even higher-order reflections will be easily lost in the noise. Also the laser pulse will undergo multiple reflections in the EO crystal. If the double-reflected laser pulse coincides with the double-reflected THz pulse one gets a contribution to the balanced detector signal at the position of the first main peak. This contribution is small since not only the THz pulse but also the laser pulse is attenuated by the double reflection. The effect can be avoided altogether if one uses a wedge-shaped EO crystal. The EO crystal then acts like a prism and deflects the direct laser beam by an angle of $(n-1)\alpha$ where α is the wedge angle and n the refractive index for laser light. The double-reflected laser beam will leave the EO crystal at a deflection angle of $(3n-1)\alpha$ and can therefore be easily separated from the direct laser beam.

$$\Gamma^*(\omega) = \Gamma_{THz}(\omega)\, T_{\text{in}}(\omega)\, T_{crystal}(\omega), \tag{4.89}$$

with $T_{in}(\omega) = 2/(1+n_{THz})$ the crystal surface transmission. The crystal function $T_{crystal}(\omega)$ incorporates the THz propagation $\exp[-(i\omega z n_{THz})/c]$ (including absorption and dispersion) with respect to the laser pulse $\exp[(i\omega z n_{gr})/c]$, resulting in

$$\begin{aligned} T_{crystal}(\omega) &= \int_0^L \exp\left(-i\frac{\omega}{c} z n_{THz}\right) \exp\left(i\frac{\omega}{c} z n_{gr}\right) dz \\ &= \frac{\exp\left[\frac{i\omega L}{c}(n_{gr} - n_{THz})\right] - 1}{\frac{i\omega}{c}(n_{gr} - n_{THz})}. \end{aligned} \tag{4.90}$$

4.13 Jones Matrix Formalism

A powerful matrix method called Jones calculus exists [209], which can be used to calculate the field properties of light propagating through an arbitrary array

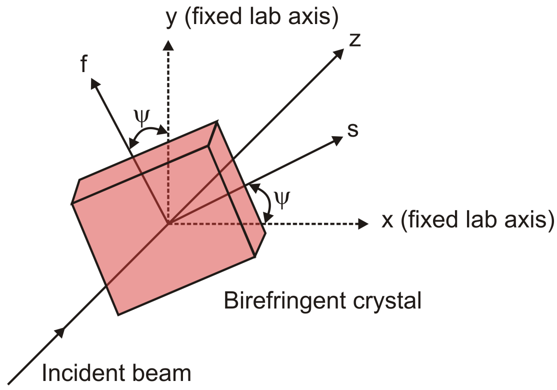

Figure 4.12: The birefringent crystal is rotated at an angle, Ψ around the z axis. The fast and slow principal dielectric axes are denoted by f and s respectively. The x and y axes are fixed in the laboratory frame (figure adapted from [12]).

of polarisers, retardation plates and electrooptic crystals. When each element is considered individually the polarisation state of the transmitted light can be attained by simple means. However, when the optical system consists of many such elements orientated at a different azimuthal angle, the computation of the transmitted beam becomes convoluted. The Jones matrix for a linearly polarised light field can be written as [12]

$$E(t) = \begin{bmatrix} E_x(t) \\ E_y(t) \end{bmatrix} = \begin{bmatrix} E_{0x}\mathrm{e}^{i\phi_x} \\ E_{0y}\mathrm{e}^{i\phi_y} \end{bmatrix}. \tag{4.91}$$

With regard to figure 4.12 it is shown that the x, y and z axes are fixed laboratory axes, and that a light beam normally incident on a crystal along the z-axis with a polarisation state can be expressed by the Jones column vector

$$\mathrm{V} = \begin{pmatrix} V_x \\ V_y \end{pmatrix}. \tag{4.92}$$

Here V_x and V_y are complex numbers representing the complex field amplitudes along x and y and respectively. In order to determine how the light propagates in the crystal, it is necessary to resolve the linear combination of fast and slow eigenwaves in the crystal. This can be realised by the coordinate transformation [12]

$$\begin{pmatrix} V_s \\ V_f \end{pmatrix} = \begin{pmatrix} \cos\psi & \sin\psi \\ -\sin\psi & \cos\psi \end{pmatrix} \begin{pmatrix} V_x \\ V_y \end{pmatrix} \equiv R(\psi) \begin{pmatrix} V_x \\ V_y \end{pmatrix}. \tag{4.93}$$

V_s and V_f are the slow and fast components of the polarisation vector $\mathbf{V}$ respectively. The angle between the slow axis and the horizontal is Ψ. These two components are eigenwaves of the retardation plate and will propagate with their own phase velocities, and on account of this difference in phase velocity, the two components undergo a different phase delay in passage through the crystal. This retardation changes the polarisation state of the emerging beam. The polarisation state of the emerging beam in the coordinate frame of the crystal can therefore be expressed as a function of the refractive indices of the fast, n_f, and slow, n_s, eigenwaves

$$\begin{pmatrix} V_s' \\ V_f' \end{pmatrix} = \begin{pmatrix} \exp\left(\frac{-in_s\omega l}{c}\right) & 0 \\ 0 & \exp\left(\frac{-in_f\omega l}{c}\right) \end{pmatrix} \begin{pmatrix} V_s \\ V_f \end{pmatrix}, \tag{4.94}$$

here l is the thickness of the plate and ω is the angular frequency of the light beam. Important to note is that the phase retardation Γ is a measure of the relative change in phase, between the modes along the fast and slow axes and not the absolute change. Typically, the birefringence of a crystal retardation plate is small meaning that the absolute phase change caused by the crystal could be hundreds of times greater than the relative phase retardation. The mean absolute phase change can be shown as [12]

$$\phi = \frac{1}{2}\left(n_s + n_f\right)\frac{\omega l}{c}. \tag{4.95}$$

We can now express equation 4.94 in terms of ϕ and Γ

$$\begin{pmatrix} V_s' \\ V_f' \end{pmatrix} = e^{-i\phi} \begin{pmatrix} e^{\frac{-i\Gamma}{2}} & 0 \\ 0 & e^{\frac{i\Gamma}{2}} \end{pmatrix} \begin{pmatrix} V_s \\ V_f \end{pmatrix}. \tag{4.96}$$

Now by transforming back into the fixed laboratory frame from the crystal coordinate system, we attain the Jones vector of the polarisation state of the emerging beam in the x,y coordinate frame

$$\begin{pmatrix} V_x' \\ V_y' \end{pmatrix} = \begin{pmatrix} \cos\psi & -\sin\psi \\ \sin\psi & \cos\psi \end{pmatrix} \begin{pmatrix} V_s' \\ V_f' \end{pmatrix}. \tag{4.97}$$

We can now merge equations 4.93, 4.96 and 4.97 together and write the transformation due to the retardation plate as

$$\begin{pmatrix} V_x' \\ V_y' \end{pmatrix} = R(-\psi)W_0R(\psi) \begin{pmatrix} V_x \\ V_y \end{pmatrix}, \tag{4.98}$$

where $R(\psi)$ is the rotation matrix shown in equation 4.93 and W_0 is the Jones matrix of equation 4.96 for the retardation plate which can be expressed as

$$W_0 = e^{-i\phi} \begin{pmatrix} e^{\frac{-i\Gamma}{2}} & 0 \\ 0 & e^{\frac{i\Gamma}{2}} \end{pmatrix}. \tag{4.99}$$

It can now be shown that a retardation plate, characterised by its phase retardation, Γ and its azimuth angle, ψ is represented by the product of three matrices [12]

$$W(\psi, \Gamma) \equiv W = R(-\psi) W_0 R(\psi) \tag{4.100}$$

$$W = \begin{pmatrix} e^{-\frac{i\Gamma}{2}} \cos^2(\psi) + e^{-\frac{i\Gamma}{2}} \sin^2(\psi) & -i \sin\left(\frac{\Gamma}{2}\right) \sin(2\psi) \\ -i \sin\left(\frac{\Gamma}{2}\right) \sin(2\psi) & e^{-\frac{i\Gamma}{2}} \sin^2(\psi) + e^{-\frac{i\Gamma}{2}} \cos^2(\psi) \end{pmatrix}. \tag{4.101}$$

The Jones matrix of a waveplate is a unitary matrix, thus a polarised beam propagating through a waveplate is described mathematically as a unitary transformation. Thus, if the polarisation states of two beams are mutually orthogonal, they will emerge from an arbitrary waveplate mutually orthogonal due to the invariant properties under unitary transformations.

Considering an ideal, thin plate polariser positioned with its transmission axis parallel to the laboratory x axis, we can express the Jones matrix as

$$P_0 = e^{-i\theta} \begin{pmatrix} 1 & 0 \\ 0 & 0 \end{pmatrix}, \tag{4.102}$$

where θ denotes the absolute phase accumulated due to the finite optical thickness of the waveplate. As before we can state the Jones matrix of a polariser rotated by an angle ψ from the x axis about z as

$$P = R(-\psi) P_0 R(\psi). \tag{4.103}$$

It can therefore be stated neglecting the absolute phase, θ that polarisers orientated so as to transmit light with the electric field vectors parallel to the x and y axis respectively can be expressed as

$$P_x = \begin{pmatrix} 1 & 0 \\ 0 & 0 \end{pmatrix}, P_y = \begin{pmatrix} 0 & 0 \\ 0 & 1 \end{pmatrix}. \tag{4.104}$$

It is now possible to find the effect of an arbitrary train of retardation plates on the state of polarised light, we simply multiply the Jones vector of the incident beam by the ordered product of the matrices of the various elements given by equation 4.100.

If we now consider a light field represented by equation 4.92, the intensity is proportional to

$$I = |V_x|^2 + |V_y|^2 \tag{4.105}$$

and if the output beam is given by

$$\mathrm{V} = \begin{pmatrix} V_x' \\ V_y' \end{pmatrix}, \tag{4.106}$$

then the transmissivity of the optical system can be calculated using

$$T_{os} = \frac{|V_x'|^2 + \left|V_y'\right|^2}{|V_x|^2 + |V_y|^2}. \tag{4.107}$$

Using the Jones Matrix framework the electro-optic effect can be modelled accurately. As equation 4.76 implies that the larger the E-field of, for example a passing electron bunch or radiation field, the more birefringence is induced in an electrooptic crystal. Thus replacing the $\Gamma/2$ term in equation 4.101 with arbitrary phase retardation, ϕ we can realise what is close to the electro-optic situation. The retardation is essentially proportional to the electric field of a passing electron pulse or radiation field at any given instant in time that is, $\phi(t) \propto E_{THz}(t)$. It is now clear that the electric field of a propagating electron bunch or radiation field will impart different phase retardations on a suitable probe beam, thus rotating the polarisations by different amounts depending on the field amplitude. This can then be observed as an intensity modulation using ellipsometry.

Chapter 5

Experimental results

5.0.1 Introduction

Rapid advances of terahertz sources and applications have been observed in recent years [210]. The availability of ultrafast femtosecond laser systems has lead to the realisation of table-top laser based THz sources. In order to characterise these THz pulses in the frequency and time domains electro-optic sampling (EOS) has become a widely used technique. The first demonstration of EOS was performed in 1995 by Wu and Zhang [211]. The EOS method relies on the Pockels effect inside an electro-optic crystal whereby a THz pulse is generated via some mechanism for example via a synchrotron source [212, 213], plasma wave generation [214, 215, 216], modulated electron beams [217], Linear mode conversion [218, 219]. The THz generations methods presented in this thesis rely on using a photoconductive antenna [220] and by the transition radiation produced from an electron bunch traversing a dielectric discontinuity [108]. The generated THz radiation is then propagated through an electro-optic sampling crystal along with a probe pulse or gate pulse which can be either short or long [221] relative to the THz pulse depending on the desired measurement method. Moreover, such techniques have been employed to retrieve 2D spatial mapping of the THz beams [222, 223].

Traditional methods of characterising electron bunch durations have involved using streak camera systems to detect light pulses generated by the electrons at a scintillating target screen. This method has been shown to have a resolution limit of 1.6 ps FWHM [224]. In other methods the electron beam is passed through a thin foil, and then the electron bunch profile is reconstructed by measuring the spectrum of the coherent part of the emitted transition radiation (usually in the THz-frequency range), and Fourier transforming this to the time domain

[197]. This method relies on the Kramers-Kronig relations for the reconstruction process and requires an extrapolation of the measured spectrum to zero frequency. Furthermore, although an asymmetric pulse shape can be obtained, the method cannot distinguish between the leading edge and the trailing edge of the pulse.

More recently scanning delay line techniques have been employed where a short probe pulse ($\simeq$ 10–100 fs) can be used to sample and reconstruct the THz field over many laser shots [225]. This has been demonstrated by Yan *et al* [225] who successfully reconstructed the Coulomb electric field of an electron beam from the FELIX institution. This was achieved by scanning a short probe laser pulse ($\tau_p \ll \tau_{THz}$) across the temporal envelope of the THz pulse inside a non-linear birefringent crystal. Implementation of this method requires an advanced knowledge of the electron bunch distribution and is subject to large shot-to-shot fluctuations in the electron beam quality. On the other hand single-shot methods, utilise a chirped pulse of considerably longer duration than the THz pulse ($\tau_p \gg \tau_{THz}$). During this technique, the chirped laser pulse and the THz pulse are temporally synchronised so that the chirped laser pulse completely envelops the THz pulse. Each wavelength component of the chirped pulse then plays the role of a short probe pulse hence the measurement can be done using a single laser shot [110, 192].

This chapter presents results on the production and detection of THz pulses produced from laser wakefield accelerated electron bunches. The CTR emitted by an electron bunch passing through the plasma-vacuum boundary is electro-optically sampled in a single laser shot to resolve the temporal structure of electron bunches [110]. The electro-optic measurements presented in this chapter rely on the transition radiation, which is essentially a 'blueprint' of the temporal profile of the electron bunch. The Pockels effect in a ZnTe crystal modifies the polarisation state of the sampling chirped probe pulse due to the E-field of the CTR. The modulated optical pulse can then be analysed using a visible spectrometer or frequency converted and measured using a cross-correlator to yield information on the bunch length characteristics. This single-shot electro-optic cross correlation technique was first developed at Strathclyde [192] and has since then been employed by other institutions [73, 226, 227].

5.0.2 Charactersiation of the ZnTe crystal

This ZnTe crystal used in the experiment had a specific $\langle 110 \rangle$ normal surface, but has no marking defining the rotational orientation within the (110). It is therefore necessary to determine the correct rotational orientation. A GaAs emitter

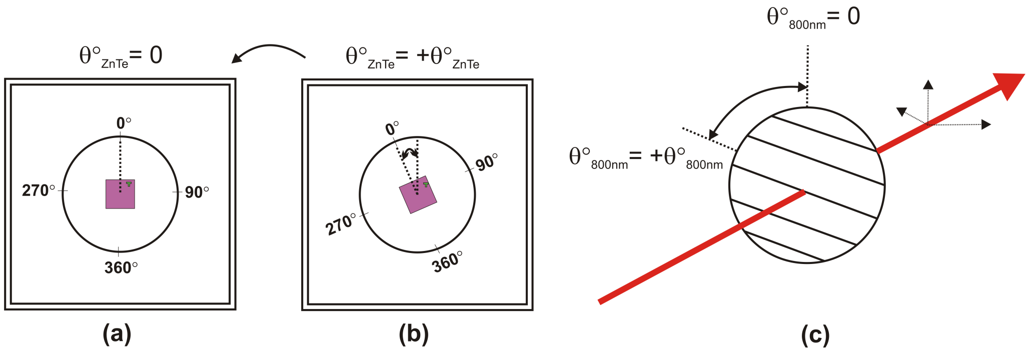

Figure 5.1: Definition of optical polarisation angle and ZnTe crystal orientation angle.

was used to generate THz radiation polarised in the horizontal plane, and the THz signal measured as a function of both crystal orientation and optical probe polarisation.

Using a waveplate and a cube polariser, the THz signal is measured using the balanced detection set-up method. In this method the quarter waveplate and the cube polariser separate orthogonal polarisations, and the THz signal is taken as the difference in intensity between these two polarisations. The ZnTe crystal was mounted in a rotational mount as shown below in figure 5.1.

In order to achieve the best electro-optic signal for the electron bunch duration measurements, the optic axis of a ZnTe crystal had to be experimentally identified prior to experimentation. Physically, this is the angle at which the ZnTe crystal should be rotated, relative to the polarisation vector of the THz electric field in order to gain the maximum phase retardation (birefringence) hence largest electro-optic signal. This characterisation was carried out using the medium power TOPS 1 kHz laser system at Strathclyde. The experimental set-up for this is depicted in figure 5.2 and figure 5.4.

In this setup a biased GaAs wafer was used as a THz radiation source. To generate THz pulses, short laser pulses of visible light ($\sim$ 800 nm, $\sim$ 45 fs) are incident on a segment of biased semiconductor wafer. These wafers can be as large as 60 mm with laser spots of equal size allowing for large surface area emission and hence higher THz powers. The applied bias voltage can vary from between 1-10 kV/cm. When the laser light is absorbed it creates electron-hole pairs in the GaAs that are subsequently accelerated in the large bias field. The promotion of electrons in to the valence band via laser excitation changes the semiconductor into a conductor on the timescale of the laser pulse and in conjunction with the bias field causes a current surge through the semiconductor. The semiconductor material GaAs is particularly good at absorbing 800 nm light due to its direct

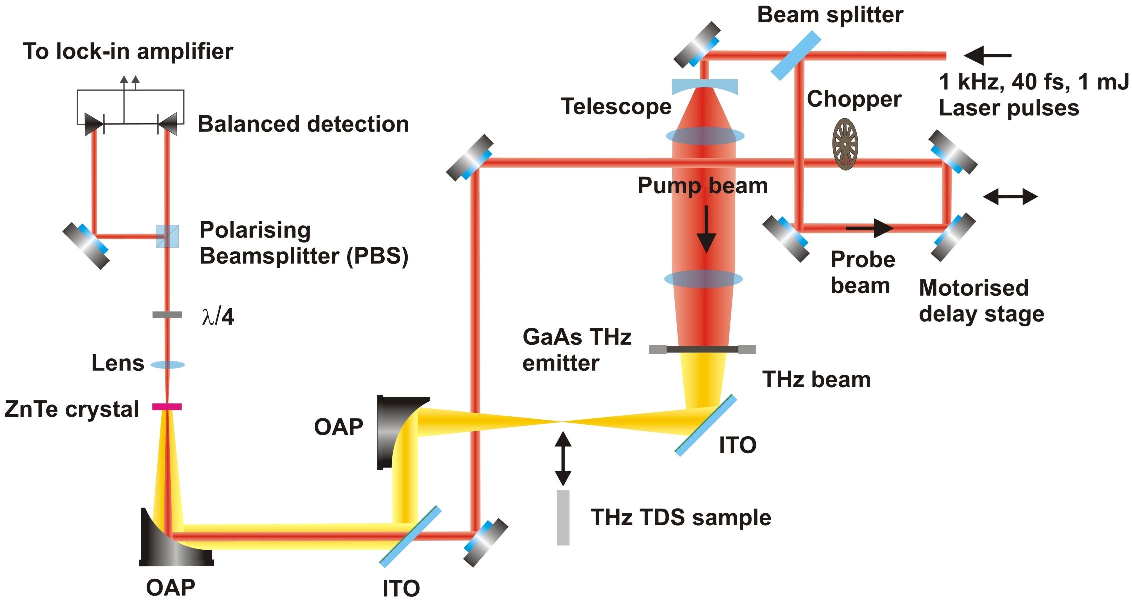

Figure 5.2: The experimental set-up used to characterise ZnTe crystals and perform THz spectroscopy measurements using the TOPS 1 kHz laser at Strathclyde.

band-gap energy of 1.42 eV (870 nm). Any accelerating charge will radiate in accordance with Maxwell's equations. Thus at a distance much greater than the THz wavelength (i.e. in the far-field) we can relate the electric field to the transient photo-current, $J(t)$, by

$$E(t) \propto \frac{\partial J(t)}{\partial t}. \tag{5.1}$$

The antenna consists of a 60 mm diameter by 500 μm thick segment of $\langle 110 \rangle$ low-temperature grown GaAs wafer (figure 5.5) with two wire electrodes bonded with silver loaded epoxy resin to the its surface. A 15 kV D.C. bias voltage was applied across the electrodes of the antenna and the rear surface was illuminated with a 40 mm diameter laser beam (λ = 800 nm, E = 500 μJ/pulse, τ_L = 45 fs). The photo-carriers, upon creation, are accelerated in the surface field generated by the 15 kV bias. The current through the antenna rises sharply after injection of the photo-carriers into the valence band by the 800 nm laser light and then decays with a constant related to the carrier lifetime ($\sim$ 1 ps) of LT-GaAs. The transient photo-current radiates into free space according to equation 5.1 which means the time varying current results in the emission of electromagnetic radiation, with the electric field being proportional to the time derivative of the current density. This implies that the main peak of the THz pulse should closely match that of the pump pulse length ($\sim$ 50 fs), however in practice the minimum pulse duration

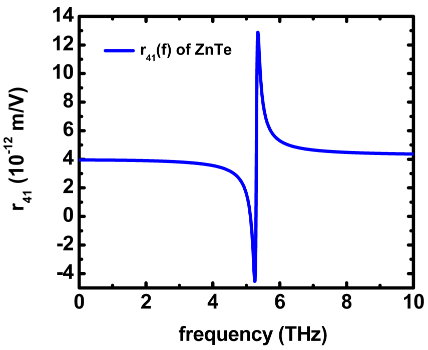

Figure 5.3: The electro-optic coefficient function for a ZnTe electrooptic crystal.

of a THz pulse produced from a photo-conductive antenna is around 500-600 fs. This is because of dynamical processes such as scattering and dispersion of the THz pulse in the GaAs which significantly broadens the THz pulse.

The electric field of the THz pulse induces birefringence - a change in the refractive index along one axis of the EOS crystal, n_e, because of the Pockels effect. The value of n_e will be modulated by an amount that depends on both the strength and direction of the THz electric field. The angle between the THz pulse polarisation and the total phase change is linearly dependent on the length of the crystal, l, refractive index of the probe beam, n_0, the electrooptic co-efficient, r_{41} (figure 5.3) at the probe wavelength, λ.

These parameters remain static under experimental conditions and it is only the THz electric field, E_{THz} that varies. This implies that the EOS method should have a flat response, however in practice phonon-bands cause deviations in the response functions. Phonon bands are low frequency absorption bands that can be very large and often occur in the THz frequency range in EO crystals. For example, the first major phonon band of ZnTe is at 5.3 THz with two weaker bands at 1.6 THz and 3.7 THz. This means that ZnTe has a very good response up to around 3 THz (larger bandwidth for thinner crystals) after which the 5.3 THz absorption band becomes significant. Phonon bands also cause strong variations in the THz refractive index around phonon resonance which is responsible for THz pulse dispersion resulting in poor phase-matching with the probe beam.

During this experiment the probe pulse was initially set to be polarised at 45 degrees relative to n_e in order to experience the maximum EO effect, hence the largest signal. The response of the electro-optic crystal can be assumed to be instantaneous relative to the pulse durations of the THz pulse and even the probe pulse. The magnitude of the birefringence effect is linearly proportional to the electro-optic co-efficient, r_{41}. A quarter wave plate followed by a polarising

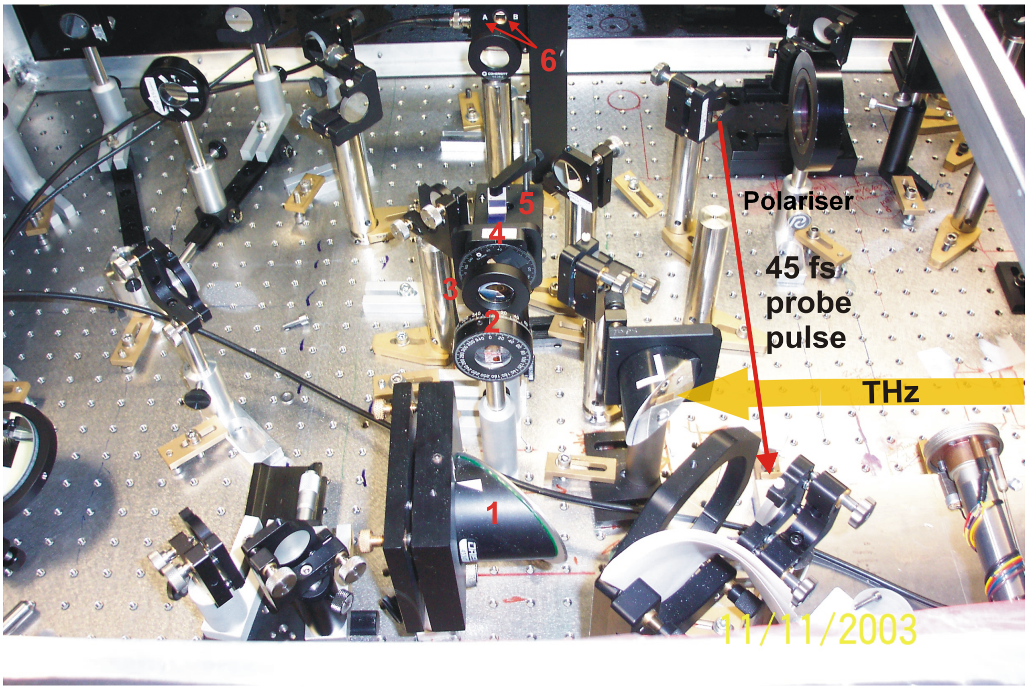

Figure 5.4: The THz characterisation experimental set-up using the TOPS 1 kHz laser at Strathclyde: 1. The off axis parabolic mirror (OAP) to focus the THz and probe beam onto the electrooptic sampling crystal (ZnTe). 2. The ZnTe detection crystal on a rotational mount. 3. Lens to collimate probe beam. 4. A Quarter Wave-Plate (QWP). A Polarising Beam-Spliter (PBS). 6. Two balanced detection diodes (A + B). The optical polarisation was altered using a polariser, positioned as shown. Reflection from the silver mirrors causes a polarisation change through inversion in the vertical plane. Allowing for this, the polarisation at the ZnTe crystal (θ_4) is related to the polarisation after the polariser by: θ_4 = -θ_1 = 180-θ_1

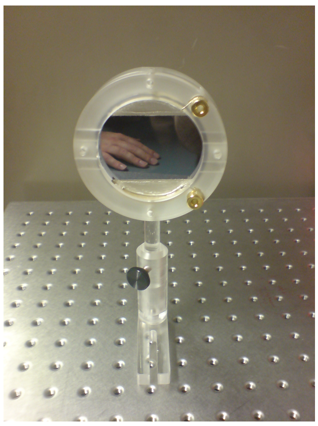

Figure 5.5: The GaAs wafer used to generate $\sim$ 0.5 ps THz pulses. The silver epoxy electrodes are seen at the top and bottom of the wafer which are connected to two gold plated electrodes to apply a p.d $\cong$ 12 kV.

beam splitter and a pair of balanced diodes resolves the change in the polarisation state of the probe pulse. The quarter wave plate has its axis at 45 degrees to the initial probe polarisation to create circularly polarised light when the probe polarisation is unchanged (i.e. no THz electric field). When this light then propagates through a polarising beam splitter the beam splits 50/50 into orthogonal s and p components which are directed onto two diodes A and B (figure 5.4). The intensity values of each incident beam are therefore equal. The diodes are wired to produce a zero output voltage when the intensity signal is the same and a positive or negative signal when the light intensity on one or the other is larger. This technique is known as balanced detection, as under normal circumstances the photodiodes are seen to be balanced with equal intensity amplitudes incident on A and B. However, in the presence of an external electric field (e.g. E_{THz}) on the EOS crystal the rotation of the polarisation state of the probe is detected as an relative intensity modulation between the two photodiodes.
From the modulation of the balanced signal, i.e. the difference between the signal of the diodes, A-B, we attain the relationship between the phase shift (retardation parameter) induced in the ZnTe detection crystal

$$|A|^2 - |B|^2 \propto \sin(\Gamma), \tag{5.2}$$

where A and B are the light amplitudes in detectors A and B respectively. To determine the peak electric field of the THz we can simply use the relation,

$$E_{THz} = \frac{\lambda \sin(\Gamma)}{2\pi n_0^3 r_{41} d}. \tag{5.3}$$

The results of the ZnTe crystal characterisation are shown graphically as polar plots in figure 5.6(a). The electro-optic signal was measured as a function of the ZnTe crystal angle through one complete revolution (360°) for various polarisations of the probe beam. These results show that assuming a horizontally polarised probe beam the optimum electro-optic signal will be observed at a crystal angle of 220°. Thus, the optical axis that would yield the largest electrooptic signal was defined and could be aligned to an arbitrary polarised electric field to be sampled.

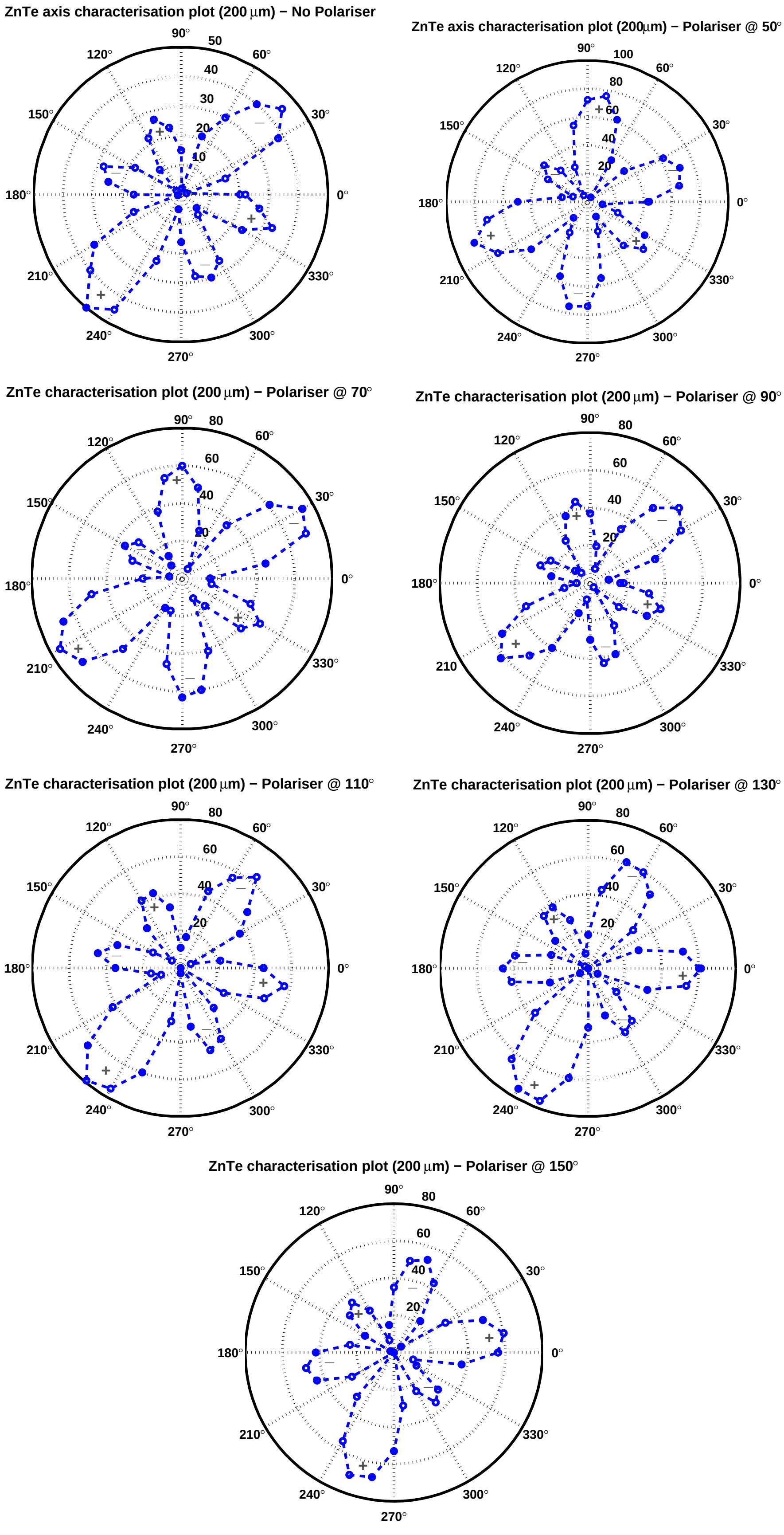

Figure 5.6: The characterisation of the optics axis of the 200 μm ZnTe crystal: Polar plots showing the electro-optic signal as a function of the ZnTe crystal rotation for various probe beam polarisations - (a) No polariser (horizontally polarised probe beam). Polariser set to (b) 50° (c) 70° (d) 90° (e) 110° (f) 130° (g) 150°

5.1 Electron bunch measurements with the Astra laser

Laser-plasma based electron accelerators are predicted to be a source of ultrashort electron bunches with pulse duration of only a few femtoseconds [75, 44] and peak currents of up to 20 kA, however, their true pulse duration has never been measured in a single-shot experiment. This chapter presents measurements of such ultrashort laser-generated bunches by means of electro-optic sampling of the THz transition radiation carried out using the ASTRA laser. The primary goals of the experiment were to characterise the energy spectra of electron bunches produced from wakefields, to measure the bunch charge of the electron bunches and ultimately to measure the temporal profile of the electron bunches. These temporal measurements can be done in the frequency domain or directly in the time domain.

In the 'chirped-pulse spectrometer method' (figure 5.8(a)) a short probe pulse is stretched using a grating pair to a pulse which has a linear chirp and duration longer than that of the electron bunch. When the electric field of an electron bunch and the chirped optical pulse co-propagate in the electro-optic crystal, the various wavelength components of the chirped pulse passing through the crystal obtain different phase retardations, corresponding to different portions of the local THz electric field. By placing the crystal between crossed polarisers, the phase retardation in the wavelength spectrum is converted into an intensity modulation. Thus, the time profile of the local electric field of the electron bunch is linearly encoded onto the wavelength spectrum of the optical probe beam. This wavelength spectrum is then dispersed in a spectrometer and recorded in a single shot with a linear diode array or a CCD camera. This is shown in figure 5.8(a).

The spectral encoding technique is however, subject to a fundamental time resolution limit due to the intrinsic coupling between amplitude modulations and the optical carrier spectrum [192]. Additional spectral modulations are thus generated, and are indistinguishable from the desired spectral modulation. This chapter presents a novel method developed at Strathclyde to temporally characterise THz pulses in a single laser shot [192]. The technique is based on non-collinear cross correlation of an amplitude modulated chirped pulse with a short probe laser pulse and is illustrated in figure 5.8(b).

This method overcomes the 'side-band' time resolution limit of spectral encoding method by measuring the intensity modulated chirped pulse directly in the time domain with the additional advantage that knowledge of the optical chirp is

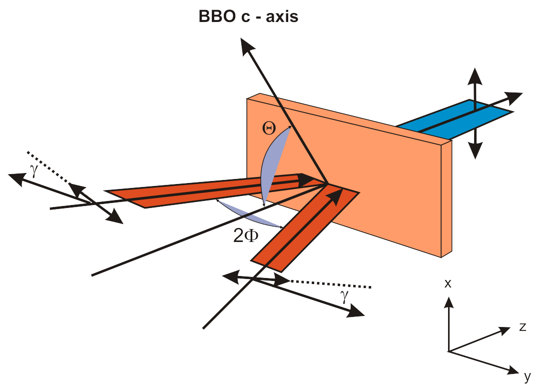

Figure 5.7: The BBO crystal geometry relative to the 1 ω laser probe beams for phasematching.

not required. This technique has been termed the single-shot 'chirped-pulse cross correlation' method. The chirped pulse carrying the modulation due to the field of the electron bunch is cross correlated with a part of the original optical pulse which has been split off before the optical stretching. Single-shot cross-correlation is based on the temporal to spatial conversion that occurs through the spatial overlap of non-collinear beams in a second-harmonic crystal [228]. Figure 5.7 shows the BBO crystal and beam geometry for correct phase-matching.

The temporal window achievable using this cross-correlation technique is given by [192]

$$\tau = 2D\sin(\Phi)/c \tag{5.4}$$

where D is the thickness of the BBO crystal and Φ is the half angle between the two IR beams being overlapped in the BBO crystal.

Autocorrelation of ultra-fast optical pulses is based on the time-to-space conversion that occurs through the spatial overlap of non-collinear beams in a SHG crystal. Using cross correlation of the chirped-pulse envelope with the transform-limited optical pulse rather than autocorrelation both provides a direct measure of the envelope and reduces the intensity required in the chirped pulse for second-harmonic generation (SHG). To increase the intensity available for SHG, a cylindrical lens gave a line focus of the chirped beam on a β-barium borate (BBO) crystal. In many THz applications there is a requirement for both high temporal resolution and a several-picosecond measurement window, which in principle one can obtain simply by using larger beam size. For our measurements the beam size and hence the temporal window, will be limited only by the dimensions of the BBO crystal.

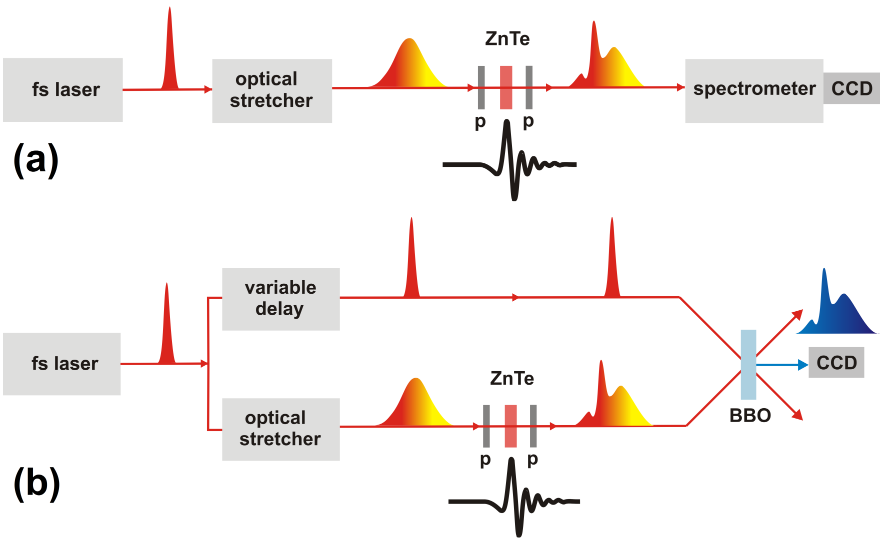

Figure 5.8: (a) The chirped pulse spectral encoding technique (frequency domain). (b) The chirped pulse cross-correlation technique (time domain).

5.1.1 Electron energy measurements

The laser system used for the production of the electron bunches was the ASTRA system at the Rutherford Appleton laboratory. The main specifications of this laser have already been illustrated in figure 3.1. The experimental set-up is depicted in figure 5.25. The 600 mJ pump beam of the ASTRA 45 fs laser pulse was used to accelerate electrons in a gas jet analogous to the experiments presented in chapter 2 [1]. The main drive laser was aligned over the gas jet by setting an expanded visible green diode laser collinear to the main infrared drive beam. This is illustrated in figure 5.9.

The electron-bunch energy spectrum was resolved using an in-house built electron spectrometer of which the dimensions and design are shown in figure 5.10-5.11. An electromagnet with variable current allowed control of the deflection of the electrons. This was used in conjunction with Fuji image plates (IP) to attain the electron energy spectrum. The image plates used were the commercially available Fuji BAS MS2325 type. These reusable radiation detectors produce an image of the area where the electrons pass through the plate via photo-stimulated luminescence. The image plates contain a 100 μm layer of the luminescent material, BaFBr:Eu^{2+}. When the accelerated electrons pass through this layer they submit energy to the europium ions, which are then excited into a metastable state. This effectively stores a dormant image of the electron beam in the plate. In order to extract the information the image plates are inserted into an Fuji BAS1800II image plate reader. This scans a helium neon laser across the plate which further

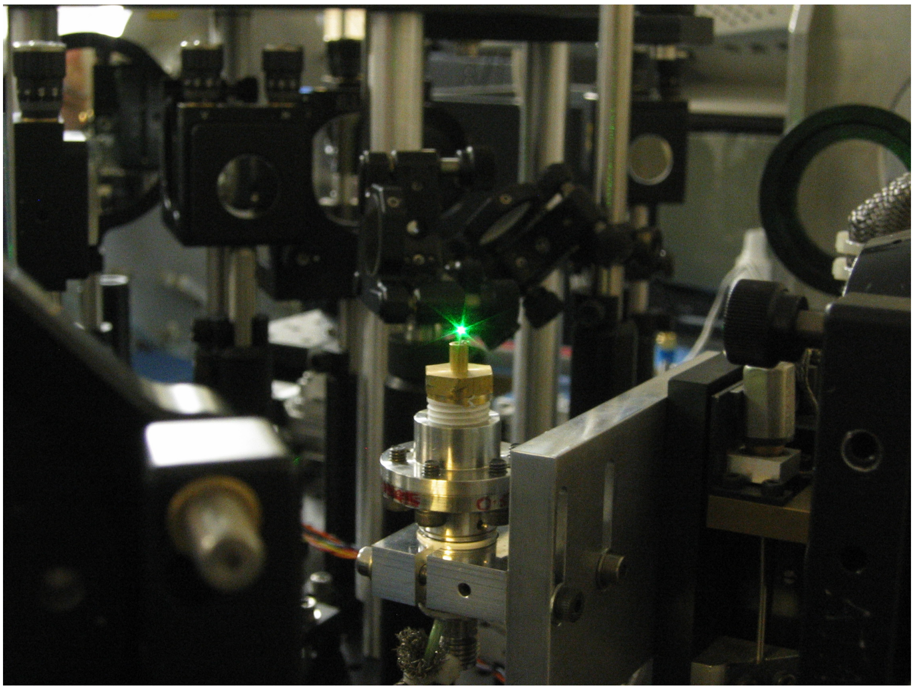

Figure 5.9: The focal spot of the green diode alignment laser positioned over the gas jet. The expanded alignment laser was set to be collinear to the main infrared drive beam and was used to align the main drive beam.

excites the europium ions into a non-metastable state. As the ions relax from this state they emit photons which are collected in a light guide and measured by a photomultiplier. This converts the optical signal into an electronic one which is then read out by the image plate reader software and integrated to obtain the electron energy spectra.

The on-axis electron energy spectrometer design used is conventional. The accelerated electrons pass through a magnetic field region which deflects them away from their axis of propagation (figure 5.12). This is because of the Lorentz force acting on the electrons due to the external magnetic field, i.e.,

$$\frac{d\mathbf{p}}{dt} = \frac{q}{\gamma m_e} p \times \mathbf{B}. \tag{5.5}$$

In the following, we assume the electron is traveling in the z direction and the magnetic field is in the x direction. For a uniform magnetic field within a circular region of radius r_b with zero field outside this region given by

$$\begin{aligned} \mathbf{B}_x(r) &= B_{\max}\hat{\mathrm{x}} \qquad \mathrm{r} \leq \mathrm{r_b}, \\ &= 0 \qquad\qquad \mathrm{r} > \mathrm{r_b}, \end{aligned} \tag{5.6}$$

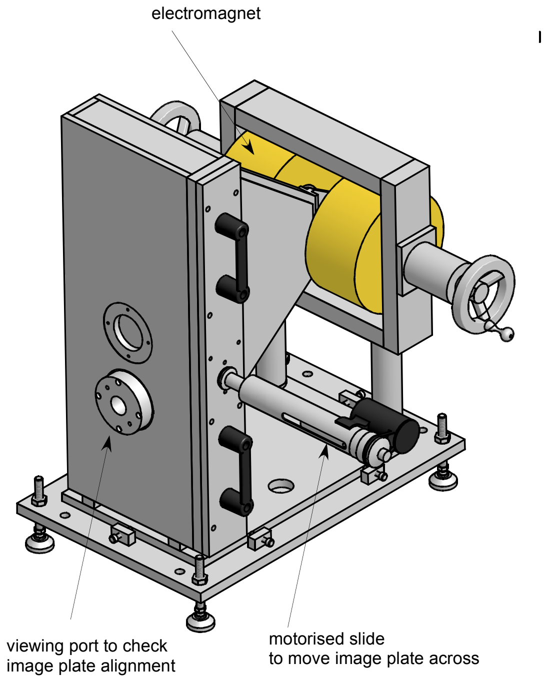

Figure 5.10: The electron spectrometer constructed at the Rutherford Appleton laboratory. The image plate rack holds 4 plates allowing for 4 laser shots to be taken before development of the plates. After each shot a new plate is translated into the electron beam axis using the motorised slide. Correct alignment can be confirmed by looking through the viewing port. (Image courtesy of B.Fell, Rutherford Appleton Laboratory.)

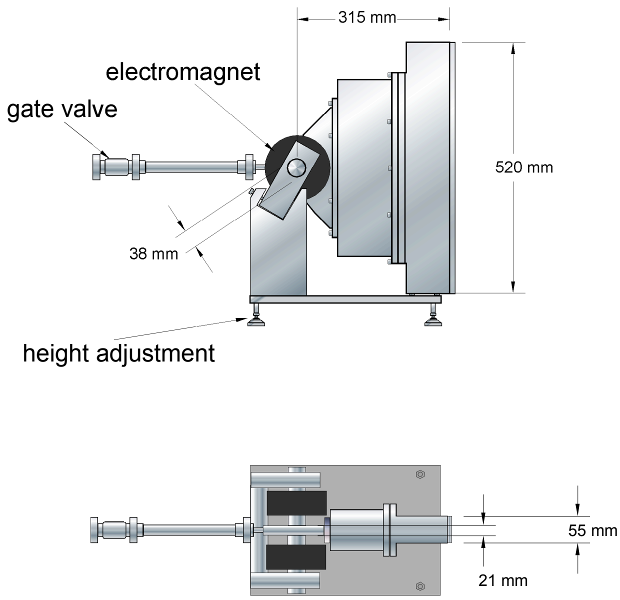

Figure 5.11: The electron spectrometer constructed at the Rutherford Appleton laboratory. (Image courtesy of B.Fell, Rutherford Appleton Laboratory.)

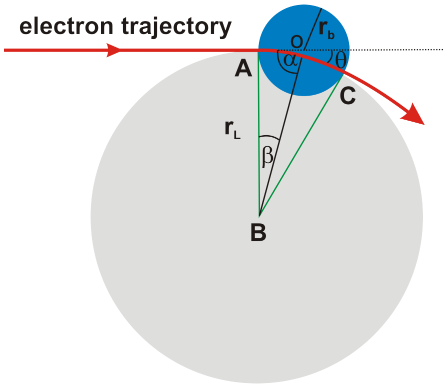

Figure 5.12: The electron trajectory in an ideal magnetic field.

there is an analytical solution for the angular deflection of electrons passing through this field. Figure 5.12 indicates the electron trajectory and the magnetic field orientation used in this calculation. The path of a relativistic electron within the magnetic field is the Larmor orbit in the $\hat{z} - \hat{y}$ plane having a radius given by [229]

$$r_L = \frac{|\mathrm{p}|}{eB_{\mathrm{max}}}, \tag{5.7}$$

where $|\mathrm{p}|$ is the electron momentum. By considering similar triangles (OBA and OBC), we can see that that the angle of deflection, θ, is related to the angle, α by

$$2\alpha + \theta = \pi. \tag{5.8}$$

Since the angle α is related to the magnetic field radius and the Larmor radius through

$$\tan\alpha = \frac{r_L}{r_b}, \tag{5.9}$$

it follows that the angular deflection of an electron with momentum $|p|$ is

$$\begin{aligned} \tan(\theta/2) &= r_b/r_L \\ &= eB_{\mathrm{max}} r_b/|\mathrm{p}|. \end{aligned} \tag{5.10}$$

The dispersion of the magnet changes linearly with the product of the field radius and field strength $r_b B_{max}$. Thus an electron spectrometer capable of measuring high energy electrons can be constructed either by having a small region of high magnetic field or a larger region of smaller magnetic field. This is particularly useful as it is not possible to increase B_{max} indefinitely due to saturation effects in the material of the magnet pole pieces. To measure high energy electrons it is therefore necessary to use magnets with large diameter pole pieces.

Figure 5.13(a) - 5.13(d) shows plots of the best electron spectra attained during experiments.

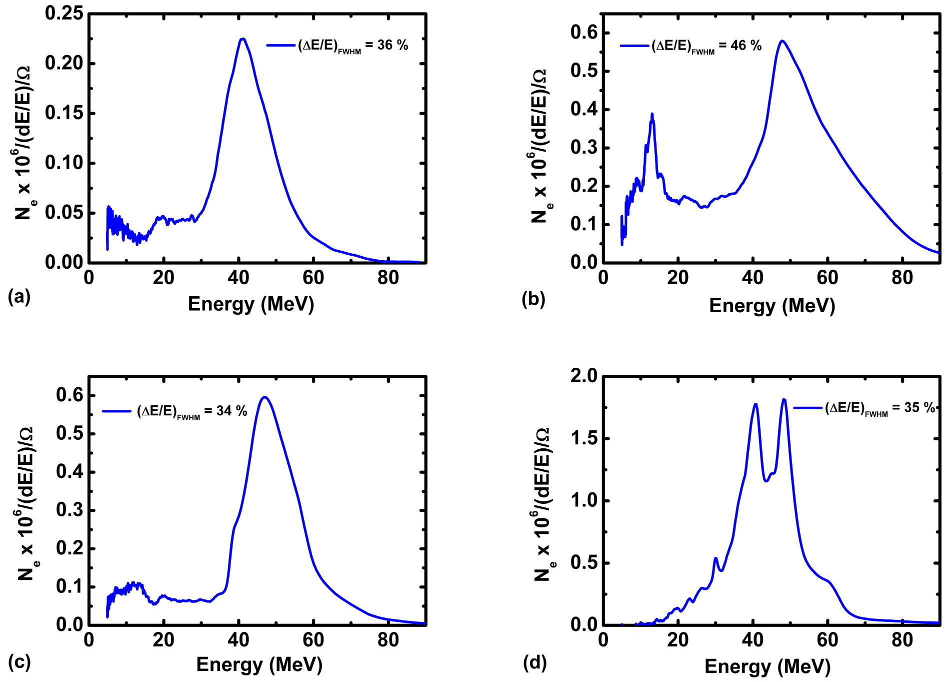

Figure 5.13: The quasi-monoenergetic electron spectra taken from the Astra wakefield accelerator. The FWHM energy spreads were (a) 36 % (b) 46 % (c) 34 % (d) 35 %. The plasma density was set to $n_e = 1.0 \times 10^{19}$ cm^{-3}.

5.1.2 Electron charge measurements

In addition to the energy spectrum of the electron beam, measurements on the electron bunch charge were also carried out using an integrating charge transformer (ICT). The ICT has a large aperture diameter of 70 mm and detected electrons in a large energy and angular range. The ICT is capable of integrating a very fast pulse with a rise time of the order of picoseconds with no significant signal loss. This kind of performance is needed to measure the very short duration electron bunches that are produced from a laser wakefield accelerator. The ICT is a capacitively shorted transformer with magnetic cores made from thin ribbons of Cobalt/Molybdenum amorphous alloy interleaved with Nickel/Iron crystalline alloy. The ICT integrates the signal with a time constant of 10 nanoseconds. As a result, the rise and fall response times are slowed down and the eddy current losses become negligible thus making the instrument a linear integrator for the very high frequency spectrum typical of an ultrashort electron bunch. The ICT output pulse charge is in exact proportion to the beam pulse charge. The sensitivity of the ICT is also called the transfer impedance. The ICT used in this experiment had a transfer impedance of 1.25 V.s/C. It is expressed in terms of the integral of the output pulse voltage as a function of the input pulse charge. Using this relationship the bunch charge was readily accessible for each laser shot. Figure 5.14(a) shows a typical raw signal from the ICT before the bunch charge was deduced by integrating the signal and calibrating using the transfer impedance. The mathematical integration function used for the analysis is shown in equation 5.11,

$$I(t) = \int_{t_1}^{t_2} V(t)dt. \tag{5.11}$$

Figure 5.14(b) shows the the bunch charge of 58 laser shots, yielding an average over the total run of 30 pC/shot.

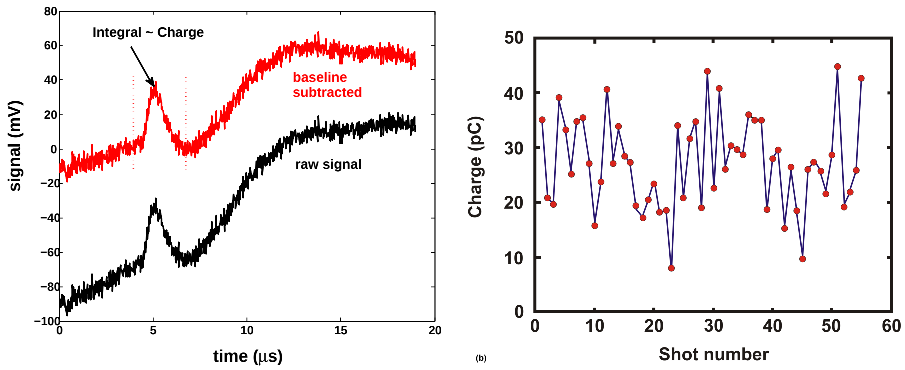

Figure 5.14: (a) The integrated current transformer signal.(b) The total bunch charge of a series of laser shots. The average bunch charge over this data set was $\sim$ 30 pC.

5.1.3 Interferometric plasma density measurements

An additional diagnostic to measure the plasma density was employed for the bunch duration experiments on Astra at RAL. As has been discussed in section 2.13 and section 2.16, the plasma density is a critical parameter for optimsing the interaction of the wakefield with the plasma electrons. For specific laser pulse parameters there exists an optimium 'sweet spot' in the density profile for maximum coupling between the laser pulse and wakefield. It is therefore very useful to employ a plasma density profiler using laser interferometry. This information can be used effectively to 'tune' the interaction.

In order to measure the plasma density profile and evolution of the laser pulse through the gas jet plasma a 50 μJ transverse probe beam was split off from the main Astra pump beam. This probe beam was on a remote variable delay stage automated by a Labview program to allow for accurate synchronisation between the probe beam and the pump beam. The probe beam was split into two arms using a 50/50 beamsplitter, which constituted a Mach-Zender interferometer. One beam passed through the gas jet in a direction orthogonal to the pump propagation direction whilst the other traversed in free-space onto a delay stage for synchronisation. They were both recombined using another 50/50 beam splitter where they formed interference fringes that were imaged onto a 12-bit CCD camera (Q-cam). By careful adjustment of the mirrors and delay stage of the free-space arm of the Mach-Zender one could attain shadographs and interferograms to obtain information on the plasma channel (position, size, density, timing relative to gas pulse) suitable for the plasma density measurements. The main probe delay stage was translated and optimised until the best quality fringes appeared on the interferogram viewed using the CCD camera.

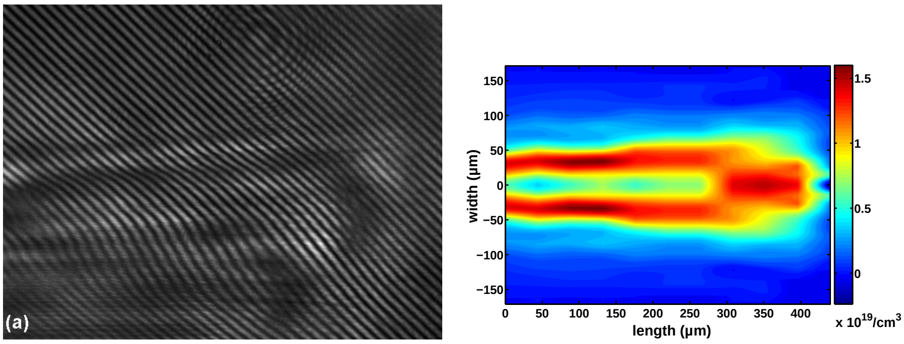

Figure 5.15: (a) The raw interferogram taken using interferometry of the plasma channel. (b) The retrieved plasma density profile using Abel inversion [13].

An example interferogram of the plasma density profile is shown in 5.15(b). The resulting phase map analysis of the plasma density was done using the IDEA code. This code is explained in reference [13] which essentially uses the inverse Abel transformation.

5.2 Simulations of the electrooptic signal

A Matlab routine was written to simulate the angular and temporal characteristics of the THz transition radiation pulse. The simulation assumed a 15 pC electron bunch with a peak energy of 40 MeV and a 25 % energy spread. The bunch radius and length was assumed to be 5 μm and 12 μm ($\sim$ 40 fs) respectively. A self focused laser intensity of 5 $\times$ 10^{20} Wcm^{-2} was assumed to focus

No of particles	100
Radius of electron beam	5 μm
Electron energy spread (MeV)	10 MeV
No of points on energy mesh	1001
No of electrons in peak	5 $\times$ 10^7
No of electrons in exp. tail	2 $\times$ 10^8
Focal length of 1st parabola	125 mm
Focal length of 2nd parabola	250 mm
Electron pulse duration	40 fs
Plasma electron density	2×10^{19} cm^{-3}
Self focused laser intensity, I_L	5×10^{20} Wcm^{-2}
a_0 parameter	15.3
Laser electric field amplitude	0.6 TV/cm
Observation angle	0.6 rad

Table 5.1: The parameters used in the simulation of the electrooptic detection of a coherent transition radiation pulse.

through a plasma electron density of 2 $\times$ 10^{19} cm^{-3}. It was necessary to include the transmission of the Teflon filter used in the experiment used to stop the parabolas imaging the transmitted laser and plasma light onto the ZnTe crystal. Figure 5.24 represents the simulated transition radiation pulse radial temporal profile.

5.2.1 Characterisation of Teflon filter

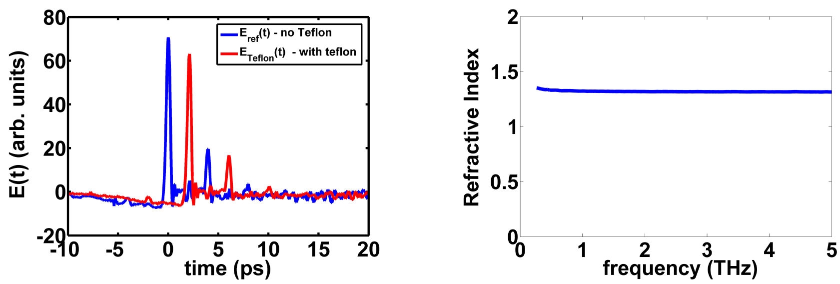

Figure 5.16: (a) The scanning delay line measurements of the THz electric field as a function of time, $E_{THz}(t)$. The blue curve shows the reference measurement taken with the THz propagating through only dry air (N_2). The red curve shows the measurement taken with the THz passing through the Teflon filter. (b) The refractive index of the Teflon filter calculated using the information in figure 5.16(a) and equations 5.12 and 5.13.

The teflon filter was characterised after the experimental campaign using Terahertz Time Domain Spectrometry (THz-TDS). The THz-TDS test bed at Strathclyde is shown in figure 5.2. All measurements were carried out in a N_2 filled box to minimise the effects of the H_2O THz absorption bands of air. The method involved; firstly, recording a reference pulse that only propagated through the nitrogen before encountering the ZnTe crystal using the scanning delay line. This was followed by taking a second measurement with the teflon sample inserted into the path of the THz radiation. In THz-TDS, subpicosecond pulses of THz radiation are measured after propagation through a sample and an identical length of free space (less the width of the sample). Analysis of the Fourier transforms of these signal pulse shapes yields the absorption and dispersion of the sample. Using the relations [230, 231]:

$$\frac{\tilde{E}_s(\omega)}{\tilde{E}_r(\omega)} = \rho(\omega)e^{-i\phi(\omega)} \tag{5.12}$$

where $\tilde{E}_s(\omega)$ and $\tilde{E}_r(\omega)$ are the Fourier transformed frequency spectra of the sample and reference respectively. The complex frequency spectra of the reference, $\tilde{E}_r(\omega)$, and of the sample, $\tilde{E}_s(\omega)$, are calculated using numerical Fourier transforms from the time domain waveforms sampled in the experiment. The analytic expressions for n_s and κ_s can be written in terms of the magnitude $\rho(\omega)$ and the phase $\phi(\omega)$ of the ratio of $\tilde{E}_s(\omega)$ to $\tilde{E}_r(\omega)$ [231]. The refractive index of the sample is thus:

$$n_s(\omega) = \phi(\omega)\frac{c}{\omega d} + 1 \tag{5.13}$$

where, d is thickness of the sample, and c is the speed of light in vacuum. The imaginary part of the refractive index, κ_s, is related to the power absorption coefficient, $\alpha(\mathrm{cm}^{-1})$, as:

$$\kappa_s(\omega) = \ln\left(\frac{4n_s(\omega)}{\rho(\omega)[n_s(\omega)+1]^2}\right)\frac{c}{\omega d} \tag{5.14}$$

where

$$\alpha_s(\omega) = \frac{2}{d}\ln\left(\frac{4n_s(\omega)}{\rho(\omega)[n_s(\omega)+1]^2}\right) \tag{5.15}$$

The Teflon transmission data was then incorporated into the main simulation. The effect on the transmitted THz frequency can be seen clearly by comparison of figures 5.18(a) and 5.19(a). The Teflon filters out the high end frequency components (5-10 THz) of the THz transition radiation pulse, however the vast majority of the radiation is in the 1-4 THz region.

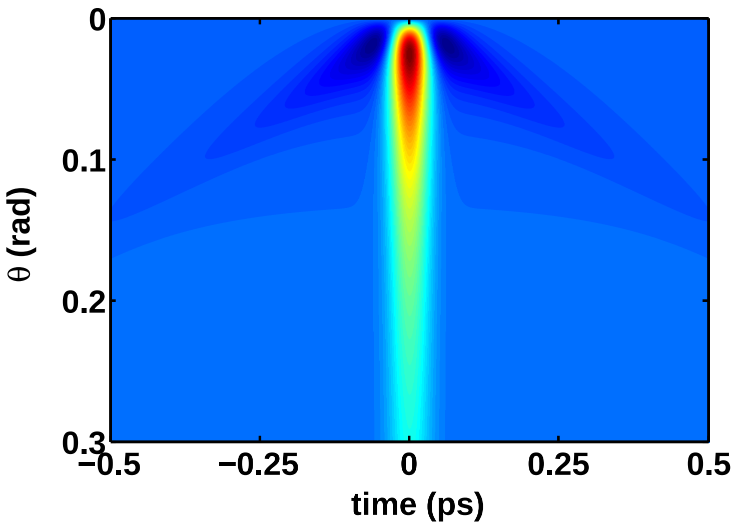

Figure 5.17: A simulation of the the electric field temporal profile ($E_{THz}(t)$) of the THz transition radiation pulse as a function of collection angle, θ.

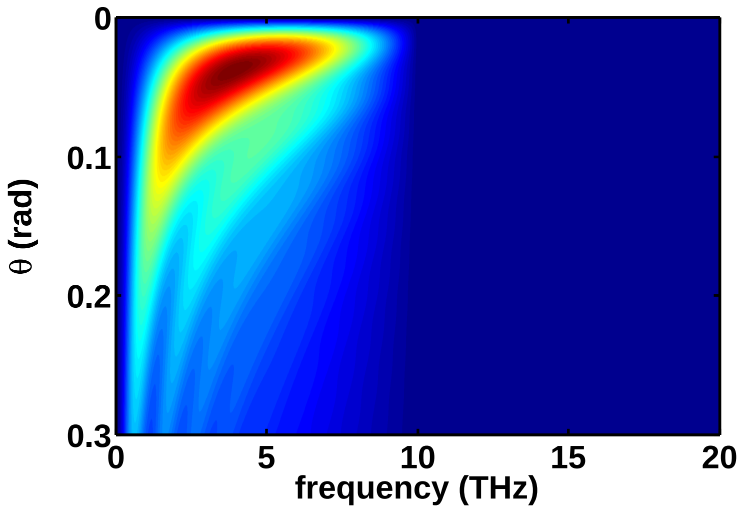

Figure 5.18: The angular frequency distribution of the THz transition radiation pulse.

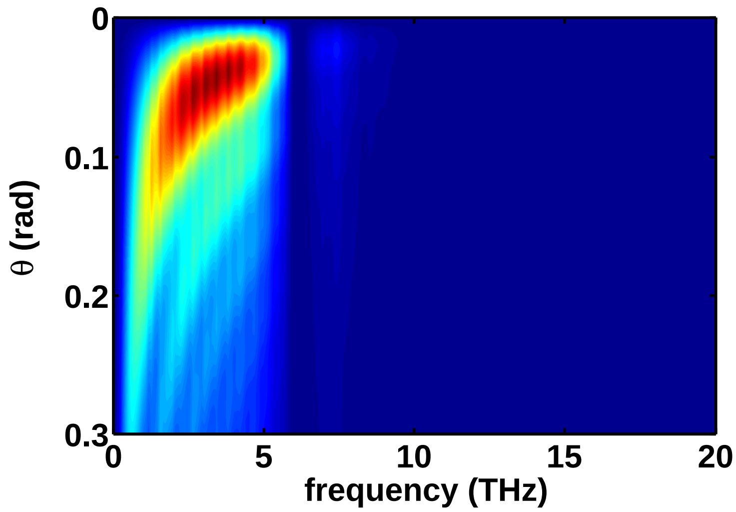

Figure 5.19: The angular frequency distribution of the THz pulse in the presence of a Teflon filter. The fringes appear in the spectrum due to real data being used for the frequency response of the Teflon filter. These oscillations are thus an noise artifact from the analysis.

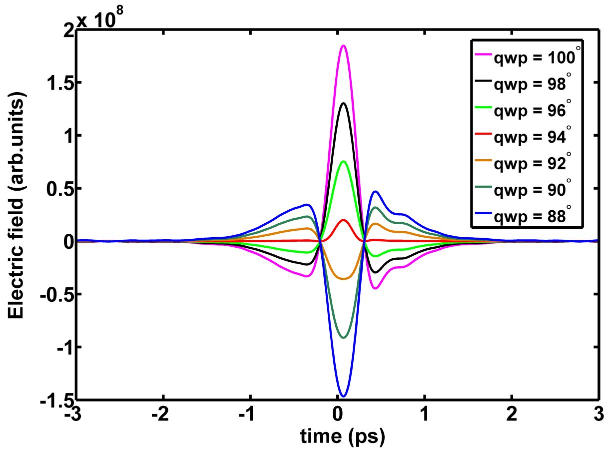

Figure 5.21: A simulation of the spectrally modulated electrooptic signal v.s. variation of the quarter waveplate.

5.3 Simulations of the electrooptic signal

The next part of the simulation involved looking at simulating the detection of the THz pulse. The response function of the ZnTe was taken according to Casalbuoni [207] and the temporal evolution of the THz pulse inside the crystal used the framework described in section 4.11. The Fresnel reflections at the crystal interfaces and dispersion were also taken into account. Figure 5.23 show the results of the simulations where each line on the plot represents a time profile snapshot as the pulse propagates through the ZnTe crystal. It can be seen that as the pulse travels through the crystal the pulse shape changes and it adopts oscillatory components.

A simulation of the electrooptic signal for the spectral encoding situation was also performed. Figure 5.22 shows the simulated electrooptic signal encoded onto a chirped pulse pedestal of 5 ps duration for various QWP angles.

Figure 5.24 shows a 3D map cross section which simulates the transition radiation electric field v.s. time as a function of radius.

5.4 Single-shot electrooptic measurements

An aluminium tape of 50 μm thickness was installed 5 mm behind the gas jet as a source for transition radiation. A photograph of this arrangement is shown in figure 5.26. The purpose of the tape drive was to allow a new fresh region of tape to be translated into the path of the electron beam after each laser shot. This was because the laser pulse ablates the foil after one single laser shot and destroys the surfaces of the radiator. The coherent transition radiation was collimated and re-

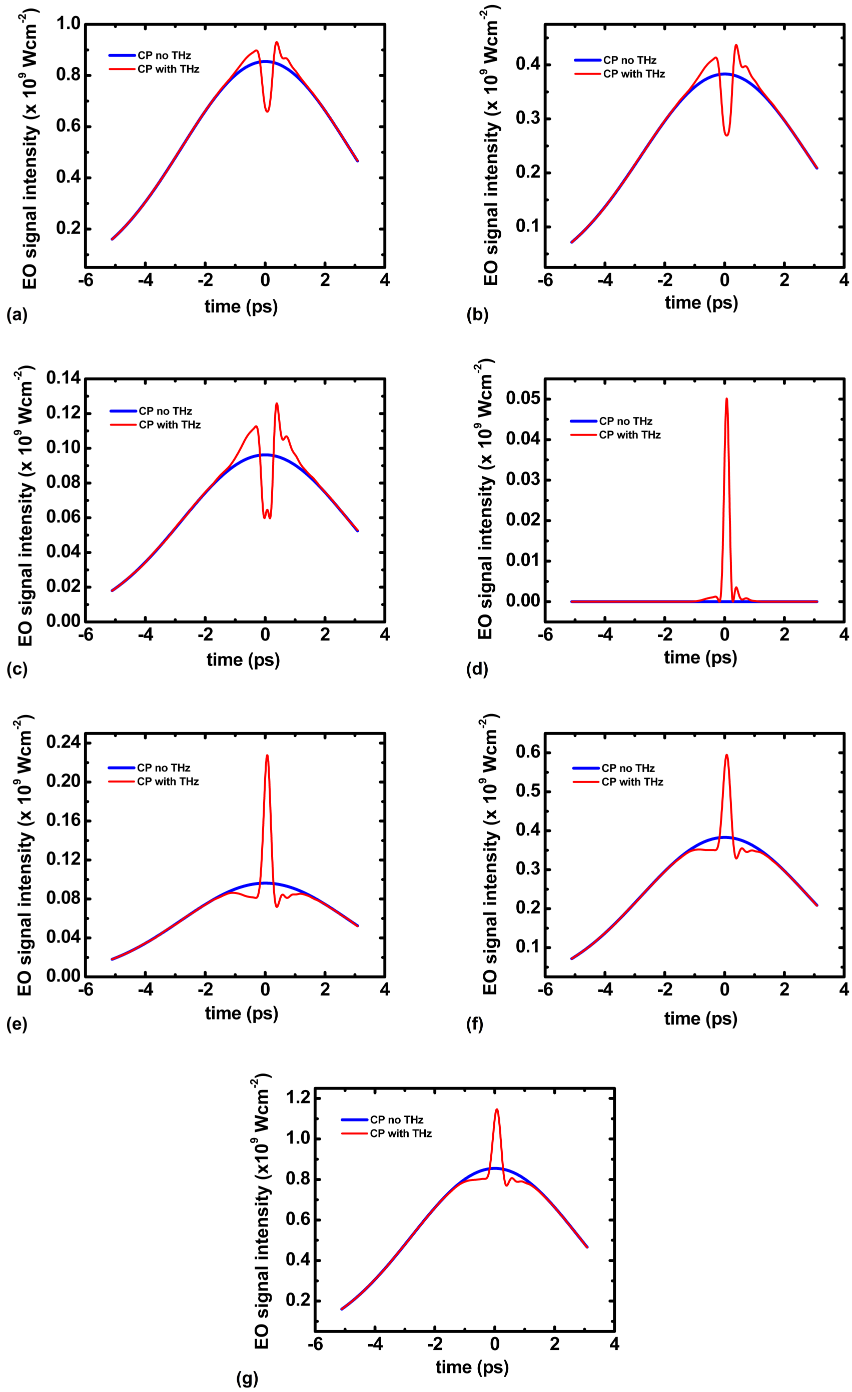

Figure 5.22: Simulations of the THz electrooptic signal at different quarter wave plate angles encoded onto the pedestal time profile of a 5 ps chirped pulse.(a) QWP angle 90°, (b) QWP angle 91°, (c) QWP angle 92°, (d) QWP angle 93°, (e) QWP angle 94°, (f) QWP angle 95°, (g) QWP angle 96°

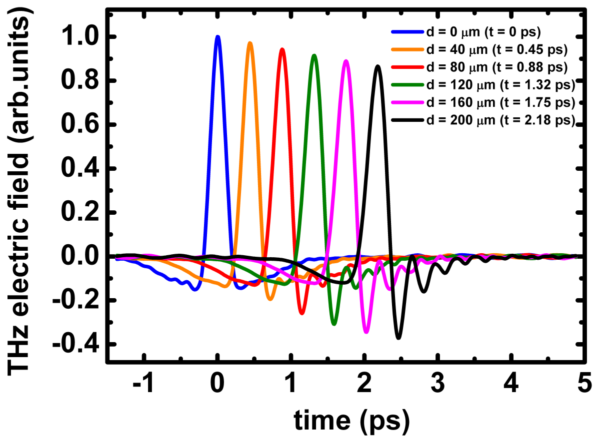

Figure 5.23: The temporal evolution of a THz–TR pulse propagating through a 200 μm thick ZnTe crystal. Each pulse corresponds to a snapshot of consecutive 40 μm steps through the ZnTe crystal.

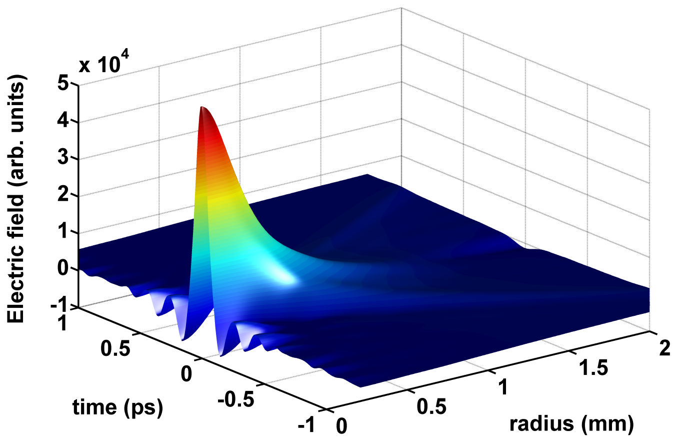

Figure 5.24: A 3D map of the simulated transition radiation pulse showing the radial temporal profile.

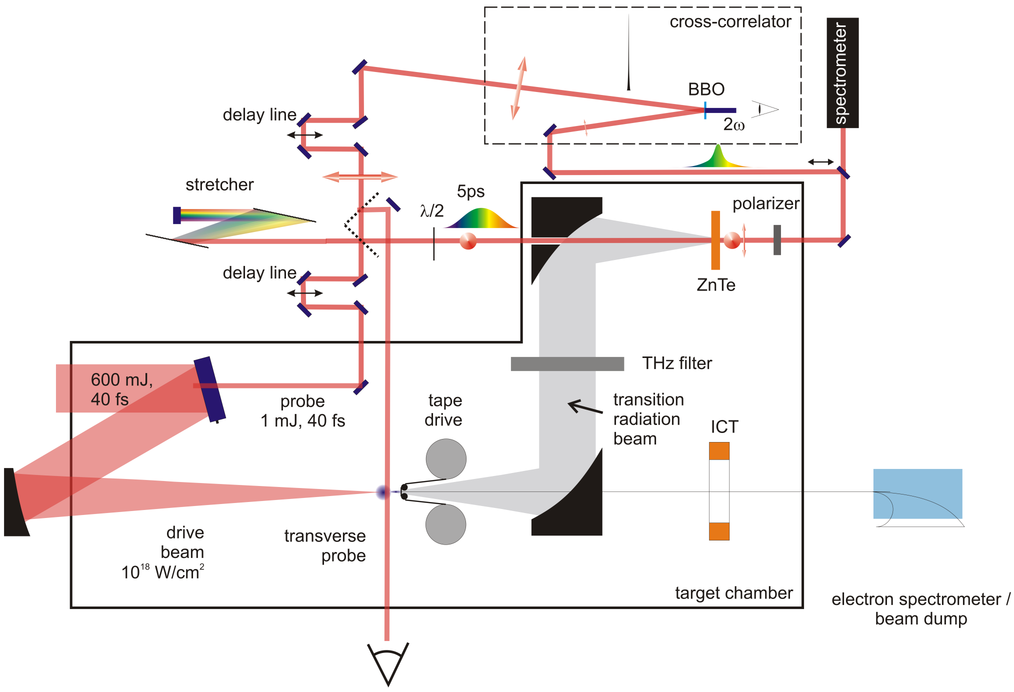

Figure 5.25: The bunch duration experimental set-up using the Astra laser at the Rutherford Appleton Laboratory using coherent transition radiation to characterise the temporal profile of laser wakefield accelerated electron bunches. Laser-accelerated electrons generate coherent transition radiation at an aluminum tape target. The CTR is imaged by two off-axis parabolas onto a ZnTe crystal, where it rotates the polarization of a chirped probe (CP) beam. The time-domain modulation of the CP is analyzed in a BBO cross-correlator.

focused into a 200 μm thick ZnTe crystal by a pair of off-axis parabolas, the first of which had a central hole for the electrons to pass through in addition to the drive laser beam which was analysed in an optical spectrometer. Between the OAPs a Teflon filter blocked any scattered radiation from the laser. Part of the ASTRA pulse was split off and (negatively) chirped to 5 ps duration in a Treacy-type grating compressor (grating pair). This chirped probe (CP) pulse was sent through the ZnTe crystal and its polarisation was changed by the transient birefringence induced by the THz field via the electro-optic Pockels effect, hereby encoding the temporal structure of the THz pulse into the CP polarization. This modified pulse was sent through a crossed polarizer setup to transfer the polarization pattern into an intensity modulation. By virtue of the CPs chirp, the temporal intensity modulation can also be detected in the spectral domain, which was used to time the CP relative to the electron pulse. Another part of the ASTRA pulse was used as a reference probe (RP) for a high-resolution cross-correlation measurement, directly in the time domain, representing the main diagnostic.

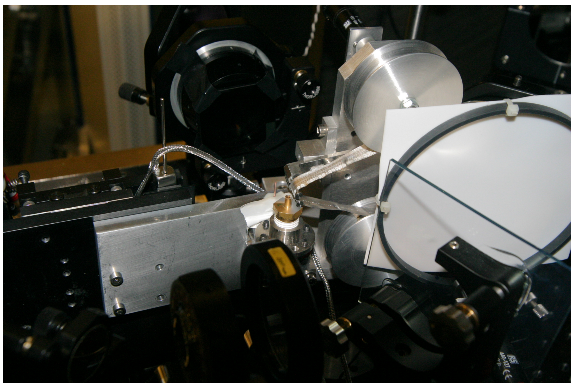

Figure 5.26: The gas jet with the up-stream aluminium foil on a tape drive used as the Transition Radiation screen.

5.5 Measurements from the cross-correlator

The cross-correlator was used as the primary diagnostic to measure the temporal profile of the electron bunches. The top right region of figure 5.25 shows the cross-correlator electrooptic system and how it was integrated into the main experimental set-up. The main probe beam (1 mJ, 40 fs) was split off from the main drive beam through the back of the last turning mirror. This probe beam was then split into two arms, a chirped arm and a transform limited short arm. Both these laser probe beams were intrinsically synchronised to the main laser system. The temporal delay between both probe lasers and the THz beam could

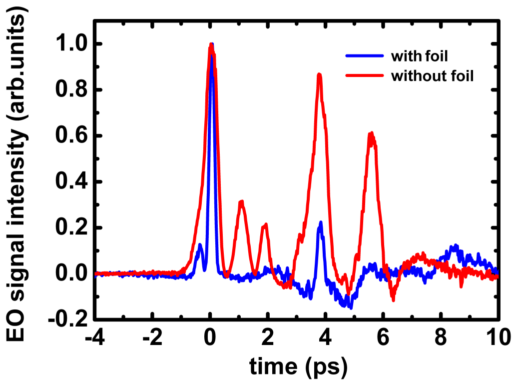

Figure 5.27: The electrooptic signal from the cross correlator with (blue curve) and without (red curve) the tape drive foil.

be carefully controlled by a delay stage. A second delay stage allowed modification of the delay of the short pulse arm with respect to the chirped pulse arm. The chirped laser beam was focused through a 200 μm thick ZnTe crystal where it was then recollimated and passed through a polariser before being sent to the BBO crystal where it overlapped with the short pulse laser beam. Both probe beams were focussed onto the BBO crystal using cylindrical lenses(y-lens) with a focal length, f = 100 mm. The beam diameter of each probe beam was $d \simeq 6$ mm (intensity FWHM), resulting in a single shot temporal window around 1500–2500 fs. The frequency doubled line focus produced by the up-conversion of each probe beam was imaged onto a CCD camera. In order to measure the spatial to temporal calibration factor, two data sets at different delays between the THz and probe beams were recorded. This yielded a value of $\sim$ 19.5 fs/pixel on the CCD camera.

Figures 5.28(a)–5.28(e) show the cross-correlator lineouts with the simulated fits superimposed onto the data. The data shows a good fit to the simulation over a quarter waveplate rotation range of 8° (90–98°).

The largest EO signal was produced when the QWP was rotated to an angle of 98°, furthermore by measuring the temporal width of the signal, a value of 200 fs FWHM was attained as the minimum measured duration of an electron bunch during the experiment.

5.6 Discussion and outlook

This thesis presented both the theoretical and experimental treatment of THz radiation produced by electron bunches from a laser wakefield accelerator. Al-

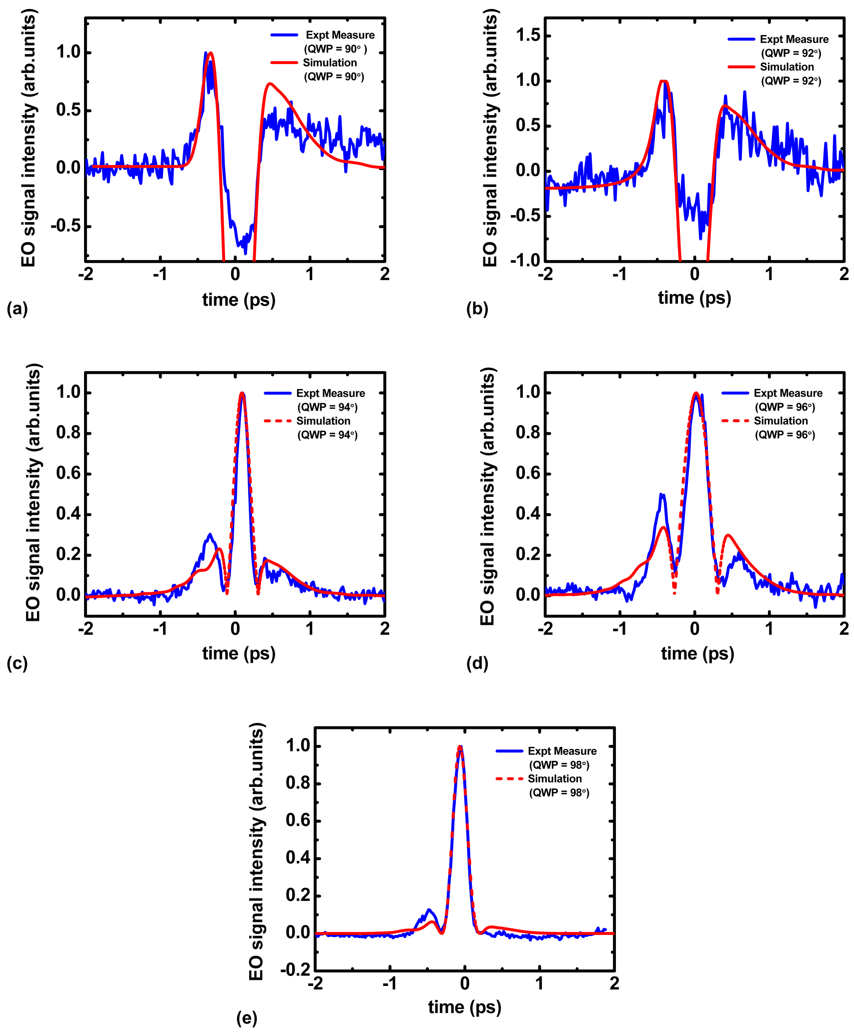

Figure 5.28: The electrooptic signal obtained at different quarter waveplate angles.

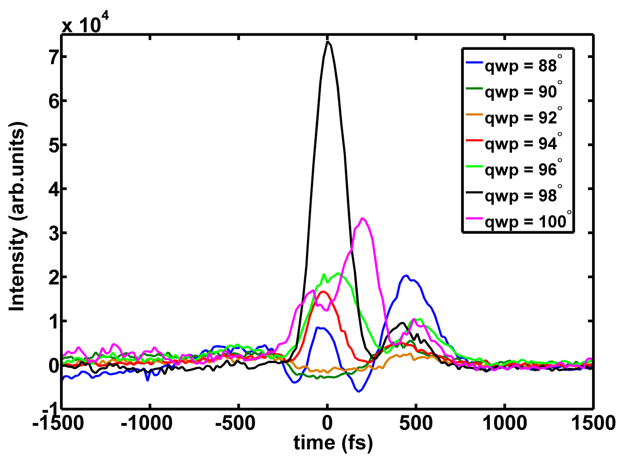

Figure 5.29: The electrooptic signal from the cross-correlator with variation of the quarter waveplate.

though electron bunch parameters such as charge, bunch energy, and bunch divegence, have been characterised extensively, little has been known about the bunch duration.

An electrooptic sampling technique (EOS) has been implemented to measure the temporal profile of the THz pulses produced from a LWFA. The change in the ZnTe crystal birefringence, induced by the THz pulse, was probed by a chirped laser pulse. In order to compare the EOS data to the simulated model, crystal effects such as absorption, dispersion, and velocity mismatch were considered. A scanning delay technique, where the delay between the short pulse laser and THz pulse was scanned has been implemented at Strathclyde in order to characterise the ZnTe crystal prior to the main experimentation at the Rutherford Appleton Laboratory. Moreover, the main diagnostic consisted of a single shot technique, based on the EOS with a chirped laser pulse in a cross-correlator system. A 200 μm ZnTe crystal with a frequency response of 0–4 THz was implemented and the EOS data demonstrated the production of femtosecond THz pulses around 200 fs (FWHM). Coherent transition radiation pulses were detected using the cross correlator for the case when the plasma–vacuum interface was acting as the radiator and for the case when a metallic foil was inserted into the electron beam path as the radiator. This was shown to 'filter' the temporal electrooptic signal and give a more defined signal on the cross-correlator. This could be due to the fact that the metallic foil has a sharper dielectric interface than the plasma vacuum interface meaning that when using the foil as opposed to the plasma the ratio between the formation length and the longitudinal size of the dielectric boundary gets larger i.e. L_{form}/L_z increases.

The main result of this experiment has set an upper limit of the measured bunch duration from a laser wakefield accelerator to be $\sim$ 200 fs. This work has been also been complemented by other groups using similar measurement techniques [204, 73, 74]. Although much progress has been made in measuring the duration of ultrashort electron bunches the resolution of the technique described in this thesis remains two orders of magnitude off what is required to resolve the 2–5 fs electron bunch lengths that are predicted to be produced from plasma accelerators. However, recently further analysis from the data collected on this experiment using THz time-domain interferometry has reduced the measurement of the bunch duration to $\sim$ 35 fs [110]. The electrooptic technique has intrinsic limitations on the best achievable resolution due to the response bandwidth of the EO crystals used for detecting the electron bunches. As seen in figure 4.10(b) the response bandwidth scales inversely with crystal thickness, thus by choosing thinner crystals a better time resolution can be achieved. However, by using thinner crystals the EO signal is reduced due to the reduced path length for polarisation rotation inside the crystal. Therefore a balance between these two effects must be carefully selected.

Alternative techniques to measure the bunch duration could involve spectrally resolving the CTR using THz detectors. In this method the transition radiation generated by the electrons from a laser wakefield accelerator could be directed onto a single element THz detector. The use of THz bandpass filters for a range of wavelengths in front of the detector element would then allow an intensity spectrum to be built up over many laser shots. Observation of a coherent 'step-up' in intensity ($I \propto Q^2$) at a certain wavelength component would then yield an average measurement of the bunch duration. A single shot version of this method may also be possible by using a THz detector element array, which could form the basis of a THz spectrometer and the coherence onset to be observed for a single laser shot. Both of the afore mentioned techniques are currently being investigated at Strathclyde.

Since the LWFA-produced electron bunch contains over 10^{10} electrons at femtosecond duration, the emitted THz radiation can be 1–2 orders of magnitude more intense from conventional laser based THz sources (e.g. optical rectification or the photoconductive antenna). Although the THz pulse energy was not measured in this experiment it has been reported that LWFA-produced THz pulses $> 10\ \mu$J are possible with peak fields of several MVcm^{-1} [204]. CTR from a LWFA is thus and excellent way to provide a unique source for high-field THz applications.

Chapter 6

Relativistic ionisation fronts

6.1 Introduction

Most tunable high power radiation sources in existence today are either free–electron sources – such as free electron lasers (FEL's), gyrotrons, or synchrotrons, that use high power electron beams, or maser and laser sources that are based on photon emission due to transitions between quantum states. In 1967, Semenova [232] and in 1978, Lampe [128] both showed that electromagnetic radiation impinging on a relativistic ionisation front can undergo frequency up-shifts. The principle involved electromagnetic radiation being reflected from an overdense ionisation front as a possible method to generate millimetre and sub-millimetre radiation [128]. Ionisation fronts can be generated by optical field induced ionisation of a background neutral gas with an intense laser pulse.

Radiation sources based on the concept of photon acceleration have received considerable attention in plasma physics, owing to their potential as a new type of tunable, ultrashort radiation source. The concept was investigated in 1989 by Wilks who theoretically demonstrated that pulses of laser light can be frequency up-shifted when co-propagated with a plasma density gradient (space and time varying plasmas) [155, 233]. Following this, experimental interest in the microwave-transient plasma interaction was renewed by the development of laser technology in the 90's that enabled the generation of relativistically propagating ionisation fronts by intense laser pulses via photo-ionisation [234]. In 1991, Mori predicted [235] that large frequency up-shifts and pulse compressions are possible even for underdense relativistic ionisation fronts when the incident radiation is transmitted into the plasma. The concept was also theoretically examined by Esarey in 1991 [236], and experimentally investigated shortly after in 1992 by Savage *et al* [237, 238] who demonstrated the first frequency up-shifts of microwave radiation impinging on an ionisation front created by an intense short laser pulse. The experiment involved frequency up-shifting 35 GHz microwave radiation to more than 116 GHz when a relativistically propagating, laser produced ionisation front interacted with microwave radiation confined in a resonant cavity. Following from this work, many other groups have investigated this phenomenon [129, 130, 239, 240, 241, 242]. The phenomenon was experimentally demonstrated in the optical range by Dias *et al* [157]. In this experiment a probe laser pulse with a central wavelength of 620 nm was co-propagated with an ionisation front and upshifts of 25 nm were demonstrated. Furthermore, photon acceleration has been observed by many groups undertaking plasma wakefield research [156] and is commonly used to infer information about the plasma properties (density, acceleration regime, etc)

An ionisation front will propagate at a velocity close to the group velocity of the laser pulse in plasma given by

$$v_g = c(1 - n_e/n_{cr})^{1/2}. \tag{6.1}$$

It is clear from equation 6.1 that the velocity of the ionisation front will be dependent on the plasma electron density. As will be discussed the velocity of the ionisation front determines the magnitude of the frequency shifts during the interaction between the front and probe. Higher frequency up-shifts are associated with faster ionisation fronts (higher γ factor). Short laser pulses reflected from these overdense relativistic moving plasma mirrors are compressed by a factor determined by the front velocity. Therefore by experimentally tuning the plasma density it is possible to 'tailor' the spectral and temporal properties of the desired pulse.

6.2 Ionisation fronts

A laser pulse can propagate in a plasma if the plasma density n_p is below the critical density $n_{cr} = m\omega_0^2/4\pi e^2$, where ω_0 denotes the central (carrier) frequency of the laser pulse. Plasmas with $n_p > n_{cr}$ are called overdense, plasmas with $n_p < n_{cr}$ are called underdense. For a given laser wavelength $\lambda_0 = 2\pi c/\omega_0$, the critical density is found to be $\pi/r_e\lambda_0^2$, where $r_e = e^2/mc^2$ is the classical electron radius. For a typical solid-state laser with a wavelength of 800 nm often used in laser wakefield acceleration, the critical density is 1.75×10^{21} cm^{-3}. The propagation velocity of the laser pulse, which is the group velocity $v_g = c(1 - n_p/n_{cr})^{1/2}$, is close to c, the speed of light in vacuum. The plasma refractive index is given by,

$$\eta_p = ck_0/\omega_0 = \sqrt{1 - n_e/\gamma n_{cr}}. \tag{6.2}$$

An intense short laser pulse propagating through a gas can generate a relativistic front by optical field induced ionisation of the background gas [234]. The ionisation front propagates with approximately the group velocity of the ionising laser pulse in the gas-plasma interface and with a rise time roughly equal to half of the laser pulse duration [157]. The maximum electron density of the front is a function of the background gas pressure and the laser pulse intensity. Higher gas backing pressures will result in high electron densities (plasma densities). This is due to more atoms, hence more electrons being more tightly confined in space. Furthermore, the type of gas used in experiments as well as the laser intensity also strongly affects the plasma density. Different gases have varying numbers of electronic states, thus ionisation potentials. In order to fully ionise a gas and hence achieve the highest electron density the laser electric field or intensity must be strong enough to overcome the Coulomb potential between the nucleus and the inner electron.

A baseline often used to define 'high' laser intensity is the hydrogen atom. From the Bohr model, one can derive many of the quantities needed to get started in laser atom interactions. Firstly, we find that at the Bohr radius, $a_B = \hbar^2/m_e e^2 = 5.3\times10^{-9}$ cm, the electric field strength is, $E_a = e/4\pi\varepsilon_0 a_B^2 \simeq 5.1\times10^9$ Vm^{-1}. This leads to the atomic intensity, $I_a = \varepsilon_0 c E_a^2/2 \approx 3.5\times10^{16}$ Wcm^{-2} which is defined as the intensity at which the laser field matches the binding strength of the electron to the atom. A laser intensity of $I_L > I_a$ will guarantee ionisation for any target material, however this can occur well below this threshold via multi-photon effects. For the laser intensities considered in this chapter over the barrier ionisation (OTBI) model describes the ionisation process. The threshold field strength at which OTBI occurs is $E_c = \frac{E_{ion}^2}{4Ze^3}$. Equating this critical field to the peak electric field of the laser yields and effective appearance intensity $I_{app} = cE_{ion}^4/128\pi Z^2 e^6$, or in more convenient form $I_{app} = 4\times10^9 (E_{ion}/\mathrm{eV})^4$ Z^{-2} Wcm^{-2} for ions created with charge Z.

After collision with the ionisation front, the photons can either be reflected by the front and propagate in vacuum or be transmitted across the front and propagate into the plasma region. In the case where the photons are completely reflected the impinging probe photon frequency is less than the plasma frequency of the ionisation front i.e. $\omega_0 \leq \omega_\eta$

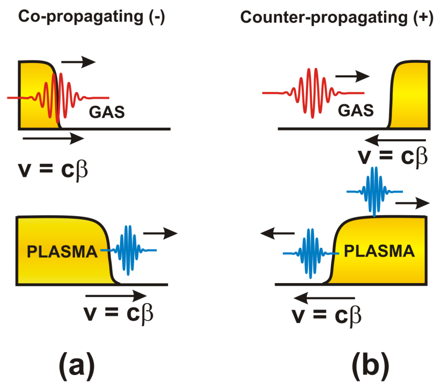

Figure 6.1: The interaction of a probe laser pulse with a relativistic ionisation front in (a) Co-propagating and (b) Counter-propagating geometry.

$$\frac{\omega_{up}}{\omega_0} = \frac{1-\beta_f\cos\theta_0}{1-\beta_f^2} + \frac{\beta_f\,|\beta_f-\cos\theta_0|}{1-\beta_f^2}, \tag{6.3}$$

for initial conditions, in vacuum, obeying the cutoff relation [157],

$$\omega_0 \leq \omega_\eta = \frac{\omega_p\sqrt{1-\beta_f^2}}{\sqrt{[1-\beta_f\cos\theta_0]^2 - \left(1-\beta_f^2\right)\sin^2\theta_0}}. \tag{6.4}$$

This regime describes the standard double relativistic Doppler up-shift in counter-propagation, but also describes the scenario when the photons are overtaken by the front and reflected into the vacuum region.

Conversely, when $\omega_0 > \omega_\eta$ the photons will propagate into the plasma region i.e. behind the front. The maximum frequency upshift in this case is [243]

$$\frac{\omega_f}{\omega_0} = \frac{1-\beta_f\cos\theta_0}{1-\beta_f^2} - \frac{|\beta_f|}{1-\beta_f^2}\sqrt{(\beta_f-\cos\theta_0)^2 - \frac{\omega_p^2}{\omega_0^2}\left(1-\beta_f^2\right)}. \tag{6.5}$$

If we now take $\theta_0 = \pi$, which is the case for counter-propagation we attain the expressions for the frequency shift associated with double Doppler shift in counter-propagating geometry.

The key feature predicted by theory is the significant difference between the frequency up-shift $\Delta\omega$ for counter and co-propagation [244], i.e.:

$$\Delta\omega = \frac{\omega_p^2}{2\omega_0}\frac{\beta_f}{1\pm\beta_f}, \tag{6.6}$$

for a one dimensional (1D) configuration in an underdense ionisation front, where the plus/minus sign indicates counter/co-propagating respectively, and $\omega_p = \sqrt{n_e e^2/\epsilon_0 m_e}$ is the maximum electron plasma frequency of the front, ω_0

is the initial frequency of the probe pulse, and β_f is the velocity of the front, normalised to the speed of light.

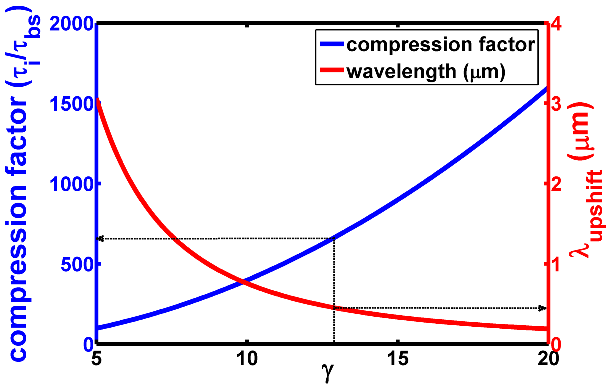

Figure 6.2: The temporal compression factor experienced by a laser pulse reflected from a relativistic ionisation front with velocity, γ (blue curve). The up-shift in wavelength of a radiation pulse plotted as a function of the front velocity (red curve).

The double Doppler up-shifted frequency of the reflected wave is given by

$$f_r = \frac{\omega_r}{\omega_0} = \frac{1 + 2\beta\cos\theta_0 + \beta^2}{1 - \beta^2}. \tag{6.7}$$

Clearly the up-shifted frequency reaches a maximum at normal incidence and then gradually decreases with the incident angle. Furthermore the angle of the reflected wave deflects from the incident angle as the front velocity, β increases and asymptotically approaches the normal direction when $\beta \to 1$.

Equation 6.7 can also be expressed in terms of the incident and reflected wave parameters

$$\omega_r^*/\omega_i^* = \frac{(1 + \beta\cos\theta_i^*)}{(1 - \beta\cos\theta_r^*)}. \tag{6.8}$$

The frequency shift occurring when a wavepacket crosses over an ionisation front without reflection is given by the expression [245]

$$\Delta\omega = \frac{\omega_p^2}{2\omega_0}\frac{\beta}{1 \pm \beta}, \tag{6.9}$$

where the initial frequency of the photon is much higher than the maximum plasma frequency behind the ionisation front, i.e. $\omega_0 \gg \omega_p$. The plus/minus sign in equation 6.9 refers to counter-propagation and co-propagation, respectively.

The physics surrounding photon acceleration can be explained as follows. As the local density at the front of the laser pulse will be smaller than at the back of the pulse. Since the phase velocity is proportional to the plasma density, the phase velocity at the front of the pulse is slower than at its back i.e. the phase peaks at the back move faster than those at the front of the laser pulse, resulting in phase ‘bunching’. This means that the wavelength of the laser will decrease and the frequency will increase. For small frequency shifts, and considering that the laser pulse remains in phase with the plasma wave $v_{g_{Laser}} = v_p$, the frequency shift is given by [236]

$$\Delta\omega = \frac{\omega_p^2}{2\omega_0}\frac{\delta n_e}{n_e}\Delta z k_p \cos(k_p\zeta), \tag{6.10}$$

where ω_0 denotes the laser central frequency, $\Delta\omega_0$ the maximum frequency shift in the laser spectrum due to the interaction of plasma, $\delta n_e/n_e$ the relative perturbation of the plasma density, $k_p = c/\omega_p$ the linear plasma wavenumber, Δz the distance along which the laser pulse interacts with the plasma, and $\zeta = z - v_p t$ the distance in the laser reference frame.

For the experiments presented in this thesis the incident electromagnetic wave was collided into the ionisation front at normal incidence ($\theta_0 = 0$). We can now write simplified expressions for the up-shifted radiation in terms of frequency

$$\omega_r = \omega_i \gamma_f^2 \left(1 + \beta_f\right)^2 \tag{6.11}$$

and wavelength

$$\lambda_r = \frac{\lambda_i}{\gamma_f^2 \left(1 + \beta_f\right)^2}. \tag{6.12}$$

A corresponding expression holds for the pulse duration of the up-shifted pulse and is given by

$$\tau_r = \frac{\tau_i}{\gamma_f^2 \left(1 + \beta_f\right)^2}. \tag{6.13}$$

Furthermore relativistic Lorentz contraction effects also cause the reflected waves angular spread to be reduced as

$$\theta_r = \frac{\theta_i}{\gamma_f^2 \left(1 + \beta_f\right)^2} \tag{6.14}$$

This effect is illustrated in figure 6.3.

Equations 6.11 to 6.14 reveal the $1/4\gamma^2$ dependence on the up-shifted: wavelength, pulse duration, and wavefront compression. An expression for the change in frequency can be expressed as

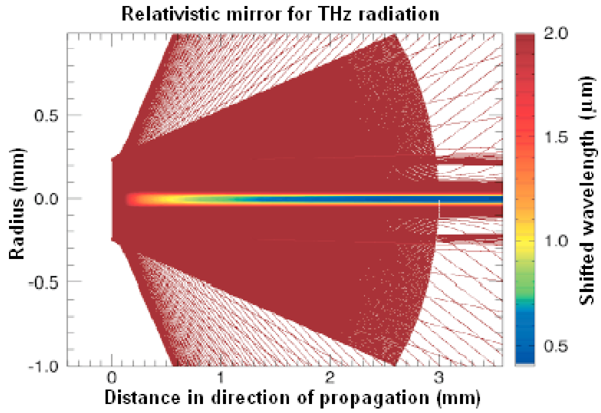

Figure 6.3: A ray tracing simulation of the up-shifted radiation. The red lines show the Lorentz radial compression of the light rays. The colour map shows the up-shift in wavelength of the backscattered radiation. (This simulation is courtesy of Golp IST group)

$$\Delta\omega = \omega_0 \frac{1+\beta}{1-\beta} - \omega_0 \tag{6.15}$$

6.3 Experimental results

6.3.1 Introduction

The main goal of the experiment was to collide a broadband THz pulse with an overdense relativistic ionisation front in counter-propagting geometry to double Doppler frequency up-shift the THz pulse into the visible region of the electromagnetic spectrum. Theoretical calculations imply that a THz pulse assuming that the ionisation front has a Lorentz factor of 12.9 ($\gamma = 12.9$). A 500 fs THz pulse would therefore experience a $1/4\gamma^2$ pulse compression, which equates to approximately 0.75 fs or 750 attoseconds, this is therefore an extremely attractive way to generate ultrashort pulses of light. Furthermore, the wavelength of the up-shifted THz radiation is decreased by the same factor. Therefore a THz pulse centred on 1 THz having a central wavelength of 300 μm would be up-shifted to 450 nm light. The bandwidth is conserved during the up-shift meaning that a 1 THz pulse with a bandwidth of 100 % will be Lorentz up-shifted to a light pulse centered on 450 nm with a 450 nm bandwidth i.e. a broadband white light pulse in the optical region of the electromagnetic spectrum. Moreover, varying the plasma density of the ionisation front changes its velocity (i.e. γ), which serves to increase or decrease the frequency and pulse duration of the up-shifted

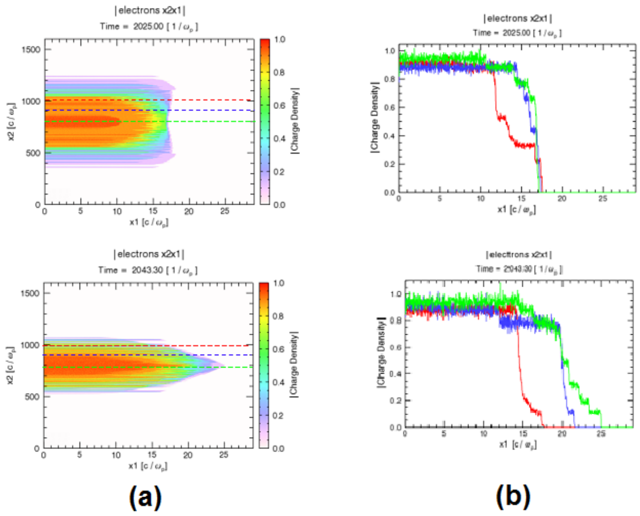

Figure 6.4: The rise time of the ionisations fronts plotted for (a) f-7.5 and (b)f-50 focussing. The Longer focal length serves to generate flatter, sharper fronts. The rise time for the long focal length (f-50) is $\sim$ 10 fs and for the short focal length (f-7.5)$\sim$ 37 fs. This simulation is courtesy of Golp IST group.

Parameter	Incident pulse	Reflected pulse	Compression factor
Wavelength	$\lambda_i = 300\ \mu m$	$\lambda_r = 450\ nm$	$1/4\gamma^2 = 666$
Frequency	$f_i = 1$ THz	$f_r = 0.6$ PHz	$1/4\gamma^2 = 666.$
Divergence	$\theta_i = 0.5$ rad	$\theta_r = 750\ \mu$rad	$1/4\gamma^2 = 666.$
Pulse width	$\tau_i = 500$ fs	$\tau_r = 750$ as	$1/4\gamma^2 = 666.$

Table 6.1: The pulse parameters of a 1 THz, 500 fs probe pulse focused onto a relativistic ionisation front with a front velocity of γ=12.9 before and after reflection.

pulse accordingly. Clearly, this an extremely attractive way to generate tunable radiation by changing the plasma density parameter. It is feasible that pulses of radiation can be 'tailored' by selecting the initial pulse parameters and variation of the plasma density. Table 6.1 shows the parameters before and after reflection of an electromagnetic terahertz pulse with a central frequency of 1 THz and a duration of 500 fs focused by an f-2 parabolic mirror on to a relativistic ionisation front with a velocity of γ=12.9.

6.3.2 The GaAs photoconductive antenna

The THz pulses were generated using a GaAs photoconductive antenna (figure 5.5) of which the physics has been discussed in section 5.0.2. Prior to the main experiment, the THz pulses from the emitter were characterised.

This involved measuring the electric field of the THz pulses using the kHz test bed based on the scanning delay technique shown in figure 5.2. The pulse duration and frequency spectrum of the THz pulses were measured using a scanning delay line and are shown in figure 5.2. The THz pulse duration was measured to be 500 fs (FWHM). By taking the Fourier transform of the temporal electric field profile $E(t)$ the frequency spectrum $E(\omega)$ was attained and is shown in figure 6.5. The frequency spectrum was found to be peaked on 0.5 THz and had a fwhm bandwidth of 100 %. Measurements were also taken to retrieve the refractive index and absorption coefficient of the GaAs wafer for THz frequencies using the framework described in section 5.2.1. Prior to this an electro-optic reference signal was taken by propagating the THz pulses through dry air in a Nitrogen purged box. A second scan was then taken with the experimental GaAs wafer (with no bias field applied) into the the THz beam path. Taking the fourier spectra of these electro-optic time signals gave the frequency response of dry air and GaAs. By comparison of these frequency spectra using equation 5.12 the refractive index of the GaAs wafer and absorption coefficient for 0.1–2 THz was obtained. A measured value of the refractive index at 1 THz was found to be $n \simeq 3.46$. This measurement was particularly important because it was needed for temporally overlapping the THz pulse with the ionisation front.

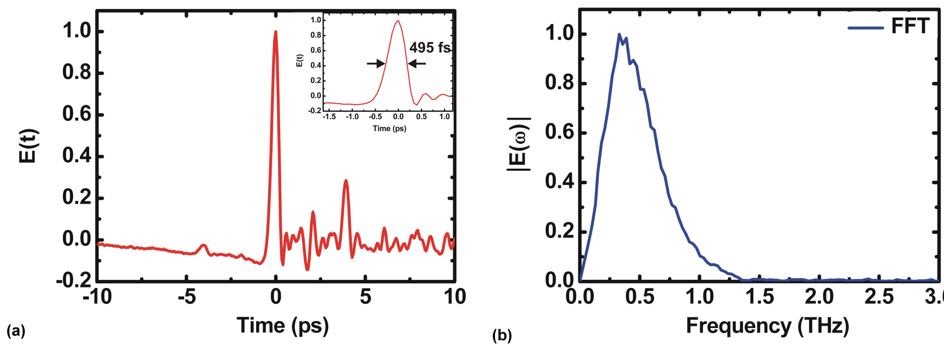

Figure 6.5: (a) The THz pulse detected by a 500 μm ZnTe crystal using a scanning delay line in conjunction with balanced detection. (b) The corresponding frequency spectrum retrieved by taking the FFT of the temporal THz signal.

6.3.3 Measurement of THz pulse energy

In order the estimate the detectability of the up-shifted radiation it is necessary to calculate the THz pulse energy before interaction with the relativistic ionisation front. The ionisation front generated in this experiment has a gamma factor of approximately 12.9, meaning that the pulse will experience a $1/4\gamma^2$ factor reduction in pulse energy. This effect has experimental detectability implications

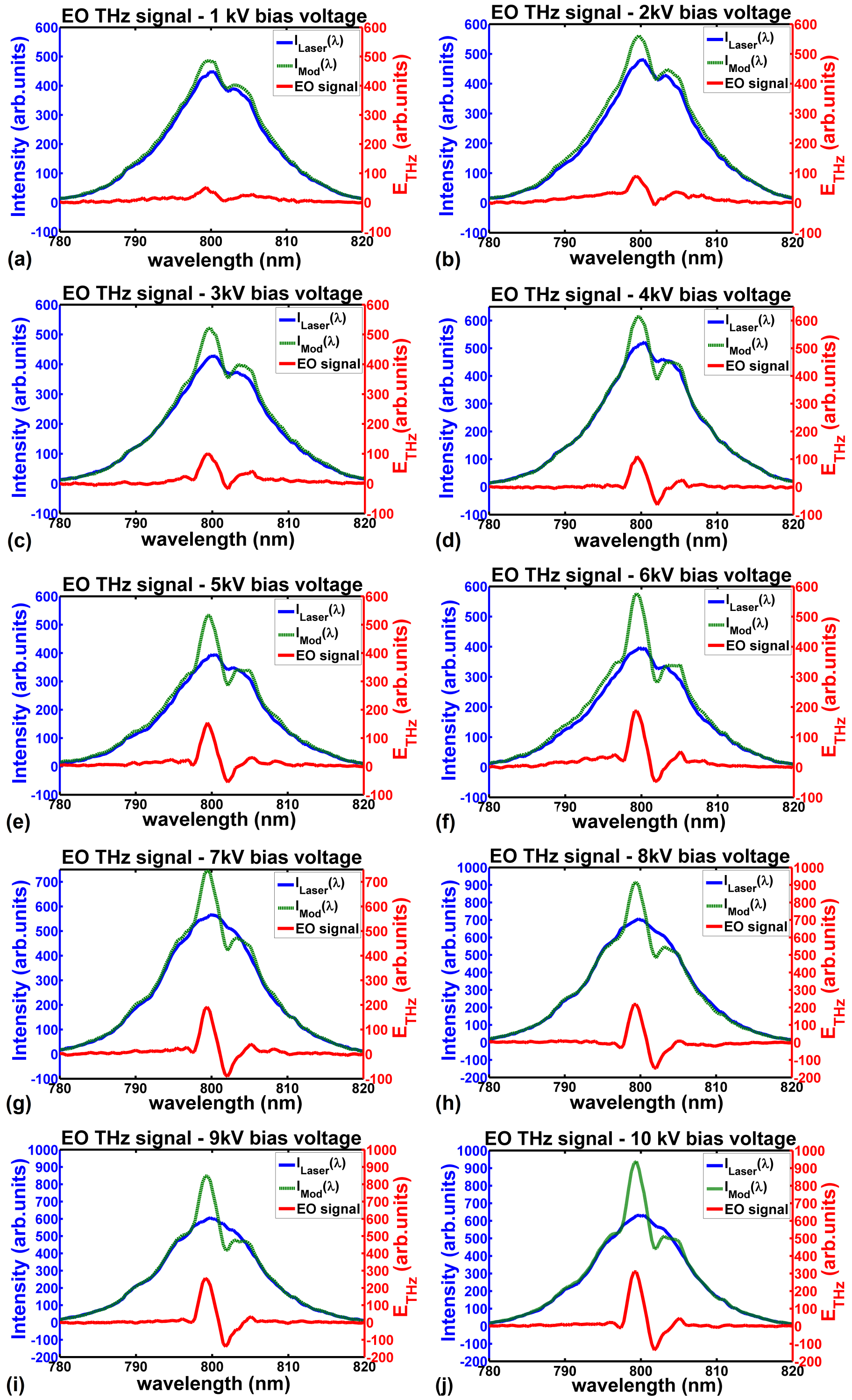

Figure 6.6: The electro-optic signal of the THz pulses from the GaAs photoconductive switch at (a) 1 kV (b) 2 kV (c) 3 kV (d) 4 kV (e)5 kV (f) 6 kV (g) 7 kV (h) 8 kV (i) 9 kV (j) 10 kV. In each figure the blue curve shows the laser spectrum with no THz present ($I_{Laser}(\lambda)$), the green curve shows the modulated laser spectrum with THz present ($I_{Mod}(\lambda)$) and the red curve shows the background subtracted EO signal.

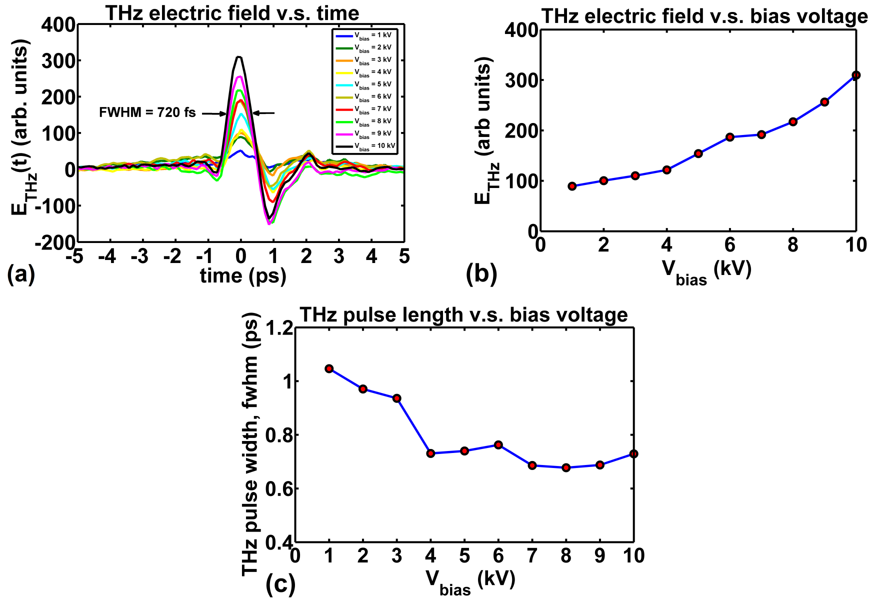

Figure 6.7: (a) The measured THz electric field, $E_{THz}(t)$, plotted for bias voltages of 1-10 kV. (b) The peak THz electric field measured as a function of the bias voltage. (c) The measured THz pulse width v.s. bias voltage.

because although the pulse energy is reduced the relative bandwidth remains unchanged i.e. the spectral density will be reduced by $1/4\gamma^2$ making it very challenging to detect the up-shifted radiation.

This leads to a factor of 670 reduction in pulse energy. Also important to consider is the $1/4\gamma^2$ reduction in reflected/up-shifted pulse energy, which when combined with the conservation of the relative bandwidth means that the up-shifted radiation pulse will have a reduced energy . Detectability of the up-shifted pulse.

The laser probe beam is p-polarised. After taking out the quarter waveplate (QWP) and the ZnTe crystal, the half waveplate (HWP) was rotated to minimize the signal on the spectrometer. In that geometry, the probe beam after the HWP becomes s-polarized and is rejected by the polarising beamsplitter cube (CVI). With this minimum transmission or extinction we optimised the position of the spectrometer using an x-y-z translation stage, to make sure the alignment of the spectrometer with respect to the laser did not change.

With the half waveplate set, the quarter waveplate (QWP) was installed into the probe beam and the signal again was minimised on the spectrometer. This means that the probe beam is still linearly polarised at that specific setting of the QWP. We then put in the ZnTe crystal. The signal on the spectrometer did not change, which indicates that there is no measurable birefringence from the crystal at that angle (we determined this to be the optimised angle for the ZnTe in previous experiments refer to chapter 5).

The absolute electric field strength of the THz pulse is easiest to determine with the quarter waveplate at 45° i.e circular polarisation. To accurately determine this angle the transmission for different angles of the QWP (without the presence of THz) was measured and is shown in figure 6.8(a). It can be seen that the maximum transmission occurs at 45°, which in fact corresponds to a setting of 45° on the rotation mount. The transmitted intensity, I_T, is now given by

$$I_T^{THz=0} = \frac{1}{2} I_0 T \tag{6.16}$$

With I_0 the intensity of the incoming probe beam and T the transmission coefficient of the crystal and the other optical components due to Fresnel reflections on the surfaces. The transmitted intensity is given by [204]

$$I_T^{THz} = \frac{1}{2} \left(1 - \cos\Gamma_{THz} \cos^2 2\delta + \sin\Gamma_{THz} \sin 2\delta\right) I_0 T \tag{6.17}$$

with δ the rotation of the quarter-wave plate and

$$\Gamma_{THz} = \frac{2\pi}{\lambda_0} n^3 r_{41} E_{THz} d \tag{6.18}$$

where λ_0 is the laser central wavelength (800 nm), d is the thickness of the ZnTe crystal (500 μm), n_{ZnTe} is the refractive index of the ZnTe crystal at 800 nm (2.85), r_{41} is the electro-optic coefficient for this crystal in this configuration (4.0 $\times$ 10^{-12} m/V) and E_{THz} is the THz electric field strength in the crystal. With the QWP at 45° (circularly polarized probe beam) we measure the effect of the THz on the transmitted signal. Equation 6.17 reduces to

$$I_T^{THz} = \frac{1}{2}\left(1 + \sin\Gamma_{THz}\right) I_0 T \tag{6.19}$$

The signal with and without the THz present is shown in figure 6.8(a). By combining equations 6.16 and 6.19 we find Γ_{THz}

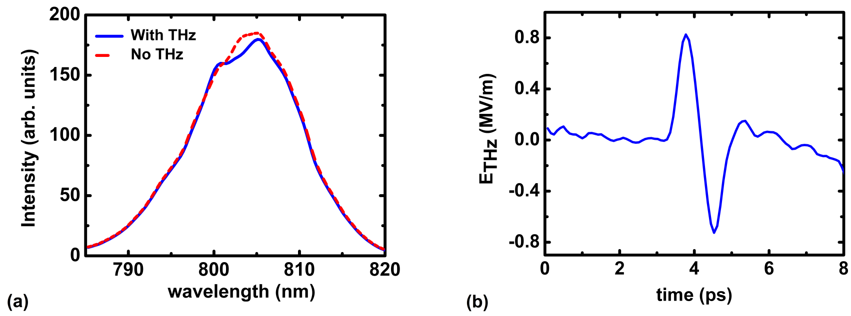

Figure 6.8: (a) The measured probe spectrum through the ZnTe crystal with no THz field applied (red curve) and with THz field applied (blue curve). (b) The measured THz electric field inside the ZnTe crystal.

Γ_{THz} is plotted in figure 6.8(b). To calculate the THz field outside the crystal, we have to correct for reflection at the surface ($t_{THz} = 2/(1 + n_{THz}) \cong 0.5$. The electric field strength of the THz pulse is then given by

$$E_{THz} = \frac{\Gamma_{THz}\lambda_0}{2\pi d n^3 r_{41}} 2 = \frac{\Gamma_{THz}\lambda_0}{\pi d n^3 r_{41}} \tag{6.20}$$

The THz pulse energy is then found by integrating over the area and the duration of the pulse

$$U_{THz} = \varepsilon_0 c d A d t \tag{6.21}$$

Integrating equation 6.20 and then numerically integrating the square of the pulse shown in figure 6.8(b) gives

$$U_{THz} = 2\pi\varepsilon_0 c \frac{(fwhm)^2}{8\ln 2} \int_t E_{THz}^2(0) dt \tag{6.22}$$

Plugging the numbers into these equation yield a value for the THz pulse energy of 2.6 nJ/pulse.

6.3.4 Measurement of THz focal spot

In order to determine the mode matching properties between the ionisation front and the focussed THz pulse it was necessary to measure the THz spot size. The THz spot size was measured using the set-up illustrated in figure **??** (to be made up with short description of layout), with a probe beam in counter propagation. The quarter waveplate was rotated to 2-3° for optimum signal-to-background ratio (near linear polarization). The crystal was imaged on the camera. The imaging was calibrated, using a 200 μm wire, which gave a conversion factor of 5.0 μm/pixel. The spot of the THz is measured by subtracting the images with and without a THz signal.

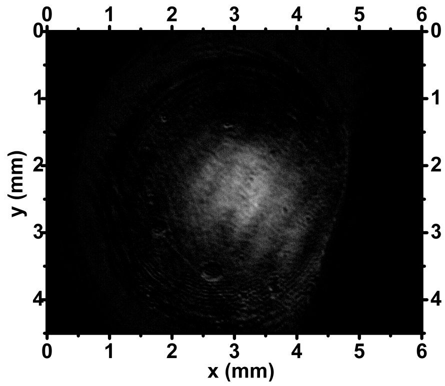

Figure 6.9: The electrooptic image of the focal region of the THz pulse.

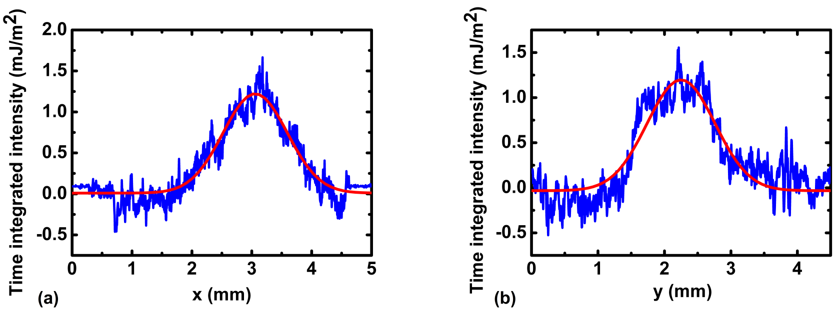

Figure 6.10: (a) An integrated intensity lineout along the x-plane of the focal region of the THz pulse encoded onto the ZnTe detector crystal. (b) An integrated intensity lineout along the y-plane of the focal region of the THz pulse encoded onto the ZnTe detector crystal.

So that the measured transmitted intensity (figure 6.9) is in fact proportional to the intensity of the THz pulse. The size of the THz focus is found by fitting a Gaussian to the horizontal and a vertical line-out through the center of the spot, shown in figure 6.10. The $1/e^2$ focussed spot width of the THz beam was measured to be 900 μm.

6.3.5 Temporal characterisation of THz pulses

In order to characterise the time profile of the THz pulses an electrooptic detection line was set up outside the vacuum chamber. Figure 6.11 shows the experimental set-up. A 1 mJ, 800 nm portion of the main pump laser beam was split off in order to illuminate the 12 kV biased GaAs wafer to generate the THz pulses. The THz radiation entered and exited the vacuum chamber through two Tsurupica windows (Microtech Instruments). Tsurupica is highly transparent in THz and visible spectral ranges and has the unique property that its refractive index is the same for THz and visible light ($n_{Tsurupica} = 1.52$). On entering the vacuum chamber the THz radiation was focused over the gas jet by an f-2 off axis parabolic mirror (f = 100 mm) with a 2 mm diameter hole in the centre (to allow backscattered radiation to be detected) it was then recollected, collimated and coupled out of the vacuum chamber by an identical parabola. This parabola had a 4 mm hole drilled through the centre to allow the focussing pump beam to pass through and focus over the gas jet. An Indium Titanium Oxide (ITO) mirror was used to direct the THz radiation to the ZnTe crystal where it could be probed using analysis of the chirped probe pulse in the spectrometer or by flipping a mirror the THz electric field could be probed using the cross-correlator set-up. Figures 6.12(a) to 6.12(d) show the background subtracted images of the $2\omega = 400$ nm light BBO crystal imaged using a 12-bit Quicam CCD camera.

The integrated lineouts are shown in figures 6.12(b) and 6.12(d) which show three distinct peaks on the X-correlator with a fwhm pulse width of ~ 500 fs.

6.3.6 Ionisation fronts

The ionisation fronts were characterised before colliding them with the THz pulses. Knowledge of the transverse dimensions and density of the ionisation fronts was necessary prior to collision experiments. The critical density for reflection of a 1 THz pulse is $n_c = 1 \times 10^{19}$ cm^{-2} therefore this criterion on the density had to be satisfied or exceeded to have a backscattered pulse. Furthermore, the THz focal spot was between 600 μm and 1 mm therefore it was important that the ionisation front had similar dimensions for maximum reflection efficiency i.e. mode matching the relativistic mirror with the THz pulse.

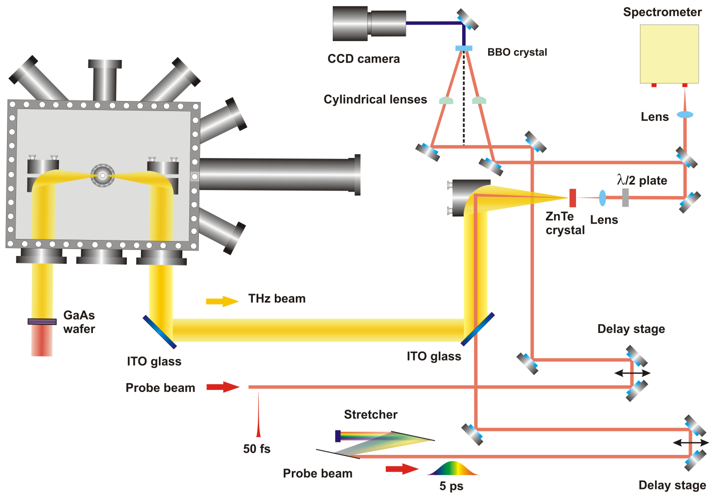

Figure 6.11: The optical layout and detection test bed used to characterise the THz pulses. The kHz laser reconstructed the THz pulses by phase matching a probe beam inside the ZnTe crystal.

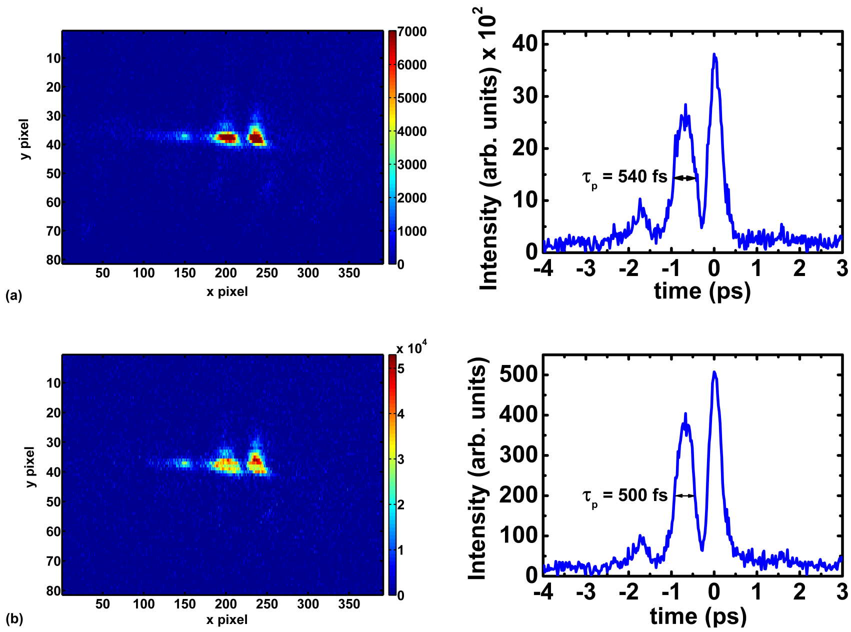

Figure 6.12: (a) A 2D false color image of the background subtracted signal from the BBO x-correlator. (b) An integrated line-out (figure 6.12(b) of the electrooptic signal from the BBO x-correlator. (c) A 2D false color image of the background subtracted signal from the BBO x-correlator. (d) An integrated line-out (figure 6.12(d) of the electrooptic signal from the BBO x-correlator.

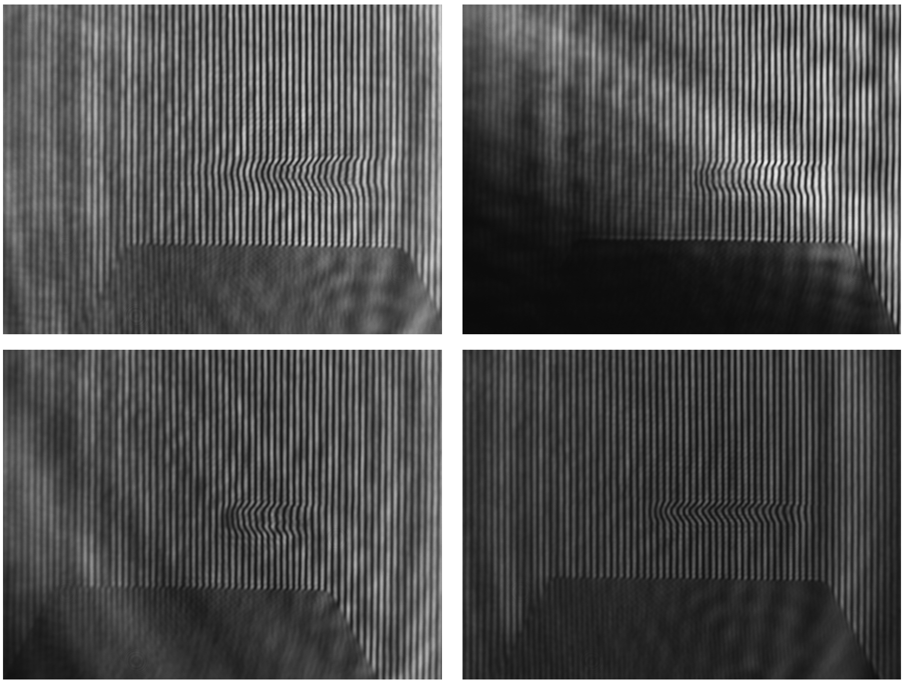

Figure 6.13: Mach-Zender interferogram images showing the ionisation front evolution through the gas jet. Delay between probe and pump = (a) (b) (c) (d).

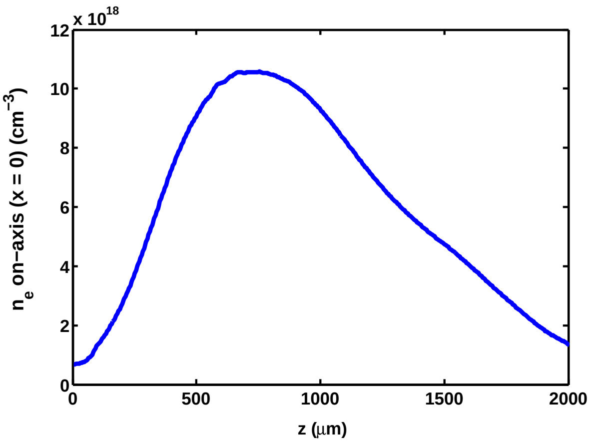

Figure 6.14: The on-axis density of the ionisation front. The peak plasma electron density was $n_e = 1.2 \times 10^{19}$. The laser energy, spot size, pulse duration, and intensity was 70 mJ, 40 μm, $\tau = 50$ fs and $I = 1.1 \times 10^{17}$ Wcm^{-2}.

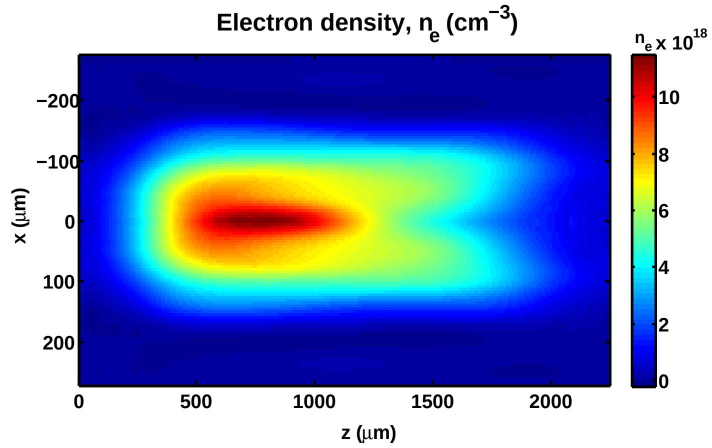

Figure 6.15: The 2D density map of the ionisation front. The peak plasma electron density was $n_e = 1 \times 10^{19}$. The transverse size of the ionisation front was approximately 200 μm.

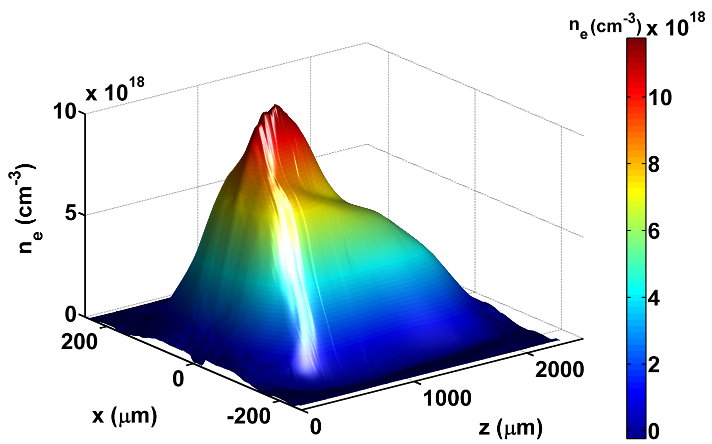

Figure 6.16: A 3D density map of the relativistic ionisation front. The peak plasma density is $n_e = 1 \times 10^{19}\text{cm}^{-3}$.

6.3.7 THz pulse collisions with ionisation fronts

After characterising the ionisation fronts and the THz pulses, experiments involving colliding the relativistic mirror with THz pulses were performed. In order to spatially overlap the front with the THz beam, the GaAs wafer was translated out of the path of the IR THz generation beam. This allowed the 1 mJ IR pulse to continue onto the THz focusing parabola and be focused over the gas jet. Shadography was used by blocking the arm of the Mach-Zender interferometer which did not pass over the gas jet. The gas jet was imaged using a f = 1000 mm lens onto a 16-bit CCD camera which allowed the shadows created by both plasmas to be viewed in real time using a trigger signal from the Stanford delay generator synchronised to the 10 Hz laser pulse train. Figure 6.17(a) shows the ionisation front colliding with THz generation IR beam.

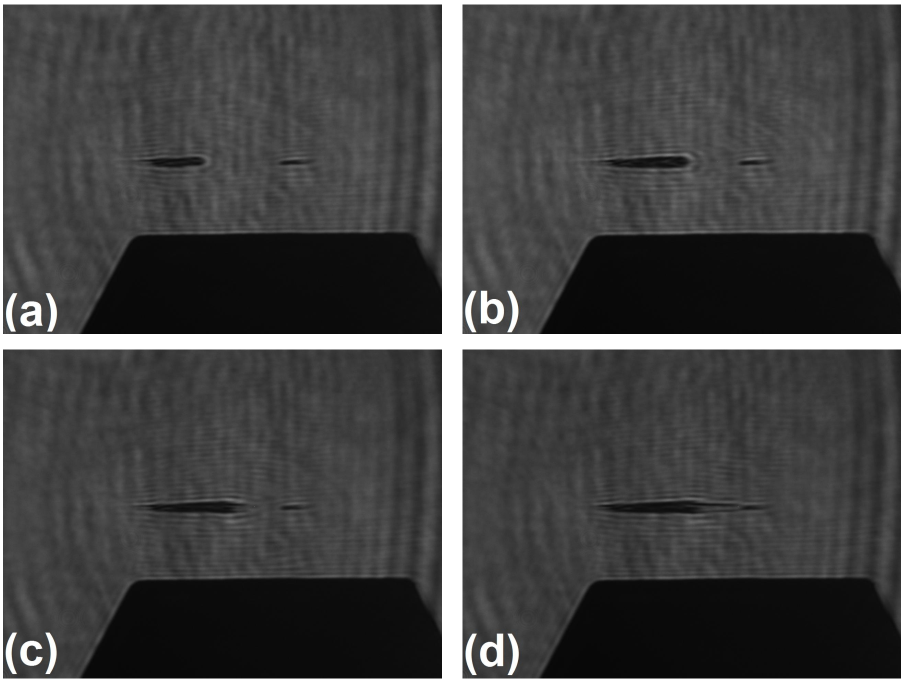

Figure 6.17: (a) Shadography images showing the technique used to overlap the THz pulse with the ionisation front in both space and time.

On the right hand side of these images one can see the 'virtual' THz pulse. This was fixed in space and time and the ionisation front was aligned to this spatially and temporally. This effectively acted as a virtual THz beam in space, and also in time albeit with a temporal offset defined by the optical thickness of the GaAs wafer at THz wavelengths. The two plasmas were overlapped in time by changing the delay stage of the drive beam (figure 6.19). After the two plasmas were overlapped the GaAs wafer was translated into the path of the THz generation beam. The delay of the pump beam was then changed to compensate for the increased phase delay imparted by the 500 μm thick GaAs wafer, i.e. optical thickness $= dn_{THz} = 500\ \mu m \times 3.5 = 1.75$ mm. This had to be divided by a factor of 2 as the delay stage is retro-reflected.

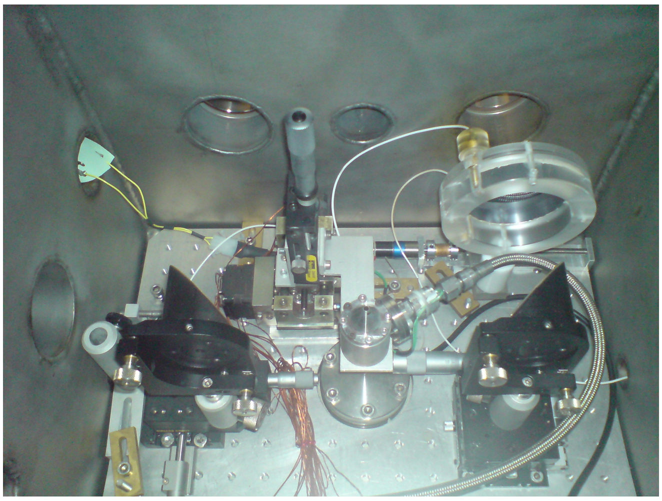

Figure 6.18: Inside the vacuum chamber used for the experiment to collide THz pulses with relativistic ionisation fronts.

The picture in figure 6.18 shows the set-up inside the vacuum chamber. The entrance port on the right hand side is where the IR beam is directed into the vacuum chamber onto the surface of the GaAs wafer. This generates a 2-3 nJ THz pulse which propagates to the parabola and is then focussed over the 4 mm supersonic gas jet. The pump beam passes through a lens and enters the chamber through a vacuum extension tube (figure 6.19). The focused beam passes through a hole in the back of the parabola shown on the right hand side of the chamber and the focal region is located at the centre of the gas jet. Both parabolas were on an x, y, z stage which helped with the alignment. In order to overlap the THz beam with the ionisation front the GaAs wafer was translated out of the path of the IR generation beam. It was then possible to follow the path of both counter-propagating beams using a piece of IR card. This allowed accurate overlap between the two beams. The left hand parabola's main purpose was to collect and re-collimate the transmitted THz radiation through the ionisation front. This diagnostic gave information about the THz power being lost after interaction with the ionisation front. The transmitted THz radiation is coupled out of the vacuum chamber and re-directed onto the ZnTe crystal in the electro-optic detection set-up external to the interaction chamber (figure 6.11)

By varying the pump delay and simultaneously measuring the THz electrooptic signal the transmission of the THz pulse through the ionisation front is mea-

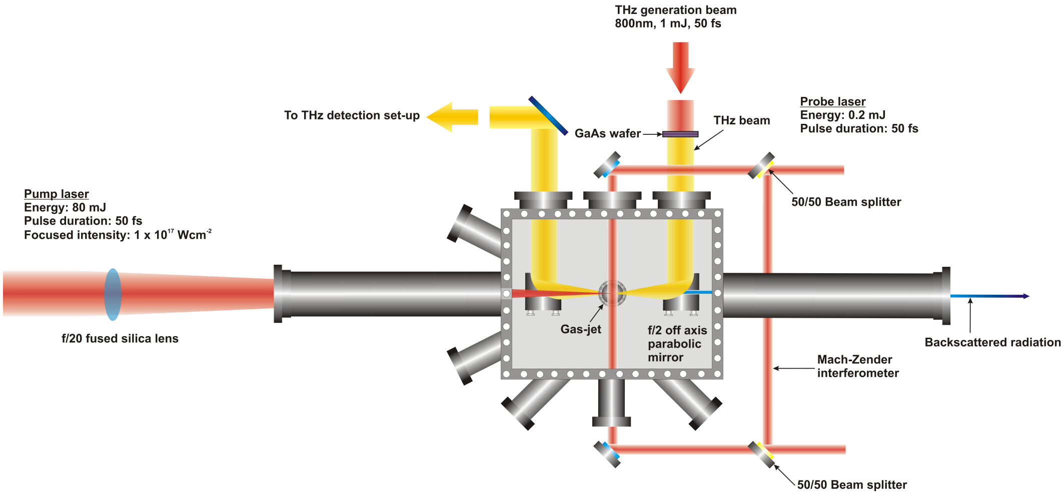

Figure 6.19: The experimental set-up used to collide a relativistic ionisation front with a THz pulse.

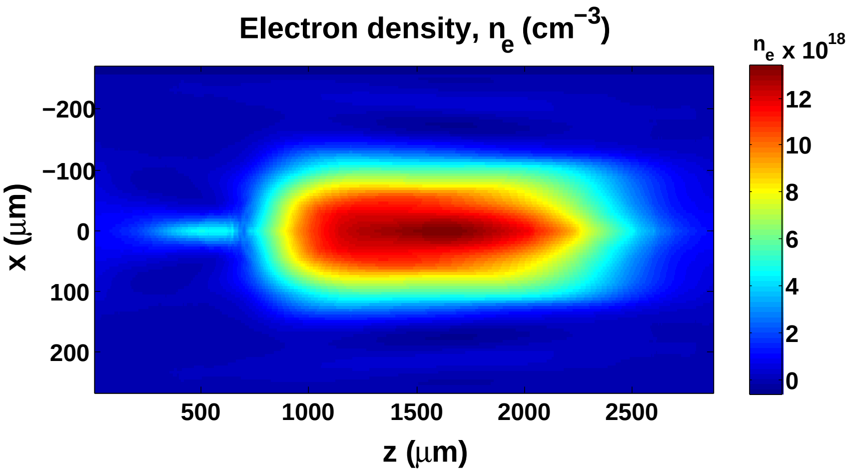

Figure 6.20: The on-axis plasma density profile of the ionisation front along the central laser axis.

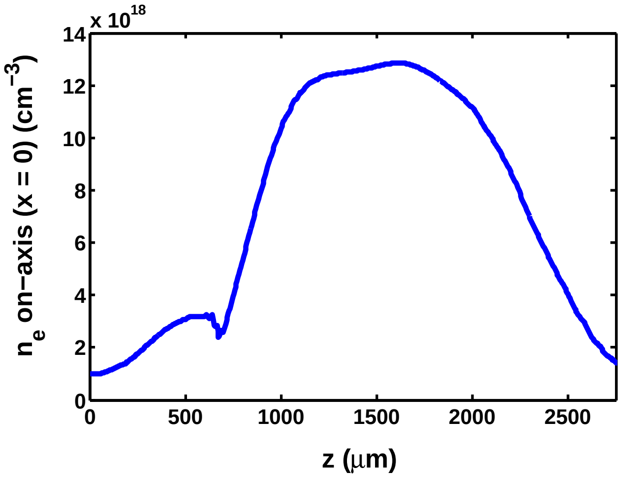

Figure 6.21: The on-axis plasma density profile of the ionisation front along the central laser axis.

sured as a function of the delay of the ionisation front relative to the THz pulse. The result of this measurement is shown in figure 6.22.

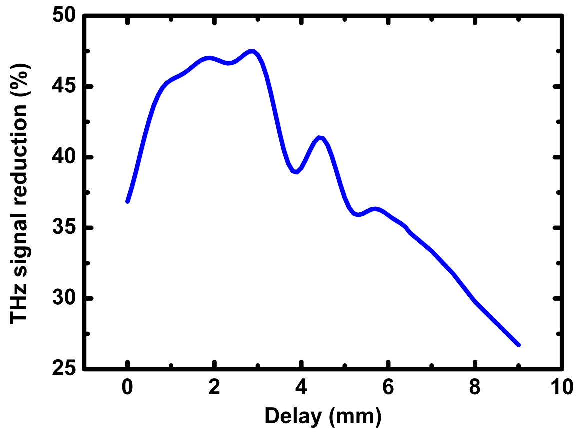

Figure 6.22: The THz electrooptic signal as a function of the delay between the ionisation front and the THz pulse.

6.4 Discussion

It has been established experimentally that the the THz pulse energy is approximately a few nanojoules. This result has implications in the detectability of the backscattered up-shifted radiation. The ionisation front possesses no kinetic energy therefore there exists no energy transfer between the ionisation front and the probe pulse This means that the up-shifted pulse energy will be of the order of $U_{THz}/4\gamma^2 = 3$ pJ

The ultimate goal of the experiment was to collide an overdense relativistic ionisation front into a THz pulse in counter-geometry and observe the Lorentz up-shifted radiation. This was a very challenging experiment for a number of reasons. Firstly it has a very complicated optical layout in that there are 6 different laser beams which require spatial and temporal synchronisation. In order to view the ionisation fronts the time delay between the drive pulse (ionisation front) and the Mach-Zender probe must be overlapped. The evolution of the front can then be scanned by varying the time delay stage on the drive beam. The two probe arms of the Mach-Zender also need to be synchronised to produce the interferences fringes that map out the phase delay when an ionisation front is present. Furthermore when the experiment was running in collision mode the THz detection external to the interaction chamber also had to be accurately aligned and temporally synchronised with the probe beams.

On a more fundamental level, it has been established experimentally that the THz pulse energy is approximately a few nanojoules. This result has implications in the detectability of the backscattered up-shifted radiation. The ionisation front possesses no kinetic energy therefore there exists no energy transfer between the ionisation front and the probe pulse This means that the up-shifted pulse energy will be of the order of $U_{THz}/4\gamma^2 = 3$ pJ. Furthermore, the conservation of bandwidth during the interaction means that a 1 THz pulse with 100 % bandwidth after up-shift will become a broadband optical pulse centred on 400 nm but with a 400 nm bandwidth. i.e. a pulse of white light radiation.The spectral density is therefore 'smeared' out over a large bandwidth and will be harder to detect using a dispersive spectrometer. For future experiments it will be essential to scale up the THz power in order to detect a reasonable signal. It may also be beneficial to use a single element detector with very high sensitivity down to the single photon level. Possible schemes to generate higher THz powers include optical rectification [247] and the generation of CTR from laser wakefield accelerators [109].

Chapter 7

Undulator radiation from laser accelerated electrons

Synchrotron radiation was first observed in 1947 by Elder and Langmuir [248] and was later confirmed through energy loss in storage rings. Since then it has been realised that synchrotron radiation is an invaluable tool for scientific exploration and is now used by scientists all around the world. Many accelerator laboratories have research projects making use of the radiation on a secondary basis to the main high energy research. However there exist many dedicated synchrotron light sources around the world today [125]. Conventional synchrotron light sources are often termed 'third generation' light sources and have been utilised as brilliant sources of incoherent radiation covering an extremely broad spectral range from terahertz frequencies to hard X-rays. Modern facilities deliver very high brightness radiation pulses at EUV and X-ray wavelengths and users span a wealth of research fields in physics, chemistry, engineering and the life and medical sciences. They have become essential tools for developing new drugs and materials and are powerful sources for imaging matter on all length scales, offering unique insights into biological function.

Free-electron lasers represent an increasingly important class of coherent optical light sources. They are known as 'fourth' generation light sources and can produce photon beams with a brightness that can be up to one billion times higher than a third generation synchrotron facility. They use the simple and elegant gain medium of an electron beam in a vacuum traversing a periodic magnetic field and have demonstrated ultrashort pulses of coherent radiation from THz to X-ray frequencies. FELs are usually based on the combination of a linear accelerator followed by a high-precision insertion device such as an undulator or wiggler. Under certain circumstances, the accelerated electrons in the insertion device bunch together more tightly than usual, to form microbunches. Over the length of the insertion device, the electrons in the microbunches begin to oscillate in phase and the radiation fields sum up coherently, to generate light with properties characteristic of conventional lasers. Because the microbunches are so tiny, the light generated comes in ultrashort pulses that can be used for strobe-like investigations of extremely rapid processes. Currently there is a wide scientific interest to produce coherent light in the water window. This means that radiation of wavelengths from 2.3–4.4 nm must be generated which puts extreme demands on the electron beam quality and peak current required to develop microbunching on the Ångström level. Unlike synchrotrons, which require high repetition rate, high average current electron beams between 1 to 10 GeV, FELs require lower energies and a more modest charge with very high peak currents with durations of less that 100 fs. Recent technological advances have heralded large increases in the average and peak brilliance delivered by X-ray free-electron laser facilities [125] [249], for example, at the LCLS in North America [250], XFEL in Europe [251] and SCSS in Asia [252]. These FEL light sources utilise radio frequency (rf) accelerating structures to produce bunches of relativistic electrons that are then injected into magnetic structures for radiation production. As has been discussed in chapter 2 conventional rf accelerators have limits on the maximum sustainable electric field in the cavity to of the order of 100 MV m^{-1} hence very large and expensive infrastructure is required to support FELs for EUV and X-ray wavelength ranges. Furthermore these large electron accelerators are also limited to produce pulse lengths nominally in the ps range, in the absence of electron bunch slicing techniques, [253] which can reduce durations to $\sim$ 100 fs. Laser wakefield accelerators offer an exciting alternative to rf accelerators. By using a plasma as the accelerating medium electric fields 3 orders of magnitude greater can be realised hence reducing acceleration lengths by a similar factor. This has huge implications on reducing the size and costs of future facilities by downsizing the infrastructure on all levels. e.g. equipment, staff, shielding etc. That aside the rf technology is fast reaching a technological plateau and facilities like the LHC at CERN are already at the top-end of how large they can feasibly be constructed spatially and financially. Moreover, LWFA can in theory produce electron bunches with pulse lengths less than a plasma wavelength which could potentially be as short as 1 fs or less. This means the peak currents of these beams can be as much as 30 kA, a property highly desirable for future generations of FELs.

This chapter presents the first ever experimental demonstration of an all optically driven synchrotron light source [6, 254]. Furthermore, a novel method of determining narrow energy spread electron beams from a laser plasma wakefield accelerator using undulator radiation has been realised [7]. This groundbreaking work paves the way for future development of this novel technology [184, 255, 256].

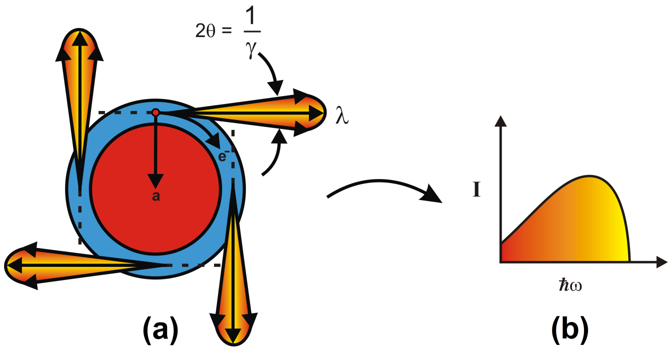

Figure 7.1: (a) The geometry of light emitted from a synchrotron light source. The light is emitted tangential to the electron trajectory as a cone of radiation with a half angle of $1/\gamma$. (b) The radiation spectrum of synchrotron light is very broadband.

7.1 Synchrotron radiation & devices

A charged particle which undergoes acceleration will radiate electromagnetic radiation [205]. If a charged particle moving with relativistic velocity is forced into a curved trajectory using a magnetic field it will acquire an angular acceleration resulting in radiation emitted as a narrow cone tangential to the path of the particle (figure 7.1). Generally, the most common way in which synchrotron radiation is produced is by directing relativistic electrons, previously accelerated using a linear accelerator (LINAC), into magnetic fields which bends the electrons into a curved trajectory. The resulting centripetal acceleration causes the electrons to emit synchrotron radiation.

There are three types of magnetic structures commonly used to produce synchrotron radiation: bending magnets, undulators and wigglers. Bending magnets cause a single curved trajectory resulting in a fan of radiation around the bend [257] (figure 7.1), which has been described as a 'sweeping searchlight x-ray beam'. Synchrotron radiation produced by bending magnets has a very broad angular distribution in the electron frame of reference. However, if one Lorentz transforms into the laboratory observation frame of reference, the angular distri-

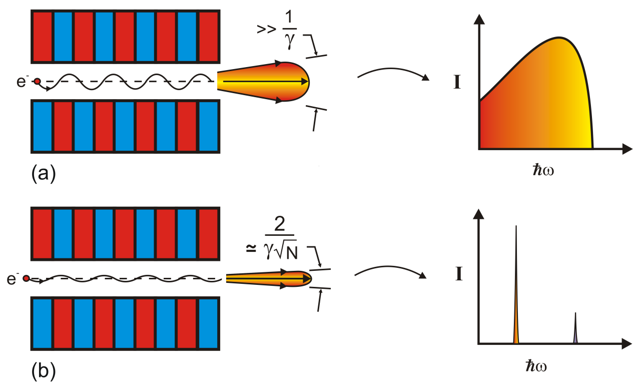

Figure 7.2: (a) The radiation emitted from a wiggler. The stronger magnetic magnetic field $K \geq 1$ gives rise to broadband light emitted into a large solid angle. (b) The radiation emitted from an undulator. The weaker magnetic magnetic field $K < 1$ gives rise to narrow-band light emitted into a small solid angle.

bution is compressed considerably resulting in a narrow radiation cone directed tangentially to the electron beam path. This radiation cone has a half angle approximately equal to

$$\theta \simeq \frac{1}{2\gamma}. \tag{7.1}$$

Undulators can be used to further compress the radiation both spectrally and spatially. They make use of periodic magneto-static structures with strong B-fields. These periodic fields cause the electrons to experience harmonic oscillations when moving in the axial direction, resulting in sinusoidal oscillations called undulations (figure 7.2(b)). These characteristic small undulations cause the resultant radiation cone to be narrow. An electron beam confined tightly in space directed into an undulator leads to radiation with a small angular divergence and relatively narrow spectral width, properties we generally associate with the coherence properties of lasers.

A stronger magnetic field variant of an undulator is called a 'wiggler'. Wigglers utilise greater B-fields to produce larger oscillation amplitudes resulting in a substantially larger radiation cone, emission bandwidth and associated radiated power (figure 7.2(a)). The non-dimensional parameter which defines the magnetic strength of a periodic magnetic structure is given by

$$K \equiv \frac{eB_0\lambda_u}{2\pi mc}, \tag{7.2}$$

where B_0 is the magnetic field and λ_u is the undulator period length. For $K < 1$ the device is known as an undulator and if $K > 1$ it is termed a wiggler.

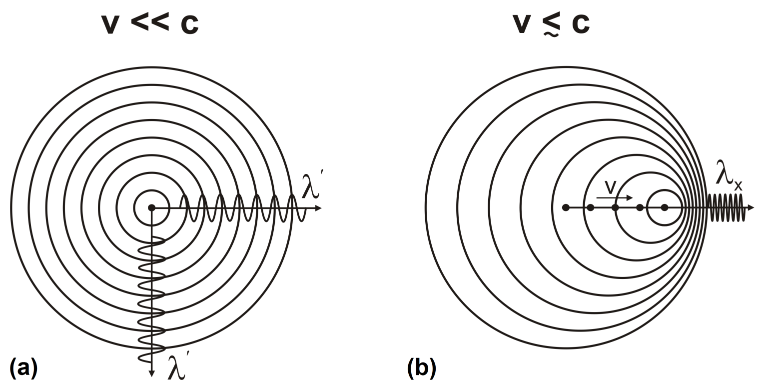

Figure 7.3: (a) The radiation from an oscillating charge moving at a non-relativistic velocity. (b) The radiation from a oscillating charge moving at a relativistic velocity. Short wavelengths are observed when the particle speed becomes comparable to the radiation speed, this serves to bunch the phase fronts together. This effect is known as the relativistic Doppler effect and is strongest on-axis, consequently the shortest wavelengths are observed here.

7.2 Undulator radiation

An electron traversing a periodic magnetic structure of moderate field strength will undergo a small amplitude oscillation and therefore radiate. If the electron oscillations are small compared to the radiation cone width, $\theta < 1/2\gamma$, the device is called an undulator. The resultant radiation is greatly reduced in wavelength, λ, from the undulator period, λ_u via Lorentz contraction and relativistic Doppler shifting by a factor $2\gamma^2$. As ,γ, can be several thousands in conventional accelerators, a typical undulator period of the order of 1 cm, can readily produce x-ray wavelengths.

Considering the frame of reference moving along with the electron beam, the electrons ‘see’ a periodic magnetic structure moving towards it with a Lorentz contracted period, λ', given by

$$\lambda' = \frac{\lambda_u}{\gamma}. \tag{7.3}$$

In the electron frame one may treat this problem as a classical radiating dipole; a point charge oscillating with an amplitude much smaller than the radiated wavelength. The frequency of this emitted radiation, in the reference frame of the electron is

$$f' = \frac{c}{\lambda'} = \frac{c\gamma}{\lambda_u}. \tag{7.4}$$

To an observer in the laboratory reference frame, Doppler shifting further reduces the radiation wavelength. The Doppler shift depends on the relative velocity and therefore the observation angle θ. From inspection of figure 7.3 it is clear that the shortest wavelength will be observed on axis where the phase fronts are closely bunched. The relativistic form of the Doppler frequency formula is

$$f = \frac{f'}{\gamma\left(1-\beta\cos\theta\right)} = \frac{c}{\lambda_u\left(1-\beta\cos\theta\right)}, \tag{7.5}$$

where $\beta \equiv v/c$ and θ is the observation angle measured from the direction of motion. The expression for the observed frequency on axis where $\theta = 0$, $\cos\theta = 1$. Hence equation 7.5 reduces to

$$f = \frac{c}{\lambda_u\left(1-\beta\right)} \tag{7.6}$$

for $\beta \simeq 1$ we have $1-\beta \simeq 1/2\gamma^2$. Therefore, the observed radiation frequency on axis is

$$f = \frac{2\gamma^2 c}{\lambda_u} \tag{7.7}$$

and the observed wavelength on axis is

$$\lambda = \frac{c}{f} = \frac{\lambda_u}{2\gamma^2}. \tag{7.8}$$

Considering Doppler shifts at small angles off axis $\theta \neq 0$, we can return to equation 7.5 and use the small angle approximation. The Taylor expansion for small angles [258] is, $\cos\theta = 1 - \theta^2/2...$; therefore,

$$\begin{aligned} f &= \frac{c}{\lambda_u\left[1-\beta\left(1-\frac{\theta^2}{2}+...\right)\right]} = \frac{c}{\lambda_u\left(1-\beta+\frac{\beta\theta^2}{2}+...\right)} \\ &= \frac{c}{\lambda_u\left(1-\beta\right)\left[1+\frac{\beta\theta^2}{2(1-\beta)}\right]} \end{aligned} \tag{7.9}$$

since $\beta \simeq 1$ and as $\beta = v/c$ approaches unity we have $1-\beta \simeq 1\ 2\gamma^2$, thus

$$f = \frac{2\gamma^2 c}{\lambda_u\left(1+\gamma^2\theta^2\right)}. \tag{7.10}$$

In terms of wavelength, $\lambda = c/f$, one has to first order

$$\lambda = \frac{\lambda_u}{2\gamma^2}\left(1+\gamma^2\theta^2\right). \tag{7.11}$$

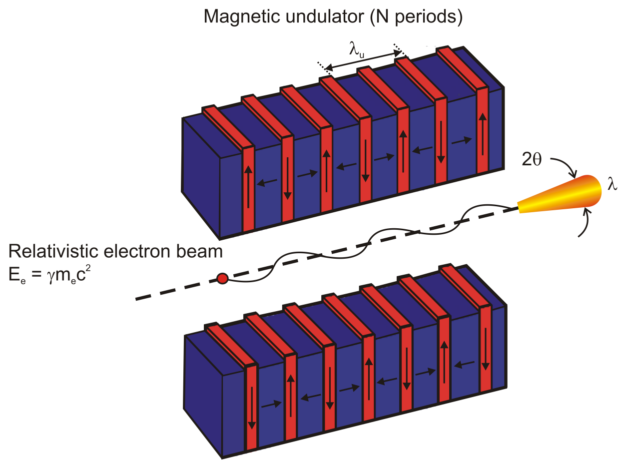

Figure 7.4: A schematic illustrating the narrow cone of undulator radiation generated by electrons whilst traversing a periodic magnet structure. The more energetic the electrons become the tighter the emission angle, θ, of the radiation cone and the shorter the emission wavelength, λ (figure adapted from [14]).

7.2.1 The undulator equation

In order to obtain a fully accurate expression for the spectral characteristics of undulator radiation, the magnetic field of the undulator has to be taken into account. The Lorentz equation is the starting point for this derivation and can be written in any frame of reference as

$$\frac{d\mathbf{p}}{dt} = q\left(\mathbf{E} + \mathbf{v} \times \mathbf{B}\right) \tag{7.12}$$

where $\mathbf{p} = \gamma m\mathbf{v}$ is the momentum, q is the charge, $\mathbf{v}$ is the velocity, and $\mathbf{E}$ and $\mathbf{B}$ are the electric and magnetic fields. To derive the undulator equation we may assume that the dominant field is the applied static $\mathbf{B}$-field associated with the magnetic undulator and that there are no applied electric fields. Furthermore, we consider the radiated electromagnetic fields due to the undulator radiation generated by the oscillating electrons to be weak in the sense that the radiated fields have negligible effect on the electron motion. To this level of approximation, we may take $\mathbf{E} \simeq 0$ in equation 7.12. In the case of free electron laser (FEL) action this would not be the case and the radiated fields lead to a modulation of the electron beam. This will discussed later in this chapter. With these approximations in place the momentum equation now becomes

$$\frac{d\mathbf{p}}{dt} = -e\left(\mathbf{v} \times \mathbf{B}\right) \tag{7.13}$$

For the undulator case with relatively weak radiated fields, we take the approxi-

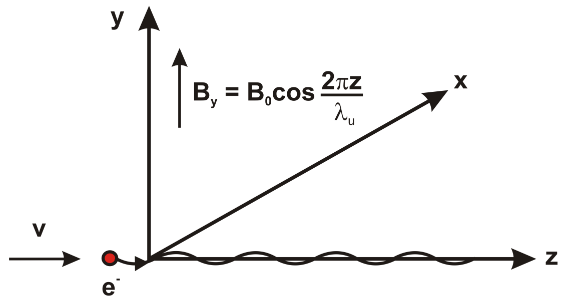

Figure 7.5: The geometry of electron motion in a periodic magnetic field.

mations $E \simeq 0$ and $\mathrm{B}_y = \mathrm{B}_0 \cos(2\pi z/\lambda_u)$ plus a negligible radiation field. Additionally, taking to the first order $v \simeq v_z$, the vector components in the x-direction give

$$m\gamma \frac{d\mathrm{v}_x}{dt} = e\mathrm{v}_z B_y. \tag{7.14}$$

substituting for B_y (geometry shown in figure 7.5 gives

$$m\gamma \frac{d\mathrm{v}_x}{dt} = e\frac{dz}{dt} B_0 \cos\left(\frac{2\pi z}{\lambda_u}\right). \tag{7.15}$$

Now we can solve for the transverse oscillation v_x. This gives rise to the primary source of undulator radiation. To first order, we will find v_x as a function of axial position z. Continuing the algebra

$$m\gamma d\mathrm{v}_\mathrm{x} = edzB_0 \cos\left(\frac{2\pi z}{\lambda_u}\right) \tag{7.16}$$

Integrating both sides gives

$$m\gamma \mathrm{v}_\mathrm{x} = \frac{eB_0\lambda_u}{2\pi} \sin\left(\frac{2\pi z}{\lambda_u}\right) \tag{7.17}$$

This is an exact solution of the simplified equation of motion, but note that z is not a linear function of time. That is, v_z is not constant, but oscillates (figure 7.5). As will be discussed in the next section, this leads to radiated harmonics of the fundamental frequency.

Rewriting equation 7.2 for completeness which is the non-dimensional magnetic strength parameter for a periodic magnet [14] as

$$K \equiv \frac{eB_0\lambda_u}{2\pi mc}. \tag{7.18}$$

or in convenient units

$$K = 0.9337 B_0(\mathrm{T})\lambda_u(\mathrm{cm}). \tag{7.19}$$

We may now express the electron's transverse velocity as

$$\mathrm{v}_x = \frac{Kc}{\gamma}\sin\left(\frac{2\pi z}{\lambda_u}\right). \tag{7.20}$$

The angle the electron motion makes with the z-axis is a sine function bounded by $\pm K/\gamma$,i.e.,

$$\tan\theta_e = \frac{\mathrm{v}_x}{\mathrm{v}_z} \simeq \frac{K}{\gamma}\sin\left(\frac{2\pi z}{\lambda_u}\right), \tag{7.21}$$

so that K is also defined as the magnetic deflection parameter. Approximating $\mathrm{v}_z = c$ the maximum electron excursion angle can be expressed as

$$|\theta_{e,\max}| \simeq \frac{K}{\gamma}. \tag{7.22}$$

This is the origin of the difference between undulator radiation and wiggler radiation. Recall that the characteristic half angle for emission of radiation is $\theta \simeq 1/2\gamma$. Thus, for magnet strength characterised by $K \leq 1$, the electron angular excursions lie within the radiation cone. This results in constructive interference effects that give undulator radiation its narrow bandwidth and narrow radiation cone characteristics.

In the strong field case, $K \gg 1$, wiggler radiation is generated. During this process interference effects do not occur due to various segments of an oscillation being widely separated in angle and therefore do not overlap in space after some propagation distance. Equation 7.20 is not a simple time harmonic, because $z = z(t)$ is only approximately equal to ct. The transverse oscillation influences the longitudinal velocity. To see this explicitly, we recall that γ is constant in a magnetic field; thus for motion in the x, z-plane ($\mathrm{v}_y = 0$),

$$\gamma \equiv \frac{1}{\sqrt{1-\frac{\mathrm{v}^2}{c^2}}} = \frac{1}{\sqrt{1-\frac{v_x^2+v_z^2}{c^2}}}. \tag{7.23}$$

Thus,

$$\frac{\mathrm{v}_z^2}{\mathrm{c}^2} = 1 - \frac{1}{\gamma^2} - \frac{\mathrm{v}_x^2}{c^2}. \tag{7.24}$$

Knowing v_x from equation 7.20, we can solve for v_z ;

$$\frac{\mathrm{v}_z^2}{\mathrm{c}^2} = 1 - \frac{1}{\gamma^2} - \frac{K^2}{\gamma^2}\sin^2\left(\frac{2\pi z}{\lambda_u}\right). \tag{7.25}$$

To first order in the small parameter K/γ,

$$\frac{\mathrm{v}_z}{c} = 1 - \frac{1}{2\gamma^2} - \frac{K^2}{2\gamma^2}\sin^2\left(\frac{2\pi z}{\lambda_u}\right), \tag{7.26}$$

where $\sin^2 k_u z = \frac{1}{2}(1 - \cos 2k_u z)$, and thus,

$$\frac{\mathrm{v}_z}{c} = 1 - \frac{1 + K^2/2}{2\gamma^2} + \frac{K^2}{4\gamma^2}\cos 2k_u z. \tag{7.27}$$

Hence, the axial velocity (z-direction) has a reduced average component and a component oscillating at twice the magnetic spatial frequency. By averaging over a single period, we can determine the average axial velocity, which plays a major role in the relativistic transformations. Defining the average quantity

$$\bar{\mathrm{v}}_z \equiv \frac{L}{T} = \frac{L}{\int_0^L dz/\mathrm{v}_z}, \tag{7.28}$$

where v_z is given in equation 7.27 and where T is the time required for the electron to travel a distance $L = N\lambda_u$. Then

$$\bar{\mathrm{v}}_z = c\left[1 - \frac{1 + K^2/2}{2\gamma^2}\right]\left[\frac{L}{\int_0^L \frac{dz}{1+\alpha\cos 2k_u z}}\right], \tag{7.29}$$

where

$$\alpha = \frac{K^2}{4\gamma^2\left[1 - \frac{1+K^2/2}{2\gamma^2}\right]}. \tag{7.30}$$

Expanding the denominator of the integral to second order in the small parameter α, one obtains

$$\bar{\mathrm{v}}_z = c\left[1 - \frac{1 + K^2/2}{2\gamma^2}\right]\left(1 - \frac{\alpha^2}{2}\right), \tag{7.31}$$

where the α^2 term is of the order $1/\gamma^4$ and thus can be ignored, so that the average axial velocity at finite K is given by

$$\frac{\bar{\mathrm{v}}_z}{c} = 1 - \frac{1 + K^2/2}{2\gamma^2}. \tag{7.32}$$

From this, we can define an effective axial value of the relativistic factor,

$$\gamma^* \equiv \frac{\gamma}{\sqrt{1+K^2/2}}, \tag{7.33}$$

where the asterisk refers to the reduction of the relativistic contraction factor by an amount $\sqrt{1+K^2/2}$. Hence equation 7.32 can be written as

$$\frac{\bar{\mathrm{v}}_z}{c} = 1 - \frac{1}{2\gamma^{*2}}. \tag{7.34}$$

As a consequence, the observed wavelength in the laboratory frame of reference is modified from that given in equation 7.11, now taking the form

$$\lambda = \frac{\lambda_u}{2\gamma^{*2}}\left(1+\gamma^{*2}\theta^2\right), \tag{7.35}$$

that is, the Lorentz contraction and relativistic Doppler shift now involve γ^* rather that γ. Expanding γ^* according to equation 7.33, one now has the undulator equation

$$\lambda = \frac{\lambda_u}{2\gamma^2}\left(1+\frac{K^2}{2}+\gamma^2\theta^2\right). \tag{7.36}$$

This equation describes the possibility of short wavelength generation through the gamma tuning term, $\lambda_u/2\gamma^2$. Clearly, high energy electron beams can thus generate x-ray wavelengths desirable for many experimental requirements. Additional tuning can be reached through the magnetic tuning term, $K^2/2$. Looking back at equation 7.2 it can be seen that K can be varied by tuning the magnetic field, B. The B-field can be altered by changing the magnetic gap. Other wavelengths may be selected through angular offsets from the undulator central axis $\gamma^2\theta^2$. This wavelength selection is usually done by defining an angular acceptance by aperturing the central radiation cone.

7.2.2 Spectral characteristics of undulator radiation

To quantify the spectral bandwidth of undulator radiation we recall equation 7.11 which to the first order described the undulator radiation wavelength in the laboratory frame and the radiation is primarily contained in a narrow cone of half angle $\theta = 1/2\gamma$. The corresponding spectral width within the central cone can be estimated by taking the difference of equation 7.11 for the defining two angles [14]. Taking the wavelength as λ on axis ($\theta = 0$), and $\lambda + \Delta\lambda$ off-axis at angle θ, then taking those ratios, one obtains

$$\frac{\Delta\lambda}{\lambda} \simeq \gamma^2\theta^2. \tag{7.37}$$

This equation shows how the radiation wavelength increases as the radiation is observed off-axis. The 'natural' bandwidth of undulator radiation is set by the number of oscillation periods, N

$$\frac{\Delta\lambda}{\lambda} = \frac{1}{N}. \tag{7.38}$$

When combining this with equation 7.37 it is clear that a narrower bandwidth radiation cone exists with a half angle

$$\theta_{cen} \simeq \frac{1}{\gamma\sqrt{N}}. \tag{7.39}$$

Physically this treatment must be modified to account for the electron motion in an undulator of finite K. We may now follow the same arguments using the corrected undulator equation 7.36. One obtains a corrected formula for the central radiation cone

$$\theta_{cen} = \frac{1}{\gamma^*\sqrt{N}} = \frac{\sqrt{1+K^2/2}}{\gamma\sqrt{N}}. \tag{7.40}$$

7.2.3 Undulator radiated power

The average power radiated by a single electron into the central radiation cone is given by

$$P_{cen,e^-} \simeq \frac{\pi e^2 c\gamma^2}{\varepsilon_0\lambda_u^2 N_u}\frac{K^2}{(1+K^2/2)^2} \tag{7.41}$$

with an associated bandwidth of $\Delta\lambda/\lambda = 1/N_u$ and a radiation cone half angle of $1/\gamma^*\sqrt{N_u}$. [14]. An important extension to this result is to the practical case of multi-electron bunches traversing the undulator. For N_e electrons radiating independently within the undulator, $N_e = IL/ec = IN_u\lambda_u/ec$, where $L = N\lambda_u$ is the length of the undulator, and I is the electron beam current. The power radiated into the central cone is then

$$P_{cen} \simeq \frac{\pi e\gamma^2 I}{\varepsilon_0\lambda_u}\frac{K^2}{(1+K^2/2)^2} \qquad K \leq 1 \tag{7.42}$$

Equations 7.41 and 7.42 are strictly valid for $K \ll 1$. This restriction is due to our neglect of K^2 terms in the axial velocity v_z. The P_{cen} formula, however, indicates a peak power at $K = \sqrt{2}$, suggesting that we explore extension of this very useful analytic result to somewhat higher K values. Kim [226] has studied undulator radiation for arbitrary K and finds an additional multiplicative factor, $f(K)$, which accounts for energy transfer to higher harmonics:

$$P_{cen,e^-} = \frac{\pi e^2 c\gamma^2}{\varepsilon_0 \lambda_u^2 N_u} \frac{K^2 f(K)}{(1+K^2/2)^2}, \tag{7.43}$$

where $f(K) = [J_0(x) - J_1(x)]^2$ and $x = K^2/4(1+K^2/2)$. For small values of K the multiplicative factor $f(K)$ can be approximated by

$$f(K) = 1 - x - \frac{x^2}{4} + \frac{3x^3}{8} + \ldots. \tag{7.44}$$

Power and energy emitted into arbitrary frequency intervals and solid angles may be calculated as well, but depend on the actual conditions. The total radiated power into the fundamental ($n = 1$), radiated into all angles and wavelengths, for small K is [14]

$$P_{tot(n=1)} = \frac{\pi e\gamma^2 I N_u}{3\varepsilon_0 \lambda_u} \frac{K^2}{(1+K^2/2)^2}. \tag{7.45}$$

The emitted radiation is usually expressed as spectral brilliance. This quantity measures the number of photons emitted per time interval (either per second - average brilliance, or per pulse length - peak brilliance), per unit area, unit solid angle and spectral bandwidth. The unit is photons/(s mm^2 mrad^2 0.1% BW).

7.2.4 Undulator harmonics

In addition to modification of the observed wavelength of the fundamental, the transverse oscillations of electrons traversing an undulator introduce higher harmonics of the electron motion. Subsequently, higher harmonics of the fundamental radiation component are produced at frequencies $h\omega_1$, and wavelengths λ_1/h where h is the harmonic number.

In order to understand how the harmonic undulator radiation scales with K considering equation 7.27 - repeated below

$$\frac{v_z}{c} = \underbrace{1 - \frac{1+K^2/2}{2\gamma^2}}_{\text{Reduced axial velocity}} + \underbrace{\frac{K^2}{4\gamma^2}\cos\left(2\cdot\frac{2\pi z}{\lambda_u}\right)}_{2\omega \text{ component of motion}} \tag{7.46}$$

which in the frame of reference moving with the electrons, gives

$$z'(t') \simeq \frac{K^2}{8k'_u}\sin 2\omega'_u t', \tag{7.47}$$

where $k'_u = \gamma^* k_u$ and $\omega'_u = \gamma^* \omega_u$. The transverse motion in this frame is

$$x'(t') \simeq -\frac{K}{k_u \gamma} \cos \omega_u \gamma^* \left(t' + \frac{z'}{c}\right). \tag{7.48}$$

To a higher degree of accuracy, we now keep the z'/c term

$$x'(t') = -\frac{K}{k'_u} \cos\left(\omega'_u t' + \frac{K^2}{8} \sin 2\omega'_u t'\right), \tag{7.49}$$

for small K

$$x'(t') = -\frac{1}{k'_u}\left(K \cos \omega'_u t' + \frac{K^3}{16} \cos 3\omega'_u t'\right). \tag{7.50}$$

Taking second derivatives to find acceleration, and squaring $|a'(t')|^2$

$$\frac{dP'}{d\Omega'} \propto n^4 K^{2n}. \tag{7.51}$$

Thus harmonics grow very rapidly for $K > 1$.

The two terms in equation 7.27 describe both the decreased axial velocity and an axial velocity modulation at twice the fundamental frequency, respectively. This is known as the second harmonic of the motion and is illustrated in figure 7.6. If the fundamental motion leads to radiation at frequency ω'_1 in the electron frame, then the axial harmonic motion causes emission of radiation at $\omega'_2 = 2\omega'_1$; hence, it is called the second harmonic radiation. The magnitude of the second harmonic scales as K^2. The second harmonic oscillations of the electrons are orthogonal to the fundamental oscillations. The fundamental radiation results from oscillations in the x-direction, while the second harmonic (and other even harmonics) result from oscillations in the z-direction. As a result the polarisation is different. Additionally when transformed into the laboratory frame, the angular distributions will be different. This is depicted in figure 7.7, which shows how the radiation patterns of the fundamental and second harmonics differ when transformed into the laboratory frame of reference.

For values of $K \geq 1$, additional harmonics will appear due to the continued mixing of harmonic motions. As K increases further $K \gg 1$, this mixing At very high $K \gg 1$, the radiated energy appears in very high harmonics, and at rather large horizontal angles $\pm K/\gamma$ (7.22). The large emission angles require large collection angles in order to spectrally merge nearby harmonics. The result is a continuum at very high photon energies, similar to that of bending magnet radiation, but increased by a factor $2N$. In all cases the observed wavelengths are governed by an extension of the undulator equation [14]

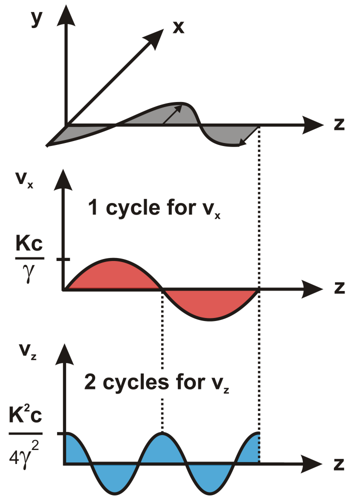

Figure 7.6: The first and second harmonic motions of electrons traversing a magnetic undulator (figure adapted from [14].

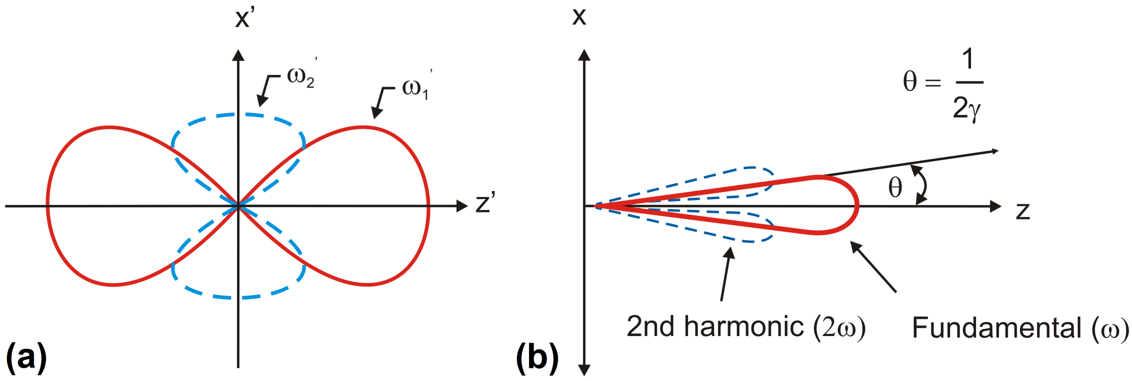

Figure 7.7: (a) The radiation patterns in the frame of reference moving with the average electron velocity and (b) the laboratory frame of reference.

$$\lambda_n = \frac{\lambda_u}{2\gamma^2 h}\left(1 + \frac{K^2}{2} + \gamma^2\theta^2\right) \tag{7.52}$$

The spectral characteristics of harmonic undulator radiation also differ depending on the observation frame of reference and is shown in figure 7.8. The narrow spectral width in the electron frame is set by the harmonic oscillation for a fixed number of periods, N, however in the laboratory frame of reference although shorter wavelengths are generated the spectrum is significantly broadened due to off-axis Doppler effects (figure 7.3)

$$\left(\frac{\Delta\lambda}{\lambda}\right)_n = \frac{1}{nN}. \tag{7.53}$$

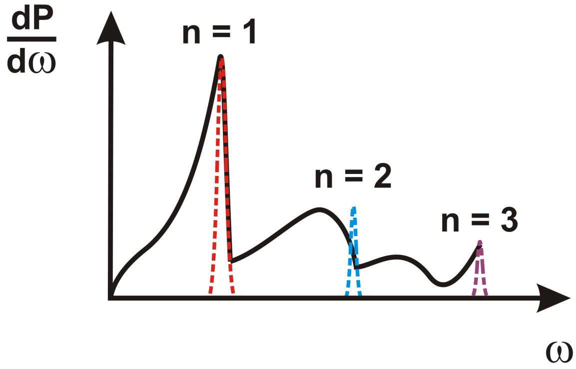

Figure 7.8: The harmonic radiation as seen in the frame of reference moving with the electron is narrow with a relative spectral bandwidth of $1/N$ (coloured dashed lines). In the laboratory frame of reference, the wavelengths are shorter, but the spectrum is broader due to off-axis Doppler effects.

7.2.5 Spectral characteristics of undulator radiation

For an undulator of N periods each electron oscillates through N cycles of its motion and thus radiates a wavetrain consisting of N well-defined cycles of the electric field (e.g. the motion in figure 7.5 exhibits 4.5 cycles). The Fourier transform of this waveform, gives the spectral content of the fields and has the form of a $(\sin x)/x$ or sinc function, where $x = N\pi u$, $u = \Delta\omega/\omega_0$, and $\Delta\omega = \omega - \omega_0$ is the frequency shift away from the central maximum at ω_0 as observed at a given angle, θ and undulator K value. An example of such a transformed waveform is shown in figure 7.9(d).

The intensity distribution observed in the laboratory frame is proportional to the square of the electric field. The normalised intensity distribution can be expressed as

$$I(\omega) \propto \left| \int_0^{N\lambda/c} \exp(-i\Delta\omega t)\mathrm{d}t \right|^2 \tag{7.54}$$

leading to the following

$$\frac{I(\omega)}{I_0} = \frac{\sin^2(\pi N\Delta\omega/\omega_0)}{(\pi N\Delta\omega/\omega_0)^2}. \tag{7.55}$$

The shape of the spectrum is shown in figure 7.9(d). The FWHM spectral linewidth of the radiation is $1/N$ centred on ω_0. This characteristic spectral output is called the 'natural' spread of radiation from an undulator and gives the narrowest possible spectral width. Such a spectrum would only be generated from an electron bunch with effectively zero energy spread and emittance, which in practical situations is not always the case. Even the most advanced particle accelerators produce electron beams with a finite size, divergence and energy spread. The total spectral width of the radiation is the sum of the contributions from broadening due to the energy, angular and natural spread components:

$$\left(\frac{\delta\lambda}{\lambda}\right)^2 = \left(\frac{2\sigma_\gamma}{\gamma}\right)^2 + \left(\theta^2\gamma^2\right)^2 + \frac{1}{N_u^2}. \tag{7.56}$$

It can be seen that an electron beam with an energy spread of $\Delta\gamma/\gamma$ corresponds to a photon energy spread of $2\sigma_\gamma/\gamma$

$$\frac{\Delta E}{E} = \frac{2\Delta\gamma}{\gamma} \tag{7.57}$$

Typically, the energy spreads in modern accelerator facilities are of the order of $\Delta\gamma/\gamma = 10^{-3}$, meaning that for undulators with over 100 periods this term has a small contribution to the spectral output.
A more significant effect is that due to the random angular motion of the electrons within the bunch.

$$\frac{\Delta E}{E} = \gamma^{*2}\alpha^2. \tag{7.58}$$

7.3 Free Electron Lasers

7.3.1 Introduction

Free-electron lasers represent an exciting class of coherent optical light sources. They use the simple and elegant gain medium of an electron beam in a vacuum traversing a periodic magnetic field and have demonstrated broad wavelength tunability and excellent optical beam quality [259]. This versatile tunability makes them extremely attractive for a variety of applications in the life sciences and medicine. Historically, the foundations of free–electron lasers go back to the early investigations of stimulated Thomson and Compton scattering carried out by Kapitza and Dirac in 1933 [260]. The physical framework of free-electron lasers evolved from the early work of H. Motz, who in 1951 proposed the theoretical grounding of the wiggler configuration now used in FEL's [261]. Subsequently, he went on to demonstrate the generation of incoherent radiation from such devices in both the millimeter and optical regimes [262]. Following this work, R. M. Phillips developed a device he termed the 'ubitron' [263] which used the same configuration of electron beam and magnetic field as proposed by Motz, but at

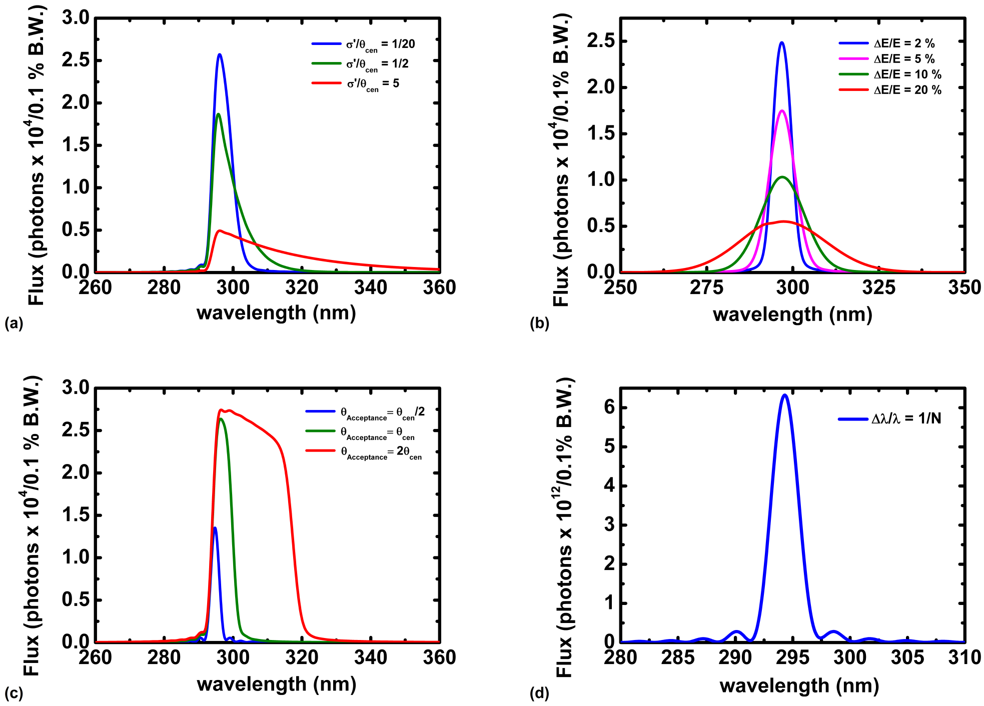

Figure 7.9: (a) The emittance spread. (b) The energy spread variation. (c) The angular spread variation. (d) The natural spread variation. The plots were calculated for a 100 MeV electron beam and an undulator with $N = 100$ periods, $K = 1$.

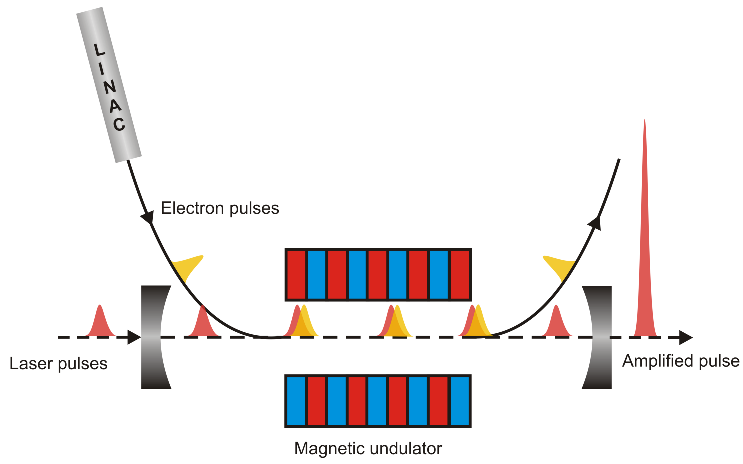

Figure 7.10: The early free electron laser which employed cavity mirrors to achieve gain in multi-pass geometry.

a high enough electron density that space-charge waves are excited in the electron beam [264]. High powers (> 1MW) and high efficiency were obtained at wavelengths from 10 cm to 5 mm. However, other devices developed at the same time, offered higher gain and the ubitron was not pursued. Then in 1970, John Madey of Stanford University, influenced by his research into synchrotron radiation, proposed what he called the Free electron laser [265]. In 1976 Madey and his co-workers went on to demonstrate gain with a free electron laser by using a 24 MeV electron beam and a 5 m wiggler to amplify the beam from a CO_2 laser [266]. A year later, mirrors were added to the system and the accelerator was operated at 43 MeV to demonstrate laser oscillation at a wavelength of 3.5 μm [267]. The obvious potential for very high lasing powers and broad wavelength tunability sparked great interest and experimental and theoretical work in FEL's expanded rapidly. In 1983 three FEL's were successfully operated, one at LURE, Orsay, France where an electron beam from a storage ring was used to achieve lasing in the visible [268]. The second was at Stanford, where a team used an electron beam from a superconducting accelerator to generate near IR radiation [269]. The third was at Los Alamos, where a newly constructed electron accelerator was used to observe lasing in the mid-infrared [270].

Since these initial systems FEL technology has progressed considerably. Current FELs are driven by state of the art electron accelerators which are typically powered by high voltage klystrons. The availability of low emittance, high current, muti GeV electron beams allows FELs to generate very high peak power, short wavelength radiation in the XUV and X-ray wavelengths.

The lack of suitable mirrors in the extreme ultraviolet and x-ray regimes prevent the operation of an FEL oscillator; consequently, there must be suitable amplification over a single pass of the electron beam through the undulator to make the FEL worthwhile, thus X-ray free-electron lasers (XFEL) utilise very long undulators lengths (tens of meters) and rely on the principle of Self-Amplified Spontaneous Emission (SASE). The SASE mechanism begins with all the electrons injected into the undulator being distributed evenly, hence they only emit incoherent spontaneous radiation. As the electrons further propagate down the undulator they can interact with this radiation and drift into microbunches separated by a distance equal to one radiation wavelength. Through this interaction, all electrons begin emitting coherent radiation in phase whereby the wave crests and wave troughs are superimposed on one another and sum up coherently. This results in an exponential increase of emitted radiation power, leading to high beam intensities and laser-like properties. Though SASE FELs can provide light with nearly full transverse coherence, the fact that they start from noise results in a photon beam that lacks longitudinal coherence. [271]. To avoid this, one can 'seed' an FEL with a laser pulse tuned to the resonance of the FEL [272] (figure 7.10). Such a temporally coherent seed can be produced by more conventional means, such as by high-harmonic generation (HHG) using an optical laser pulse [273]. This results in coherent amplification of the input signal; in effect, the output laser quality is characterized by the original seed pulse parameters. While HHG seeds are available at wavelengths down to the extreme ultraviolet, seeding is currently not feasible at x-ray wavelengths due to the lack of conventional x-ray lasers.

As has been discussed the synchrotron undulator radiation from an electron beam is substantially enhanced when the electron beam is pre-bunched either periodically, at a frequency, ω, within the spectral range of the synchrotron undulator radiation, or in single bunches of duration shorter than the optical period of the radiation frequency ($T = 2\pi/\omega$) [274]. In the first case the emitted radiation is entirely monochromatic and coherent, and in the second case its spectral range is equal to the undulator radiation bandwidth ω/N_u, where N_u is the number of undulator periods. In both cases, the emission power is proportional to the number of electrons per bunch squared, N_e^2, instead of just being proportional to the number of electrons or the beam current, as is the case for conventional synchrotron undulator radiation. This kind of enhanced radiation emission is a phenomenon of superradiance [275] as it stems from coherent constructive interference involving the summation of the electric field amplitudes of the radiation wavepackets emitted by all the electrons. Thus, the E field amplitude of the total radiation field is proportional to the number of electrons in the bunch N_b (or the beam bunching current I_b). Consequently the total emitted radiation energy or power is proportional to N_b^2 (or I_b^2).

A landmark experiment carried out in 2002 [257] demonstrated that this scheme can provide very high intensity radiation at THz frequencies using a magnetic dipole to generate coherent synchrotron radiation (CSR).

In 1997 Jaroszynski *et al* directly observed superradiance (SR) from an FEL oscillator [276]. In this work it was shown that the intensity and pulse duration of ultrashort superradiant pulses depends on the square and the inverse square root of the electron current, respectively.

Having discussed the current status of FEL systems it is now appropriate to discuss how laser wakefield accelerators can enhance this technology. As has been discussed a potential and very attractive alternative to rf electron acceleration is based on the laser wakefield accelerator. A laser wakefield accelerator married with a periodic magnetic undulator to produce synchrotron radiation has excellent potential as a compact, brilliant source of short wavelength radiation. To achieve very high energies conventional synchrotrons require long and expensive multi-staged accelerators. Their high cost is due to the numerous high power microwave sources required, the electron beam containment equipment (vacuum pumps, superconducting magnets etc), the highly engineered accelerator system and the huge shielding infrastructures needed to safely house them. Usually, the electron beam must be maintained in a vacuum which requires the use of numerous pumps along the beam path. This equipment is bulky and expensive.

A potentially revolutionary way of driving an FEL is to use an electron beam from a plasma wakefield accelerator. Advantages of using LWFA's include reduced cost and size of infrastructure but also because in principle they can produce intrinsically short electron bunch durations of < 5 fs. This means that LWFA's can generate electron beams with very high peak currents which is necessary for efficient gain in the next generation of FEL amplifiers. For a long undulator the intensity gain of an injected or spontaneous field grows exponentially along the undulator, until it reaches a saturation value. The gain is given by $I = (I_0/9)\exp(2z/L_g)$, where z is the propagation distance and L_g is the gain length given by, $\mathrm{L_g} = \lambda_u/2\sqrt{3}\pi\rho$. The gain length is a function of the electron beam energy γ, peak current, I_p and normalised emittance ε_n and is quantified by the FEL parameter, ρ. For a matched electron beam, ρ is given by $\rho = 1.1\gamma^{-1}B_u\lambda_u^{4/3}I_p^{1/3}\varepsilon_n^{-1/3}$. The FEL output intensity will saturate after a distance of approximately 10 times the gain length, $10L_g$ and the intensity at saturation is about ρ times the beam energy.

7.3.2 Spontaneous emission

So far the radiation that has been discussed is simply the radiation emitted by the electrons travelling along the undulator in the absence of any other fields. This weak, incoherent radiation shares the same fundamental mechanism to the spontaneous emission in a conventional laser and it represents the 'noise' from which laser oscillation grows. This undulator or wiggler radiation is incoherent because the electrons passing through the magnetic structure are randomly positioned inside the electron beam, thus the waves they emit have random phases with respect to one another 7.11(a). The field amplitude corresponding to the sum of these randomly phased waves, is proportional to the square root of the number of electrons in the beam. The optical intensity, or power, which is proportional to the square of the field amplitude, is therefore proportional to the number of electrons in the beam, that is, the electron beam current.

7.3.3 FEL coherence

We can understand how a free electron laser develops coherence by examining the behavior of a single electron in an undulator when a coherent optical beam is present. Considering an optical beam propagating parallel to the electron, then the electric field or ponderomotive force is transverse to the electron's motion. In the electron frame of reference one sees the electron oscillating transversely to the undulator axis. The electron motions are thus parallel or anti-parallel to the electric field of the optical beam. Near resonance, the optical frequency is matched to the electron frequency in the electron frame of reference. Thus, if the electron and the electric field are in phase, the electric field will always point in the same direction as the electron motion. This causes the electron to lose energy. Conversely, considering an electron which is half a wavelength out of phase (either in front or behind) with the electric field then this will gain energy. After a short time, the more energetic electrons will catch up to the less energetic ones, and the electron beam which initially consisted of randomly distributed electrons soon consists of bunches of electrons spaced at the optical wavelength. The brilliance of radiation from an undulator can be greatly enhanced if the electron beam is bunched on the wavelength scale. This can be achieved by either pre-bunching the beam on the wavelength scale or as already discussed producing a density modulation or bunching with a periodicity close to the resonance wavelength of

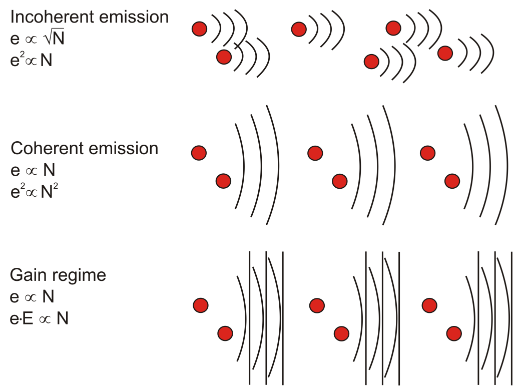

Figure 7.11: A schematic illustrating the emission regimes.(a) Incoherent emission is observed when the electrons are randomly positioned within the bunch, hence the emitted waves also have random phases.(b) Coherent emission can be achieved when the electron bunch structure is less than the Lorentz shifted radiation wavelength (all electrons emit in phase with one another).(c) Bunching of the electrons caused from interactions with a laser beam leads to powerful coherent lasing.

the undulator (equation 7.36). The free electron laser relies on the electron beam bunching caused by the interaction of the ponderomotive force of an externally injected optical field or spontaneously emitted radiation with the undulator field. Furthermore the bunching leads to field enhancement which further bunches the electron beam resulting in an instability and high amplification gain. The waves radiated by the initially random electrons then add in phase with one another, and the amplitude of the sum is proportional to the number of electrons. The intensity of the radiation, which is proportional to the square of the field amplitude, is then proportional to the square of the number of electrons. The sum of the fields $E(k,r)$ radiated by an ensemble of electrons in an undulator or wiggler gives an intensity,

$$\left\langle |E(k)|^2 \right\rangle = N_e \int f(k,r)E(k,r)^2 dr + N_e\left(N_e - 1\right)\left(\int f(k,r)E(k,r)dr\right)^2, \tag{7.59}$$

where $f(k,r)$ is the bunch form factor giving the probability of an electron being located at r and N_e is the number of electrons in the bunch.

7.3.4 Electron beam emittance

Electron beam emittance is a very important parameter when considering electron beams as drivers of FELs. The emittance parameter is a measure of the transverse spatial quality of a given electron beam. Advanced accelerators aim to keep

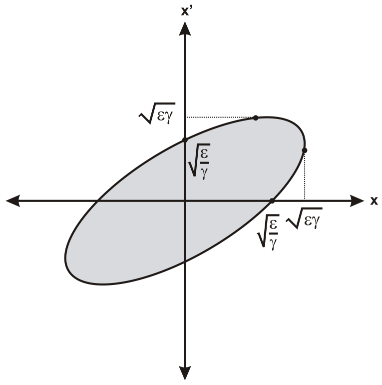

Figure 7.12: The parameters of an electron beam with an elliptical envelope in the phase plane.

the emittance minimised in order to avoid spectral broadening of the produced undulator radiation. The un-normalised r.m.s. emittance, $\varepsilon_{r.m.s.}$ of an electron beam of radius, r_e is analogous to the wavelength of the laser beam (i.e. has units of length), is given by

$$\varepsilon_{r.m.s.} = \pi\sigma_{\beta\perp}r_e = k_\beta r_e^2, \tag{7.60}$$

where $\sigma_{\beta\perp}$ is the variance of the normalised transverse velocities and $k_\beta = 2\pi/\lambda_\beta$ is the betatron wavenumber. To describe the transverse motions of the electrons as they travel down the undulator axis it is useful to introduce the transverse phase plane of the electrons. The transverse phase plane is a similar concept to the longitudinal phase plane used to describe the motions of the electrons in the energy and phase. The canonical variables of the transverse motions are x, p_x, and y, p_y. However, it is conventional to use the coordinates x, x', and y, y' where in the paraxial approximation,

$$x' = \frac{dx}{dz} = \frac{dx/dt}{dz/dt} = \frac{\partial H/\partial p_x}{\partial H/\partial p_z} = \frac{p_x}{p_z} \approx \frac{p_x}{\beta\gamma mc}. \tag{7.61}$$

A similar equation holds for y'. The electron orbits as they propagate along the undulator axis (z-direction)

$$\varepsilon_x = \sqrt{\left(\langle x^2\rangle \langle x'^2\rangle - \langle xx'\rangle^2\right)}, \tag{7.62}$$

where the brackets indicate an average over the electron in the beam, with a similar equation holding for ε_y. The r.m.s. emittance is defined as the transverse momentum/phase space area of the electron beam [229].
where p_x and x are the transverse momenta and coordinates of an electron re-

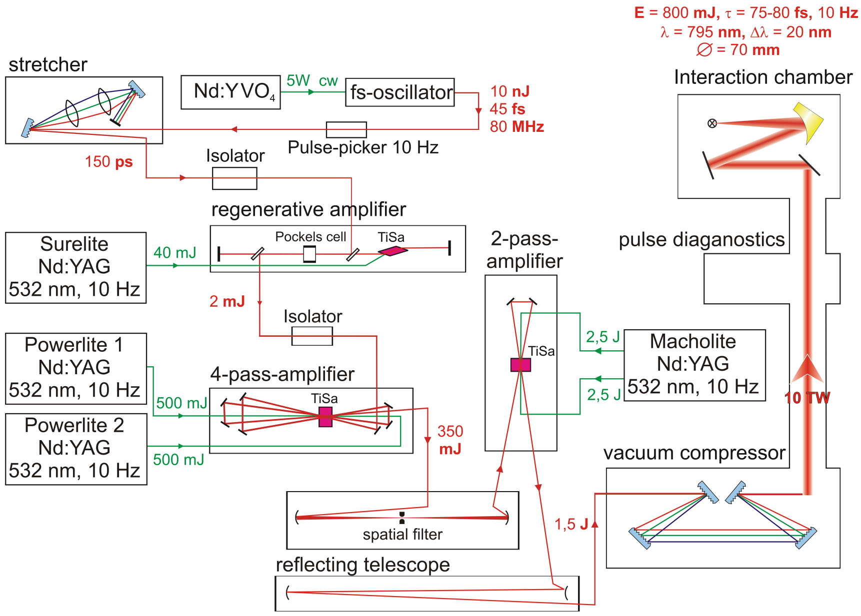

Figure 7.13: A schematic overview of the Jena 10 TW Titanium:Sapphire laser system (JETI) based on CPA technique.

spectively,

$$\varepsilon_{r.m.s.} = \sqrt{\left(\langle x^2 \rangle \left\langle \left(\frac{p_x}{m_e c}\right)^2 \right\rangle - \left\langle \frac{x p_x}{m_e c} \right\rangle^2\right)}. \tag{7.63}$$

The normalised emittance, $\varepsilon_n = \beta_z \gamma \varepsilon_{r.m.s.}$ governs the broadening through the $\gamma\theta$ term in equation 7.36. Under optimum conditions the electron beam will be 'matched' to the undulator, meaning that the betatron wavelength, $\lambda_\beta \approx L_u$, where L_u is the undulator length. When the Fresnel number $F = r_e/\lambda_\beta L_u \approx 1$ and the electron beam divergence, given by $\theta \approx \varepsilon_{r.m.s.}/r_e$, matches the diffraction angle of radiation emitted by the undulator ($\theta \approx \lambda/r_e$) i.e. when $\theta^2 \approx 2k_\beta \varepsilon_{r.m.s.}$. The brilliance is maximised when the divergence of the electron beam is

$$\theta_{matched} \approx 2\sqrt{\frac{\lambda_u \varepsilon_n}{K_u}}. \tag{7.64}$$

7.4 Experimental results

7.4.1 Experimental details

The JETI laser system

An overview of the JETI layout is given in figure 7.13 Like all high intensity laser systems, JETI is based on the chirped pulse amplification principle (CPA) [15].

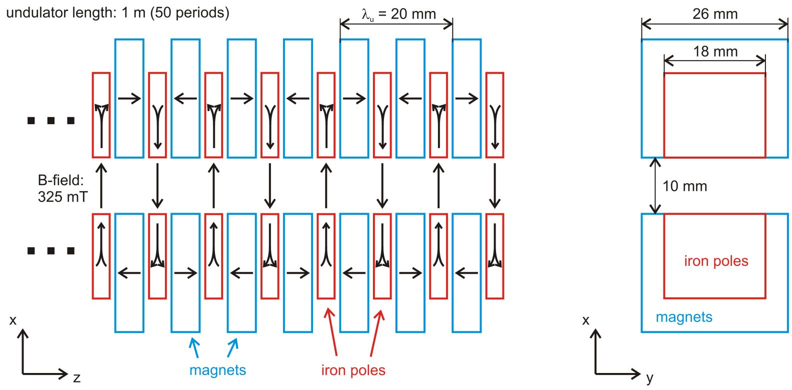

Figure 7.14: An illustration showing the undulator dimensions and magnetic construction.

The laser front end consists of a commercial Ti:S oscillator ('Tsunami', Spectra Physics), which is pumped by a 5W cw-Neodymium:YVO4 laser ('Verdi', Coherent) and delivers pulses of 10 nJ energy with 45 fs pulse duration (FWHM of laser intensity) at a central wavelength of $\lambda = 795$ nm. Before entering the first of three amplifiers, the initial repetition rate of 80 MHz is reduced to a 10 Hz pulse train by a Pockels cell-based pulse picker. The pulses are then stretched by a double-pass grating stretcher, which introduces a positive chirp ($d^2\phi/dt^2 = d\omega/dt > 0$), where ϕ is the spectral phase of the pulse and ω is the laser angular frequency) to increase the pulse duration to 150 ps. These pulses then enter a regenerative amplifier, which increases the pulse energy to a saturation value of 2.5 mJ after 12 round trips. The regenerative amplifier is followed by an ultra-fast Pockels cell to suppress pre-pulses and reduce contributions of amplified spontaneous emission (ASE). The remaining two amplification stages are both multi-pass amplifiers (a '4-pass butterfly' and '2-pass butterfly') pumped by frequency-double Nd:YAG lasers ('Powerlite' and 'Macholite' series, Continuum), which increase the pulse energy to 320 mJ and a final maximum energy of 1.35 J, respectively. Between the two multi-passes, a spatial mode filter (pinhole) is located at an intermediate focus to smooth the beam profile. A telescope then collimates the laser to a $1/e^2$-beam diameter of approximately 7 cm, before it enters the 4-grating vacuum compressor. The initial pulse duration cannot be recovered completely due to gain narrowing and nonlinear dispersion imposed during the amplification process, and the final pulse duration amounts to $\tau_{laser} = 80$ fs. The transmission efficiency of the compressor is limited to about 65% resulting in a total pulse power of 10 TW available for experiments at JETI.

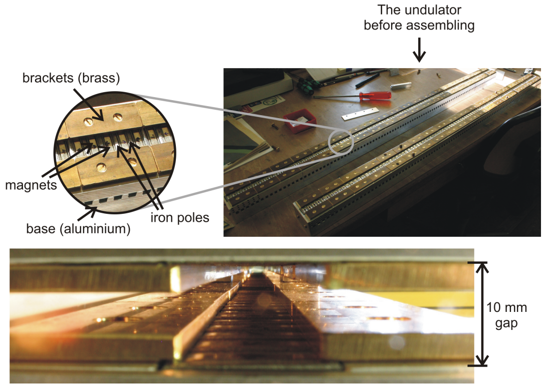

Figure 7.15: The two halves of the undulator before construction.

7.4.2 The undulator

The undulator was constructed from permanent magnets in a hybrid structure with a period of λ_u = 2 cm and a length of 1 m (N_u = 50 periods). The gap between the magnets was set to 10 mm and the maximum magnetic field strength on axis was B_0 = 330 mT. This yielded an undulator parameter K=0.6. The first and last 3 periods of the undulator were equipped with ferromagnetic screws allowing adjustment of the magnetic field for on-axis injection and ejection of the electrons. Figure 7.16(a) displays the measured B-field on axis and the electron trajectories calculated using the following equations:

$$\ddot{y}(z) = -\frac{q}{\gamma m} c B_x(z) \tag{7.65}$$

$$\dot{y}(z) = -\frac{q}{\gamma m} \int B_x(z) \mathrm{d}z \tag{7.66}$$

Integrating again yields an expression for the electron trajectory in the vertical direction (y plane)

$$y(z) = -\frac{q}{\gamma m} \frac{1}{c} \int \int B_x(z) \mathrm{d}^2 z \tag{7.67}$$

The result is shown graphically in figure 7.16(c), which shows the electron trajectories with an without the adjustment of the ferromagnetic screws to tailor the undulator magnetic field for on-axis injection and ejection of the electron beams.

On-axis ejection of the electrons was essential to the experiment in order to direct the electron beam into the permanent magnet spectrometer after interaction with the undulator magnetic field. This allowed resolution of the electron energy and corresponding undulator radiation to be collected and correlated for each laser shot.

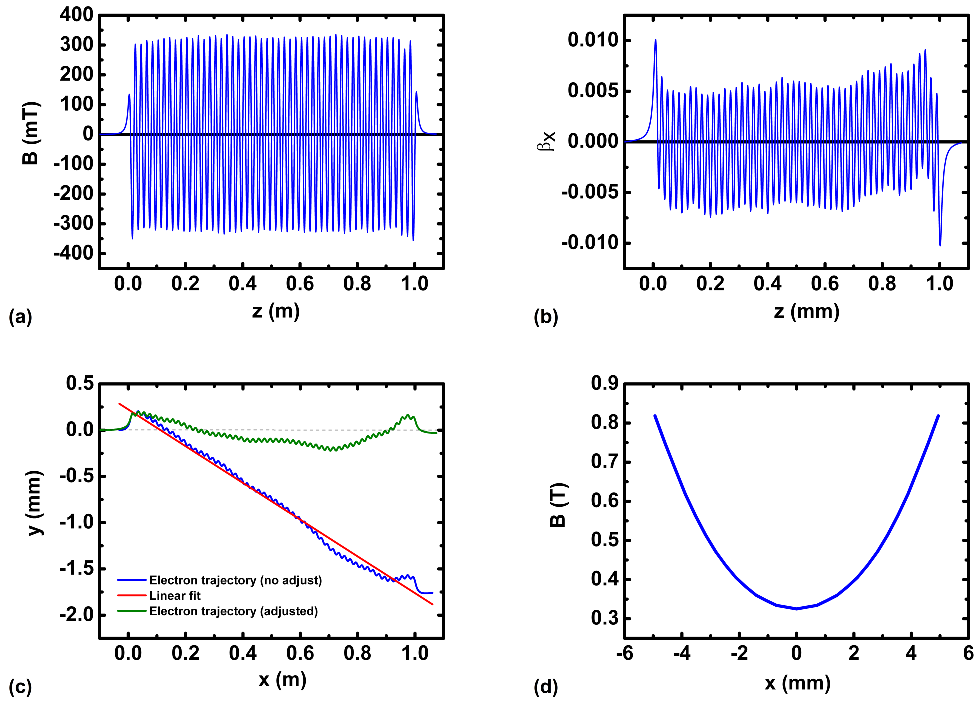

Figure 7.16: (a) The measured on-axis magnetic field of the undulator as a function of z. (b) The calculated electron trajectories in the $x - -z$ plane. (c) The magnetic field along x direction on axis as function of z. (d) The trajectory of an electron with $\gamma = 100$, injected on axis. The electron exits parallel to the axis with a negligible offset of 30 μm.

7.4.3 The electron spectrometer

An in-house constructed electron spectrometer was used to measure the electron energy spectra. The design was based on permanent magnets inside an iron yoke as seen in figure 7.20. The input aperture was circular and had a diameter of 2 cm. The magnetic field inside the spectrometer extended 20 cm in length along the z-axis, 10 cm in width along the x-axis, and 2 cm in the y-axis. The peak field strength was measured to be 720 mT. The magnetic field deflected the electrons on to a Konica KR scintillating screen which radiates green photons when excited by an electron beam. The screen was monitored using a CCD camera for online electron detection, covering an electron energy detection window from 14 MeV to 85 MeV. The electron charge calibration of the scintillating screen was carried out by comparing the response to previously calibrated Fuji BAS-MS2025 image plates [180, 181]. This was done by inserting the image plates 15 mm in front of the scintillating screen and comparing the two signals from the plate and the

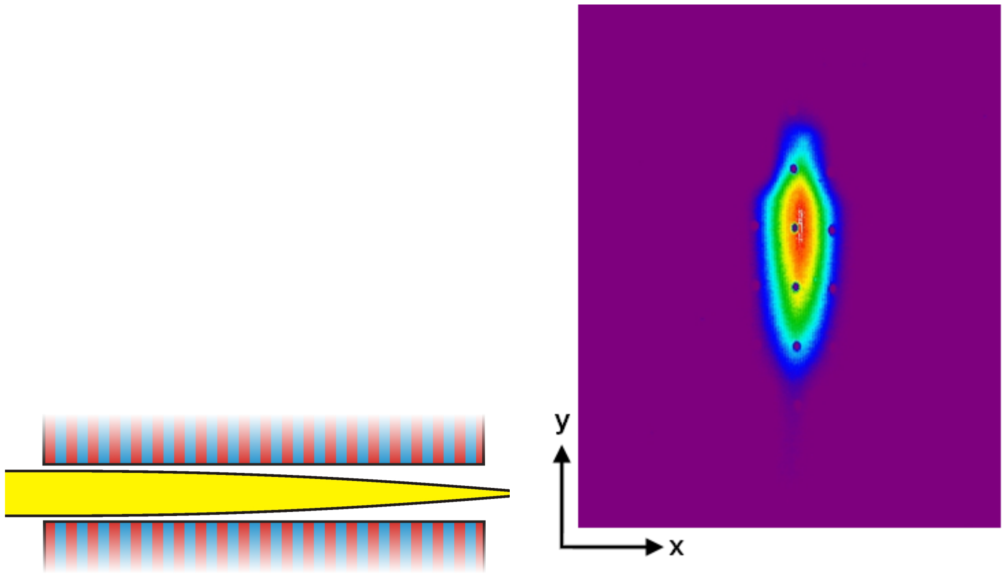

Figure 7.17: A schematic illustration showing how the undulator focuses the electron beam in the x plane (left). The measured transverse electron beam profile measured after the undulator using Lanex scintillating screen (right).

screen for the same electron shots. The data for the response of the image plates and the scintillating screen were taken from [181], respectively. The spectrometer dispersion was theoretically determined by particle tracking using the GPT code [277] based on measurements of the magnetic field which included fringe field edge effects.

As can be seen from figure 7.20, the electron energy dispersion is approximately linear for energies above 30 MeV. The sensitivity was determined to be better than 0.5 pC/MeV, which depends on imaging, camera type, stray light protection and imaging plate processing. The energy axis calibration across the length of the scintillation strip was done by calculations of the energy dispersion of the electrons. The large input aperture allowed the detection of highly divergent and spatially fluctuating electron beams, however although this increased the electron throughput and detection statistics it came with a caveat. The large acceptance range of the input beam coordinates in the x-y plane yielded a large uncertainty in the input position of the electron beam relative to the spectrometer axis. An electron beam entering the spectrometer with a certain horizontal x-offset from the axis, will have a corresponding offset on the scintillating screen or energy axis after dispersion, yielding a false offset in the energy measurement. In order to eliminate this energy dependency on input position the beam must enter the spectrometer collinear to the axis. Additionally, if the beam enters with a certain vertical y-offset or divergence, the off axis electrons experience a

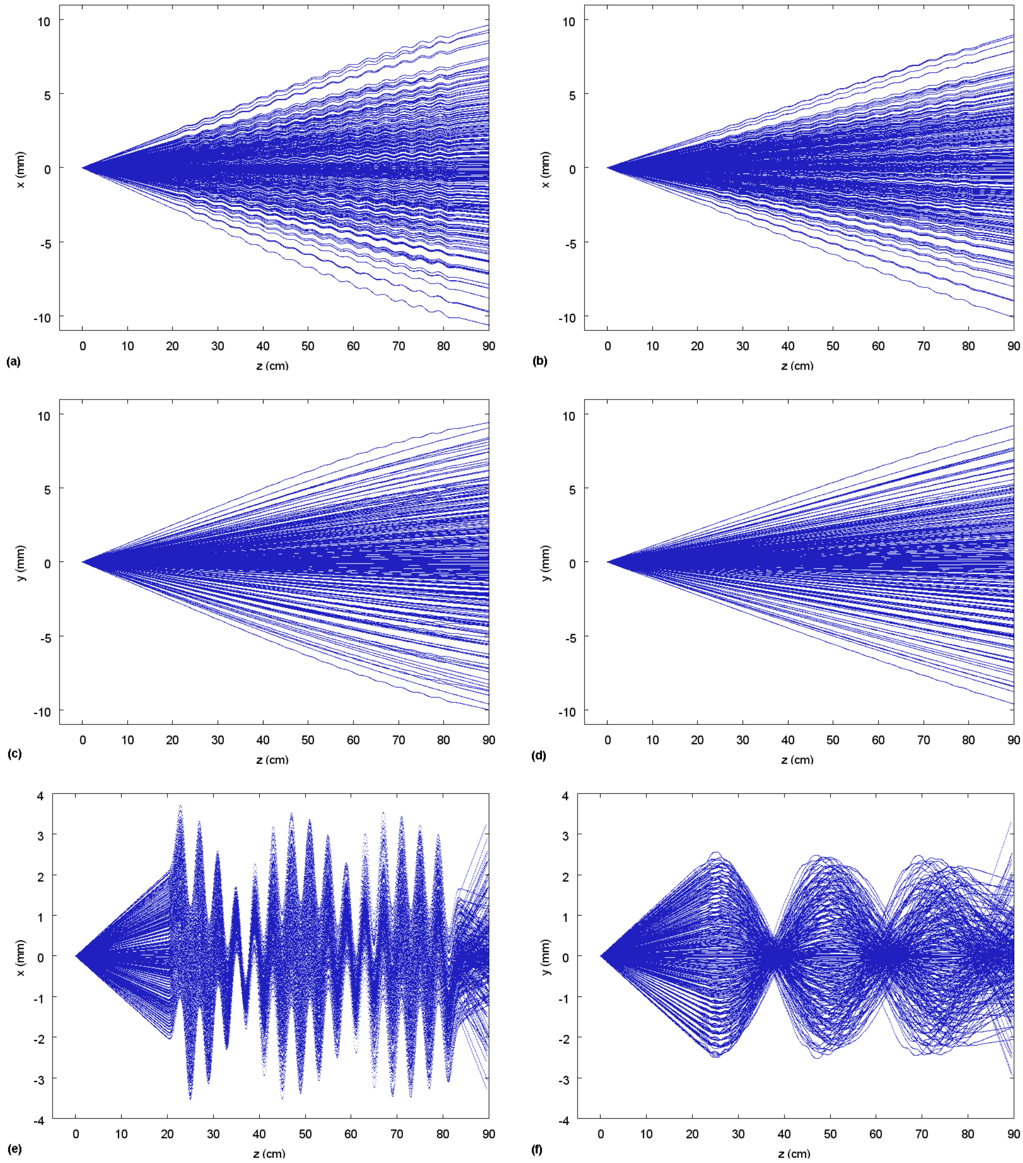

Figure 7.18: The calculated electron trajectories through the undulator in (a) The $z-x$ plane for a 30 MeV electron bunch. (b) The $z-x$ plane for a 50 MeV electron bunch. (c) The $z-y$ plane for a 30 MeV electron bunch. (d) The $z-y$ plane for a 50 MeV electron bunch. (e) The $z-y$ plane for a 1.5 MeV electron bunch. (f) The $z-y$ plane for a 1.5 MeV electron bunch.

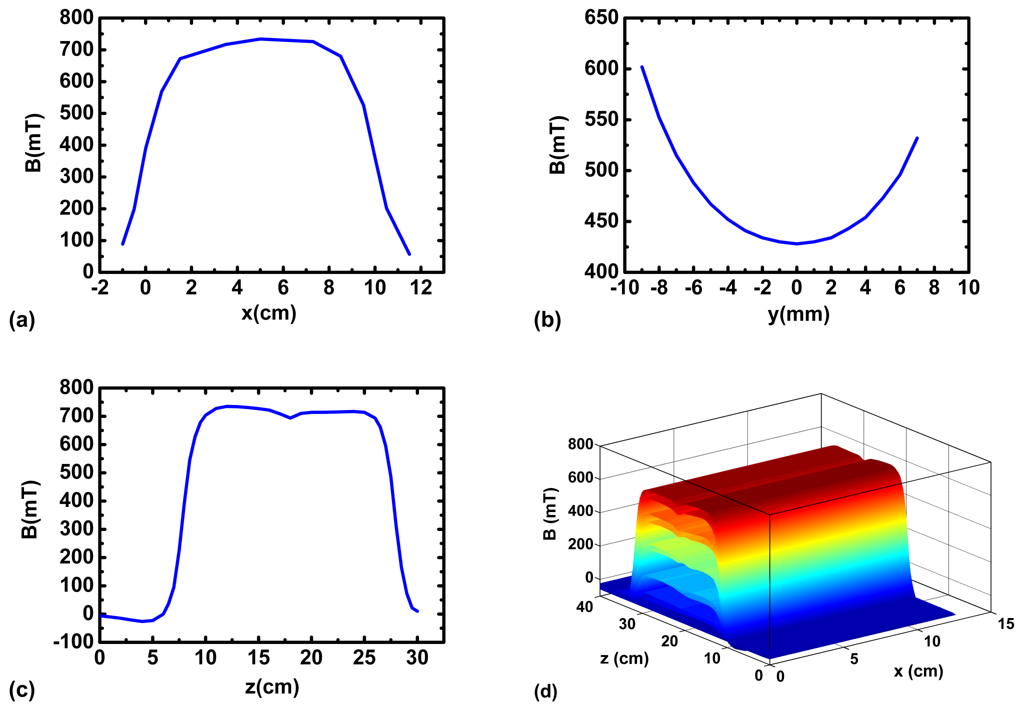

Figure 7.19: The measured magnetic field of the electron spectrometer in the (a) x-plane (b) y-plane and (c) z-plane. (d) An interpolated 3D magnetic field map of the electron spectrometer in the x-z plane.

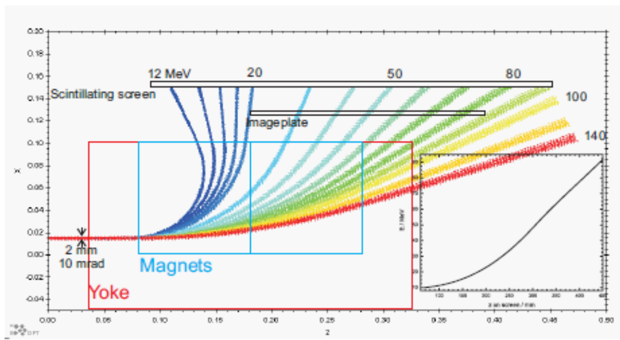

Figure 7.20: The simulated electron trajectories for the in-house constructed electron spectrometer.Scheme of the detection of electron trajectories inside the electron spectrometer. The magnetic field was measured in 3D and a particle tracking simulation with GPT was carried out. Electron beams with different energies but uniform input emittance were tracked through. The focusing effect for low energy beams can be seen from the width at the screen of beams with different energies. The inset shows the electron energy calibration graph. The dispersion is for energies above 30 MeV approximately linear.

stronger magnetic field due to the increased field strength increases vertically on approach toward the magnets. This explains the occurrence of 'C-shaped' electron beams which need to be deconvolved with a 2D energy calibration which includes the y-dependency. Furthermore, electron beams with high divergence increase the uncertainty in the measured electron energy spread. An electron beam with a high divergence in dispersive horizontal plane (x-axis) will appear as a broadening of the energy spectrum after dispersion inside the electron spectrometer. The input beam size of the electron beam in the dispersive plane is therefore directly coupled to the resolution of the energy spread measurement, hence without previous knowledge of the electron beam divergence this cannot be discriminated from the true energy spread of the bunch.

Ideally, in order to avoid this effect the electron spectrometer should to first order focus the electron beams onto the scintillating screen across the full detection window of electron energies. In this set-up the scintillating screen would be placed at the focal plane of the spectrometer which would eliminate the energy spread relationship with divergence. Without focusing only electron beams with zero emittance would not contribute to this error in the energy spread value. A reasonable practice is to determine the divergence from the beam size in the non-dispersing direction of the screen (vertical y-axis), and assume that the divergence in x is the same. This technique requires transverse beam profile measurements with a scintillating screen in advance in order to substantiate this assumption.

A collimator aperture which defines a small acceptance angle along the spectrometer axis could be implemented to reduce the input position and divergence related uncertainties, however the spatial beam fluctuations made this impractical. Furthermore, simultaneous measurements of the electron beam input position in the x-y plane and beam divergence was not possible as insertion of a scintillating screen in front of the input aperture would have a detrimental effect on electron beam quality.

7.4.4 Experimental set-up

The synchrotron radiation from the undulator was collected by an AR-coated planoconvex lens of 47 mm diameter and 105 mm focal length, and focused into the entrance slit plane of the optical spectrometer. This was a symmetrical 200 mm Czerny-Turner spectrometer, equipped with a thermoelectrically cooled CCD camera (Andor DO-420 BN). The camera was shielded with lead against X-rays from electrons stopping in the vacuum vessel walls. The $26{:}6\times6{:}7\mathrm{mm}^2$ CCD chip (1024×256 pixels) was operated in hardware binning mode, merging arrays

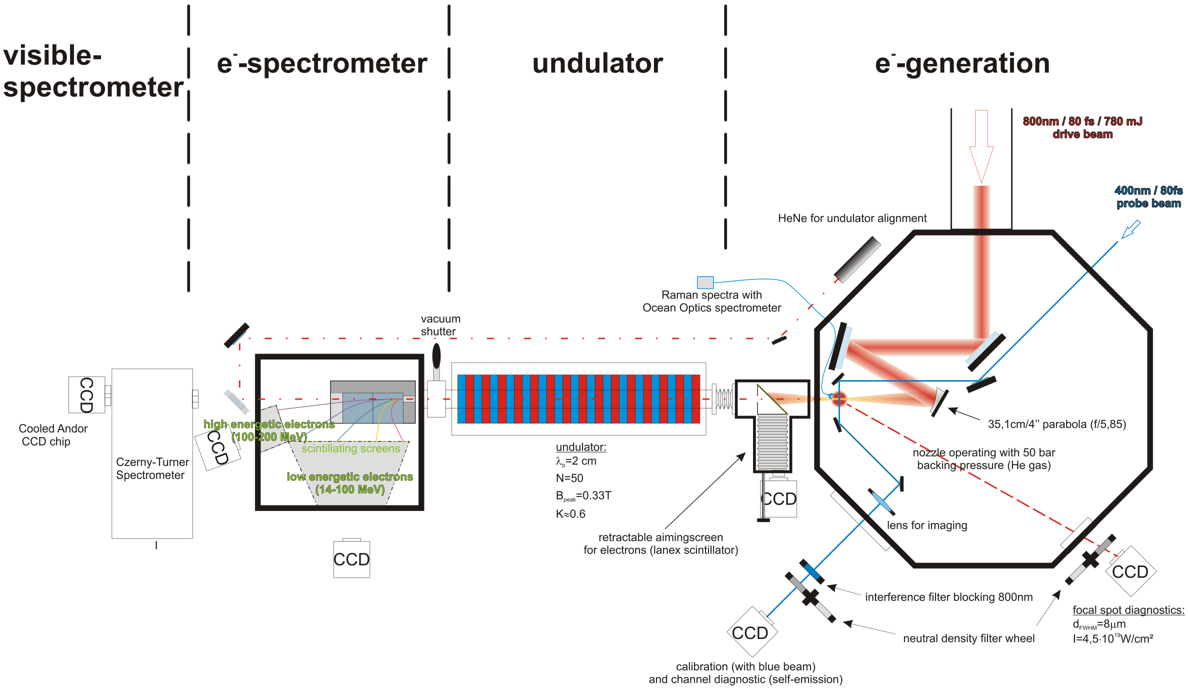

Figure 7.21: A schematic illustration of the experimental set-up to produce undulator radiation from laser wakefield accelerated electron bunches.

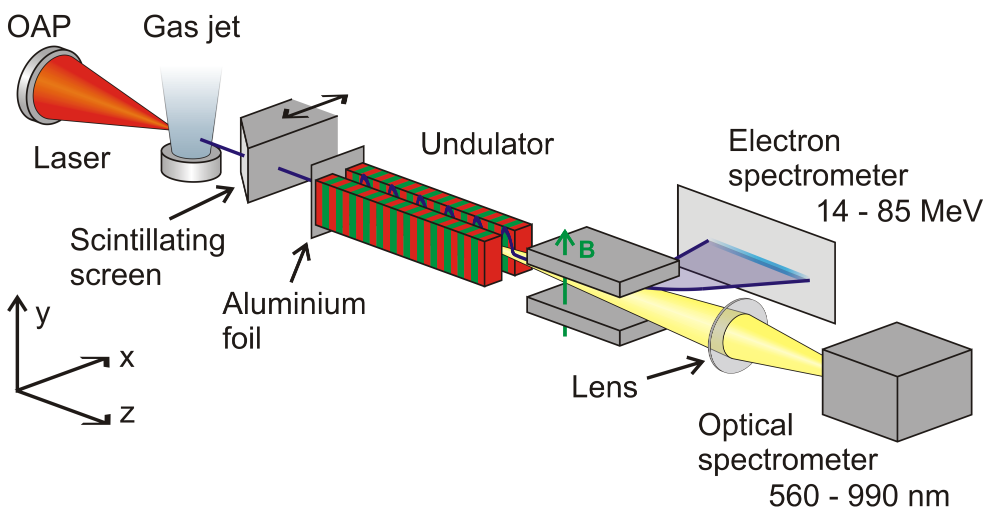

Figure 7.22: A 3D cartoon of the experimental set-up

of 8×12 pixels together to form superpixels. This was useful since there was no need for high spectral resolution, and thermal noise as well as quantization errors are reduced in this mode. The spectral range was set to 560 nm - 990 nm. The wavelength calibration was accomplished with a Hg-vapour lamp. The spectrometer efficiency was carefully calibrated with a HeNe laser, a fast shutter and parallel exposure time measurements. Due to the intrinsically parallel photon detection within each CCD pixel, saturation of the signal from the ultra-short pulses does not occur. To correct for the quantum effeciency of the detector, the manufacturer's data was used. Ray tracing simulations of the optical system, carried out with Zemax, showed that the collection angle for undulator radiation is just about 2 mrad which is significantly smaller than from geometrical estimation. The light source to be imaged by the lens into the slit plane is extended one metre in depth and therefore difficult to image onto the slit plane. With this simple lens, a signifcant loss of photon flux cannot be avoided. In the experiment, the longitudinal center of the undulator was imaged onto the slit plane.

7.4.5 Electron beam measurements

In order to successfully observe synchrotron radiation from laser wakefield accelerated electron beams it was imperative to generate the best possible electron beams in the experiment. As has been discussed in section 7.2.5 the electron beam quality is fundamental to the spectral characterstics of the observed undulator radiation. Electron beams with low energy spread and low angular divergence were a necessity to produce detectable undulator radiation at optical wavelengths. A rigorous characterisation of the beams produced from the gas jet plasma was therefore necessary prior sending the electrons through the undulator. In order to generate the highest possible intensity using the laser energy available for experiments, the laser focal spot had to be minimised before the start of each experimental day. This was done using the set-up depicted in figure 7.23

The focal spot diagnostic consisted of an optical breadboard mounted to a translation stage. The breadboard included a microscope objective with a mirror behind the output to direct the laser onto a CCD camera for observation. The gas jet was translated in the horizontal x-plane and the focal spot diagnostic was translated upwards in the vertical y-plane until the focal spot of the laser entered the objective lens. The laser focus was then imaged onto a CCD camera and optimised by iterative translation of the final turning mirror before the parabola and the also the x-y-z translation of the parabola. In most cases after switch on of the laser the focal spot was astigmatic and had to be carefully optimised.

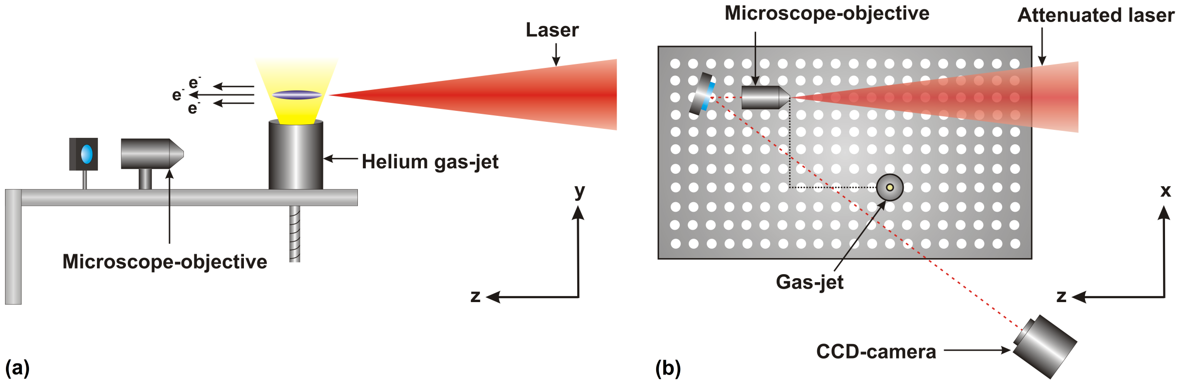

Figure 7.23: The focal spot measurement diagnostic used to optimise the laser focus prior to electron acceleration experiments.

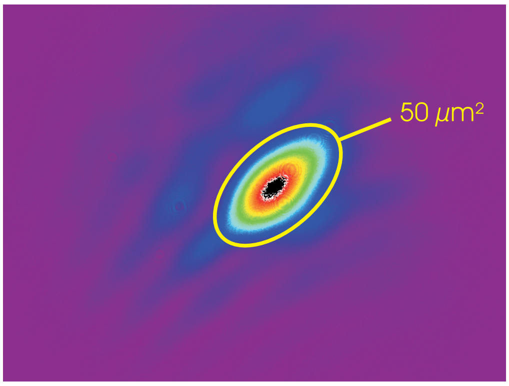

Figure 7.24: The transverse image of the focal spot captured using the focal spot measurement diagnostic. The $1/e^2$ spot diameter was approximately 5 μm.

Figure 7.24 shows a typical profile of an optimised laser focal spot before the start of electron acceleration experiments. The f-2 paraboloid mirror yielded a spot diameter ($2w_0$) of 5 μm

Before any attempt was made to resolve the energy spectrum of electron beams a retractable scintillating screen (figure 7.25) was inserted into the beam path 50 cm upstream of the gas-jet. This preliminary step was essential in order to attain the correct electron beam pointing along the central axis of the electron spectrometer and the undulator which was previously defined using a HeNe alignment laser (figure 7.21). Moreover, the scintillating screen was an extremely useful diagnostic to optimise the electron beam divergence and reproducibility of electron beam generation.

During the first laser shots to produce electrons, it was apparent through observation of the Lanex screen (figure 7.26(a)) that the electron beam pointing was significantly off-centre to the central axis. The electrons are ejected with an angular offset to the central axis, even when the drive laser pulse is collinear to the

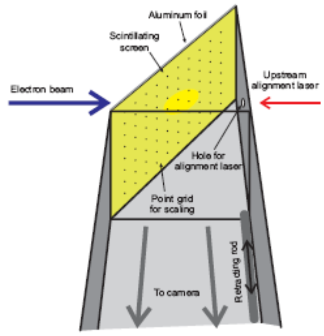

Figure 7.25: The retractable Lanex screen insert used to align and optimise the electron beam prior to injection into the electron spectrometer and undulator.

desired axis. In order to correct for this effect an iterative alignment procedure had to be implemented and is shown in figure 7.27

During this procedure the parabola had to be translated in small increments in the x direction to slowly move it off the central axis, each time the laser was re-centred onto the parabola and the parabola was then re-optimised using the focus spot monitor diagnostic. After each iteration the electron beam pointing was observed on the retractable Lanex screen diagnostic. The increments slowly improved the beam pointing until an optimum angle between the drive laser and the central axis of 7° was found. Figure 7.26(d) shows the electron beam travelling along the central axis after the electron beam steering procedure.

7.4.6 Transverse diagnostics of plasma channels

Transverse imaging of plasma channels is an invaluable diagnostic when seeking to optimise electron beam properties. Plasma diagnostics monitor the interaction region and can give important insights into the properties and strength of the laser wakefield. The imaging of the channels is also an excellent spatial indicator when optimising the gas jet position relative to the drive laser pulse. Figure 7.29(b) shows a typical plasma channel under optimum conditions. The plasma emits light depending on the interaction. The gas jet density and spatial overlap relative to the drive pulse were carefully adjusted during on-line observation of plasma channel emission intensity. In addition to this a 2ω transverse ultra-short probe beam can also be employed which makes various time resolved detection schemes possible. It also serves as a 'backlight' or 'sidelight' to create a shadowogram image of the gas jet for spatial optimisation (figure 7.29(a)).

A fully ionized plasma at a pressure of about one atmosphere is a very bright

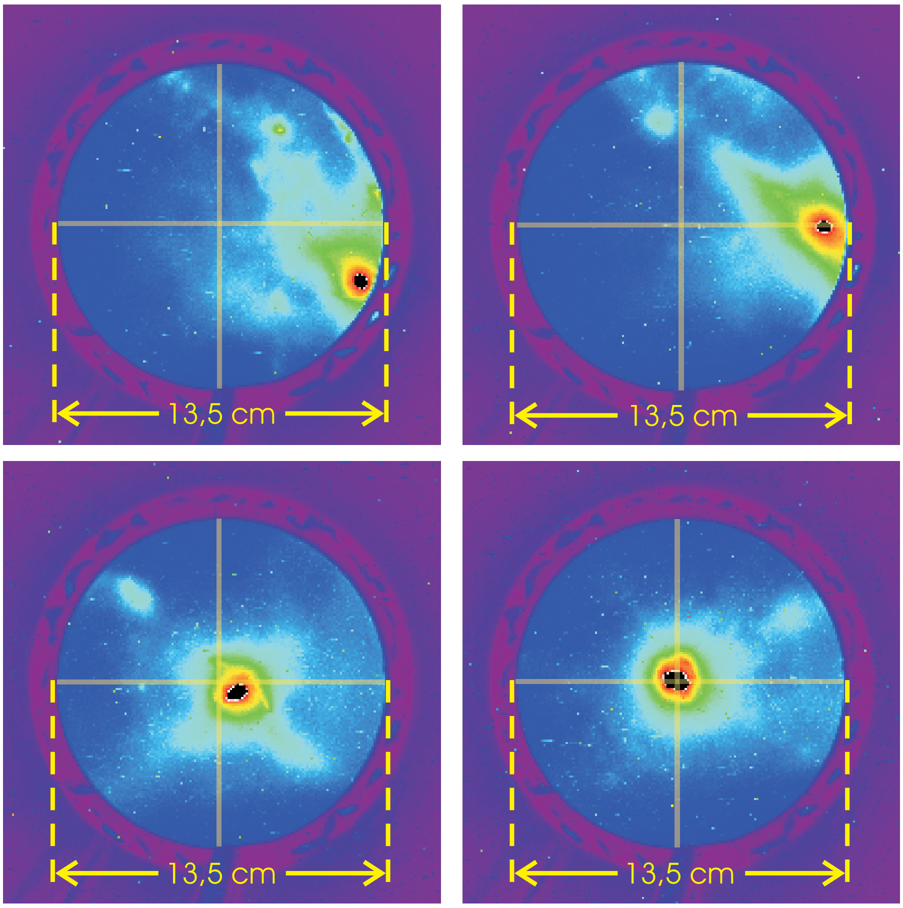

Figure 7.26: The Lanex screen images at various points during the procedure of electron beam steering. The bottom left image shows the optimised electron beam pointing along the central axis.

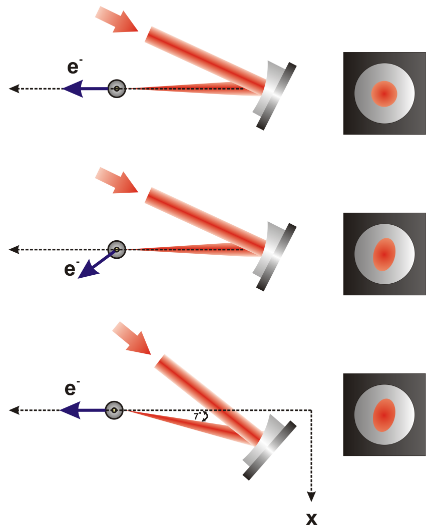

Figure 7.27: The procedure used to steer the electron beam down the electron spectrometer and undulator central axis. (a) The drive laser was aligned to be co-linear to the central axis with the assumtion the electrons would follow the direction of the laser. (b) This was found not to be the case; An angular off-set of the electron beam relative to central axis caused by a 'ponderomotive side kick' was observed on the Lanex screen. (c) This effect was compensated for by re-adjusting and carefully realigning the parabola and final turning mirror to steer the electron beam down the central axis. A 7 ° angular off-set of the parabola relative to the central axis yielded the optimum electron beam pointing.

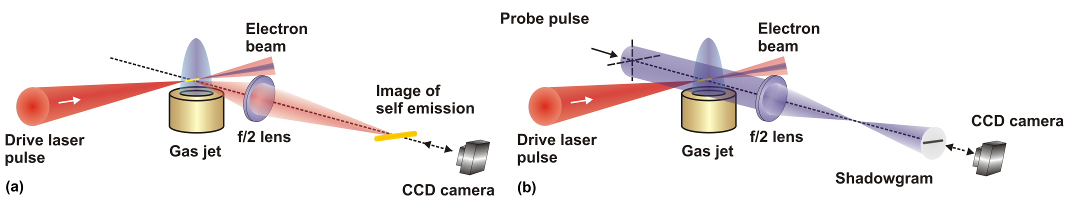

Figure 7.28: An illustration of the configurations for transverse plasma observation. (a) Imaging of the interaction region onto a CCD camera yields time-integrated images of the 2ω Thomson-scattered light and accompanying plasma emission. (b) Combining this imaging with an 2ω ultra-short probe beam gives time-resolved images. The probe resolves plasma refractive index gradients and reveals intricate structure of the channels. The ionisation front can also be easily observed as it propagates through the neutral gas.

light source. Due to collisions and recombination, a wide continuum is emitted. Further emissions typical for electron acceleration were introduced in section 2.22, which are nonlinear Thomson-scattering. Figure 7.28(a) shows a sketch of the setup in order to image the self-emitted light onto a camera. This is a basic setup which may be modifed and extended. Not shown are the camera and additional filters. Neutral filters can adjust the intensity to the camera's sensitivity, interference filters can identify and distinguish different emission processes

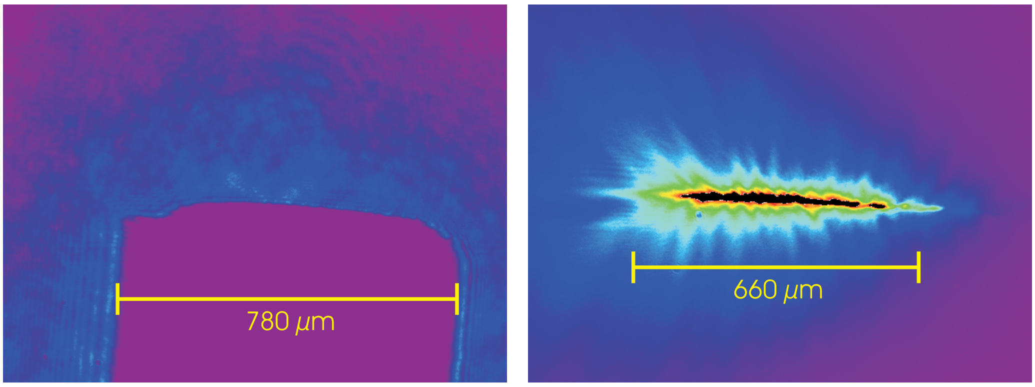

Figure 7.29: The shadowgraph of the gas jet (left). The Thomson scattered plasma channel (right).

The plasma recombines after the interaction and emits broadband radiation. Nonlinear Thomson-scattering, however, occurs at harmonics of the laser. In the experiments, small frequency intervals were observed with the help of interference filters for the laser frequency ($\lambda \approx 800$ nm) or second harmonic ($\lambda \approx 400$ nm). In the present work, only position and length of the emission were of interest where precise intensity profile measurements were made. The edge of the emission indicates the position of laser focus with respect to the gas jet position; length, profile and brightness of the emission enable to estimate the interaction process like channel formation, self-focusing or filamentation.

7.4.7 Undulator radiation from LWFA

The experiment to produce undulator synchrotron radiation using laser accelerated electrons has been carried out using the JETI laser at Jena [10]. This laser delivers 85 fs duration laser pulses centered at a wavelength of 795 nm, and with an energy of up to 430 mJ on target. The experimental set-up is displayed in figure 7.21 and described in detail in [254]. The laser pulses are focused by an f/6, 30° off-axis parabolic mirror to a spot diameter of 11 μm (FWHM), yielding a peak intensity of 5 $\times 10^{18}$ Wcm^{-2} and a normalised vector potential $a_0 = 1.5$. A

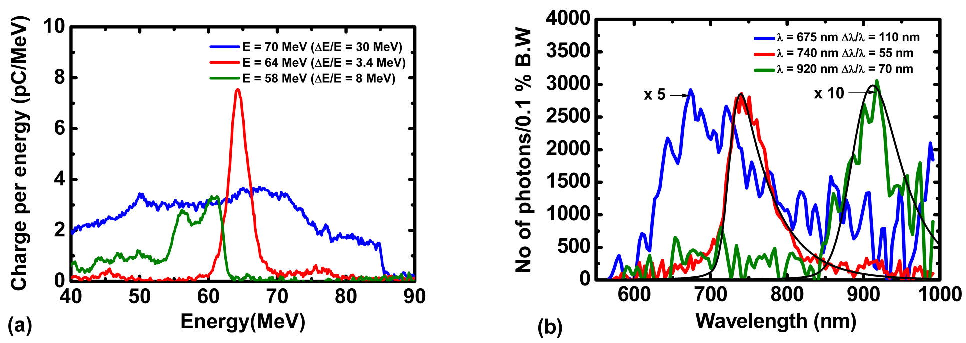

Figure 7.30: (a) The electron spectra shown for electron beams with energies of 58 MeV (green line), 64 MeV (red line) and 70 MeV (blue line). (b) The corresponding undulator spectra for the electron shots shown in figure 7.30(a). The 58 MeV electron shot corresponds to the λ=920 nm undulator spectrum (green line). The 64 MeV electron shot corresponds to the λ=675 nm undulator spectrum (blue line) and the 70 MeV electron shot corresponds to the λ=920 nm undulator spectrum (green line).

pulsed supersonic helium gas jet, placed at the laser beam focus, produces a 2 mm diameter gas plume with a peak density of 2×10^{19} cm^{-3}. Nonlinear Thomson scattering from the plasma, at the second harmonic of the laser, is observed in the direction perpendicular to the laser polarisation and is used to measure the length and position of the channel, as shown in figure 7.29. The electron beam divergence and pointing are observed on a removable Lanex scintillating screen [181, 180] (figure 7.26) and optimised by moving the gas jet position, direction of the laser beam and tuning the gas density. This optimisation procedure is also an essential step to steer the electron beam down the undulator axis. An example of an optimised transverse electron beam profile with a r.m.s. beam divergence of 2 mrad is shown in figure 7.26. This divergence is consistent with a normalised emittance of $\epsilon_n = 1\ \pi$ mm mrad.

Following optimisation of the electron beam properties, the scintillating screen is removed and the electrons are allowed to traverse the undulator, which is placed 40 cm downstream of the gas jet. A 50 period fixed-gap permanent magnet undulator, with wavelength $\lambda_u = 2$ cm and pole gap of 10 mm, produces an on-axis peak magnetic field of $B_u = 0.33$ T resulting in a deflection parameter $a_u = eB_u\lambda_u/2\pi m_0 c = 0.6$. The undulator is placed in a vacuum chamber and has the fields of the initial and ultimate three periods carefully trimmed to ensure on-axis injection and exit of electrons. This shortens the undulator slightly, which marginally increases the homogeneous $(1/N_u)$ component of the undulator spectrum. A 1 cm thick, 1 cm diameter lead aperture protects the undulator magnets from off-axis electron beams.

After traversing the undulator electrons are deflected by the magnetic field of an electron spectrometer (constructed from 200 mm $\times$ 100 mm permanent magnets, separated by a 20 mm gap, giving a central magnetic field strength 0.72 T) placed 185 cm downstream of the gas jet. A scintillating screen (Lanex, Konica KR) and a Charge Coupled Device (CCD) camera detect the deflected electrons over an energy range of 14 – 85 MeV. The scintillation screen intensity has been calibrated using an imaging plate (Fuji BAS - MS2025) to give an absolute measure of the charge per unit energy [180]. This takes into account both the response of the image plate and the scintillating screen.

Undulator radiation is collected within a collection angle of 3 mrad and focused onto the entrance slit plane of a symmetric 200 mm Czerny–Turner spectrometer with a 105 mm focal length fused silica lens. A thermo-electrically cooled CCD camera (Andor DO-420 BN) is used to measure the spectrum of the undulator radiation. The CCD chip (1,024 $\times$ 256 pixels) is operated in a hardware binning mode, by merging 8 $\times$ 12 pixels arrays into superpixels. The spectral range is set to 540 – 990 nm and the spectrometer and detector efficiency carefully calibrated using a standard visible-light source. The optical spectrometer is shielded against direct exposure from the laser and plasma light by a 15 μm thick aluminium foil placed in front of the undulator.

Linearly polarised undulator radiation is produced by the periodic transverse acceleration imparted to the electrons by the Lorentz force of the magnetic field of the undulator. The main spectral characteristics of the undulator radiation can be modeled using the well known undulator equation:

$$\lambda = \frac{\lambda_u}{2h\gamma_z^2} = \frac{\lambda_u}{2h\gamma^2}\left(1 + \frac{a_u^2}{2} + \gamma^2\vartheta^2\right). \tag{7.68}$$

From this it can be seen that the peak wavelength emission depends on the undulator period, λ_u, and the electron energy, $E_e = \gamma m_e c^2$, where γ is the Lorentz factor, h is the harmonic order and ϑ is the angle w.r.t. the electron beam axis. The small reduction in the longitudinal velocity due to periodic deflection results in a slight increase in the wavelength of the emitted radiation by a factor $(1 + a_u^2/2)$. The wavelength also exhibits an angular dependence through the $\gamma^2\vartheta^2$ term. The central radiation cone angular half width can be approximated as $\vartheta_{cen} = 1/\gamma\sqrt{N_u}$, which is approximately 1 – 1.3 mrad for the electron energies of the wakefield accelerator.

Given the known trajectory of an electron in the undulator, the radiation fields can be calculated by directly evaluating the retarded field of the Liénard-Wiechert potential [205].

To help characterise the beam we consider the total brightness of the beam of radiation impinging on a surface as the power per unit area of the source from a unit solid angle. The brilliance, which is defined by $S_\omega = 2\epsilon_0 c\,|E|^2 \times$ area, is the power radiated (per unit frequency, beam area and solid angle) by a collimated electron beam of current density j_b. This is given by [259]

$$S_\omega(\omega,\vartheta) \approx \frac{k^2 L_u^2 e j_b}{32 c\epsilon_0 \pi^2 \gamma^2}\,|A_u(\vartheta)|^2 \left[\frac{\sin(\nu)}{\nu}\right]^2 \tag{7.69}$$

where ϑ is the angle between observation and motion directions and the normalised detuning parameter, ν, is given by

$$\nu = \pi N_u \left(\frac{\lambda_u}{2\lambda\gamma^2}\left(1+\frac{a_u^2}{2}-\gamma^2\vartheta^2\right)-1\right), \tag{7.70}$$

and the coefficient A_u is given by [259]. Radiation over a spectral width $\delta\lambda_{\mathrm{FWHM}}$ is emitted within an angle of approximately $\delta\vartheta_{\mathrm{FWHM}}$. For angles less than $N_u^{1/2}\delta\vartheta_{FWHM}/2$, $A_u(\vartheta) \approx A_u(0)$ where

$$A_u(0) \approx a_u\left[J_0\left(\frac{a_u^2}{4+2a_u^2}\right) - J_1\left(\frac{a_u^2}{4+2a_u^2}\right)\right]. \tag{7.71}$$

for the fundamental frequency. The spectrum consists of equally spaced odd harmonics on axis and both even and odd harmonics off axis, for a planar undulator. The spectrum of each harmonic is a sinc function, $(\sin\nu^2/\nu^2)$, giving a FWHM spectral width of

$$\frac{\delta\lambda_{\mathrm{FWHM}}}{\lambda} \approx \frac{0.9}{N_u h}. \tag{7.72}$$

For a particular harmonic, the solid angle of radiation emitted into the first lobe is

$$\delta\vartheta_{\mathrm{FWHM}} \approx \frac{0.9}{(N_u h)^{1/2}} \cdot \frac{1+a_u^2/2}{\gamma}, \tag{7.73}$$

with all harmonics emitted into the solid angle $\vartheta_{\mathrm{FWHM}} \approx 1/\gamma_z = (1+a_u^2/2)^{1/2}/\gamma$ for an on-axis electron beam.

7.4.8 Undulator radiation as an electron beam diagnostic

The work in this chapter is based on the publication

- **J. G. Gallacher**, M. P. Anania, E. Brunetti, F. Budde, A. Debus, B. Ersfeld,

K. Haupt, M. R. Islam, O. Jäckel, S. Pfotenhauer, A. J. W. Reitsma, E. Rohwer, H.-P. Schlenvoigt , H. Schwoerer, R. P. Shanks, S. M. Wiggins, D. A. Jaroszynski, "A method of determining narrow energy spread electron beams from a laser plasma wakefield accelerator using undulator radiation", *Physics of Plasmas*, **16**, 093102, (2009).

To investigate the correspondence between the electron energy spectra and the undulator radiation spectra, several electron and optical spectra have been measured simultaneously. Figure 7.30 shows three representative pairs of measurements indicating the peak energy E, the full-width at half-maximum (FWHM) spectral width, $\delta E/E$, the peak wavelength, λ, and the FWHM spectral bandwidth, $\delta\lambda/\lambda$. Consistent with equation 7.52, the wavelength decreases with increasing electron energy [6]. This characteristic scaling is clearly observed for both the fundamental ($h = 1$) and second harmonic ($h = 2$) emission [254]. Due to the limited spectral range of the optical spectrometer system, the fundamental and second harmonic signals could not be observed simultaneously. The measured radiation spectrum agrees well with predictions using equation 7.52 and numerical simulations [5] shown in figure 7.30(b) for wavelengths between 740 nm and 920 nm.

Undulator radiation provides a 'signature' or 'fingerprint' of the transverse and longitudinal electron beam characteristics. Thus, analysis of the undulator radiation spectra provides an attractive alternative method of characterising the electron beam properties with high resolution, compared with using a conventional magnetic spectrometer, particularly at high electron energies. To demonstrate this technique, an analysis of the experimental spectra shown in figure 7.30(a), corresponding to $E = 64$ MeV, $\Delta E = 3.4$ MeV, $\lambda = 740$ nm, $\Delta\lambda = 55$ nm, will be presented. These are re-plotted in figure 7.31 for clarity. The corresponding measured FWHM widths of the electron spectra vary between 5.3% and 15% (σ_γ/γ in the range 2.2% – 6.2%).

The finite divergence and energy spread of the electron beam reduces the brilliance of the beam and smears out the spectrum as

$$S_\omega(\omega, \vartheta) = \int S_0(\omega, \gamma, \vartheta - \vartheta_e) F(\gamma, \vartheta_e) d\gamma d\vartheta_e, \tag{7.74}$$

where ϑ_e is the direction of electrons and S_0, is the distribution for a perfect beam with $\delta\gamma = 0$ and $\delta\vartheta = 0$ [14]. $F(\gamma, \vartheta_e)$ is the energy and angular probability distribution of the beam. The total spectral width of the radiation is the sum of contributions from broadening due to the energy, angular and natural spread components:

$$\left(\frac{\delta\lambda}{\lambda}\right)^2 = \left(\frac{2\sigma_\gamma}{\gamma}\right)^2 + \left(\vartheta^2\gamma^2\right)^2 + \frac{1}{N_u^2}. \tag{7.75}$$

To minimise the spectral width and thus maximise the brilliance, the second term, $\left(\vartheta^2\gamma^2\right)^2$, can be reduced by matching the electron beam to the undulator, which minimises the beam divergence ϑ. To minimise the divergence the betatron wavelength, λ_β, which is analogous to the Rayleigh range of a laser beam, should be made approximately equal to the undulator length [229]. The r.m.s. emittance is defined as the transverse momentum/position phase-space area of the beam [229]:

$$\epsilon_{\text{r.m.s.}} = \left(\langle x^2\rangle \left\langle \left(\frac{p_x}{m_e c}\right)^2 \right\rangle - \left\langle \frac{x p_x}{m_e c} \right\rangle^2 \right)^{\frac{1}{2}}, \tag{7.76}$$

where p_x and x are the transverse momenta and coordinates of an electron, respectively. The edge or envelope emittance is four times as large. The un-normalised r.m.s. emittance, $\epsilon_{\text{r.m.s.}}$, of an electron beam of radius r_e is analogous to the wavelength of a laser beam (i.e. has units of length) and is given by

$$\epsilon_{\text{r.m.s.}} = \pi\sigma_{\beta_\perp} r_e = k_\beta r_e^2, \tag{7.77}$$

where $\sigma_{\beta_\perp}$ is the variance of the (normalised) transverse velocities and $k_\beta = 2\pi/\lambda_\beta = a_u k_u/2\gamma$ is the betatron wavenumber. The normalised emittance, $\epsilon_n = \beta_z\gamma\epsilon_{\text{r.m.s.}}$ governs the broadening through $\gamma\vartheta$. The minimum beam divergence that is consistent with the smallest average beam radius gives $\lambda_\beta \approx L_u$, which occurs when the Fresnel number $F = r_e^2/\lambda L_u \approx 1$ and the electron beam divergence (given by $\vartheta \approx \epsilon_{\text{r.m.s.}}/r_e$) matches the diffraction angle of radiation emitted by the undulator ($\vartheta \approx \lambda/r_e$) i.e. when

$$\vartheta^2 = 2k_\beta\epsilon_{\text{r.m.s.}}, \tag{7.78}$$

and the brilliance is maximised, which is approximately 0.4 mrad for our parameters and a matched beam. However, in this case the electron beam was not focused into the undulator. Thus the dominant broadening contribution comes from the divergence of the beam, $\vartheta^2\gamma^2 \approx 6\%$ corresponding to the beam divergence of approximately 2 mrad. The natural width is $1/N_u = 2.3\%$, taking into account the alteration of the first and last three periods for electron injection and exit. For the spectrum of figure 7.31(b), $(\delta\lambda/\lambda)_{\text{FWHM measured}} = 7.4\%$, which gives an initial upper limit of 7.0% on the combined contributions from energy and angular spreads. The electron energy spectral width σ_γ/γ is limited to below 1.8%, which is smaller than the value of 2.4% obtained directly from the measured electron energy spectrum (red line in figure 7.31(a)).

To evaluate the actual electron beam energy spread, the measured spectra can be deconvoluted from the measured spectrum using the respective instrument response functions. This has been carried out for both the electron energy spectrum (figure 7.31(a)) and the undulator radiation spectrum (figure 7.31(b)). In each case, the deconvoluted spectrum $\mathcal{S}_T$ is given by:

$$\mathcal{S}_T = \mathcal{F}^{-1}\left(\frac{\mathcal{F}(\mathcal{C}_T)}{\mathcal{F}(\mathcal{R}_T)}\right), \tag{7.79}$$

where $\mathcal{F}$ denotes the Fourier transform, $\mathcal{C}_T$ is the convoluted measured spectrum and $\mathcal{R}_T$ is the instrument response function. The instrument response function for the electron spectrometer has been simulated using the General Particle Tracer (GPT) code [278] and is illustrated in figure 7.31(a) by the blue line. The equivalent σ_γ/γ for the spectrometer is 1.6 %. This simulation takes into account all the relevant electron beam parameters and space charge effects.

For the corresponding radiation spectrum, the instrument response function of the undulator has been estimated using the three contributions to the measured spectral width of Equation 7.75 such that:

$$\mathcal{R}_T = \mathcal{F}^{-1}(\mathcal{F}(r_N) * \mathcal{F}(r_\theta) * \mathcal{F}(r_\gamma)), \tag{7.80}$$

where r_N, r_θ and r_γ are the response functions due to natural broadening, angular spread and energy spread, respectively which means that this response function refers back to the beam energy spread. However, as discussed above, the dominating term is due to the angular spread and so the overall undulator response function is presented in figure 7.31(b) by the green line (the corresponding σ_γ/γ is 1.2%). The deconvoluted spectrum (blue line in figure 7.31(b)) therefore provides a final spectral width of $\sigma_\gamma/\gamma = 1.2\%$. As a final check on the validity of this technique, this deconvoluted undulator spectrum has been convoluted with the electron spectrometer response function which gives a spectral width of 2.3% which is very close to the measured width of 2.2%. This confirms that the actual electron energy spread is close to 1%. The analysis has also been carried out for other experimental data shots with good agreement obtained between the measured and reconstructed spectra.

This method demonstrates the use of an undulator as a high resolution compact electron spectrometer of arbitrary resolution where the resolution depends

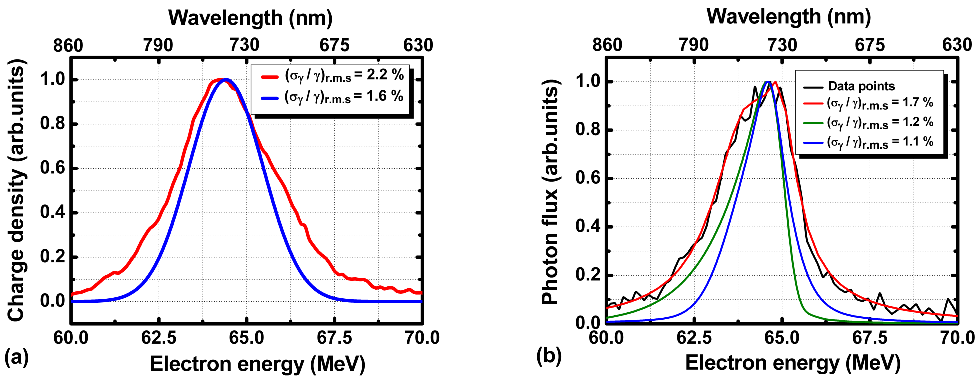

Figure 7.31: (a) The electron spectra data points (red line). The simulated instrument response function of the electron spectrometer, $\sigma_\gamma/\gamma = 1.6\%$ (blue line). (b) The undulator radiation spectra data points (black line). A best-fit curve to the data points, $\sigma_\gamma/\gamma = 1.7\%$ (red line). The simulated instrument response function of the magnetic undulator, $\sigma_\gamma/\gamma = 1.2\%$ (green line). The deconvoluted undulator spectrum, $\sigma_\gamma/\gamma = 1.1\%$ (blue line). Note: The upper and lower axes in these plots give the respective wavelength and energy (Equation 7.52).

on the number of undulator periods. At high electron energies an undulator is a very compact non-intercepting on-line alternative to very large magnetic dipole electron spectrometers.

The energy spread is reduced when the electrons are close to the dephasing length $L_d \approx \lambda_p \gamma_\phi^2/\pi$, i.e. when the electron beam reaches its maximum energy $\gamma \approx 2(\lambda_p/\lambda_0)^2$, where $\gamma_\phi = \lambda_p/\lambda_0$ is the Lorentz factor associated with the group velocity of the laser. Insight into the generation of narrow energy spread beams is gained from laser wakefield simulations. These have been carried out using a self-consistent reduced model that includes modifications of the laser pulse due to the local spatio-temporal refractive index modifications due to the plasma density variations of the wake [279]. To simulate self-injection, the electron bunch is injected at an optimal position into the wake behind the laser pulse. The bunch has a random initial phase-space distribution, consistent the energy spread and emittance. The model is implemented in a two dimensional slab geometry where both the laser pulse and the electron bunch are treated as collections of macro-particles of finite size. The evolution of the laser pulse $a(r,t)$ is calculated on a spatial grid, on which the macro-particles are treated classically by solving the classical equations of motion for the coupled dynamics of laser pulse, wakefield, and electron bunch. This correctly models "beam loading" which modifies the wake field created by the laser pulse. As an initial condition we have considered a bunch occupying a volume of about 1 μm^3, and a laser potential of $a_0 = 2$ with a spot size of 10 μm, plasma density $n_0 = 1.2 \times 10^{19}$ cm^{-3}, and an electron bunch charge 10 pC and 18 pC, as shown in figure 7.32.

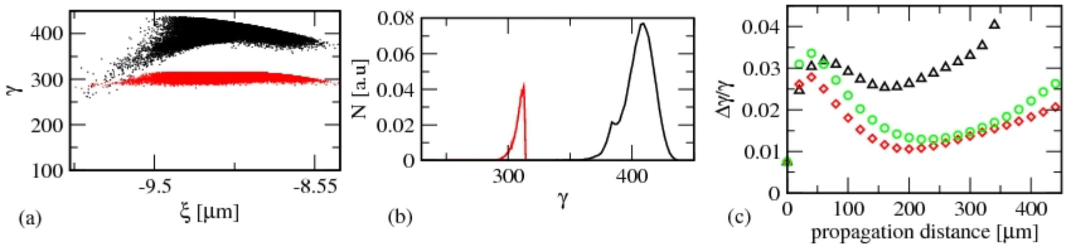

Figure 7.32: (a) Shows the spatial distribution of Lorentz factor of electrons at dephasing length (black for no beam loading, red and green for beam loading with 18 pC and 10 pC of charge respectively), and (b) spectrum. Here (c) shows the energy compression as a function of propagation distance; triangle for no beam loading, square for beam loading when electron bunch charge is 18 pC (circle and triangle for beam loading when the bunch charge is 10 pC and 18 pC respectively).

We observe lower energy spread for the beam loaded case ($< 2\%$) because the electron bunch is accelerated by a uniform electrostatic field due to flattening of the potential. Without beam loading, the leading part of the electron bunch experiences a weaker acceleration field than the trailing part, which leads to a larger energy spread as observed in the simulations.

7.4.9 Undulator radiation v.s. Transition radiation

The following section compares the simulated undulator radiation photon yields with that of transition radiation produced when laser produced electron bunches traverse a metallic foil before proceeding into the undulator. To calculate the expected undulator radiation we utilise equation 7.69 to retrieve spectral density and angular distributions of the undulator radiation in the far-field.

The Undulator fundamental radiation has a characteristic cone peaked on axis with a half angle given by equation 7.40. This is in contrast to the Transition Radiation, which has null intensity on-axis and the radiation is emitted in two lobes each peaked at an angle of $1/\gamma$.

The undulator radiation is more spatially and spectrally localised than the transition radaition. This is shown in figure 7.33–7.36 respectively, which shows the simulated undulator radiation and transition radiation for a 10 fs, 10 pC, 80 MeV Gaussian electron bunch.

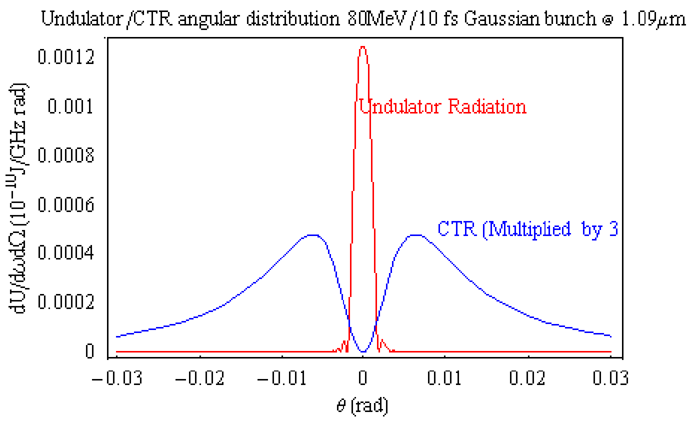

Figure 7.33: The angular distribution of the CTR (blue line) and undulator radiation (red line) for a 10 fs Gaussian bunch in the farfield.

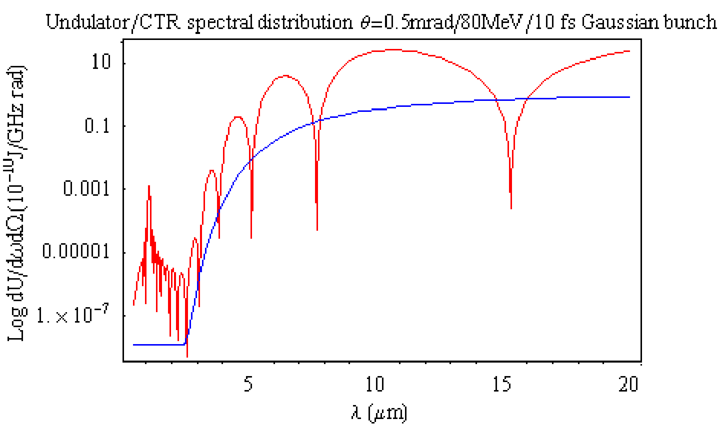

Figure 7.34: The wavelength dependence of the CTR (blue line) and undulator radiation (red line) for a 10 fs Gaussian bunch in the farfield for a collection angle of 0.5 mrad.

Collection angle	θ_{cen}**=1.9 mrad**	$\theta = 1/\gamma$	θ**=10 mrad**
no of photons, UR	8.2×10^5	1.24×10^6	1.2×10^6
no of photons, TR	194	1.0×10^4	2.9×10^4

Table 7.1: The total photon numbers integrated over various collection angles (1.9 mrad, $1/\gamma$ mrad and 10 mrad respectively) over the wavelength window of the undulator fundamental (0.95–1.2μm) for a 10 fs Gaussian bunch.

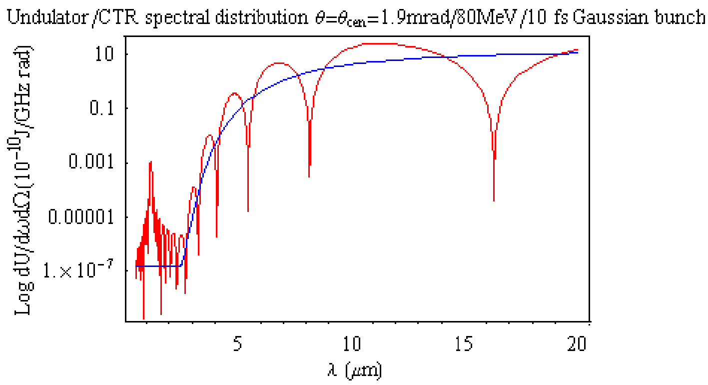

Figure 7.35: The wavelength dependence of the CTR (blue line) and undulator radiation (red line) for a 10 fs Gaussian bunch in the farfield for a collection angle of 1.9 mrad.

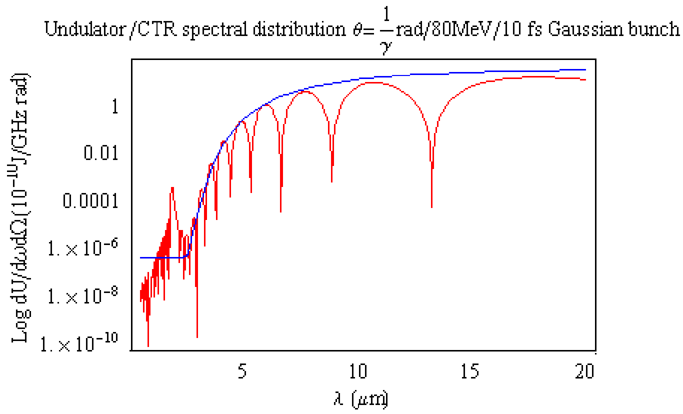

Figure 7.36: The wavelength dependence of the CTR (blue line) and undulator radiation (red line) for a 10 fs Gaussian bunch in the farfield for a collection angle of $1/\gamma$ mrad.

By inspection of Table 7.1 is it evident that the undulator radiation should be one to two orders of magnitude greater than the transition radiation for the collection angle of the experiment presented in this thesis.

7.4.10 Second harmonic undulator radiation

Several of laser shots recorded, showed similar behavior of matching peak energies and wavelengths according to equation 7.52. All shots which exhibit a spectral charge density greater than 1 pC / MeV in the range of 55 MeV to 75 MeV, produced a signal on the optical spectrometer. Each shot with a signal on the optical spectrometer shows a corresponding intense peak in that energy range, except a few shots which show a even higher charged peaks in the range of 40 MeV–50 MeV. Those shots produced second harmonic undulator radiation, which for those energies is in the detection range of the optical spectrometer. For these shots, the electron spectral intensity had to be above 7 pC / MeV in order to produce a detectable optical signal which is a rare event. The recorded second harmonic spectra are indeed very faint with a typical signal-to-noise ratio SNR $\leq$ 2 and are therefore not presented. This behavior is consistent with simulations of undulator radiation with SPECTRA [5], based on the actual undulator parameters, which exhibit an intensity ratio of 10:1 for fundamental to second harmonic undulator radiation. Hence, in order to produce a detectable second harmonic signal, the spectral charge density has to be 10 times larger than for fundamental radiation.

7.5 Discussion and outlook

The development of tabletop wakefield accelerators has progressed rapidly over the past five years since the first observation of monoenergetic electrons from gas jets in 2004 [1, 3, 2, 48] and the generation of GeV beams in 2006 from 3 cm long plasma waveguides [4]. In addition to an increase of beam energy, the charge, stability, and reproducibility of LWFA electron beams have also been dramatically improved through controlled injection via a counter-propagating laser pulse [30] and better control of laser stability [184]. This improvement in beam quality paves the way for forthcoming optically driven tabletop synchrotron light sources based on narrow energy spread GeV electron beams. As an example, consider a 1 GeV laser-produced electron beam [4] as a driver of the ALPHA-X undulator [255] (λ_u = 1.5 cm, N_u = 200, a_u = 0.7). This would lead to a 2.5 nm wavelength, ultrashort, incoherent radiation pulses with a peak bril-

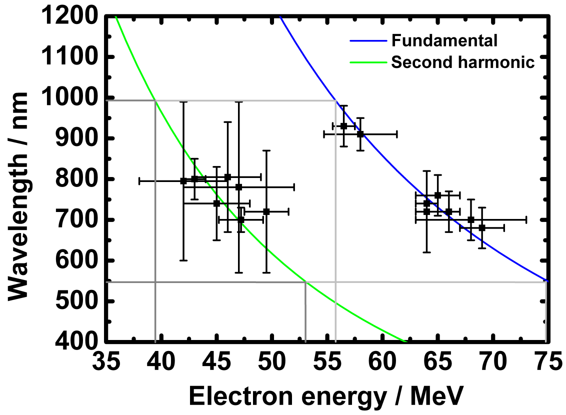

Figure 7.37: Correlation between measured electron spectra peak energies and undulator-radiation spectra peak wavelengths. The solid lines display the theoretical relation between electron energy and undulator-radiation wavelength according to equation 7.36 for (blue, $n = 1$) the fundamental and (green, $n = 2$) second harmonic. The gray bars arise from the detection range for optical radiation (560–990 nm) and guide to ranges for electron energies where electrons should produce an optical signal. Note: The error bars do not show an error in the sense of an uncertainty but the width of the electron and optical spectrometer signal, respectively.

liance of $B \sim 10^{23}$photons/s mrad^2 mm^2 0.1% bandwidth. Direct generation of coherent undulator radiation is more challenging as it requires electron bunches shorter than the emitted wavelength. Coherent emission from a pre-bunched beam will lead to infrared and far-infrared radiation [280]. However, to reach the UV or x-ray spectral region one must rely on the SASE mechanism. This involves microbunching of the electron beam with a wavelength periodicity due to the combined action of the amplified beam with the undulator field. The future generation of SASE free-electron lasers driven by laser wakefield accelerators will require excellent electron beam quality. It has been shown by Jaroszynski *et al* [280, 276] that the limit of acceptable energy spread for light field growth in an undulator should be less than 2 times the Pierce parameter, $\sigma_\gamma/\gamma_r \leq 2\rho$. If we consider sending an electron beam with a peak current of $I_{pk} = 1$ kA down an undulator with a magnetic field of $B_u = 1$ T, and a period of $\lambda_u = 1$ cm. The Pierce parameter for a helical undulator can be calculated to be $\rho = 1.136 B_u \lambda_u^{4/3} I_{pk}^{1/3}/\gamma_r$.

The growth in intensity of an injected or spontaneous field in a FEL amplifier is given by $I = I_0 exp(gz)$, where z is the propagation distance, $g = 4\pi\rho 3^{1/2}/\lambda_u$ [281, 282], which is a function of the beam energy γ, peak current, I_pk and normalised emittance, ε_n. For a matched electron beam, the FEL gain parameter is given by $\rho = 1.1\gamma^{-1} B_u \lambda_u^{4/3} I_{pk}^{1/3} \varepsilon_n^{-1/3}$. The matched electron beam radius from laser-plasma accelerators ($\varepsilon_n < 1$ mm mrad) is the order of a plasma wake wavelength, giving $\rho \approx 0.01$–0.001, for the electron beam parameters expected from a laser-plasma accelerator, and a gain length $L_g = \lambda_u/2\pi\sqrt{3}\rho$ of between 10 and 100 undulator periods, which is sufficient to obtain saturation in a 200 period for the largest ρ value and about 100 periods for $\rho = 10^{-3}$. With a $\lambda_u = 1.5$ cm undulator saturation should be reached with a 100 m long undulator. However, the main advantage of using a laser-driven plasma wakefield accelerator to drive a FEL is that the peak current could be between 10–30 kA. With injection of an external field from high harmonic generation in a gas the saturation length could be decreased further.

To obtain growth we need $\delta\gamma/\gamma < \rho$ and $\varepsilon_n < 4\lambda\beta\gamma\rho/\lambda_u$ or $\varepsilon_n < \gamma\lambda$ (matched). A 4 nm source assuming a 1 GeV beam with 100 pC of charge and a duration of 10 fs we obtain a peak current of $I_{pk} = 10$ kA and a $\rho \approx 0.005$, which gives a gain length of $10\lambda_u$ and a constraint on the energy spread of $\delta\gamma/\gamma \approx 0.1$–$0.5$ %, which may be achievable using a wakefield accelerator. FEL sources at x-ray wavelengths are less compact because the dependence of the gain on electron energy, $\rho \propto \gamma^{-1}$ leads to a lower gain and therefore the requirement of a longer undulator to achieve saturation.

To significantly shorten the undulator length SACSE could be used to enhance the start-up power. this has the additional benefit that the non-linear regime is entered promptly and the superradiant pulses should evolve self-similarly leading to very high efficiencies and extremely short, smooth and stable pulses. Pulses as short as a few attoseconds should be feasible in future x-ray FEL sources because the gain bandwidth is automatically increased in this regime. An FEL operating in the water window would require a beam of short duration electron bunches with an energy of about 1 GeV. For these conservative estimates the challenge is to obtain an emittance $\varepsilon_n < 1$ mm mrad [186] and an energy spread $\delta\gamma/\gamma < 0.01$ [281, 282].

In order for a superradiant light field to grow the energy spread must obey [19]

$$\frac{\sigma_\gamma}{\gamma} \leq 2\rho \tag{7.81}$$

similarly, the beam angular spread, which is a function of emittance, produces a longitudinal energy spread and thus also limits the gain analogous to increasing the spectral width of spontaneous undulator radiation (equation 7.56)

$$\frac{\sigma_{\gamma(\varepsilon_r)}}{\gamma_r} = \frac{k_\beta k_r \varepsilon_r}{2k_u} = \frac{\lambda_u \varepsilon_r}{2\lambda_\beta \lambda_r}, \tag{7.82}$$

which for a matched undulator $\lambda_\beta \approx L_g \approx \lambda_u/4\pi\rho$ reduces to

$$\frac{\sigma_{\gamma(\varepsilon_r)}}{\gamma_r} = \frac{2\pi\rho\varepsilon_r}{\lambda_r}. \tag{7.83}$$

This sets a limit to the emittance

$$\frac{\sigma_{\gamma(\varepsilon_r)}}{\gamma_r} < 2\rho \rightarrow \pi\varepsilon_r < \lambda_r \rightarrow \pi\varepsilon_n < \gamma_r\lambda_r. \tag{7.84}$$

The magnetic field of an undulator or wiggler is not the only way to exert a transverse force on a relativistic charged beam. Electrostatic forces or propagating electromagnetic fields are alternatives. Compton or Thomson backscattering from a laser beam, where the laser field acts as an undulator has long been considered as a means of converting laser photons to very high photon energies using relatively low energy electron beams [283]. Compton scattering occurs when the scattered photon energy is greater than the rest energy of the electron, $\hbar\omega > mc^2$. A high frequency laser beam is Doppler shifted by a factor of $4\gamma^2$ and appears to the electron as an effective undulator, thus all the theory discussed above on undulator and synchrotron radiation applies, with the undulator period L_u replaced by $\lambda/2$. When $a_0 > 1$ the characteristic wiggler type of radiation is often called non-linear Thomson or Compton scattering. An undulator parameter of $a_u \approx a_0 \approx 1$ requires an intensity of around 10^{18} Wcm^{-2} for 1 μm radiation. It is thus challenging to obtain a large diameter laser beam at this intensity so that the field seen in the electron frame appears as a plane wave, and sufficiently long and flat-topped, so that the Compton backscattered spectrum is narrow. Furthermore, the interaction length is limited by the Rayleigh length and/or the betatron wavelength and results in a radial variation of a_0. Compton backscattering is a very effective way to produce gamma rays. For example if one backscatters a 800 nm radiation pulse into a 1 GeV electron beam photon energies of 23 MeV can be produced. There have been several studies exploring the potential of using a laser-plasma accelerator to produce Compton backscattered photons at x-ray wavelengths [284, 285]. These studies indicate the potential of producing femtosecond duration x-ray pulses.

In conclusion, we have demonstrated the first all optically driven undulator radiation source. Ultrashort electron bunches in the range 55-70 MeV generated from a plasma wakefield accelerator have been used in conjunction with a static undulator to generate synchrotron radiation in the visible wavelength regime. Furthermore, analysis of the undulator radiation spectra has demonstrated that the electron energy spread is narrower than can be measured using this magnetic electron spectrometer. This is an important step towards the use of laser wakefield accelerators as drivers of synchrotron and FEL sources which may utilise the ultra-high electron peak current to significantly reduces the gain length and increases the tolerance with respect to the energy spread and the emittance. Extension of this experiment into the UV and x-ray wavelength regime and eventual coherent emission (SASE) of light will be an invaluable tool. The use of plasma undulators are also being investigated to shorten the undulator period [286, 287]. This not only allows the use of less energetic electrons to reach a certain wavelength but shows great promise as future compact X-ray sources.

Bibliography

[1] T. Tanaka and H. Kitamura. Spectra: A synchrotron radiation calculation code. *J. Synchrotron Rad.*, 8:1221, 2001.

[2] H.-P. Schlenvoigt, K. Haupt, A. Debus, F. Budde, O. Jäckel, H. Pfotenhauer, S.and Schwoerer, E. Rohwer, J. G. Gallacher, E. Brunetti, R. P. Shanks, S. M. Wiggins, and D. A. Jaroszynski. A compact synchrotron radiation source driven by a laser-plasma wakefield accelerator. *Nature Phys.*, 4:130–133, 2008.

[3] J. G. Gallacher, M. P. Anania, E. Brunetti, F. Budde, A. Debus, B. Ersfeld, K. Haupt, M. R. Islam, O. Jäckel, S. Pfotenhauer, A. J. W. Reitsma, E. Rohwer, H.-P. Schlenvoigt, H. Schwoerer, R. P. Shanks, S. M. Wiggins, and D. A. Jaroszynski. A method of determining narrow energy spread electron beams from a laser plasma wakefield accelerator using undulator radiation. *Physics of Plasmas*, 16(9):093102, 2009.

[4] Donald Umstadter. Relativistic laser-plasma interactions. *J. Phys. D: Appl. Phys.*, 36:R151–R165, 2003.

[5] S. P. D. Mangles. *Measurements of Relativistic Electrons from Intense Laser-Plasma Interactions*. PhD thesis, Plasma Physics Group, Imperial College, 2005.

[6] S. P. D. Mangles, C. D. Murphy, Z. Najmudin, A. G. R. Thomas, J. L. Collier, A. E. Dangor, E. J. Divall, P. S. Foster, J. G. Gallacher, C. J. Hooker, et al. Monoenergetic beams of relativistic electrons from intense laserplasma interactions. *Nature*, 431:535–538, 2004.

[7] C. Ziener. *Aufbau eines 12 Terawatt Titan:Saphir-Lasers zur effzienten Erzeugung charakteristischer Röntgenstrahlung*. PhD thesis, Friedrich-Schiller-Universität, Jena, 2001.

[8] B. Hidding, K.-U. Amthor, B. Liesfeld, H. Schwoerer, S. Karsch, S. M. Geissler, L. Veisz, K. Schmid, J. G. Gallacher, S. P. Jamison, D. Jaroszynski, G. Pretzler, and R. Sauerbrey. Generation of quasimonoenergetic electron bunches with 80-fs laser pulses. *Phys. Rev. Lett*, 96:105004, 2006.

[9] A. Yariv. *Optical Electronics in Modern Communications.* Oxford University Press, Inc., 1997.

[10] M. Hipp, J. Woisetschläger, P. Reiterer, and T. Neger. Digital evaluation of interferograms. *Elsevier - Measurement*, 36:53–66, 2004.

[11] D. Attwood. *Soft X-Rays and Extreme Ultraviolet Radiation.* Cambridge University Press, 1999.

[12] D. Strickland and G. Mourou. Compression of amplified chirped optical pulses. *Opt. Commun*, 56:219, 1985.

[13] P. Maine, D. Strickland, P. Bado, M. Pessot, and G. Mourou. Generation of ultrahigh peak power pulses by chirped-pulse amplification. *IEEE J. Quantum. Electron*, 24:398–403, 1988.

[14] S. M. Pfotenhauer. *Generation of monoenergetic ion beams with a laser accelerator.* PhD thesis, Friedrich-Schiller-Universität Jena, 2009.

[15] V. Yanovsky, V. Chvykov, G. Kalinchenko, P. Rousseau, T. Planchon, T. Matsuoka, A. Maksimchuk, J. Nees, G. Cheriaux, G. Mourou, and K. Krushelnick. Ultra-high intensity 300 tw laser at 0.1 hz repetition rate. *Opt. Express*, 16:2109, 2008.

[16] D. A. Jaroszynski, R. Bingham, and R. A. (Editors) Cairns. *Laser-Plasma Interactions.* CRC Press – Taylor & Francis Group, Boca Raton, 2009.

[17] R. Bingham, J. T. Mendonca, and P. K. Shukla. Plasma based charged particle accelerators. *Plas. Phys. Contr. Fus.*, 46:R1–R23, 2004.

[18] T. Tajima and J. M. Dawson. Laser electron accelerator. *Phys. Rev. Lett.*, 43(4):267–270, Jul 1979.

[19] M. L. Perl, G. S. Abrams, A. M. Boyarski, M. Breidenbach, D. D. Briggs, F. Bulos, W. Chinowsky, J. T. Dakin, G. J. Feldman, C. E. Friedberg, D. Fryberger, G. Goldhaber, G. Hanson, F. B. Heile, B. Jean-Marie, J. A. Kadyk, R. R. Larsen, A. M. Litke, D. Lüke, B. A. Lulu, V. Lüth, D. Lyon,

C. C. Morehouse, J. M. Paterson, F. M. Pierre, T. P. Pun, and P. A. Rapidis. The discovery of tau lepton. *Phys. Rev. Lett.*, 35(22):1489–1492, Dec 1975.

[20] F. Abe, H. Akimoto, A. Akopian, M. G. Albrow, S. R. Amendolia, D. Amidei, J. Antos, C. Anway-Wiese, S. Aota, G. Apollinari, T. Asakawa, W. Ashmanskas, M. Atac, P. Auchincloss, F. Azfar, P. Azzi-Bacchetta, N. Bacchetta, W. Badgett, S. Bagdasarov, M. W. Bailey, J. Bao, P. de Barbaro, A. Barbaro-Galtieri, V. E. Barnes, B. A. Barnett, P. Bartalini, and G. Bauer. Observation of top quark production in collisions with the collider detector at fermilab. *Phys. Rev. Lett.*, 74(14):2626–2631, Apr 1995.

[21] A Wright and R. Webb. The large hadron collider. *Nature*, 448:269, 2007.

[22] C. Joshi, W. B. Mori, T. Katsouleas, J. M. Dawson, J. M. Kindel, and D. W. Forslund. Ultrahigh gradient particle-acceleration by intense laser-driven plasma-density waves. *Nature*, 311:525, 1984.

[23] P. Muggli, B. E. Blue, C. E. Clayton, S. Deng, F.-J. Decker, M. J. Hogan, C. Huang, R. Iverson, C. Joshi, T. C. Katsouleas, S. Lee, W. Lu, K. A. Marsh, W. B. Mori, C. L. O'Connell, P. Raimondi, R. Siemann, and D. Walz. Meter-scale plasma-wakefield accelerator driven by a matched electron beam. *Phys. Rev. Lett.*, 93(1):014802, Jun 2004.

[24] I. Blumenfeld, C. E. Clayton, F. J. Decker, M. J. Hogan, C. Huang, R. Ischebeck, R. Iverson, C. Joshi, T. Katsouleasothers, N. Kirby, et al. Energy doubling of 42 gev electrons in a metre-scale plasma wakefield accelerator. *Nature*, 445:741–744, 2007.

[25] K. Krushelnick, Z. Najmudin, S. P. D. Mangles, A. G. R. Thomas, M. S. Wei, B. Walton, A. Gopal, E. L. Clark, A. E. Dangor, S. Fritzler, C. D. Murphy, P. A. Norreys, W. B. Mori, J. Gallacher, D. Jaroszynski, and R. Viskup. Laser plasma acceleration of electrons: Towards the production of monoenergetic beams. *Physics of Plasmas*, 12(5):056711, 2005.

[26] J. Faure, Y. Glinec, A. Pukhov, S. Kiselev, S. Gordienko, E. Lefebvre, J.-P. Rousseau, F. Burgy, and V. Malka. A laser-plasma accelerator producing monoenergetic electron beams. *Nature*, 431:541–544, 2004.

[27] C. G. R. Geddes, Cs. Toth, J. van Tilborg, E. Esarey, C. B. Schroeder, D. Bruhwiler, C. Nieter, J. Cary, and W. P. Leemans. High-quality elec-

tron beams from a laser wakefield accelerator using plasma-channel guiding. *Nature*, 431:538–541, 2004.

[28] W. P. Leemans, B. Nagler, A. J. Gonsalves, Cs. Tóth, K. Nakamura, C. G. R. Geddes, E. Esarey, C. B. Schroeder, and S. M. Hooker. Gev electron beams from a centimetre-scale accelerator. *Nature Phys*, 2:696–699, 2006.

[29] K. Nakamura, B. Nagler, Cs. Tóth, C. G. R. Geddes, C. B. Schroeder, E. Esarey, and W. P. Leemans. Gev electron beams from a centimeter-scale channel guided laser wakefield accelerator. *Phys. Plasmas*, 14:056708, 2007.

[30] J. Faure, C. Rechatin, A. Norlin, A. Lifschitz, Y. Glinic, and V. Malka. Controlled injection and acceleration of electrons in plasma wakefields by colliding laser pulses. *Nature*, 444:737–739, 2006.

[31] N. H. Matlis, S. Reed, S. S. Bulanov, V. Chvykov, G. Kalintchenko, T. Matsuoka, P. Rousseau, V. Yanovsky, A. Maksimchuk, S. Kalmykov, G. Shvets, and M. C. Downer. Snapshots of laser wakefields. *Nature Phys*, 2:749–753, 2006.

[32] T. Ditmire. Petawatt laser probes nature at texas university. *Physics Today*, 61:27, 2008.

[33] K. Schmidt, L. Veisz, F. Tavella, S. Benavides, R. Tautz, D. Herrmann, A. Buck, B. Hidding, A. Marcinkevicius, U. Schramm, et al. Few-cycle laser-driven electron acceleration. *Phys. Rev. Lett*, 102:124801, 2009.

[34] Rauand Bernhard, Tajima T., and Hojoand H. Coherent electron acceleration by subcycle laser pulses. *Phys. Rev. Lett.*, 78(17):3310–3313, Apr 1997.

[35] J. Krall, A. Ting, E. Esarey, and P. Sprangle. Enhanced acceleration in a self-modulated-laser wake-field accelerator. *Phys. Rev. E*, 48(3):2157–2161, Sep 1993.

[36] C. A. Coverdale, C. B. Darrow, C. D. Decker, W. B. Mori, K-C. Tzeng, K. A. Marsh, C. E. Clayton, and C. Joshi. Propagation of intense subpicosecond laser pulses through underdense plasmas. *Phys. Rev. Lett.*, 74(23):4659–4662, Jun 1995.

[37] W. B. Mori, C. D. Decker, D. E. Hinkel, and T. Katsouleas. Raman forward scattering of short-pulse high-intensity lasers. *Phys. Rev. Lett.*, 72(10):1482–1485, Mar 1994.

[38] C. D. Decker, W. B. Mori, and T. Katsouleas. Particle-in-cell simulations of raman forward scattering from short-pulse high-intensity lasers. *Phys. Rev. E*, 50(5):R3338–R3341, Nov 1994.

[39] W. B. Mori. The physics of the nonlinear optics of plasmas at relativistic intensities for short-pulse lasers. *IEEE J. Quantum. Electron*, 33:1942, 1997.

[40] P. Sprangle, E. Esarey, J. Krall, and G. Joyce. Propagation and guiding of intense laser pulses in plasmas. *Phys. Rev. Lett.*, 69:2200–2203, 1992.

[41] D. Umstadter, S.-Y. Chen, A. Maksimchuk, G. Mourou, and R. Wagner. Nonlinear optics in relativistic plasmas and laser wake field acceleration of electrons. *Science*, 273:472, 1996.

[42] T. M. Antonsen and P. Mora. Self-focusing and raman scattering of laser pulses in tenuous plasmas. *Phys. Rev. Lett.*, 69(15):2204–2207, Oct 1992.

[43] W. T. Chen, T. Y. Chien, C. H. Lee, J. Y. Lin, J. Wang, and S. Y. Chen. Optically controlled seeding of raman forward scattering and injection of electrons in a self-modulated laser-wakefield accelerator. *Phys. Rev. Lett.*, 92(7):075003, Feb 2004.

[44] E. Esarey, B. Hafizi, R. Hubbard, and A. Ting. Trapping and acceleration in self-modulated laser wakefields. *Phys. Rev. Lett*, 80:5552–5555, 1998.

[45] K. Nakajima, D. Fisher, T. Kawakubo, H. Nakanishi, A. Ogata, Y. Kato, Y. Kitagawa, R. Kodama, K. Mima, H. Shiraga, K. Suzuki, K. Yamakawa, T. Zhang, Y. Sakawa, T. Shoji, Y. Nishida, N. Yugami, M. Downer, and T. Tajima. Observation of ultrahigh gradient electron acceleration by a self-modulated intense short laser pulse. *Phys. Rev. Lett.*, 74(22):4428–4431, May 1995.

[46] A. Pukhov and J. Meyer-ter Vehn. Laser wake field acceleration: the highly non-linear broken-wave regime. *Appl. Phys. B*, 74:355, 2002.

[47] A. Pukhov, S. Kiselev, I. Kostyukov, O. Shorokhov, and S. Gordienko. Relativistic laser-plasma bubbles: new sources of energetic particles and x-rays. *Nuclear Fusion*, 44:S191, 2004.

[48] S. P. D. Mangles, A. G. R. Thomas, M. C. Kaluza, O. Lundh, F. Lindau, A. Persson, F. S. Tsung, Z. Najmudin, W. B. Mori, C.-G. Wahlström, et al. Laser-wakefield acceleration of monoenergetic electron beams in the first plasma-wave period. *Phys. Rev. Lett*, 96:215001, 2006.

[49] A. Pukhov and J. Meyer-ter Vehn. Relativistic laser-plasma interaction by multi-dimensional particle-in-cell simulations. *Phys. Plasmas*, 5:1880, 1998.

[50] A. Pukhov, Z. M. Sheng, and J. Meyer-ter Vehn. Particle acceleration in relativistic laser channels. *Phys. Plasmas*, 6:2847, 1999.

[51] V. Malka, J. Faure, J. R. Marqus, F. Amiranoff, J. P. Rousseau, S. Ranc, J. P. Chambaret, Z. Najmudin, and B. Walton. Characterization of electron beams produced by ultrashort (30 fs) laser pulses. *Phys. Plasmas*, 8:2605, 2001.

[52] J. M. Dawson and C. Oberman. High-frequency conductivity and the emission and absorption coefficients of a fully ionized plasma. *Phys. Fluids*, 5:517, 1962.

[53] F.F Chen. Excitation of large amplitude plasma waves. *Phys. Scr*, T30:14–23, 1990.

[54] T. P. Coffey. Breaking of large amplitude plasma oscillations. *Phys. Fluids*, 14:1402–1406, 1971.

[55] T. Katsouleas and W. Mori. Wave-breaking amplitude of relativistic oscillations in a thermal plasma. *Phys. Rev. Lett.*, 61:90–93, 1988.

[56] A. Modena, Z. Najmudin, A. E. Dangor, C. E. Clayton, K. A. Marsh, Joshi. C., V. Malka, C. B. Darrow, C. Danson, D. Neely, and F. N. Walsh. Electron acceleration from the breaking of relativistic plasma-waves. *Nature*, 377:606, 1995.

[57] R. F. Hubbard, D. Kaganovich, B. Hafizi, C. I. Moore, P. Sprangle, A. Ting, and A. Zigler. Simulation and design of stable channel-guided laser wakefield accelerators. *Phys. Rev. E*, 63(3):036502, Feb 2001.

[58] P. Sprangle, B. Hafizi, J. R. Peñano, R. F. Hubbard, A. Ting, A. Zigler, and T. M. Antonsen. Stable laser-pulse propagation in plasma channels for gev electron acceleration. *Phys. Rev. Lett.*, 85(24):5110–5113, Dec 2000.

[59] A. G. Thomas, Z. Najmudin, S. P. Mangles, C. D. Murphy, A. E. Dangor, C. Kamperidis, K. L. Lancaster, W. B. Mori, P. A. Norreys, W. Rozmus, and K. Krushelnick. Effect of laser-focusing conditions on propagation and monoenergetic electron production in laser-wakefield accelerators. *Phys. Rev. Lett.*, 98:095004, 2007.

[60] D. J. Spence, P. D. S. Burnett, and S. M. Hooker. Measurement of the electron-density profile in a discharge-ablated capillary waveguide. *Opt. Lett.*, 24:993–995, 1999.

[61] D. J. Spence and S. M. Hooker. Simulations of the propagation of high-intensity laser pulses in discharge-ablated capillary waveguides. *Journal of the Optical Society of America B*, 17:1565–1570, 2000.

[62] S. M. Hooker, D. J. Spence, and R. A. Smith. Guiding of high-intensity picosecond laser pulses in a discharge-ablated capillary waveguide. *J. Opt. Soc. Am. B*, 17:90–98, 2000.

[63] D. J. Spence, A. Butler, and S. M. Hooker. First demonstration of guiding of high-intensity laser pulses in a hydrogen-filled capillary discharge waveguide. *J. Phys. B. Atomic and Molecular Physics*, 34:4103–4112, 2001.

[64] A. Butler, D. J. Spence, and S. M. Hooker. Guiding of high-intensity laser pulses with a hydrogen-filled capillary discharge waveguide. *Phys. Rev. Lett.*, 89:185003, 2002.

[65] D. A. Jaroszynski, R. Bingham, E. Brunetti, B. Ersfeld, J. Gallacher, B. van der Geer, R. Issac, S. P. Jamison, D. Jones, M. de Loos, A. Lyachev, V Pavlov, A Reitsma, Y. Saveliev, G. Vieux, and S. M. Wiggins. Radiation sources based on laserplasma interactions. *Phil. Trans. R. Soc. A*, 364(1840):689–710, Mar 2006.

[66] G. Pellegrini, P. Roy, R. Bates, D. Jones, K. Mathieson, J. Melone, V. O'Shea, K. M. Smith, I. Thayne, P. Thornton, J. Linnros, W. Rodden, and M. Rahman. Technology development of 3d detectors for high-energy physics and imaging. *Nucl. Instrum. Meth. Phys. Res. A*, 487:19, 2002.

[67] G. Rice, D. Jones, K. S. Kim, J. M. Girkin, D. Jaroszynski, and M. D. Dawson. Micromachining of gallium nitride, sapphire, and silicon carbide with ultrashort pulses. *Proc. SPIE Int. Soc. Opt. Eng.*, 5147:299, 2003.

[68] P. Volfbeyn, E. Esarey, and W. P. Leemans. Guiding of laser pulses in plasma channels created by the ignitor-heater technique. *Phys. Plasmas*, 6:2269, 1999.

[69] F. B. Kiewiet. *Generation of ultra-short, high-brightness relativistic electron bunches*. PhD thesis, Technische Universiteit Eindhoven, 2003.

[70] C. Pellegrini, J. Rosenzweig, G. Travish, K. Bane, R. Boyce, G. Loew, P. Morton, H.-D. Nuhn, J. Paterson, P. Pianetta, T. Raubenheimer, J. Seeman, R. Tatchyn, V. Vylet, H. Winick, K. Halbach, K.-J. Kim, M. Xie, D. Prosnitz, E.T. Scharlemann, R. Bonifacio, L. De Salvo, and P. Pierini. The slac soft x-ray high power fel. *Nucl. Instrum. Meth. Phys. Res. A*, 341:326–330, 1994.

[71] G. Berden, S. P. Jamison, A. M. MacLeod, W. A. Gillespie, B. Redlich, and A. F. G. van der Meer. Electro-optic technique with improved time resolution for real-time, nondestructive, single-shot measurements of femtosecond electron bunch profiles. *Phys. Rev. Lett*, 93:114802, 2004.

[72] G. Berden, W. A. Gillespie, S. P. Jamison, E.-A. Knabbe, A. M. MacLeod, A. F. G. van der Meer, P. J. Phillips, H. Schlarb, B. Schmidt, P. Schmüser, and B. Steffen. Benchmarking of electro-optic monitors for femtosecond electron bunches. *Phys. Rev. Lett.*, 99(16):164801, Oct 2007.

[73] J. van Tilborg, C. B. Schroeder, C. V. Filip, Cs. Tóth, C. G. R. Geddes, G. Fubiani, R. Huber, R. A. Kaindl, E. Esarey, and W. P. Leemans. Temporal characterization of femtosecond laser-plasma-accelerated electron bunches using terahertz radiation. *Phys. Rev. Lett*, 96:014801, 2006.

[74] J. van Tilborg, C. B. Schroeder, C. V. Filip, C. Tóth, C. G. R. Geddes, G. Fubiani, E. Esarey, and W. P. Leemans. Terahertz radiation as a bunch diagnostic for laser-wakefield-accelerated electron bunches. *Phys. Plasmas*, 13:056704, 2006.

[75] K-C. Tzeng, W. B. Mori, and T. Katsouleas. Electron beam characteristics from laser-driven wave breaking. *Phys. Rev. Lett*, 79:5258, 1997.

[76] M. Borghesi, A. J. Mackinnon, D. H. Campbell, D. G. Hicks, S. Kar, P. K. Patel, D. Price, L. Romagnani, A. Schiavi, and O. Willi. Multi-mev proton source investigations in ultraintense laser-foil interactions. *Phys. Rev. Lett.*, 92(5):055003, Feb 2004.

[77] L. J. Perkins et al. The investigation of high intensity laser driven micro neutron sources for fusion materials research at high fluence. *Nucl. Fusion*, 40:1, 2000.

[78] W. P. Leemans, E. Esarey, J. van Tilborg, P. A. Michel, C. B. Schroeder, C. Toth, C. G. R. Geddes, and B. A. Shadwick. Radiation from laser accelerated electron bunches: Coherent terahertz and femtosecond x-rays. *IEEE Trans. Plasma Sci*, 33:8–22, 2005.

[79] W. B. Mori. Overview of laboratory plasma radiation sources. *Physica Scripta*, T52:28–35, 1994.

[80] M. Roth, T. E. Cowan, M. H. Key, S. P. Hatchett, C. Brown, W. Fountain, J. Johnson, D. M. Pennington, R. A. Snavely, S. C. Wilks, K. Yasuike, H. Ruhl, F. Pegoraro, S. V. Bulanov, E. M. Campbell, M. D. Perry, and H. Powell. Fast ignition by intense laser-accelerated proton beams. *Phys. Rev. Lett.*, 86(3):436–439, Jan 2001.

[81] M. Temporal, J. J. Honrubia, and S. Atzeni. Numerical study of fast ignition of ablatively imploded deuterium-tritium fusion capsules by ultra-intense proton beams. *Phys. Plasmas*, 9:3098, 2002.

[82] M. I. K. et al Santala. Production of radioactive nuclides by energetic protons generated from intense laser-plasma interations. *Appl. Phys. Lett*, 78:19, 2001.

[83] S. et al Fritzler. Proton beams generated with high intensity lasers: Applications to medical isotope production. *Appl. Phys. Lett*, 83:3039, 2003.

[84] I. et al Spencer. Laser generation of proton beams for the production of short-lived positron emitting radioisotopes. *Nucl. Instrum. Methods Phys. Res. B Beam Interact. Mater. Atoms*, 183:449, 2001.

[85] K. W. D. Ledingham, P. McKenna, and R. P. Singhal. Applications for nuclear phenomena generated by ultra-intense lasers. *Science*, 300:1107, 2003.

[86] K. W. D. et al Ledingham. High power laser production of short-lived isotopes for positron emission tomography. *J. Phys. D Appl. Phys*, 37:2341, 2004.

[87] S. V. Bulanov, T. Z. Esirkepov, V. S. Khoroshkov, A. V. Kunetsov, and F. Pegoraro. Oncological hadrontherapy with laser ion accelerators. *Phys. Lett. A*, 299:240, 2002.

[88] S. V. Bulanov and V. S. Khoroshkov. Feasibility of using laser ion accelerators in proton therapy. *Plasma Phys. Rep.*, 28:453, 2002.

[89] E. Fourkal and C. Ma. Laser-accelerated carbon ion beams for radiation therapy. *Med. Phys*, 30:1448, 2003.

[90] E. Fourkal, R. Price, C. Ma, and A. Pollack. Energy and intensity modulated radiation therapy using laser accelerated proton beams. *Med. Phys*, 31:1884, 2004.

[91] V. et al Malka. Practicability of protontherapy using compact laser systems. *Med. Phys.*, 31:1587, 2004.

[92] J. A. Cobble, R. P. Johnson, T. E. Cowan, N. Renard-Le Galloudec, and M. Allen. High resolution laser-driven proton radiography. *J. Appl. Phys*, 92:1775, 2002.

[93] H. Habara, R. Kodama, Y. Sentoku, N. Izumi, Y. Kitagawa, K. A. Tanaka, K. Mima, and T. Yamanaka. Fast ion acceleration in ultraintense laser interactions with an overdense plasma. *Phys. Rev. E*, 69(3):036407, Mar 2004.

[94] I. Spencer, K. W. D. Ledingham, P. McKenna, T. McCanny, R. P. Singhal, P. S. Foster, D. Neely, A. J. Langley, E. J. Divall, C. J. Hooker, R. J. Clarke, P. A. Norreys, E. L. Clark, K. Krushelnick, and J. R. Davies. Experimental study of proton emission from 60-fs, 200-mj high-repetition-rate tabletop-laser pulses interacting with solid targets. *Phys. Rev. E*, 67(4):046402, Apr 2003.

[95] E. L. Clark, K. Krushelnick, M. Zepf, F. N. Beg, M. Tatarakis, A. Machacek, M. I. K. Santala, I. Watts, P. A. Norreys, and A. E. Dangor. Energetic heavy-ion and proton generation from ultraintense laser-plasma interactions with solids. *Phys. Rev. Lett.*, 85(8):1654–1657, Aug 2000.

[96] T. et al Ditmire. High-energy ions produced in explosions of superheated atomic clusters. *Nature*, 386:54, 1997.

[97] G. Pretzler, A. Saemann, A. Pukhov, D. Rudolph, T. Schätz, U. Schramm, P. Thirolf, D. Habs, K. Eidmann, G. D. Tsakiris, J. Meyer-ter Vehn, and K. J. Witte. Neutron production by 200 mj ultrashort laser pulses. *Phys. Rev. E*, 58(1):1165–1168, Jul 1998.

[98] W. P. Leemans, D. Rodgers, P. E. Catravas, C. G. R. Geddes, G. Fubiani, E. Esarey, B. A. Shadwick, R. Donahue, and A. Smith. Gamma-neutron activation experiments using laser wakefield accelerators. *Phys. Plasmas*, 8:2510, 2001.

[99] S. Fritzler, Z. Najmudin, V. Malka, K. Krushelnick, C. Marle, B. Walton, M. S. Wei, R. J. Clarke, and A. E. Dangor. Ion heating and thermonuclear neutron production from high-intensity subpicosecond laser pulses interacting with underdense plasmas. *Phys. Rev. Lett.*, 89(16):165004, Sep 2002.

[100] K. L. et al Lancaster. Characterization of li-7(p,n)be-7 neutron yields from laser produced ion beams for fast neutron radiography. *Phys. Plasmas*, 11:3404, 2004.

[101] J. M. et al Yang. Neutron production by fast protons from ultraintense laser-plasma interactions. *J. Appl. Phys*, 96:6912, 2004.

[102] L. Disdier, J. P. Garconnet, G. Malkaand, and J. L. Miquel. Fast neutron emission from a high energy ion beam produced by a high-intensity subpicosecond laser pulse. *Phys. Rev. Lett*, 82:1454, 1999.

[103] C. Toupin, E. Lefebvre, and G. Bonnaud. Neutron emission from a deuterated solid target irradiated by an ultraintense laser pulse. *Phys. Plasmas*, 8:1011, 2001.

[104] P. A. et al Norreys. Neutron production from picosecond laser irradiation of deuterated targets at intensities of 10(19) wcm(-2). *Plasma Phys. Control. Fusion*, 40:175, 1998.

[105] G. Grillon, Ph. Balcou, J.-P. Chambaret, D. Hulin, J. Martino, S. Moustaizis, L. Notebaert, M. Pittman, Th. Pussieux, A. Rousse, J-Ph. Rousseau, S. Sebban, O. Sublemontier, and M. Schmidt. Deuterium-deuterium fusion dynamics in low-density molecular-cluster jets irradiated by intense ultrafast laser pulses. *Phys. Rev. Lett.*, 89(6):065005, Jul 2002.

[106] M. Tabak, J. Hammer, M. E. Glinsky, W. L. Kruer, S. C. Wilks, J. Woodworth, E. M. Campbell, M. D. Perry, and R. J. Mason. Ignition and high gain with ultrapowerful lasers. *Phys. Plasmas*, 1:1626–1634, 1994.

[107] R. Kodama, P. A. Norreys, K. Mima, A. E. Dangor, R. G. Evans, H. Fujita, Y. Kitagawa, K. Krushelnick, T. Miyakoshi, N. Miyanaga, T. Norimatsu, S. J. Rose, T. Shozaki, K. Shigemori, A. Sunahara, M. Tampo, K. A. Tanaka, Y. Toyama, T. Yamanaka, and M. Zepf. Fast heating of ultrahigh-density plasma as a step towards laser fusion ignition. *Nature*, 412:798–802, 2001.

[108] W. P. Leemans, C. G. R. Geddes, J. Faure, Cs. Tóth, J. van Tilborg, C. B. Schroeder, E. Esarey, G. Fubiani, D. Auerbach, B. Marcelis, M. A. Carnahan, R. A. Kaindl, J. Byrd, and M. C. Martin. Observation of terahertz emission from a laser-plasma accelerated electron bunch crossing a plasma-vacuum boundary. *Phys. Rev. Lett*, 91(7):074802, 2003.

[109] W. P. Leemans, J. van Tilborg, J. Faure, C. G. R. Geddes, C. Toth, C. B. Schroeder, E. Esarey, G. Fubiani, and G. Dugan. Terahertz radiation from laser accelerated electron bunches. *Phys. Plasmas*, 11:2899, 2004.

[110] A. D. Debus, M. Bussmann, U. Schramm, R. Sauerbrey, C. D. Murphy, Zs. Major, R. Hörlein, L. Veisz, K. Schmid, J. Schreiber, K. Witte, S. P. Jamison, J. G. Gallacher, D. A. Jaroszynski, M. C. Kaluza, B. Hidding, S. Kiselev, R. Heathcote, P. S. Foster, D. Neely, E. J. Divall, C. J. Hooker, J. M. Smith, K. Ertel, A. J. Langley, P. Norreys, and J. L. Collier. Electron bunch length measurements from laser-accelerated electrons using single-shot thz time-domain interferometry. *Phys. Rev. Lett.*, 104(8):084802, Feb 2010.

[111] S. Düsterer, H. Schwoerer, W. Ziegler, C. Ziener, and R. Sauerbrey. Optimization of euv radiation yield from laser-produced plasma. *Appl. Phys. B*, 73:693–698, 2001.

[112] P. Salieres and M. Lewenstein. Generation of ultrashort coherent xuv pulses by harmonic conversion of intense laser pulses in gases: Towards attosecond pulses. *Meas. Sci. Tech*, 12:1818–1827, 2000.

[113] M. Schnurer, C. Spielmann, P. Wobrauschek, C. Streli, N. H. Burnett, C. Kan, K. Ferencz, R. Koppitsch, Z. Cheng, T. Brabec, and F. Krausz.

Coherent 0.5-kev x-ray emission from helium driven by a sub 10 fs laser. *Phys. Rev. Lett*, 80:3236–3238, 1998.

[114] J. Seres et al. Source of coherent kiloelectronvolt x-rays. *Nature*, 433:596, 2005.

[115] Y. Glinec, J. Faure, L. Le Dain, S. Darbon, T. Hosokai, J. J. Santos, E. Lefebvre, J. P. Rousseau, F. Burgy, B. Mercier, and V. Malka. High-resolution g-ray radiography produced by a laser-plasma driven electron source. *Phys. Rev. Lett*, 94:025003, 2004.

[116] B. Dromey, M. Zepf, A. Gopal, K. Lancaster, M. S. Wei, K. Krushelnick, M. Tatarakis, N. Vakakis, S. Moustaizis, R. Kodama, M. Tampo, C. Stoeck, R. Clarke, H. Habara, D. Neely, S. Karsch, and P. Norreys. High harmonic generation in the relativistic limit. *Nature Phys*, 2:456–459, 2006.

[117] B. Dromey, S. Kar, C. Bellei, D. C. Carroll, R. J. Clarke, J. S. Green, S. Kneip, K. Markey, S. R. Nagel, P. T. Simpson, L. Willingale, P. McKenna, D. Neely, Z. Najmudin, K. Krushelnick, P. A. Norreys, and M. Zepf. Bright multi-kev harmonic generation from relativistically oscillating plasma surfaces. *Physical Review Letters*, 99(8):085001, 2007.

[118] E. Brunetti, R. Issac, and D. A. Jaroszynski. Quantum path contribution to high-order harmonic spectra. *Phys. Rev. A*, 77(2):023422, Feb 2008.

[119] B. Dromey, D. Adams, R. Hörlein, Y. Nomura, S. G. Rykovanov, D. C. Carroll, P. S. Foster, S. Kar, K. Markey, P. McKenna, D. Neely, M. Geissler, Tsakiris G. D., and M. Zepf. Diffraction-limited performance and focusing of high harmonics from relativistic plasmas. *Nature Physics*, 5:146–152, 2009.

[120] P. B. Corkum, N. H. Burnett, and M. Y. Ivanov. Subfemtosecond pulses. *Opt. Lett*, 19:1870–1872, 1994.

[121] P. B. Corkum and F. Krausz. Attosecond science. *Nature Phys*, 3:381–387, 2007.

[122] D. H. Auston, K. P. Cheung, J. A. Valdmanis, and D. A. Kleinman. Cherenkov radiation from femtosecond optical pulses in electro-optic media. *Phys. Rev. Lett.*, 53:1555, 1984.

[123] C. Rolland and P. B. Corkum. Generation of 130-fsec midinfrared pulses. *J. Opt. Soc. Am. B*, 3:1625, 1986.

[124] H. N. Chapman. X-ray imaging beyond the limits. *Nature Materials*, 8:299–301, 2009.

[125] D. H. Bilderback, P. Elleaume, and E. Weckert. Review of third and next generation synchrotron light sources. *J. Phys. B: At. Mol. Opt.Phys.*, 38:S773–S797, 2005.

[126] R. Fedele, G. Miano, and V. G. Vaccaro. The plasma undulator. *Physica Scripta*, T30:192–197, 1990.

[127] M. Kando, Y. Fukuda, A. S. Pirozhkov, J. Ma, I. Daito, L.-M. Chen, T. Zh. Esirkepov, K. Ogura, T. Homma, Y. Hayashi, H. Kotaki, A. Sagisaka, M. Mori, J. K. Koga, H. Daido, S. V. Bulanov, T. Kimura, Y. Kato, and T. Tajima. Demonstration of laser-frequency upshift by electron-density modulations in a plasma wakefield. *Physical Review Letters*, 99(13):135001, 2007.

[128] M. Lampe, E. Ott, and J. H. Walker. Interaction of electromagnetic waves with a moving ionization front. *Phys. Fluids*, 21(1):42–54, 1978.

[129] C. H. Lai, R. Liou, T. C. Katsouleas, P. Muggli, R. Brogle, C. Joshi, and W. B. Mori. Demonstration of microwave generation from a static field by a relativistic ionization front in a capacitor array. *Phys. Rev. Lett*, 77(23):4764, 1996.

[130] W. B. Mori, T. Katsouleas, J. M. Dawson, and C. H. Lai. Conversion of dc fields in a capacitor array to radiation by a relativistic ionization front. *Phys. Rev. Lett*, 74(4):542, 1995.

[131] M. Kando, A. S. Pirozhkov, K. Kawase, T. Zh. Esirkepov, Y. Fukuda, H. Kiriyama, H. Okada, I. Daito, T. Kameshima, Y. Hayashi, H. Kotaki, M. Mori, J. K. Koga, H. Daido, A. Ya. Faenov, T. Pikuz, J. Ma, L.-M. Chen, E. N. Ragozin, T. Kawachi, Y. Kato, T. Tajima, and S. V. Bulanov. Enhancement of photon number reflected by the relativistic flying mirror. *Phys. Rev. Lett.*, 103(23):235003, Dec 2009.

[132] D.A. Jaroszynski, B. Ersfeld, G. Giraud, S. Jamison, D.R. Jones, R.C. Issac, B.M.W. McNeil, A.D.R. Phelps, G.R.M. Robb, H. Sandison, G. Vieux, S.M. Wiggins, and K. Wynne. The strathclyde terahertz to optical pulse source (tops). *Nuclear Instruments and Methods in Physics Research A*, 445:317–319, 2000.

[133] O. Chekhlov, J. Collier, R.J. Clark, C. Hernandez-Gomez, A. Lyachev, P. Matousek, I.O. Musgrave, D. Neely, P.A. Norreys, I. Ross, Y. Tang, T.B. Winstone, and B.E. Wyborn. The 10 pw opcpa vulcan laser upgrade. *Lasers and Electro-Optics 2009 and the European Quantum Electronics Conference. CLEO Europe - EQEC 2009. European Conference on*, page 1, 2009.

[134] C. J. Hooker, J. L. Collier, O. Chekhlov, R. Clarke, E. Divall, K. Ertel, B. Fell, P. Foster, S. Hancock, and A. Langley. The astra gemini project - a dual-beam petawatt ti:sapphire laser system. *J PHYS IV*, 133:673–678, 2006.

[135] A. Dubietis, G. Jonusauskas, and A. Piskarskas. Powerful femtosecond pulse generation by chirped and stretched pulse parametric amplification in bbo crystal. *Optics Communications*, 88(4-6):437–440, 1992.

[136] I. N. Ross, P. Matousek, M. Towrie, A. J. Langley, and J. L. Collier. The prospects for ultrashort pulse duration and ultrahigh intensity using optical parametric chirped pulse amplifiers. *Optics Communications*, 144(1-3):125 – 133, 1997.

[137] Luis O. Silva, F. Fiza, R.A. Fonseca, J.L. Martins, S.F. Martins, J. Vieira, C. Huang, W. Lu, F. Tsung, M. Tzoufras, and W.B. Mori. Laser electron acceleration with 10 pw lasers. *Comptes Rendus Physique*, 10(2–3):167–175, 2009. Laser acceleration of particles in plasma.

[138] N. Fleurot, C. Cavailler, and J.L. Bourgade. The laser megajoule (lmj) project dedicated to inertial confinement fusion: Development and construction status. *Fusion Engineering and Design*, 74:147–154, 2005.

[139] J. Ebrardt et al. Lmj project status. *J. Phys.: Conf. Ser.*, 112:032005, 2008.

[140] C. BIbeau, P. J. Wegner, E. I . Moses, and B. E. Warner. Generating powerful ultraviolet beams with the worlds largest laser. *Laser Focus World*, 42:113–117, 2006.

[141] C. A. Haynam et al. The national ignition facility 2007 laser performance status. *J. Phys.: Conf. Ser.*, 112:032004, 2008.

[142] M. Dunne. A high-power laser fusion facility for europe. *Nature Phys*, 2:2–5, 2006.

[143] Stefano Atzeni, Angelo Schiavi, and Claudio Bellei. Targets for direct-drive fast ignition at total laser energy of 200–400 kj. *Physics of Plasmas*, 14(5):052702, 2007.

[144] S. Atzeni, A. Schiavi, J. J. Honrubia, X. Ribeyre, G. Schurtz, Ph. Nicolaï, M. Olazabal-Loumé, C. Bellei, R. G. Evans, and J. R. Davies. Fast ignitor target studies for the hiper project. *Physics of Plasmas*, 15(5):056311, 2008.

[145] B. Ersfeld and D. A. Jaroszynski. Superradiant linear raman amplification in plasma using a chirped pump pulse. *Phys. Rev. Lett.*, 95(16):165002, Oct 2005.

[146] A. Lyachev. *High gain ultra-short laser pulse Raman amplification in plasma*. PhD thesis, University of Strathclyde, 2007.

[147] M. Dreher, E. Takahashi, J. Meyer-ter Vehn, and K.-J. Witte. Observation of superradiant amplification of ultrashort laser pulses in a plasma. *Phys. Rev. Lett.*, 93(9):095001, Aug 2004.

[148] W. Cheng, Y. Avitzour, Y. Ping, S. Suckewer, N. J. Fisch, M. S. Hur, and J. S. Wurtele. Reaching the nonlinear regime of raman amplification of ultrashort laser pulses. *Phys. Rev. Lett.*, 94(4):045003, Feb 2005.

[149] C.-H. Pai, M.-W. Lin, L.-C. Ha, S.-T. Huang, Y.-C. Tsou, H.-H. Chu, J.-Y. Lin, J. Wang, and S.-Y. Chen. Backward raman amplification in a plasma waveguide. *Phys. Rev. Lett.*, 101(6):065005, Aug 2008.

[150] Youbo Zhao, Tana E. Witt, and Robert J. Gordon. Efficient energy transfer between laser beams by stimulated raman scattering. *Phys. Rev. Lett.*, 103(17):173903, Oct 2009.

[151] V. M. Malkin, G. Shvets, and N. J. Fisch. Ultra-powerful compact amplifiers for short laser pulses. 7(5):2232–2240, 2000.

[152] T. Tajima and G. Mourou. Zettawatt-exawatt lasers and their applications in ultrastrong-field physics. *Phys. Rev. ST Accel. Beams*, 5(3):031301, Mar 2002.

[153] P. Gibbon. *Short Pulse Laser Interactions with Matter*. Imperial College Press, 2005.

[154] A. E. Siegman. *Lasers*. University Science Books, Mill Valley, C. A., 1986.

[155] S. C. Wilks, J. M. Dawson, W. B. Mori, T. Katsouleas, and M. E. Jones. Photon accelerator. *Phys. Rev. Lett*, 62(22):2600, 1989.

[156] C. D. Murhpy, R. Trines, J. Vieira, A. J. W. Reitsma, R. Bingham, J. L. Collier, E. J. Divall, P. S. Foster, C. J. Hooker, A. J. Langley, P. A. Norreys, R. A. Fonseca, F. Fiuza, L. O. Silva, J. T. Mendona, W. B. Mori, J. G. Gallacher, R. Viskup, D. A. Jaroszynski, S. P. D. Mangles, A. G. R. Thomas, K. Krushelnick, and Z. Najmudin. Evidence of photon acceleration by laser wake fields. *Phys. Plasmas*, 13:033108, 2006.

[157] J. M. Dias, C. Stenz, N. Lopes, X. Badiche, F. Blasco, A. Dos Santos, L. Oliveira e Silva, A. Mysyrowicz, A. Antonetti, and J. T. Mendonca. Experimental evidence of photon acceleration of ultrashort laser pulses in relativistic ionization fronts. *Phys. Rev. Lett*, 78(25):4773–4776, 1997.

[158] J. F. Drake, P. K. Kaw, Y. C. Lee, G. Schmidt, C. S. Liu, and M. N. Rosenbluth. Parametric instabilities of electromagnetic waves in plasmas. *Phys. Fluids.*, 17:778–785, 1974.

[159] W. L. Kruer. *The Physics of Laser-Plasma Interaction.* Addison-Wesleyand New York, 1988.

[160] C. B. Darrow, C. Coverdale, M. D. Perry, W. B. Mori, C. Clayton, K. Marsh, and C. Joshi. Strongly coupled stimulated raman backscatter from subpicosecond laser-plasma interactions. *Phys. Rev. Lett.*, 69(3):442–445, Jul 1992.

[161] J. Mathews and R. L. Walker. *Mathematical Methods of Physics. 2nd edn.* Addison-Wesley, Redwood City, CA, 1970.

[162] M. N. Rosenbluth and C. S. Liu. Excitation of plasma waves by two laser beams. *Phys. Rev. Lett.*, 29:701–705, 1972.

[163] T. Katsouleas, S. Wilks, P. Chen, J. M. Dawson, and J. J. Su. Beam loading in plasma accelerators. *Part. Accel*, 22:81–99, 1987.

[164] John M. Dawson. Nonlinear electron oscillations in a cold plasma. *Phys. Rev.*, 113(2):383–387, Jan 1959.

[165] S. V. Bulanov, F. Pegoraro, A. M. Pukhov, and A. S. Sakharov. Transverse-wake wave breaking. *Phys. Rev. Lett*, 78:4205–4208, 1997.

[166] C. B. Schroeder, E. Esarey, B. A. Shadwick, and W. P. Leemans. Trapping, dark current, and wave breaking in nonlinear plasma waves. *Phys. Plasmas*, 13:033103, 2006.

[167] S. Bulanov, N. Naumova, F. Pegoraro, and J. Sakai. Particle injection into the wave acceleration phase due to nonlinear wake wave breaking. *Phys. Rev. E*, 58(5):R5257–R5260, Nov 1998.

[168] P. Tomassini, M. Galimberti, A. Giulietti, D. Giulietti, L. A. Gizzi, L. Labate, and F. Pegoraro. Production of high-quality electron beams in numerical experiments of laser wakefield acceleration with longitudinal wave breaking. *Phys. Rev. ST Accel. Beams*, 6(12):121301, Dec 2003.

[169] J. B. Rosenzweig. Trapping, thermal effects, and wave breaking in the nonlinear plasma wake-field accelerator. *Phys. Rev. A*, 38(7):3634–3642, Oct 1988.

[170] E. Esarey, B. A. Shadwick, P. Catravas, and W. Leemans. Nonlinear pump depletion and electron dephasing in laser wakefield accelerators. *AIP Conference Proceedings*, 737:578–584, 2004.

[171] E. Esarey, P. Sprangle, J. Krall, and A. Ting. Overview of plasma-based accelerator concepts. *IEEE Trans. Plasma Sci.*, 24:252, 1996.

[172] W. Horton and T. Tajima. Pump depletion in the plasma-beat-wave accelerator. *Phys. Rev. A*, 34(5):4110–4119, Nov 1986.

[173] T. P. Rowlands-Rees, C. Kamperidis, S. Kneip, A. J. Gonsalves, S. P. D. Mangles, J. G. Gallacher, E. Brunetti, T. Ibbotson, C. D. Murphy, P. S. Foster, M. J. V. Streeter, F. Budde, P. A. Norreys, D. A. Jaroszynski, K. Krushelnick, Z. Najmudin, and S. M. Hooker. Laser-driven acceleration of electrons in a partially ionized plasma channel. *Phys. Rev. Lett.*, 100(10):105005, Mar 2008.

[174] P. Sprangle, E. Esarey, and A. Ting. Nonlinear theory of intense laser-plasma interactions. *Phys. Rev. Lett.*, 64:2011–2014, 1990.

[175] P. Volfbeyn, P. B. Lee, J. Wurtele, W. P. Leemans, and G. Shvets. Driving laser pulse evolution in a hollow channel laser wakefield accelerator. *Phys. Plasmas*, 4:3403, 1997.

[176] M. Born and E. Wolf. *Principles of Optics, Seventh (expanded) edition.* Cambridge University Press, 1999.

[177] Szu-yuan. Chen, A. Maksimchuk, and D. Umstadter. Experimental observation of relativistic nonlinear thomson scattering. *Nature*, 396:653–655, 1998.

[178] K. Ta Phuoc, E. Esarey, V. Leurent, E. Cormier-Michel, C. G. R. Geddes, C. B. Schroeder, A. Rousse, and W. P. Leemans. Betatron radiation from density tailored plasmas. *Phys. Plasmas*, 15:063102, 2008.

[179] B. Hidding, G. Pretzler, M. Clever, F. Brandl, F. Zamponi, A. Lübcke, T. Kämpfer, I. Uschmann, E. Förster, U. Schramm, R. Sauerbrey, E. Kroupp, L. Veisz, K. Schmid, S. Benavides, and S. Karsch. Novel method for characterizing relativistic electron beams in a harsh laser-plasma environment. *Rev. Sci. Instrum.*, 78:083301, 2007.

[180] K. A. Tanaka, T. Yabuuchi, T. Sato, R. Kodama, Y. Kitagawa, T. Takahashi, Toshiji Ikeda, Yoshihide Honda, and Shuuichi Okuda. Calibration of imaging plate for high energy electron spectrometer. *Rev. Sci. Instrum.*, 76:013507, 2004.

[181] Y. Glinec, J. Faure, A. Guemnie-Tafo, V. Malka, H. Monard, J.P. Larbre, V. De Waele, J. L. Marignier, and M. Mostafavi. Absolute calibration for a broad range single shot electron spectrometer. *Rev. Sci. Instrum.*, 77(10):103301, 2006.

[182] A. J. Gonsalves, T. P. Rowlands-Rees, B. H. P. Broks, J. J. A. M. van der Mullen, and S. M. Hooker. Transverse interferometry of a hydrogen-filled capillary discharge waveguide. *Physical Review Letters*, 98(2):025002, 2007.

[183] C. G. R. Geddes, K., G. R. Plateau, Cs. Toth, E. Cormier-Michel, E. Esarey, C. B. Schroeder, J. R. Cary, and W. P. Leemans. Plasma-density-gradient injection of low absolute-momentum-spread electron bunches. *Physical Review Letters*, 100(21):215004, 2008.

[184] S. M. Wiggins, M. P. Anania, E. Brunetti, S. Cipiccia, B. Ersfeld, M. R. Islam, R. Issac, G. Raj, R. P. Shanks, G. Vieux, G. Welsh, A. Gillespie, A. MacLeod, M. Poole, and D. A. Jaroszynski. Progress toward a laser-driven x-ray free-electron laser. *SPIE Newsroom*, 2009.

[185] Nasr A. M.Hafz, Tae Moon Jeong, Il Woo Choi, Seong Ku Lee, Ki Hong Pae, Victor V. Kulagin, Jae Hee Sung, Tae Jun Yu, Kyung-Han Hong, Tomonao Hosokai, John R. Cary, Do-Kyeong Ko, and Jongmin Lee. Stable generation

of gev-class electron beams from self-guided laserplasma channels. *Nature Photonics*, 2:571–577, 2008.

[186] S. Fritzler, E. Lefebvre, V. Malka, F. Burgy, A. E. Dangor, K. Krushelnick, S. P. D. Mangles, Z. Najmudin, J.-P. Rousseau, and B. Walton. Emittance measurements of a laser-wakefield-accelerated electron beam. *Phys. Rev. Lett.*, 92(16):165006, Apr 2004.

[187] R. P. Shanks, M. P. Anania, E. Brunetti, S. Cipiccia, B. Ersfeld, J. G. Gallacher, R. C. Issac, M. R. Islam, G. Vieux, G. H. Welsh, S. M. Wiggins, and D. A. Jaroszynski. Pepper-pot emittance measurement of laser-plasma wakefield accelerated electrons. *Proc. SPIE*, 7359:735907, 2009.

[188] R. C. Issac, G. Vieux, G. H. Welsh, R. Shanks, E. Brunetti, S. Cipiccia, M. P. Anania, X. Yang, S. M. Wiggins, M. R. Islam, B. Ersfeld, J. Farmer, G. Raj, S. Chen, D. Clark, T. McCanny, and D. A. Jaroszynski. Electron beam pointing stability of a laser wakefield accelerator. *Proc. SPIE*, 7359:735915, 2009.

[189] F. Wojda, K. Cassou, G. Genoud, M. Burza, Y. Glinec, O. Lundh, A. Persson, G. Vieux, E. Brunetti, R. P. Shanks, D. Jaroszynski, N. E. Andreev, C.-G. Wahlström, and B. Cros. Laser-driven plasma waves in capillary tubes. *Phys. Rev. E*, 80(6):066403, Dec 2009.

[190] S. M. Hooker, E. Brunetti, E. Esarey, J. G. Gallacher, C. G. R. Geddes, A. J. Gonsalves, D. A. Jaroszynski, C. Kamperidis, S. Kneip, K. Krushelnick, W. P. Leemans, S. P. D. Mangles, C. D. Murphy, B. Nagler, Z. Najmudin, K. Nakamura, P. A. Norreys, D. Panasenko, T. P. Rowlands-Rees, C. B. Schroeder, C. s. Töth, and R. Trines. Gev plasma accelerators driven in waveguides. *Plasma Phys. Control. Fusion*, 49:B403–B410, 2007.

[191] X. Zhu. Ultrashort high quality electron beam from laser wakefield accelerator using two-step plasma density profile. *Rev. Sci. Instrum.*, 81:033307, 2010.

[192] S. P. Jamison, Jingling Shen, A. M. MacLeod, W. A. Gillespie, and D. A. Jaroszynski. High-temporal-resolution, single-shot characterization of terahertz pulses. *Opt. Lett*, 28:1710, 2003.

[193] I. Wilke, A. M. MacLeod, W. A. Gillespie, G. Berden, G. M. H. Knippels, and A. F. G. van der Meer. Single-shot electron-beam bunch length measurements. *Phys. Rev. Lett*, 88:124801, 2002.

[194] U. Happek, A. J. Sievers, and E. B. Blum. Observation of coherent transition radiation. *Phys. Rev. Lett.*, 67(21):2962–2965, Nov 1991.

[195] T. Takahashi, Y. Shibata, F. Arai, K. Ishi, T. Ohsaka, M. Ikezawa, Y. Kondo, T. Nakazato, S. Urasawa, R. Kato, S. Niwano, and M. Oyamada. Coherent transition radiation at submillimeter and millimeter wavelengths. *Phys. Rev. E*, 48(6):4674–4677, Dec 1993.

[196] Yukio Shibata, Kimihiro Ishi, Toshiharu Takahashi, Toshinobu Kanai, Fumitaka Arai, Shin-ichi Kimura, Toshiaki Ohsaka, Mikihiko Ikezawa, Yasuhiro Kondo, Ryukou Kato, Shigekazu Urasawa, Toshiharu Nakazato, Satoshi Niwano, Masahiro Yoshioka, and Masayuki Oyamada. Coherent transition radiation in the far-infrared region. *Phys. Rev. E*, 49(1):785–793, Jan 1994.

[197] Pamela Kung, Hung-chi Lihn, Helmut Wiedemann, and David Bocek. Generation and measurement of 50-fs (rms) electron pulses. *Phys. Rev. Lett.*, 73(7):967–970, Aug 1994.

[198] Hung-chi Lihn, Pamela Kung, Chitrlada Settakorn, Helmut Wiedemann, and David Bocek. Measurement of subpicosecond electron pulses. *Phys. Rev. E*, 53(6):6413–6418, Jun 1996.

[199] M. Ding, H. H. Weits, and D. Oepts. Coherent transition radiation diagnostic for electron bunch shape measurement at felix. *Nuclear Instruments and Methods in Physics Research Section A: Accelerators, Spectrometers, Detectors and Associated Equipment*, 393:504–509, 1997.

[200] A. H. Lumpkin, N. S. Sereno, W. J. Berg, M. Borland, Y. Li, and S. J. Pasky. Characterization and mitigation of coherent-optical-transition-radiation signals from a compressed electron beam. *Phys. Rev. ST Accel. Beams*, 12(8):080702, Aug 2009.

[201] R. Lai and A. J. Sievers. Phase problem associated with the determination of the longitudinal shape of a charged particle bunch from its coherent far-ir spectrum. *Phys. Rev. E*, 52(4):4576–4579, Oct 1995.

[202] A. Tremaine, J. B. Rosenzweig, S. Anderson, P. Frigola, M. Hogan, A. Murokh, C. Pellegrini, D. C. Nguyen, and R. L. Sheffield. Observation of self-amplified spontaneous-emission-induced electron-beam microbunching using coherent transition radiation. *Phys. Rev. Lett.*, 81(26):5816–5819, Dec 1998.

[203] A. H. Lumpkin, R. Dejus, W. J. Berg, M. Borland, Y. C. Chae, E. Moog, N. S. Sereno, and B. X. Yang. First observation of z-dependent electron-beam microbunching using coherent transition radiation. *Phys. Rev. Lett*, 86:79, 2001.

[204] J. van Tilborg. *Coherent terahertz radiation from laser-wakefield-accelerated electron beams*. PhD thesis, Eindhoven : Technische Universiteit Eindhoven, 2006.

[205] J. D. Jackson. *Classical electrodynamics*. John Wiley & Sons, Inc, 1998.

[206] V. L. Ginzburg. *The Propagation of Electromagnetic Waves in Plasmas*. Oxford, New York, Pergamon Press, 1964.

[207] S. Casalbuoni, H. Schlarb, B. Schmidt, and P. Schmüser. Far-infrared transition and diffraction radiation, part 1: Production, diffraction effects and optical propagation. Technical report, TESLA Report 2005-15, 2005.

[208] S. Casalbuoni, H. Schlarb, B. Schmidt, P. Schmüser, B. Steffen, and A. Winter. Numerical study on the electro-optic sampling of relativistic electron bunches. Technical report, TESLA Report Report 2005-01, 2005.

[209] R. C. Jones. New calculus for the treatment of optical systems. *Journal of the Optical Society of America*, 31:488493, 1941.

[210] A. G. Davies, E. H. Linfield, and M. B. Johnston. The development of terahertz sources and their applications. *Phys. Med. Biol.*, 47:3679–3689, 2002.

[211] Q. Wu and X.-C. Zhang. Free-space electro-optic sampling of terahertz beams. *Applied Physics Letters*, 67(24):3523–3525, 1995.

[212] M. Abo-Bakr, J. Feikes, K. Holldack, P. Kuske, W. B. Peatman, U. Schade, G. Wüstefeld, and H.-W. Hübers. Brilliant, coherent far-infrared (thz) synchrotron radiation. *Phys. Rev. Lett*, 90(9):094801, 2003.

[213] F. Wang, D. Cheever, M. Farkhondeh, W. Franklin, E. Ihloff, J. van der Laan, B. McAllister, R. Milner, C. Tschalaer, D. Wang, D. F. Wang, A. Zolfaghari, T. Zwart, G. L. Carr, Podobedov. B., and Sannibale. F. Coherent thz synchrotron radiation from a storage ring with high-frequency rf system. *Phys. Rev. Lett*, 96:064801, 2006.

[214] R. Kersting, K. Unterrainer, G. Strasser, H. F. Kauffmann, and E. Gornik. Few-cycle thz emission from cold plasma oscillations. *Phys. Rev. Lett*, 79(16):3038–3041, 1997.

[215] H. Hamster, A. Sullivan, S. Gordon, W. White, and R. W. Falcone. Subpicosecond, electromagnetic pulses from intense laser-plasma interaction. *Phys. Rev. Lett*, 71(17):2725–2728, 1993.

[216] H. Hamster, A. Sullivan, S. Gordon, and R. W. Falcone. Short-pulse terahertz radiation from high-intensity-laser-produced plasmas. *Phys. Rev. E*, 49:671, 1994.

[217] J. M. Byrd, Z. Hao, M. C. Martin, D. S. Robin, F. Sannibale, R. W. Schoenlein, A. A. Zholents, and M. S. Zolotorev. Tailored thz pulses from a laser-modulated electron beam. *Phys. Rev. Lett*, 96:164801, 2006.

[218] Z.-M. Sheng, K. Mima, and J. Zhang. Powerful terahertz emission from laser wake fields excited in inhomogeneous plasmas. *Phys. Plasmas*, 12:123103, 2005.

[219] Z.-M. Sheng, K. Mima, J. Zhang, and H. Sanuki. Emission of electromagnetic pulses from laser wakefields through linear mode conversion. *Phys. Rev. Lett*, 94:095003, 2005.

[220] S. P. Jamison, B. Ersfeld, and D. A. Jaroszynski. Role of propagating ionisation fronts in semiconductor generation of sub-ps thz radiation. *Current Applied Physics*, 4:217–220, 2004.

[221] Zhiping Jiang and X.-C. Zhang. Electro-optic measurement of thz field pulses with a chirped optical beam. *Appl. Phys. Lett*, 72:1945, 1998.

[222] Q. Wu, T. D. Hewitt, and X.-C. Zhang. Two-dimensional electro-optic imaging of thz beams. *Appl. Phys. Lett*, 69:1026, 1996.

[223] Zhiping Jiang and X.-C. Zhang. 2d measurement and spatio-temporal coupling of few-cycle thz pulses. *Opt. Express*, 5:243, 1999.

[224] A. H. Lumpkin, B. X. Yang, W. J. Berg, J. W. Lewellen, N. S. Sereno, and U. Happek. Electron beam bunch length characterizations using incoherent and coherent transition radiation on the aps sase fel project. *Nucl Instrum Meth A*, 445:356–361, 2000.

[225] X. Yan, A. M. MacLeod, W. A. Gillespie, G. M. H. Knippels, D. Oepts, A. F. G. van der Meer, and W. Seidel. Subpicosecond electro-optic measurement of relativistic electron pulses. *Phys. Rev. Lett*, 85:3404, 2000.

[226] Kim K. Y., B. Yellampalle, G. Rodriguez, R. D. Averitt, A. J. Taylor, and J. H. Glownia. Single-shot, interferometric, high-resolution, terahertz field diagnostic. *Appl. Phys. Lett*, 88:041123, 2006.

[227] U. Schmidhammer, V. De Waele, J.-R. Marqus, N. Bourgeois, and M. Mostafavi. Single shot linear detection of 0.0110 thz electromagnetic fieldselectro-optic sampling with a supercontinuum in balanced detection. *Appl. Phys. B: Lasers and Optics*, 94:95–101, 2008.

[228] Kazutaka Oba, Pang-Chen Sun, Yuri T. Mazurenko, and Yeshaiahu Fainman. Femtosecond single-shot correlation system: a time-domain approach. *Applied optics*, 38:3810–3817, 1999.

[229] J. D. Lawson. *The physics of charged particle beams.* Oxford University Press, London, 1988.

[230] G. Gallot and D. Grischkowsky. Electro-optic detection of terahertz radiation. *J. Opt. Soc. Am. B*, 16(8):1204–1212, 1999.

[231] G. Gallot, Jiangquan Zhang, R. W. McGowan, T.-I. Jeon, and D. Grischkowsky. Measurements of the thz absorption and dispersion of znte and their relevance to the electro-optic detection of thz radiation. *Appl. Phys. Lett*, 74:3450, 1999.

[232] V. I. Semenova. A compact synchrotron radiation source driven by a laser-plasma wakefield accelerator. *Sov. Phys. Radiophys.*, 10(8):599–604, 1967.

[233] S. C. Wilks, J. M. Dawson, and W. B. Mori. Frequency up-conversion of electromagnetic radiation with use of an overdense plasma. *Phys. Rev. Lett*, 61(3):337, 1988.

[234] M. D. Perry, O. L. Landen, A. Szöke, and E. M. Campbell. Multiphoton ionization of the noble gases by an intense 1014-w/$cm2$ dye laser. *Phys. Rev. A*, 37(3):747–760, Feb 1988.

[235] W. B. Mori. Generation of tunable radiation using an underdense ionization front. *Phys. Rev. A*, 44(8):5118–5121, Oct 1991.

[236] E. Esarey, G. Joyce, and P. Sprangle. Frequency up-shifting of laser pulses by copropagating ionization fronts. *Phys. Rev. A*, 44(6):3908, 1991.

[237] R. L. Savage Jr., C. Joshi, and W. B. Mori. Frequency upconversion of electromagnetic radiation upon transmission into an ionization front. *Phys. Rev. Lett*, 68(7):946, 1992.

[238] R. L. Savage Jr, R.P. Brogle, W.B. Mori, and C. Joshi. Frequency upshifting and pulse compression via underdense relativistic ionization fronts. *IEEE Trans. Plasma Sci.*, 21:5–19, 1993.

[239] W. Yu, Z. Xu, Z. Sheng, and X. Feng. Realization of relativistic reflectors with the use of an electron beam and ionization front. *Journal of Physics D: Applied Physics*, 26(11):2093–2095, 1993.

[240] T. Higashiguchi, N. Yugami, H. Gao, T. Niiyama, S. Sasaki, E. Takahashi, H. Ito, and Y. Nishida. Experimental observation of further frequency upshift from dc to ac radiation converter with perpendicular dc magnetic field. *Phys. Rev. Lett*, 85(21):4542, 2000.

[241] D. Hashimshony, A. Zigler, and K. Papadopoulos. Conversion of electrostatic to electromagnetic waves by superluminous ionisation fronts. *Phys. Rev. Lett*, 86(13):2806–2809, 2001.

[242] N. Yugami, T. Niiyama, T. Higashiguchi, H. Gao, S. Sasaki, H. Ito, and Y. Nishida. Experimental observation of short-pulse upshifted frequency microwaves from a laser-created overdense plasma. *Phys. Rev. E*, 65:036505, 2002.

[243] J. M. Dias, N. C. Lopes, L. O. Silva, G. Figueira, and J. T. Mendonca. Two-dimensional collision of probe photons with relativistic ionization fronts. *Phys. Rev. E*, 65:036404, 2002.

[244] J. M. Dias, N. C. Lopes, L. O. Silva, G. Figueira, J. T. Mendonca, C. Stenz, F. Blasco, A. Dos Santos, and A. Mysyrowicz. Photon acceleration of ultrashort laser pulses by relativistic ionization fronts. *Phys. Rev. E*, 66:056406, 2002.

[245] J. T. Mendonça and L. O. e Silva. Regular and stochastic acceleration of photons. *Phys. Rev. E*, 49:3520, 1994.

[246] K. L. Yeh, M. C. Hoffmann, J. Hebling, and K. A. Nelson. Generation of 10 μj ultrashort terahetz pulses by optical rectification. *Appl. Phys. Lett.*, 90:171121, 2007.

[247] F. R. Elder, A. M. Gurewitsch, R. V. Langmuir, and H. C. Pollock. Radiation from electrons in a synchrotron. *Phys. Rev.*, 71(11):829–830, Jun 1947.

[248] J. Feldhaus, J. Arthur, and J. B. Hastings. X-ray free-electron lasers. *J. Phys. B: At. Mol. Opt. Phys.*, 38:S799–S819, 2005.

[249] B. McNeil. Free electron lasers: First light from hard x-ray laser. *Nature Photonics*, 3:375–377, 2009.

[250] A. Aghababyan, M. Altarelli, C. Altucci, G. Amatuni, P. Anfinrud, P. Audebert, V. Ayvazyan, N. Baboi, J. Baehr, V. Balandin, et al. XFEL: The European X-ray Free-Electron Laser, Technical Design Report, DESY,Hamburg, 2006-097, 2006.

[251] T. Tanaka and T. (Eds.) Shintake. SCSS X-FEL Conceptual Design Report, Riken Harima Institute, Hyogo, Japan, 2005.

[252] S. Khan, K. Holldack, T. Kachel, R. Mitzner, and T. Quast. Femtosecond undulator radiation from sliced electron bunches. *Phys. Rev. Lett*, 97:074801, 2006.

[253] H.-P. Schlenvoigt, K. Haupt, A. Debus, F. Budde, O. Jackel, S. Pfotenhauer, J.G. Gallacher, E. Brunetti, R.P. Shanks, S.M. Wiggins, D. A. Jaroszynski, E. Rohwer, and H. Schwoerer. Synchrotron radiation from laser-accelerated monoenergetic electrons. *IEEE Trans. Plasma Sci*, 36(4):1773, 2008.

[254] B. J. A. Shepherd and J. A. Clarke. Construction and testing of a pair of focusing undulators for alpha-x. *EPAC*, (THPLS126–(3580)), 2006.

[255] M. Fuchs, R. Weingartner, A. Popp, Z. Major, S. Becker, J. Osterhoff, I. Cortrie, B. Zeitler, R. Hörlein, G. D. Tsakiris, U. Schramm, T. P. Rowlands-Rees, S. M. Hooker, D. Habs, F. Krausz, S. Karsch, and F. Grüner. Laser-driven soft-x-ray undulator source. *Nature. Phys*, 5:826–829, 2009.

[256] G. L. Carr, M. C. Martin, W. R. McKinney, K. Jordan, G. R. Neil, and G. P. Williams. High-power terahertz radiation from relativistic electrons. *Nature*, 420:153, 2002.

[257] A. Croft and R. Davison. *Mathematics for Engineers*. Addison Wesley, 1999.

[258] P. Luchini and H. Motz. *Undulators and free-electron lasers*. Clarendon Press, Oxford, 1990.

[259] P. L. Kapitza and P. A. M. Dirac. The reflection of electrons from standing light waves. *Proc. Cambridge Phil. Soc.*, 29:297–300, 1933.

[260] H. Motz. Applications of the radiation from fast electron beams. *Journal of Applied Physics*, 22(5):527–535, 1951.

[261] H. Motz, W. Thon, and R. N. Whitehurst. unknown title. *Journal of Applied Physics*, 24(7):826–833, 1953.

[262] R. M. Phillips. The ubitron, a high-power traveling-wave tube based on a periodic beam interaction in unloaded waveguide. *IRE Trans. Elec. Dev.*, 7:231, 1960.

[263] Norman M. Kroll and Wayne A. McMullin. Stimulated emission from relativistic electrons passing through a spatially periodic transverse magnetic field. *Phys. Rev. A*, 17(1):300–308, Jan 1978.

[264] John M. J. Madey. Stimulated emission of bremsstrahlung in a periodic magnetic field. *Journal of Applied Physics*, 42(5):1906–1913, 1971.

[265] Luis R. Elias, William M. Fairbank, John M. J. Madey, H. Alan Schwettman, and Todd I. Smith. Observation of stimulated emission of radiation by relativistic electrons in a spatially periodic transverse magnetic field. *Phys. Rev. Lett.*, 36(13):717–720, Mar 1976.

[266] D. A. G. Deacon, L. R. Elias, J. M. J. Madey, G. J. Ramian, H. A. Schwettman, and T. I. Smith. First operation of a free-electron laser. *Phys. Rev. Lett.*, 38(16):892–894, Apr 1977.

[267] M. Billardon, P. Elleaume, J. M. Ortega, C. Bazin, M. Bergher, M. Velghe, Y. Petroff, D. A. G. Deacon, K. E. Robinson, and J. M. J. Madey. First operation of a storage-ring free-electron laser. *Phys. Rev. Lett.*, 51(18):1652–1655, Oct 1983.

[268] J. A. Edighoffer, G. R. Neil, C. E. Hess, T. I. Smith, S. W. Fornaca, and H. A. Schwettman. Variable-wiggler free-electron-laser oscillation. *Phys. Rev. Lett.*, 52(5):344–347, Jan 1984.

[269] R. Warren, B. Newnam, J. Winston, W. Stein, L. Young, and C. Brau. Results of the los alamos free-electron laser experiment. *IEEE Journal of Quantum Electronics*, pages 391–401, 1983.

[270] R. Bonifacio, L. De Salvo, P. Pierini, N. Piovella, and C. Pellegrini. Spectrum, temporal structure, and fluctuations in a high-gain free-electron laser starting from noise. *Phys. Rev. Lett.*, 73(1):70–73, Jul 1994.

[271] L.-H. Yu, M. Babzien, I. Ben-Zvi, L. F. DiMauro, A. Doyuran, W. Graves, E. Johnson, S. Krinsky, R. Malone, I. Pogorelsky, J. Skaritka, G. Rakowsky, L. Solomon, X. J. Wang, M. Woodle, V. Yakimenko, S. G. Biedron, J. N. Galayda, E. Gluskin, J. Jagger, V. Sajaev, and I. Vasserman. High-Gain Harmonic-Generation Free-Electron Laser. *Science*, 289(5481):932–934, 2000.

[272] L. H. Yu, L. DiMauro, A. Doyuran, W. S. Graves, E. D. Johnson, R. Heese, S. Krinsky, H. Loos, J. B. Murphy, G. Rakowsky, J. Rose, T. Shaftan, B. Sheehy, J. Skaritka, X. J. Wang, and Z. Wu. First ultraviolet high-gain harmonic-generation free-electron laser. *Phys. Rev. Lett.*, 91(7):074801, Aug 2003.

[273] A. Gover, F. V. Hartemann, G. P. Le Sage, N. C. Luhmann, R. S. Zhang, and C. Pellegrini. Time and frequency domain analysis of superradiant coherent synchrotron radiation in a waveguide free-electron laser. *Phys. Rev. Lett.*, 72(8):1192–1195, Feb 1994.

[274] R. H. Dicke. Coherence in spontaneous radiation processes. *Phys. Rev.*, 93(1):99, Jan 1954.

[275] D. A. Jaroszynski, P. Chaix, N. Piovella, D. Oepts, G. M. H. Knippels, A. F. G. van der Meer, and H. H. Weits. Superradiance in a short-pulse free-electron-laser oscillator. *Phys. Rev. Lett.*, 78(9):1699–1702, Mar 1997.

[276] S.B. van der Geer, O.J. Luiten, M.J. de Loos, G. Pöplau, and U. van Rienen. 3d space-charge model for gpt simulations of high brightness electron bunches. *Institute of Physics Conference Series*, (175):101, 2005.

[277] B. van der Geer and M. de Loos. The General Particle Tracer code, 2001.

[278] A. J. W. Reitsma, R. A. Cairns, R. Bingham, and D. A. Jaroszynski. Efficiency and energy spread in laser-wakefield acceleration. *Phys. Rev. Lett*, 94:085004, 2005.

[279] D. A. Jaroszynski, R. J. Bakker, A. F. G. van der Meer, D. Oepts, and P. W. van Amersfoort. Coherent startup of an infrared free-electron laser. *Phys. Rev. Lett.*, 71(23):3798–3801, Dec 1993.

[280] R. Bonifacio, B. W. J. McNeil, and P. Pierini. Superradiance in the high-gain free-electron laser. *Phys. Rev. A*, 40(8):4467–4475, Oct 1989.

[281] R. Bonifacio, N. Piovella, and B. W. J. McNeil. Superradiant evolution of radiation pulses in a free-electron laser. *Phys. Rev. A*, 44(6):R3441–R3444, Sep 1991.

[282] W. P. Leemans, C. E. Clayton, K. A. Marsh, and C. Joshi. Stimulated compton scattering from preformed underdense plasmas. *Phys. Rev. Lett.*, 67(11):1434–1437, Sep 1991.

[283] K. Ta Phuoc, A. Rousse, M. Pittman, J. P. Rousseau, V. Malka, S. Fritzler, D. Umstadter, and D. Hulin. X-ray radiation from nonlinear thomson scattering of an intense femtosecond laser on relativistic electrons in a helium plasma. *Phys. Rev. Lett.*, 91(19):195001, Nov 2003.

[284] H. Schwoerer, B. Liesfeld, H.-P. Schlenvoigt, K.-U. Amthor, and R. Sauerbrey. Thomson-backscattered x rays from laser-accelerated electrons. *Phys. Rev. Lett.*, 96(1):014802, Jan 2006.

[285] R. L. Williams, C. E. Clayton, C. Joshi, C. Fellow, and T. C. Katsouleas. Studies of classical radiation emission from plasma wave undulators. *IEEE Trans. Plasma Sci*, 21(1):156, 1993.

[286] C. Joshi, T. Katsouleas, J. M. Dawson, Y. T. Yan, and J. M. Slater. Plasma wave wigglers for free-electron lasers. *IEEE J. Quantum Electron.*, QE–23(9):1571, 1987.

List of publications

• A. D. Debus, M. Bussmann, U. Schramm, R. Sauerbrey, C. D. Murphy, Zs. Major, R. Hörlein, L. Veisz, K. Schmid, J. Schreiber, K. Witte, S. P. Jamison, **J. G. Gallacher**, D. A. Jaroszynski, M. C. Kaluza, B. Hidding, S. Kiselev, R. Heathcote, P. S. Foster, D. Neely, E. J. Divall, C. J. Hooker, J. M. Smith, K. Ertel, A. J. Langley, P. Norreys, J. L. Collier, and S. Karsch, "Electron Bunch Length Measurements from Laser-Accelerated Electrons Using Single-Shot THz Time-Domain Interferometry", *Phys. Rev. Lett.*, **104**, 084802 (2010).

• **J. G. Gallacher**, M. P. Anania, E. Brunetti, F. Budde, A. Debus, B. Ersfeld, K. Haupt, M. R. Islam, O. Jäckel, S. Pfotenhauer, A. J. W. Reitsma, E. Rohwer, H.-P. Schlenvoigt , H. Schwoerer, R. P. Shanks, S. M. Wiggins, D. A. Jaroszynski, "A method of determining narrow energy spread electron beams from a laser plasma wakefield accelerator using undulator radiation", *Physics of Plasmas*, **16**, 093102, (2009).

• R. P. Shanks, M. P. Anania, E. Brunetti, S. Cipiccia, B. Ersfeld, **J. G. Gallacher**, R. C. Issac, M. R. Islam, G. Vieux, G. H. Welsh, S. M. Wiggins, and D. A. Jaroszynski,"Pepper-pot emittance measurement of laser-plasma wakefield accelerated electron", *Proc. SPIE*, **7359**, 735907 (2009).

• J. H. Sun, **J. G. Gallacher**, G. J. H. Brussaard, N. Lemos, R. Issac, Z. X. Huang, J. M. Dias, and D. A. Jaroszynski,"Electro-optic measurement of terahertz pulse energy distribution", *Rev. Sci. Instrum.*, **80**, 113103 (2009).

• H.-P. Schlenvoigt, K. Haupt, A. Debus, F. Budde, O. Jäckel, S. Pfotenhauer, H. Schwoerer, E. Rohwer, **J. G. Gallacher**, E. Brunetti, R. P. Shanks, S. M. Wiggins and D. A. Jaroszynski, "A compact synchrotron radiation source driven by a laser-plasma wakefield acceleration", *Nature Phys*, **4**, 130 (2008).

• H.-P. Schlenvoigt, K. Haupt, A. Debus, F. Budde, O. Jäckel, S. Pfotenhauer, **J. G. Gallacher**, E. Brunetti, R. P. Shanks, S. M. Wiggins, D. A. Jaroszynski, E. Rohwer and H. Schwoerer, "Synchrotron radiation from Laser-Accelerated Monoenergetic Electrons", *IEEE Trans. Plasma Sci.*, **36**, 1773 (2008).

• T. P. Rowlands-Rees, C. Kamperidis, S. Kneip, A. J. Gonsalves, S. P. D. Mangles, **J. G. Gallacher**, E. Brunetti, T. Ibbotson, C. D. Murphy, P. S. Foster, M. J. V. Streeter, F. Budde, P. A. Norreys, D. A. Jaroszynski, K. Krushelnick, Z. Najmudin, and S. M. Hooker, "Laser-Driven Acceleration of Electrons in a Partially Ionized Plasma Channel", *Phys. Rev. Lett.*, **100**, 105005 (2008).

• A. G. R. Thomas, C. D. Murphy, S. P. D. Mangles, A. E. Dangor, P. Foster, **J. G. Gallacher**, D. A. Jaroszynski, C. Kamperidis, K. L. Lancaster, P. A. Norreys, R. Viskup, K. Krushelnick, and Z. Najmudin,"Monoenergetic Electronic Beam Production Using Dual Collinear Laser Pulse", *Phys. Rev. Lett.*, **100**, 255002 (2008).

• Hooker, S. M. and Brunetti, E. and Esarey, E. and **J. G. Gallacher** and Geddes, C. G. R. and Gonsalves, A. J. and Jaroszynski, D. A. and Kamperidis, C. and Kneip, S. and Krushelnick, K. and Leemans, W. P. and Mangles, S. P. D. and Murphy, C. D. and Nagler, B. and Najmudin, Z. and Nakamura, K. and Norreys, P. A. and Panasenko, D. and Rowlands-Rees, T. P. and Schroeder, C. B. and Töth, C. s. and Trines, R., "GeV plasma accelerators driven in waveguides", *Plasma Phys. Control. Fusion*, **49**, B403-B410 (2007).

• J. H. Sun, **J. G. Gallacher**, N. Limos, R. Issac, J. M. Dias, Z. X. Huang, and D. A. Jaroszynski,"High energy terahertz pulse emission from GaAs illuminated by a femtosecond laser", *Proc. SPIE*, **6840**, 68401B (2007).

• B. Hidding, K.-U. Amthor, B. Liesfeld, H. Schwoerer, S. Karsch, M. Geissler, L. Veisz, K. Schmid, **J. G. Gallacher**, S.P. Jamison, D. Jaroszynski, G. Pretzler and R. Sauerbrey, "Generation of Quasi-monoenergetic Electron Bunches with 80-fs Laser Pulse" *Phys. Rev. Lett.*, **96**, 105004 (2006).

• C. D. Murphy, R. Trines, J. Vieira, A. J. W. Reitsma, R. Bingham, J. L. Collier, E. J. Divall, P. S. Foster, C. J. Hooker, A. J. Langley, P. A. Norreys, R. A. Fonseca, F. Fiuza, L. O. Silva, J. T. Mendona, W. B. Mori, **J. G.**

Gallacher, R. Viskup, D. A. Jaroszynski, S. P. D. Mangles, A. G. R. Thomas, K. Krushelnick and Z. Najmudin, "Evidence of photon acceleration by laser wake fields", *Phys. Plasmas*, **13**, 033108 (2006).

• S. P. D. Mangles, K. Krushelnick, Z. Najmudin, M. S. Wei, B. Walton, A. Gopal, A. E. Dangor, S. Fritzler, C. D. Murphy, A. G. R. Thomas, W. B. Mori, **J. Gallacher**, D. Jaroszynski, P. A. Norreys and R. Viskup, "The generation of mono-energetic electron beams from ultrashort pulse laserplasma interaction", *Phil. Trans. R. Soc. A*, **364**, 663 (2006).

• D. A. Jaroszynski, R. Bingham, E. Brunetti, B. Ersfeld, **J. Gallacher**, B. van der Geer, R. Issac, S. P. Jamison, D. Jones, M. de Loos, A. Lyachev, V. Pavlov, A. Reitsma, Y. Saveliev, G. Vieux and S. M. Wiggins,"Radiation sources based on laser-plasma interaction", *Phil. Trans. R. Soc. A*, **364**, 689 (2006).

• K. Krushelnick, Z. Najmudin, S. P. D. Mangles, A. G. R. Thomas, M. S. Wei, B. Walton, A. Gopal, E. L. Clark, A. E. Dangor, S. Fritzler, C. D. Murphy, P. A. Norreys, W. B. Mori, **J. Gallacher**, D. Jaroszynski, and R. Viskup, "Laser plasma acceleration of electrons Towards the production of monoenergetic beam", *Phys. Plasmas*, **12**, 056711 (2005).

• S. P. D. Mangles, C. D. Murphy, Z. Najmudin, A. G. R. Thomas, J. L. Collier, A. E. Dangor, E. J. Divall, P. S. Foster, **J. G. Gallacher**, C. J. Hooker, D. A. Jaroszynski, A. J. Langley, W. B. Mori, P. A. Norreys, F. S. Tsung, R. Viskup, B. R. Walton, and K. Krushelnick, "Monoenergetic beams of relativistic electrons from intense laser-plasma interaction", *Nature*, **431**, 535 (2004).

• R. C. Issac, G. Vieux, B. Ersfeld, E. Brunetti, S. P. Jamison, **J. Gallacher**, D. Clark, and D. A. Jaroszynski, "Ultra hard x rays from krypton clusters heated by intense laser field", *Phys. Plasmas*, **11**, 3491 (2004).